

Optimal Control, Safety Technology, and Electromagnetic Compatibility in the Driving System of Electric Vehicle

Lead Guest Editor: Yong Chen

Guest Editors: Xu Li, Fengjun Yan, Kelin Jia, and Darong Huang





**Optimal Control, Safety Technology,
and Electromagnetic Compatibility in
the Driving System of Electric Vehicle**

Journal of Control Science and Engineering

**Optimal Control, Safety Technology,
and Electromagnetic Compatibility in
the Driving System of Electric Vehicle**

Lead Guest Editor: Yong Chen

Guest Editors: Xu Li, Fengjun Yan, Kelin Jia, and Darong Huang



Copyright © 2018 Hindawi. All rights reserved.

This is a special issue published in “Journal of Control Science and Engineering.” All articles are open access articles distributed under the Creative Commons Attribution License, which permits unrestricted use, distribution, and reproduction in any medium, provided the original work is properly cited.

Editorial Board

Raquel Caballero-Águila, Spain
Hung-Yuan Chung, Taiwan
Ming-Cong Deng, Japan
Haiping Du, Australia
Ricardo Dunia, USA
Meng Joo Er, Singapore
Peilin Fu, USA
Furong Gao, Hong Kong
Carlos-Andrés García, Spain
Fengshou Gu, UK
Benoit Iung, France
Seiichiro Katsura, Japan
James Lam, Hong Kong
William MacKunis, USA
Radek Matušů, Czech Republic

Shengwei Mei, China
J.-A. Méndez-Pérez, Spain
Paolo Mercorelli, Germany
José Sánchez Moreno, Spain
Daniel Morinigo-Sotelo, Spain
Sing Kiong Nguang, New Zealand
Enrique Onieva, Spain
B. Ould Bouamama, France
Petko Petkov, Bulgaria
Manuel Pineda-Sanchez, Spain
Daniela Proto, Italy
Ruben Puche-Panadero, Spain
Gerasimos Rigatos, Greece
Michela Robba, Italy
Mario Russo, Italy

Roberto Sacile, Italy
Yang Shi, Canada
Pierluigi Siano, Italy
Gangbing Song, USA
Zoltan Szabo, Hungary
Javad M. Velni, USA
K. C. Veluvolu, Republic of Korea
Antonio Visioli, Italy
Yongji Wang, China
Ai-Guo Wu, China
Wen Yu, Mexico
Gang Zheng, France
Mohamed Zribi, Kuwait

Contents

Optimal Control, Safety Technology, and Electromagnetic Compatibility in the Driving System of Electric Vehicle

Yong Chen , Xu Li, Fengjun Yan, Kelin Jia, and Darong Huang 

Editorial (2 pages), Article ID 9202450, Volume 2018 (2018)

Stability Evaluation of Fault Diagnosis Model Based on Elliptic Fourier Descriptor

YanZhu Hu , Yu Hu , XinBo Ai, HuiYang Zhao, Zhen Meng, WenJia Tian, and Jiao Wang 

Research Article (10 pages), Article ID 1238231, Volume 2018 (2018)

A New Cooperative Anomaly Detection Method for Stacker Running Track of Automated Storage and Retrieval System in Industrial Environment

Darong Huang , Mengting Lin , Lanyan Ke , and Zhenping Deng 

Research Article (12 pages), Article ID 1938490, Volume 2018 (2018)

Improvement of Low-Frequency Radiated Emission in Electric Vehicle by Numerical Analysis

Feng Gao , Chengkai Ye , Zilong Wang, and Xu Li

Research Article (8 pages), Article ID 5956973, Volume 2018 (2018)

Robust H_{∞} Output-Feedback Yaw Control for Vehicles with Differential Steering

Paul Oke , Sing Kiong Nguang , and Wentai Qu

Research Article (11 pages), Article ID 7129240, Volume 2018 (2018)

Event-Triggered Bipartite Consensus of Single-Integrator Multi-Agent Systems with Measurement Noise

Cui-Qin Ma , Yun-Bo Zhao, and Wei-Guo Sun

Research Article (9 pages), Article ID 7186737, Volume 2018 (2018)

PID Control for Electric Vehicles Subject to Control and Speed Signal Constraints

Amanda Danielle O. da S. Dantas , André Felipe O. de A. Dantas , João Tiago L. S. Campos ,

Domingos L. de Almeida Neto , and Carlos Eduardo T. Dórea 

Research Article (11 pages), Article ID 6259049, Volume 2018 (2018)

An Electrical Insulator Defects Detection Method Combined Human Receptive Field Model

Li Guo , Yu Liao , Hongying Yao, Jinhao Chen, and Manran Wang

Research Article (9 pages), Article ID 2371825, Volume 2018 (2018)

Backstepping Control with Disturbance Observer for Permanent Magnet Synchronous Motor

Yong-Hong Lan  and Lei-Zhou

Research Article (8 pages), Article ID 4938389, Volume 2018 (2018)

Performance Analysis and Comparison for High Maneuver Target Track Based on Different Jerk Models

Qinghai Meng, Bowen Hou, Dong Li, Zhangming He, and Jiongqi Wang 

Research Article (6 pages), Article ID 6432485, Volume 2018 (2018)

An Equivalent Circuit Model for Lithium Battery of Electric Vehicle considering Self-Healing Characteristic

Zhaodi Pei , Xiaoxu Zhao, Huimei Yuan, Zhen Peng, and Lifeng Wu 

Research Article (11 pages), Article ID 5179758, Volume 2018 (2018)

Estimating Remaining Useful Life for Degrading Systems with Large Fluctuations

Dang-Bo Du, Jian-Xun Zhang , Zhi-Jie Zhou , Xiao-Sheng Si, and Chang-Hua Hu 

Research Article (11 pages), Article ID 9182783, Volume 2018 (2018)

Editorial

Optimal Control, Safety Technology, and Electromagnetic Compatibility in the Driving System of Electric Vehicle

Yong Chen ¹, Xu Li,² Fengjun Yan,³ Kelin Jia,⁴ and Darong Huang ⁵

¹*School of Automation Engineering, and Institute of Electric Vehicle Driving System and Safety Technology, University of Electronic Science and Technology of China (UESTC), Chengdu, 611731, China*

²*Chongqing Changan Automobile Co Ltd, Chongqing 400023, China*

³*Department of Mechanical Engineering McMaster University Hamilton ON L8S 4L7, Canada*

⁴*Scania Group, Vagnmakarvägen 1, Södertälje, 15187, Sweden*

⁵*School of Information Science and Engineering, Chongqing Jiaotong University, Chongqing, 400074, China*

Correspondence should be addressed to Yong Chen; yhencd@uestc.edu.cn

Received 9 December 2018; Accepted 9 December 2018; Published 24 December 2018

Copyright © 2018 Yong Chen et al. This is an open access article distributed under the Creative Commons Attribution License, which permits unrestricted use, distribution, and reproduction in any medium, provided the original work is properly cited.

The objective of this special issue is to address recent research trends and developments in the optimal control, safety technology, and electromagnetic compatibility in the driving system of electric vehicle. A substantial number of papers were submitted, and after a thorough peer review process, eleven papers were selected to be included in this special issue. These papers cover PID control for electric vehicles, stability evaluation of fault diagnosis, Event-Triggered Bipartite Consensus, robust control for vehicle, an equivalent circuit model for lithium battery of electric vehicle, cooperative anomaly detection method, electrical insulator defects detection, Target Track, low frequency radiated emission in electric vehicle, estimating remaining useful life, and backstepping control for motor. We believe that the original papers collected in this special issue highlight the contemporary topics in research related to optimal control and safety technology and will introduce readers to the latest advances in the field.

The paper by A. F. O. de A. Dantas et al. proposes a PID control for electric vehicles subject to input armature voltage and angular velocity signal constraints. The demonstrate controller constraints can improve the electric vehicle DC motor dynamic and consequently protect the motor from overvoltage, and it should be considered in the tuning process. Its author is with the Universidade Potiguar, Brazil.

The paper by Y. Hu et al. is aiming at the stability evaluation of the fault diagnosis model based on the characteristic clustering, where an image edge detection method based

on the Elliptic Fourier Descriptor (EFDSE) is proposed to evaluate the stability of the fault diagnosis model, which applies similarity measurement of image to effective evaluation of faulty diagnosis algorithm. The effectiveness of the stability evaluation is verified by the fault data of the motor bearings. Its author is with Beijing University of Posts and Telecommunications, China.

The paper by C.-Q. Ma et al. presents event-triggered bipartite consensus of single-integrator multiagent systems being investigated in the presence of measurement noise. A time-varying gain function is proposed in the event-triggered bipartite consensus protocol to reduce the negative effects of the noise corrupted information processed by the agents. Its authors are with Qufu Normal University, China

The paper by P. Oke et al. examines the problem of designing a robust H1 output feedback yaw controller with both input and output constraints for four independently in-wheel driven Electric Vehicles (EVs) with differential steering. Specifically, the controller aims are to ensure the stability and improve the performance of the EV despite variations in the road adhesion coefficient, longitudinal velocity, and external disturbance. Finally, the capability of the developed controller is simulated on a vehicle model with uncertain road conditions and longitudinal velocities. Its author is with the University of Auckland, New Zealand.

The paper by L. Wu et al. proposes a self-healing characteristic based equivalent circuit model of lithium battery. The mathematical description of the lithium battery in the

self-healing process is obtained through the analysis of the equivalent circuit model. Based on experimental platform, an experiment considering self-healing characteristics was performed. Result shows that the self-healing characteristic based lithium battery equivalent circuit model can describe the voltage of the lithium battery accurately during the self-healing process. Its author is with Capital Normal University, China.

The paper by D. Huang et al. proposes a cooperative detection method based on Pulse Coupling Neural Network (PCNN) and wavelet transform theory to detect the abnormal points of the stacker running rail in industrial environment by analyzing the variation signals. The experimental simulation and example simulation show that the cooperative detection method based on PCNN and wavelet transform theory can effectively detect and locate the anomaly points of the stacker running tracks. The expansibility in engineering applications is promising. The paper was reviewed three times by the editor Daniel Morinigo-Sotelo, because the paper is related to the guest editor Darong Huang, who is with Chongqing Jiaotong University, China.

The paper by Y. Liao et al. proposes an insulator defect detection method inspired by human receptive field model, which meets the requirements for detecting defect insulator in a simple background. In this method, the defect detection combine human receptive field model of human visual system is constructed and applied on the different insulators, so as to achieve accurate detection of the insulator defected parts. Experimental results show that the method can accurately and robustly detect the defect (such as cracks and damages) of electrical insulator in case of noise affect. Its author is with Hubei University for Nationalities, China

The paper by Bo. Hou et al. presents four Jerk models commonly used in the maneuvering target track. The performance of different Jerk models for target track with the state variables and the characters are compared. The Jerk model is widely used for the track of the maneuvering targets. The mathematical simulations show that Jerk model with self-adaptive noise variance has the best robustness while other models may diverge when the initial error is much larger. If the process noise level is much lower, the track accuracy for four Jerk models is similar and stationary in the steady track situation, but it will be descended greatly in the much highly maneuvering situation. Its author is with National University of Defense Technology, China

The paper by F. Gao et al. proposes a methodology for improving of vehicle-level radiated electromagnetic interference (EMI) in electric vehicle (EV). This methodology predicts vehicle-level radiated EMI by using the multiport network theory, based on analyzing the contribution from each electronic component to find out the main EMI source. To validate its effectiveness, the proposed methodology is applied in an actual EV for low-frequency radiate demissions. Simulation in a commercially available electromagnetics software and measurement in the EV are combined to predict the vehicle-level emissions, and then the electronic component with the greatest EMI that causes failure to meet the EMC standard is identified. After improving this component, the vehicle-level radiated emission is reduced to comply with the

EMC standard, proving that the presented numerical method is effective. The proposed methodology can also be used in other EMC issues, regardless of the amount of interference sources and sensitive equipment. The paper was reviewed three times by the editor Daniela Proto, because the paper is related to the guest editor Xu Li's group; the author is with Chongqing University, China.

The paper by C.-H. Hu et al. proposes a new degradation model for remaining useful life (RUL) estimation based on the volatility of degradation data. Degradation model base RUL prediction method has been one of the most important parts in prognostics and health management; at last, two practical cases show that the proposed model can deal with the degradation data with many fluctuations better and get the more reasonable result which is convenient for maintenance decision. Its author is with High-tech institute of Xi'an, China

The paper by Y.-H. Lan et al. presents a disturbance observer-based (DOB) backstepping speed tracking control method, for the speed tracking control problem of Permanent Magnet Synchronous Motor (PMSM). The obtained controller can achieve high precision speed tracking and disturbance rejection. Finally, some results of evaluative experiments verified the effectiveness of the proposed method for high-performance control and disturbance rejection for the PMSM drive. Its author is with Xiangtan University, China

Conclusion

The eleven papers are from eleven universities or institutes and from three countries. The topic is an interesting topic, and many researchers required delaying the call for paper, but there are also some regrets, as EV researcher, EV company, and EV administer could not present their studies.

Conflicts of Interest

All editors declare that there are no conflicts of interest or private agreement with companies regarding the publication of their papers.

Acknowledgments

We would like to thank all the authors who contributed to this special issue. Many thanks are due to our expert reviewers and our editor group. This publication would not be possible without the participation of them.

*Yong Chen
Xu Li
Fengjun Yan
Kelin Jia
Darong Huang*

Research Article

Stability Evaluation of Fault Diagnosis Model Based on Elliptic Fourier Descriptor

YanZhu Hu , **Yu Hu** , **XinBo Ai**, **HuiYang Zhao**,
Zhen Meng, **WenJia Tian**, and **Jiao Wang** 

School of Automation, Beijing University of Posts and Telecommunications, No. 10 Xi Tu Cheng Road, Beijing/100876, China

Correspondence should be addressed to Yu Hu; hu_yu@bupt.edu.cn

Received 1 June 2018; Accepted 24 July 2018; Published 15 November 2018

Academic Editor: Yong Chen

Copyright © 2018 YanZhu Hu et al. This is an open access article distributed under the Creative Commons Attribution License, which permits unrestricted use, distribution, and reproduction in any medium, provided the original work is properly cited.

The performance evaluation of fault diagnosis algorithm is an indispensable link in the development and acceptance of the fault diagnosis system. Aiming at the stability evaluation of the fault diagnosis model based on the characteristic clustering, an image edge detection method based on the Elliptic Fourier Descriptor (EFDSE) is proposed to evaluate the stability of the fault diagnosis model, which applies similarity measurement of image to effective evaluation of faulty diagnosis algorithm. The quantitative evaluation index of the diagnostic capability of characterization based cluster fault diagnosis model is used to provide reference for the acceptance and reliability of the diagnosis results. Finally, the effectiveness of the stability evaluation is verified by the fault data of the motor bearings.

1. Introduction

With the development of modern industrial technology and information technology, manufacturing systems in various fields such as new energy, communication, computer, and industry are becoming more and more complex. Due to the complexity of the structure and the influence of various potential factors, the system inevitably exists as the hidden trouble. Once the hidden danger is induced, the personnel and economic loss of different degree will be caused. Therefore, the method of system fault diagnosis has become the focus of researchers. There are three common fault diagnosis methods: fault diagnosis based on control model [1], diagnosis based on statistical method [2], and fault diagnosis based on Artificial Intelligence [3]. At present, a large number of studies have focused on optimizing the stability of the fault diagnosis model, usually measured by the degree of diagnosis, and the higher the stability of the model in practical application is, the more cost will be paid. Therefore, it is necessary to analyse the effect of model stability on the effectiveness of fault diagnosis. However, there is still a lack of unified system for measuring the accuracy of models. The main methods are relative deviation and residual squared sum method [4] which are error analysis method,

grey correlation theory [5] and ED train based on statistical data, Confidence interval [6], etc. The grey correlation theory can realize the diagnosis of multi data input, but it can only be applied within the range of the same characteristic parameters and cannot be used to compare with fault diagnosis with parameters of different feature ranges. Residual squared sum method is an evaluation method for regression model. It is not conducive to relative comparison between different fault diagnosis models, which is influenced by the absolute value of the dependent variable and the independent variable. The confidence interval index is based on the hypothesis that the result of the training data group's diagnosis conforms to the normal distribution. It will produce a large number of errors in the case of small data, and the upper limit of confidence interval does not converge to 1 with the increase of the accuracy. Therefore, it is not suitable for models with high accuracy in fault diagnosis.

On the basis of the above research, considering the true distribution of the fault diagnosis output, the stability evaluation method of fault diagnosis model based on Elliptic Fourier Descriptor is proposed, which apply similarity measurement to evaluation of faulty diagnosis algorithm and can provide objective evaluation without understanding the parameters of the fault diagnosis model, when using the fault

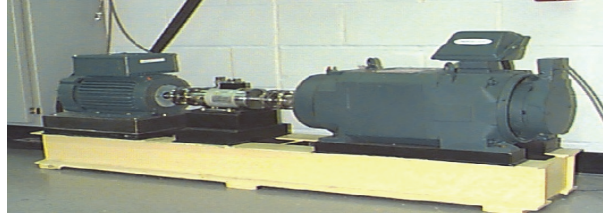


FIGURE 1: An experimental platform for fault simulation of motor bearing.

TABLE 1: Partial drive end and fan end of bearing fault data.

i	DE	FE	i	DE	FE	i	DE	FE
1	-0.0028	-0.2472	13	-0.2110	0.0119	26	0.2659	0.2786
2	-0.0963	0.1428	14	-0.0468	0.1824	27	0.0218	-0.0351
3	0.1137	0.0033	15	0.2021	-0.0754	28	-0.1639	0.1545
4	0.2573	-0.1068	16	-0.0145	-0.0536	29	0.1420	0.1999
5	-0.0583	0.1360	17	-0.1628	0.0805	30	0.2311	-0.0980
6	-0.1260	-0.0051	18	0.1092	-0.1389	31	-0.1075	0.0105
7	0.2074	-0.0625	19	0.1871	-0.0555	32	-0.1402	0.0988
8	0.1727	0.2735	20	-0.1593	0.1650	33	0.1915	-0.0555
9	-0.2199	0.1473	21	-0.1377	-0.1582
10	-0.1561	-0.0925	22	0.2505	0.0370
11	0.2240	0.1709	23	0.1075	0.3096
12	0.1137	0.0427	24	-0.2469	-0.0857	n

diagnosis model based on the feature clustering to diagnosis faulty. The application example of motor bearing diagnosis is compared and verified, which proves that the method proposed in this paper is effective.

2. System Description and Model

In order to train and verify the new technology and new theory of motor bearing fault, a motor bearing state evaluation system developed by Rockwell has obtained a series of motor performance database [7] which can be used to verify or improve the performance evaluation of motor. Some projects that have been or are making use of these databases include Winsnode state assessment technology, model-based diagnosis technology, and motor speed determination algorithm. The experimental platform is shown in Figure 1.

As shown in Figure 1, the train stand consists of a 2 hp motor (left), a torque transducer/encoder (center), a dynamometer (right), and control electronics (not shown). The train bearings support the motor shaft. Single point faults were introduced to the train bearings using electrodischarge machining with fault diameters of 7 mils, 14 mils, 21 mils, 28 mils, and 40 mils (1 mil=0.001 inches). See FAULT SPECIFICATIONS for fault depths. SKF bearings were used for the 7, 14, and 21 mils diameter faults, and NTN equivalent bearings were used for the 28 mil and 40 mil faults. Drive end and fan end bearing specifications, including bearing geometry and defect frequencies, are listed in the BEARING SPECIFICATIONS.

Vibration data was collected using accelerometers, which were attached to the housing with magnetic bases.

Accelerometers were placed at the 12 o'clock position at both the drive end and the fan end of the motor housing. During some experiments, an accelerometer was attached to the motor supporting base plate as well. Vibration signals were collected using a 16 channel DAT recorder and were post processed in a Matlab environment. All data files are in Matlab (*.mat) format. Digital data was collected at 12,000 samples per second, and data was also collected at 48,000 samples per second for drive end bearing faults. Speed and horsepower data were collected using the torque transducer/encoder and were recorded by hand.

Outer raceway faults are stationary faults; therefore placement of the fault relative to the load zone of the bearing has a direct impact on the vibration response of the motor/bearing system. In order to quantify this effect, experiments were conducted for both fan and drive end bearings with outer raceway faults located at 3 o'clock (directly in the load zone), at 6 o'clock (orthogonal to the load zone), and at 12 o'clock.

Data files are in Matlab format. Each file contains fan and drive end vibration data as well as motor rotational speed. For all files, the following item in the variable name indicates

DE: drive end accelerometer data

FE: fan end accelerometer data

BA: base accelerometer data

time: time series data

RPM: rpm during training

Part of the data is shown in Table 1 part of the drive end bearing failure data.

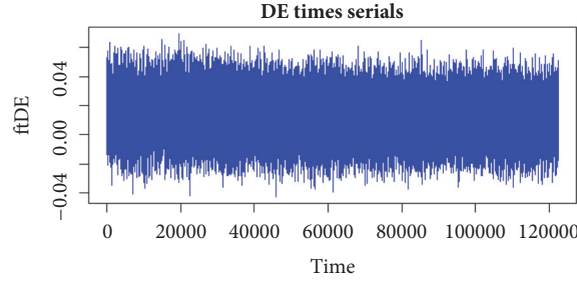


FIGURE 2: DE time series.

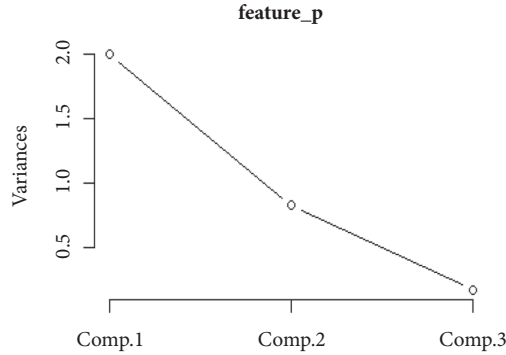


FIGURE 3: DE eigenvector principal component analysis.

3. Fault Diagnosis Model Based on Feature Clustering

Clustering analysis is a kind of unsupervised learning. It does not need to define the classes in advance or give a training sample to indicate what the data should have. Data sets can be divided into a number of different classes, and the intraclass data have very high similarity. This is very applicable where no standard information signs can be identified, such as fault diagnosis. Because some system parameters, environmental interference and noise are difficult to be confirmed accurately in the real environment, it is difficult to establish an accurate model of fault diagnosis model. Based on the data driven method, it avoids the mathematical modeling of the process and can be learned through historical data when the information of the diagnosis of the object mechanism is not clear. It can learn and model through historical data to complete the fault diagnosis. Commonly used clustering algorithms are Kmeans [8], BRICH [9], EM, DBSCN [10], CLARANS [11], etc. This paper mainly studies the stability evaluation method of fault diagnosis model (EFDSE). Therefore, Clara, Kmeans, and Dbscan are directly used for fault diagnosis of motor driven end bearing (DE) based on feature clustering. These clustering algorithms are distance-based clustering and density-based clustering, respectively. The data DE is a time series, as shown in Figure 2

In the process of fault diagnosis of motor bearings, the effect of fault feature extraction determines the final diagnosis rate. The peak to average ratio (PAR), kurtosis (KURTOSIS), and bias (SKEWNESS) of the vibration data cover the distribution features, statistical characteristics, and linear

characteristics of the vibration, which can effectively reflect the main characteristics of the vibration events. Therefore, this paper regards these three characteristics as the basis of fault diagnosis, specific calculation method, and specific calculation method (1)(2)(3):

$$PAR = E \left\{ \max \frac{(y^2)}{E(y^2)} \right\} \quad (1)$$

y: peak power

$$K = \frac{\int_{-\infty}^{+\infty} [x(t) - \bar{x}]^4 p(x) dx}{\sigma^4} \quad (2)$$

$$S = \frac{E(X - \bar{x})^3}{\sigma^3} \quad (3)$$

$x(t)$: instantaneous amplitude; \bar{x} : mean amplitude; $p(x)$: probability density; σ : standard deviation

Because of some eigenvectors of vibration may have certain correlation, the stability of clustering fault diagnosis models will be affected. Therefore, removing relevant eigenvectors is the first step to accomplish fault diagnosis. In this paper, principal component analysis (PCA) is used to extract unrelated feature vectors. The calculation results are shown in Figure 3. It can be seen that PAR and KURTOSIS can represent the feature vectors of DE, as shown in Table 2.

In order to effectively verify the reliability of the proposed evaluation method, this paper adopts DB (Davies-Bouldin) [12], Dunn Validity Index (DVI) [13], and Silhouette coefficient (SC) [14]. More than ten indexes of clustering evaluation are used to pre-evaluate the optimal number of

TABLE 2: DE eigenvector table.

i	PAR	KURT	i	PAR	KURT	i	PAR	KURT
1	3.2648	-0.3647	10	3.1979	-0.1333	19	3.4168	1.0757
2	3.0934	-0.3537	11	3.1780	-0.2197	20	3.7441	1.3899
3	3.0752	-0.4350	12	3.2202	-0.2486	21	3.7571	1.5904
4	3.0823	-0.4159	13	3.8729	1.5753	22	3.7994	1.5775
5	3.2896	0.0833	14	3.7868	1.7356	23	3.7263	1.3241
6	3.3391	0.2690	15	3.6880	1.5991	24	3.5290	0.6109
7	3.3191	0.1479	16	3.6230	1.4547
8	3.2075	0.2307	17	4.1758	1.8610
9	3.5993	-0.1001	18	3.5839	1.7459	n

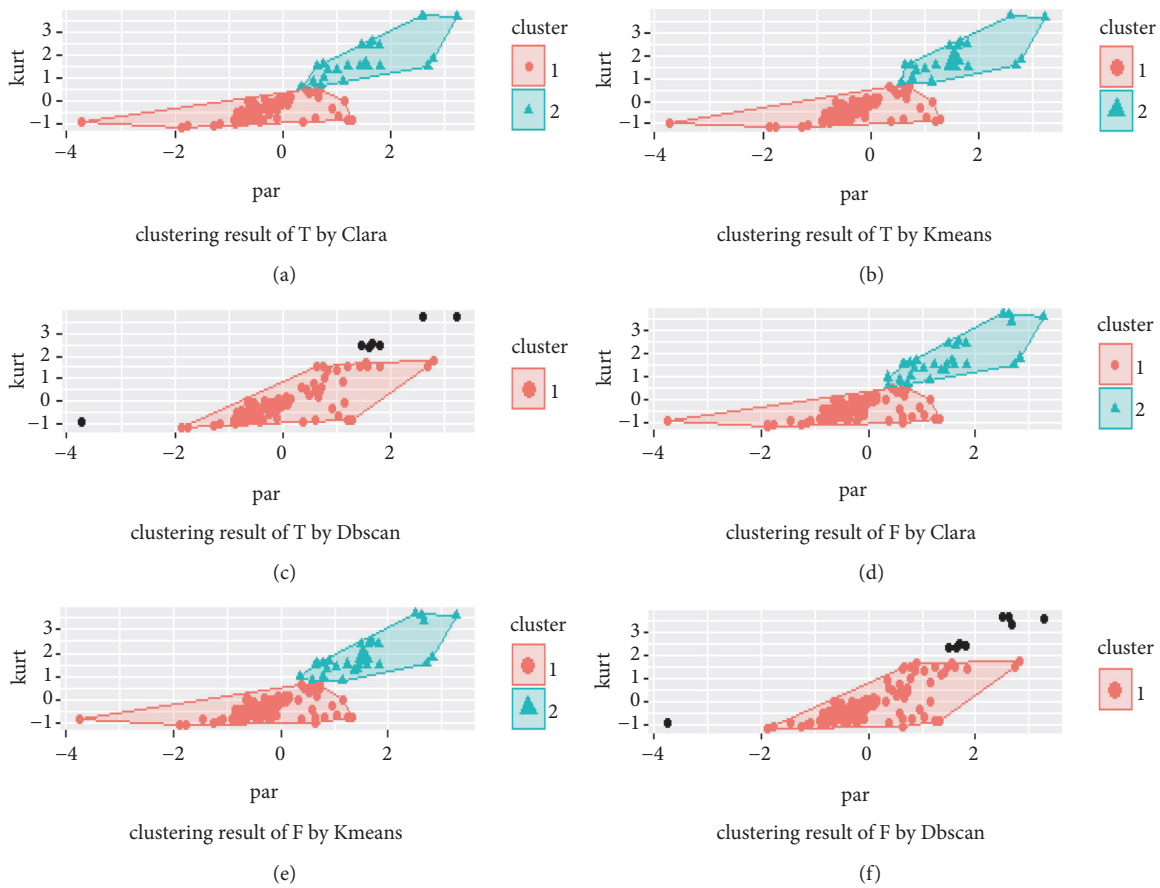


FIGURE 4: (a) Results of Clara clustering of T sets. (b) Results of Kmeans clustering of T sets. (c) Results of Dbscan clustering of T sets. (d) Results of Clara clustering of F sets. (e) Results of Kmeans clustering of F sets. (f) Results of Dbscan clustering of F sets.

DE eigenvectors, and motor bearing faults are classified into two categories. That is to say, Clara, Kmeans, and Dbscan will be used to divide the faults into two categories by means of Euclidean distance, respectively. In order to verify the effectiveness of the proposed method, the training sets T is randomly extracted from the feature sets F according to the proportion of 3:1, and then the training set T and the feature set F are divided into two categories, respectively. The results of the classification are as in Figure 4.

The first class data corresponding to the training set T and the feature set F are extracted respectively. See Figure 5.

In order to evaluate the stability of the fault diagnosis model based on feature clustering, the 2D points need to be mapped to a graphic based on a certain rule. This paper will use Dirichlet tessellation to accomplish points mapped. The Dirichlet (Delaunay) mosaic, also known as Voronoi Diagram or Thiessen Polygon, is a structure of computational geometry, which can be used for qualitative analysis, statistical analysis, and adjacent analysis [15]. In this paper, the Euclidean distance between any two points in the first category is computed. Any point is seen as the vertex of a triangle will be connected to two nearest points of Euclidean

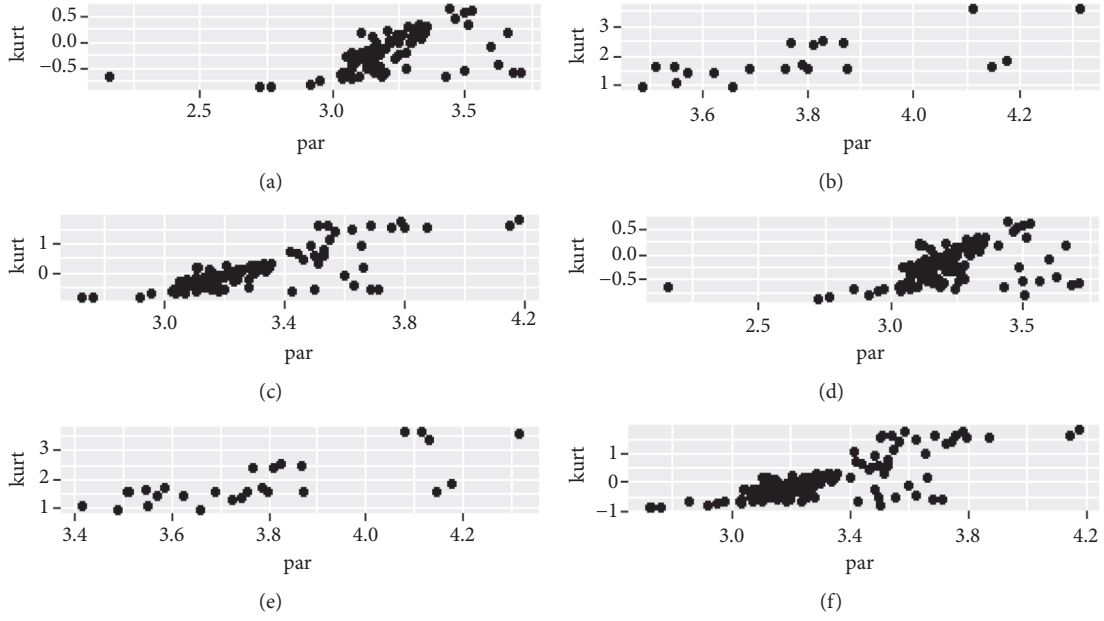


FIGURE 5: (a) The class I of Clara clustering of T sets. (b) The class I of Kmeans clustering of T sets. (c) The class I of Dbscan clustering of T sets. (d) The class I of Clara clustering of F sets. (e) The class I of Kmeans clustering of F sets. (f) The class I of Dbscan clustering of F sets.

distance, and Delaunay triangulation can be obtained by N iterations. All triangle of the common point is recorded, the circle center of the triangle is found, and the clockwise connection of the center of the center is the corresponding Thiessen Polygon. The time complexity of the triangle is the complexity of the polygon. The algorithm flow is as follows.

Hypothesis: $(X, Y) = \{(x_1, y_1), (x_2, y_2), (x_3, y_3), \dots, (x_n, y_n)\}$. It represents the point set P consisting of N nonrepeating points on the plane, and the specific steps of constructing the Delaunay triangulation of point set P is as follows.

The N points are mainly based on X coordinates and are sorted by Y coordinates.

Step 1. The N points are sorted by mainly based on X coordinates.

Step 2. Structural process is as follows:

- (i) If $N = 2$, return
- (ii) If $N = 3$, three points are connected to construct a triangulation net and return
- (iii) The N points are divided into subsets P_l and P_r on the basis of evenly principle or nearest neighbor principle
- (iv) Construct triangular net $DT(P_l)$ of P_l
- (v) Construct triangular net $DT(P_r)$ of P_r
- (vi) $DT(P_l)$ merge with $DT(P_r)$ and put back

Step 3. Merge process

- (i) For given $DT(P_l)$ and $DT(P_r)$, calculate convex hull of P_l and P_r
- (ii) Obtain the top tangent UCT and the bottom tangent BCT

- (iii) Start from BCT , according to left endpoint, right endpoint, and their adjacent points to complete $DT(P_l)$ and merge with $DT(P_r)$ until the UCT is encountered.

The Voronoi diagram of the class I of T sets and F sets is shown in Figure 6.

4. EFDSE Algorithm

4.1. Edge Detection. Canny edge detection operator has obvious advantages compared with Roberts Cross operator, Prewitt operator, Sobel operator, and Kirsch operator. So in this article, edge detection is performed by Canny operator to identify its contour boundaries.

First, in order to smooth the image to reduce the obvious noise influence on the edge detector, the image adopted is the Gauss filter to check the image by Gauss filter whose size is 2×2 , as follows:

$$H_{ij} = \frac{1}{2\pi} \exp\left(-\frac{(i - (k+1))^2 + (j - (k+1))^2}{2\sigma^2}\right) \quad (4)$$

If a window A whose size is 3×3 in the image is, pixel e will be filtered. Then, after Gauss filtering, the brightness value of the pixel e is

$$e = H * A = \begin{bmatrix} h_{11} & h_{12} & h_{13} \\ h_{21} & h_{22} & h_{23} \\ h_{31} & h_{32} & h_{33} \end{bmatrix} * \begin{bmatrix} a & b & c \\ d & e & f \\ g & h & i \end{bmatrix} \quad (5)$$

$$= \text{sum} \left(\begin{bmatrix} a \times h_{11} & b \times h_{12} & c \times h_{13} \\ d \times h_{21} & e \times h_{22} & f \times h_{23} \\ g \times h_{31} & h \times h_{32} & i \times h_{33} \end{bmatrix} \right)$$

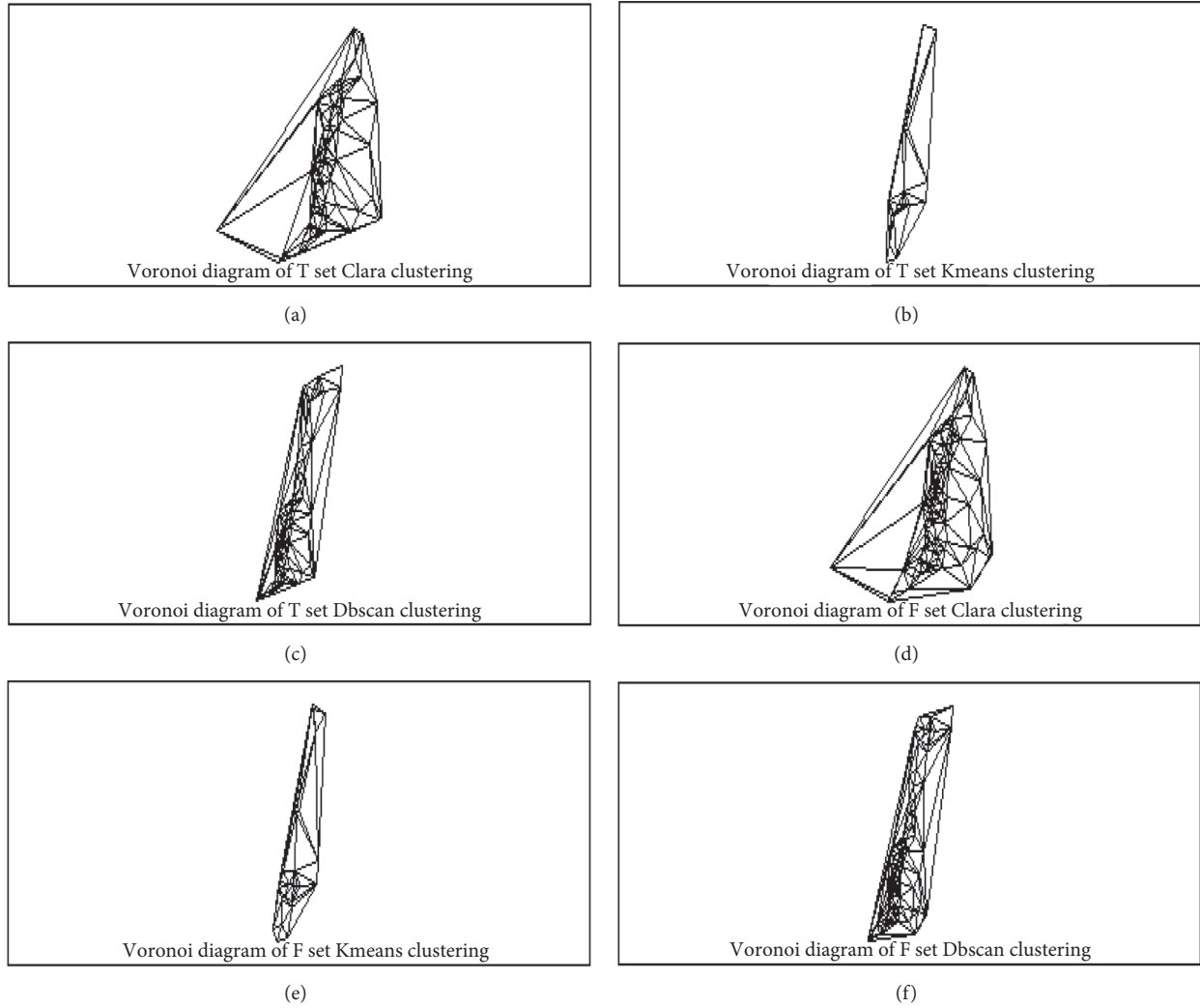


FIGURE 6: (a) Voronoi diagram of T set clara clustering. (b) Voronoi diagram of T set kmeans clustering. (c) Voronoi diagram of T set dbscan clustering. (d) Voronoi diagram of F set clara clustering; (e) Voronoi diagram of F set kmeans clustering. (f) Voronoi diagram of F set Dbscan clustering.

where $*$ is a convolution symbol; *sum*: the sum of all elements in the representation matrix. The Canny algorithm uses four operators to detect the horizontal, vertical, and diagonal edges of the image. The operator of the edge detection returns the first-order value θ of the horizontal and vertical directions G_y ; thus the gradient intensity G and θ which is direction gradient of the pixels can be determined.

$$G = \sqrt{G_x^2 + G_y^2} \quad (6)$$

$$\theta = \arctan\left(\frac{G_y}{G_x}\right)$$

The gradient strength of the current pixel is compared with the two pixels along the positive and negative gradient direction. If the gradient intensity of the current pixel is maximum compared to the other two pixels, the pixel is retained as the edge point; otherwise the pixel is suppressed, which is called the maximum value suppression. After exerting

maximum suppression, there are still some edge pixels caused by the change of noise and color. In order to solve these stray responses, the selection of high and low threshold is established. If edge pixels are higher than the high threshold, the edge pixels are marked as strong edge pixels; if the gradient value of the edge pixels is less than the high threshold is larger than the low threshold, the edge pixels are recorded as the weak edge pixels, but if the 8 neighborhood pixels of the weak edge pixels have one strong edge pixel, they can be retained as edge points; if the edge pixels are pixels, the edge pixels can be retained as edge pixels. The gradient is less than the low threshold, and it is suppressed. Figure 6 is detection by Canny operator. Their Edge contour IS detected (see Figure 7).

4.2. Fourier Descriptor. Shape is one of the most important visual features of a target. The existing shape representation methods can be divided into two categories: shape representation based on region feature and shape representation based

$$\begin{aligned}
&= \frac{a_0}{2} + \sum_{k=1}^{\infty} \left[\frac{a_k - jb_k}{2} e^{jkwt} + j \frac{a_k + jb_k}{2} e^{-jkwt} \right] \\
&= c_0 + \sum_{k=1}^{\infty} [c_k e^{jkwt} + c_{-k} e^{-jkwt}] = \sum_{k=1}^{\infty} [c'_k e^{jkwt}]
\end{aligned} \tag{8}$$

If we define $c_k = c_{k1} - jc_{k2}$, $c_{-k} = c_{k1} + jc_{k2}$
Then, (8) can be derived by

$$\begin{aligned}
c(t) &= c_0 + 2 \sum_{k=1}^{\infty} \left[c_{k1} \left(\frac{e^{jkwt} + e^{-jkwt}}{2} \right) \right. \\
&\quad \left. - jc_{k2} \left(\frac{-e^{jkwt} + e^{-jkwt}}{2} \right) \right] = c_0 \\
&\quad + 2 \sum_{k=1}^{\infty} [c_{k1} \cos(kwt) + c_{k2} \sin(kwt)] = c_0 \\
&\quad + \sum_{k=1}^{\infty} [a_k \cos(kwt) + b_k \sin(kwt)]
\end{aligned} \tag{9}$$

where a_k and b_k are said to Fourier Descriptor

Then, c_k and c_{-k} can be derived by (8) and (9)

$$\begin{aligned}
c_k &= \frac{a_k - jb_k}{2}, \\
c_{-k} &= \frac{a_k + jb_k}{2}
\end{aligned} \tag{10}$$

The coefficients in (9) can be obtained by considering the orthogonal property. Thus, one way to compute values for the descriptors is

$$\begin{aligned}
a_k &= \frac{2}{T} \int_0^T c(t) \cos(kwt) dt, \\
b_k &= \frac{2}{T} \int_0^T c(t) \sin(kwt) dt
\end{aligned} \tag{11}$$

4.3. Fourier Description of the Edge Features of Fault Classification. Determining a starting point (x_0, y_0) of the target boundary and moving along the counter clockwise direction at a certain speed, the boundary of the boundary point coordinates can be used to describe the boundary. The cluster boundary curve of the first class data set is defined as

$$s(t) = x(t) + jy(t), \quad t = 0, 1, \dots, N-1 \tag{12}$$

t is the unit arc length along with boundary circle. In order to describe the outline of the image, the selected starting point needs to circle along the boundary curve. So, $s(t)$ is a periodic function of a period in which periodic is 2π . In order to obtain the Elliptic Fourier Descriptor of the boundary curve, Fourier series expansion is first carried out, and it can be expanded by 1D Fourier series.

$$s_k = \frac{1}{T} \int_0^T s(t) e^{-jkw t} dt \tag{13}$$

Then an expression of ellipse coefficient can be computed by (12)

$$s_k = s_{xk} + js_{yk} \tag{14}$$

Then

$$\begin{aligned}
s_{xk} &= \frac{1}{T} \int_0^T x(t) e^{-jkwt} dt, \\
s_{yk} &= \frac{1}{T} \int_0^T y(t) e^{-jkwt} dt
\end{aligned} \tag{15}$$

According to the relationship between trigonometric function and exponential function, there are

$$\begin{aligned}
s_{xk} &= \frac{a_{xk} - jb_{xk}}{2}, \\
s_{yk} &= \frac{a_{yk} - jb_{yk}}{2}, \\
s_{x-k} &= \frac{a_{xk} + jb_{xk}}{2}, \\
s_{y-k} &= \frac{a_{yk} + jb_{yk}}{2}
\end{aligned} \tag{16}$$

Then

$$\begin{aligned}
a_{xk} &= \frac{2}{m} \sum_i^m x_i \cos(kwit), \\
b_{xk} &= \frac{2}{m} \sum_i^m x_i \sin(kwit), \\
a_{yk} &= \frac{2}{m} \sum_i^m y_i \cos(kwit), \\
b_{yk} &= \frac{2}{m} \sum_i^m y_i \sin(kwit)
\end{aligned} \tag{17}$$

m is the number of sampling points in the contour curve, it is usually the half of the number of pixels in the contour curve, and x_i and y_i is the value at the sample point $x(t)$ and $y(t)$ when they lie in i . According to (16) and (17), s_k can be regarded as the sum of complex numbers. That is,

$$\begin{aligned}
s_k &= A_k - jB_k, \\
s_{-k} &= A_k + jB_k
\end{aligned} \tag{18}$$

Here

$$\begin{aligned}
A_k &= \frac{a_{xk} + ja_{yk}}{2}, \\
B_k &= \frac{b_{xk} + jb_{yk}}{2}
\end{aligned} \tag{19}$$

Equation (13) can be expressed:

$$\begin{aligned}
c(t) &= c_0 \\
&\quad + \sum_1^{\infty} (A_k - jB_k) e^{jkwt} + \sum_{-\infty}^{-1} (A_k + jB_k) e^{jkwt}
\end{aligned} \tag{20}$$

TABLE 3: Elliptical Fourier Description on the edge of fault classification.

Training set T	0.0039	0.0079	0.0157	0.0196	0.0235	0.0275	0.0314	0.0353
Feature set F	0.0034	0.068	0.0101	0.0135	0.0169	0.0203	0.0237	0.0271

TABLE 4: The index of stability Clara Kmeans Dbscan.

Index	Clara	kmeans	Dbscan
within.cluster.ss	26.26355	25.70769	49.13795
avg.silwidth	0.719723	0.734621	0.706651
EFDSE	0.8162398	0.993007	0.6741096

Then, (21) is called Elliptical Fourier Description

$$EFD = \frac{|A_k|}{|A_1|} + \frac{|B_k|}{|B_1|} \quad (21)$$

According to (21), the Ellipse Fourier Descriptor of the fault classification contour curve is to be obtained and is normalized, shown in Table 3.

4.4. Stability Evaluation of Fault Diagnosis Model Based on Elliptical Fourier Descriptor. Assume that the class I contour edge descriptor of the training set T and the feature set F is *EFD1* and *EFD2*, respectively. This paper shows that if the stability of the fault diagnosis model based on the feature clustering is good, and the cohesiveness of the class center is stronger. That is to say, when adding or removing the same characteristic of data to a certain class, changed degree of boundary shape of the cluster is very small and vice versa. Therefore, we define the similarity of the contour shapes of the two fault classification results defined as the stability evaluation criteria of the fault diagnosis model, as shown in

$$sim = \frac{|\text{cov}(EFD1, EFD2)|}{\sigma_{EFD1} * \sigma_{EFD2}} \in [0, 1] \quad (22)$$

$\text{cov}()$ represents the covariance of the two descriptors; σ represents the standard deviation of the descriptor vectors. The range of *sim* is $[0, 1]$. Value of *sim* is close to 1; then stability of fault diagnostic is better.

5. Experimental Results and Discussion

The clustering results are usually verified by two kinds of techniques: one is the intracluster distance such as the within.cluster.ss calculation that is the square of each internal distance. The more similar the characteristics of the data in cluster, the better the clustering effect. The other is the distance between clusters such as the average contour coefficient calculated by avg.silwidth. The larger the value, the larger the difference of the data feature of different classes and the better the data area diversity of the clustering algorithm. The within.cluster.ss index and avg.silwidth index of the three clustering results are compared with the EFDSE index in this paper (show in Table 4). As seen from the table, EFDSE indicates that diagnosis effect of Kmeans is the best, Clara is the second, and the Dbscan is the worst. It is consistent with

the conclusion of avg.silwidth and within.cluster.ss, which proves that proposed EFDSE method in this paper is effective for the stability evaluation of the fault diagnosis model based on the feature clustering.

6. Conclusion

EFDSE that map the fault classification results in 2D graphic, using graphic edge detection technology. By extracting the feature vectors of the contour curves of fault classification results, the contour shape similarity is calculated to evaluate the effect of fault diagnosis. It is a new method of stability evaluation based on feature clustering fault diagnosis model. It applies similarity measurement of image to valuation of faulty diagnosis algorithm. In the case of unknown data samples and data methods, the stability of the model fault diagnosis effect is evaluated only by the visual contour feature vectors of the fault classification results. From the experimental method and principle, the evaluation is applicable to the stability evaluation of fault diagnosis models based on feature clustering. But used clustering algorithm should be distance-based clustering and density-based clustering. Making EFDSE is fit for more and more faulty diagnosis method is our work direction in future.

Data Availability

The data used to support the findings of this study are available from the corresponding author upon request.

Conflicts of Interest

The authors declare that they have no conflicts of interest.

Acknowledgments

The authors thank all challenge participants for their invaluable contribution. This paper is supported by National key research and development plan (2016YFC0701309) and by the National Natural Science Foundation of China (61627816).

References

- [1] W. Wang, L. Cui, and D. Chen, "Multi-scale morphology analysis of acoustic emission signal and quantitative diagnosis

- for bearing fault,” *Acta Mechanica Sinica*, vol. 32, no. 2, pp. 265–272, 2016.
- [2] X. Chen, S. Wang, B. Qiao, and Q. Chen, “Basic research on machinery fault diagnostics: Past, present, and future trends,” *Frontiers of Mechanical Engineering*, vol. 13, no. 2, pp. 264–291, 2018.
- [3] M. Witczak, M. Mrugalski, and J. Korbicz, “Towards Robust Neural-Network-Based Sensor and Actuator Fault Diagnosis: Application to a Tunnel Furnace,” *Neural Processing Letters*, vol. 42, no. 1, pp. 71–87, 2015.
- [4] Du. Kun, *water supply network hydraulic model checking and leakage location research*, Chongqing University, 2014.
- [5] K. S. Prasad, S. R. Chalamalasetti, and N. R. Damera, “Application of grey relational analysis for optimizing weld bead geometry parameters of pulsed current micro plasma arc welded inconel 625 sheets,” *The International Journal of Advanced Manufacturing Technology*, vol. 78, no. 1-4, pp. 625–632, 2015.
- [6] Y. Xiyun, L. Yuqi, and L. Jianlin, “method of calculating confidence interval of energy storage photovoltaic power station based on four division method,” *Journal of electrical technology*, vol. 15, pp. 136–144, 2017.
- [7] *Fault data of motor bearing*, 2009, <http://csegroups.case.edu/bearingdatacenter/pages/download-data-file>.
- [8] S. H. Steinberg, “United States of America,” p. 765, 1954.
- [9] T. Zhang, R. Ramakrishnan, and M. Livny, “BIRCH: a new data clustering algorithm and its applications,” *Data Mining and Knowledge Discovery*, vol. 1, no. 2, pp. 141–182, 1997.
- [10] T. Marwala, *Condition Monitoring Using Computational Intelligence Methods*, Springer London, London, 2012.
- [11] A. Hinneburg and D. A. Keim, “A General Approach to Clustering in Large Databases with Noise,” *Knowledge and Information Systems*, vol. 5, no. 4, pp. 387–415, 2003.
- [12] D. L. Davies and D. W. Bouldin, “A cluster separation measure,” *IEEE Transactions on Pattern Analysis and Machine Intelligence*, vol. PAMI-1, no. 2, pp. 224–227, 1978.
- [13] J. C. Dunn, “A fuzzy relative of the ISODATA process and its use in detecting compact well-separated clusters,” *Journal of Cybernetics*, vol. 3, no. 3, pp. 32–57, 1973.
- [14] A. F. Mcdaid, D. Greene, and N. Hurley, *Normalized Mutual Information to evaluate overlapping community finding algorithms*, Computer Science, 2011.
- [15] J. E. Goodman, *Handbook of discrete and computational geometry*, J. O’Rourke, Ed., CRC Press Series on Discrete Mathematics and its Applications, Boca Raton, FL, USA, 1997.
- [16] M. Nikolic, E. Tuba, and M. Tuba, “Edge detection in medical ultrasound images using adjusted Canny edge detection algorithm,” in *Proceedings of the 24th Telecommunications Forum, TELFOR 2016*, Serbia, November 2016.
- [17] H. A. A. Alasadi and M. A. Abed, *Object Recognition Using Artificial Fish Swarm Algorithm on Fourier Descriptors*, Social Science Electronic Publishing, 2017.
- [18] D. Zhang and G. Lu, “Enhanced generic Fourier descriptors for object-based image retrieval,” *IEEE International Conference on Acoustics, Speech, and Signal Processing*, 2011.
- [19] S. S. Li, Y. D. Huang, and J. W. Yang, “Affine Invariant Ring Fourier Descriptors,” *International Conference on Wavelet Analysis and Pattern Recognition*, 2013.
- [20] B. Belkhaoui, A. Toumi, and A. Khalfallah, “Fusion Fourier descriptors from the EM,” *International Journal of Computer & Information Technology*, 2014.

Research Article

A New Cooperative Anomaly Detection Method for Stacker Running Track of Automated Storage and Retrieval System in Industrial Environment

Darong Huang , Mengting Lin , Lanyan Ke , and Zhenping Deng 

College of Information Science and Engineering, Chongqing Jiaotong University, Chongqing 400074, China

Correspondence should be addressed to Mengting Lin; 622170070012@mails.cqjtu.edu.cn

Received 29 March 2018; Revised 28 September 2018; Accepted 25 October 2018; Published 11 November 2018

Academic Editor: Daniel Morinigo-Sotelo

Copyright © 2018 Darong Huang et al. This is an open access article distributed under the Creative Commons Attribution License, which permits unrestricted use, distribution, and reproduction in any medium, provided the original work is properly cited.

Considering the complexity and the criticality of the stacker equipment, in order to solve the problem that the stop accuracy of the stacker reduces or even fails to work due to abrasion of the running rail, this paper proposes a cooperative detection method based on Pulse Coupling Neural Network (PCNN) and wavelet transform theory to detect the abnormal points of the stacker running rail in industrial environment by analyzing the variation signals. First of all, considering the fact that the data is mixed up with noises because of the environment at the site and the possibility of the data acquisition equipment breaking down, a noise reduction method for the vibration signal data of stacker is constructed based on PCNN. Then, the basic theory of wavelet transform is introduced and then the rules of judging anomaly points on stackers' running tracks are discussed based on wavelet transform. In addition, a cooperative detection method based on PCNN and wavelet transform theory is carried out based on the space-time distribution feature of the vibration of the stacker orbits in the industrial environment. Then the rationality of the proposed algorithm is verified by simulation through data provided by State Grid Measuring Center of China. This paper constructs a model of the abnormal point detection of the stackers in an industrial environment. The experimental simulation and example simulation show that the cooperative detection method based on PCNN and wavelet transform theory can effectively detect and locate the anomaly points of the stacker running tracks. The expansibility in engineering applications is promising. Lastly, some conclusions are discussed.

1. Introduction

As is known to all, the stacker is a key equipment of automated storage and retrieval system (ASRS) in industrial environment. In practice scene of ASRS, the main function of the stacker is to grab, move, and stack goods from one shelf to another. Thus, the stability of stacker running track will influence the accuracy of grabbing and moving goods in practical engineering. As one of the key components of the stacker equipment, the track of the stacker is divided into upper and lower track. In fact, the stacking machine would wear, crack, sag, and bulge by long time running. And these defects will reduce the accuracy of the stacking machine. If the field engineer cannot detect and repair the defect as soon as possible, they may even cause the whole equipment to be

worn and shut down. So, how to detect the anomaly point of stacker running rail is very important for safety performance of the whole system.

In anomaly detection, domestic and foreign researchers have made a lot of progress in all aspects. Since the 1980s, the anomaly detection problem has been widely researched in the field of statistics. For examples, [1] presented an anomaly detection algorithm based on statistical theory. Unfortunately, practice has proved that the computing results of the statistical method are not ideal, because the distribution characteristics of the data must be known in advance. Obviously, the shortage limits the application scope of the method. To solve the defect, some improved detection algorithms were put forward combining with distance in [2, 3]. The obvious characteristic of the improved algorithm is required to have

a lot of domain knowledge of real systems or equipment. However, it is known to us all that the running performance of real systems or equipment is affected by various factors. Therefore, it is difficult to determine the input parameters of the algorithm. In other words, it has some disadvantages such as instability and high algorithm complexity. Thus, once the testing data is incomplete, it is difficult to determine the degree of abnormal [4]. In particular, when the data has features such as high-dimensional and sparseness, the performance of the algorithm is very poor. In order to solve the problem caused by sparse data, Rastogi and Ramaswamy proposed an improved algorithm based on density in [5]. The method can avoid the limitation of the dependence of distance to a certain context. To better handle testing data to find the abnormal data point, some detecting ideas based on depth continue to appear. For instance, some researchers presented the anomaly detection algorithm based on depth to mark each record as a point in the k dimension space. In fact, the typical DEEPLOC algorithm was proposed by Struyf and Rousseeuw in [6]. One big advantage of the algorithm is that the depth value of each point may be given according to the definition of depth. The detection rule is that a record with a smaller depth is more likely to be an anomaly point than a larger one. Thus, once the data set is organized by the depth value, the algorithm only needs to carry out the outlier detection on the lower layer of the depth value. Meanwhile, the outlier detection is not required in the record on a layer with a large depth value.

Furthermore, Zhou S and Xu W have constructed the local anomaly detection algorithm based on the deviation in [7]. The algorithm and rule may solve the problem that the existing local anomaly detection algorithms do not perform data object partition. But in real running process of the systems, the high dimensional test data would lead to increased computational complexity [8]. So, the trick to find out the abnormal point from high-dimension data set is to reduce its dimensionality. Aiming at the high dimensionality of the data set, some researchers introduced the concept of local projection scoring (LPS) and proposed an efficient abnormal point detection method of high-dimensional data in [9]. Of course, some new algorithms (for instance, neural network [10] and clustering algorithm [11]) continue to be introduced and presented to detect and monitor the abnormal points of test data. The simulation results show that these models and methods are effective in real engineering and application.

In addition, some scholars had discussed the anomaly detection in the frequency domain. For instance, to overcome the disadvantages that the window size does not change with frequency, the wavelet transform theory is usually introduced to compensate for the localization defects of the short-time Fourier transform [12]. The characteristics of multiresolution (also called multiscale) can be used to observe signal gradually from coarse to fine. The detection and observational modes are favorable for detecting singularities of the signal step by step. So, the wavelet theorem is also an ideal signal time-frequency analysis and processing tools. Among them, the most representative algorithm is the time series anomaly detection method based on wavelet transform proposed in [12].

Although the engineers and scholars have made a lot of achievements in the field of the detection of anomaly spot, the identifying and detection of abnormal data is still in its infancy of research for the stacker of ASRS. The practice application results show that there are still some problems in the methods of safety supervisory of the stacker of ASRS. As is known to all, the running performance of stacker is affected by various factors such as running environment, structural characteristics, and the optimal goal of the whole system. Hence, how to implement the detection of the abnormal points is the kernel problem of safety maintenance of stacker in ASRS. At present, there are some research achievements about the detection of a stacker's running performance. But the research is mainly focused on the structure analysis or the design of the system, and few people have done their researches from the perspective of abnormal point's detection [13]. In recent years, many new algorithms are presented and proposed based on Internet, OPC, and the fault tree to analyze the data set acquired and measured from the running state of the stacker in [14]. In engineering application, the detecting ability of the remote fault of stacker may meet the desired purpose using the proposed algorithm presented in [15, 16]. Meanwhile, Kai Zhang and his coauthors have discussed and analyzed the monitoring method based on the multimode and multivariate statistics to monitor the running state of stacker crane in [17, 18]. Experimental results show that the anomaly detection method is effective.

However, because the running state of stacker is influenced by the state of the stacker's component, the scene environment, the data acquisition equipment, and so on, the data set acquired from the system will contain a lot of noise. Obviously, the noise of data will reduce the accuracy of abnormal point's judgment. Therefore, deleting and cleaning the noise from testing data is necessary to implement and accomplish the monitoring of running state of whole stacker system. To restrain the interferences of strong background noise, Huang D.R. and his coauthors have constructed a cooperated denoising algorithm for rolling bearing of stacker in [19]. The simulation results have verified the effectiveness of health monitoring of ASRS. Notice that, in the previous scenario, the actual monitoring data obtained from the real stacker is the aliasing vibration signal. So, how to accomplish the separation of multivibration signal is a difficult problem in vibration process. If the method is reasonable, the detecting accuracy of stacker's running abnormal points will be greatly improved.

Based on the analysis and the thesis above, to ensure the effectiveness of the incomplete data processing of real system, it is necessary to construct and design a cooperative anomaly detection algorithm so that the abnormal spot can be detected and located as quickly as possible in on-site industrial environment. Notice that the timing of the real time data process is vital in the industrial environment, and then the data signal needs to be treated from coarse to fine as soon as possible. On the basis, the Pulse Coupling Neural Network (PCNN) presented in [20, 21] is introduced to denoise, because it has the advantage that the industrial data process does not depend on precise mathematics model. Meanwhile, due to the fact that the wavelet transform may complete the itemization

of the data collection, it is introduced to construct and establish the abnormal point detecting algorithm to locate the stacker's defect through the pure data processed by PCNN.

Hence, the rest of this paper will discuss the details of the algorithm and thesis. The layout of the rest of the paper is organized as follows: Section 2 will introduce the basic concepts of PCNN and the modified PCNN is introduced to construct the data denoising model. In Section 3, in order to locate the anomaly points, the wavelet transform is introduced as the anomaly detection and location algorithm. Also, the cooperative anomaly judgment algorithm and rule for anomaly detection will be discussed in detail combined with modified PCNN and wavelet transform. In addition, the algorithm flow chart is also drawn. Later, the contrast experiments and numerical simulation to detect the abnormal point of stacker running track are carried out to verify the effect of the algorithm and rule using data provided by State Grid Measuring Center of China. Finally, some conclusions and the directions for future engineering application are discussed according to the real stacker running track of ASRS in industrial environment.

2. Improved PCNN Denoising Model and Algorithm for Vibration Signals of Stacker Running Track

In a real working condition, the actual vibration signals measured from this system will be unavoidably affected by many complicated environmental factors. Obviously, the data package usually includes strong noises. So, to guarantee the effectiveness of anomaly detection for stacker running track, a reasonable data preprocessing procedure is very crucial to eliminate the noises that are contained in the dataset. In this context, constructing an effective denoising model and algorithm to process the original signal is of great theoretical and practical significance for the condition monitoring of the stacker running track.

However, most industrial monitoring and control applications require high performance, timeliness, and reliability. Then, most administrators and engineers hope to effectively operate the system without knowing the accurate model. Based on this thesis, the PCNN will be introduced later. On this basis, an improved PCNN denoising model and algorithm are analyzed and designed according to the actual situation to ensure the timeliness and stability of the performance of the stacker running track.

2.1. Basic Theory of PCNN. As we all know, PCNN is presented by Eckhorn based on the observed synchronous pulse transmission after the experiments of the cerebral cortex of the animals [22]. In fact, due to its scale invariance, rotation invariance, intensity invariance, distortion invariant, and other characteristics, PCNN is widely used in image smoothing, image segmentation, image edge detection, image fusion, optimal solution, and so on. Moreover, in theory, the PCNN model has similar group neurons synchronization release pulse characteristic and the accurate model is not needed to parse the structure of dataset. Thus, the engineers not only

reveal the inherent ability of PCNN, but also explore the application of PCNN in the signal denoising. So, the basic concept of PCNN will be introduced in the next context.

According to [22], the PCNN model can be expressed by the following equation:

$$F_{ij}[n] = e^{-\tau_{F_{ij}}} F_{ij}[n-1] + V_F \sum_{k,l} M_{ijkl} Y_{kl}[n-1] + S_{ij} \quad (1)$$

$$L_{ij}[n] = e^{-\tau_{L_{ij}}} L_{ij}[n-1] + V_L \sum_{k,l} W_{ijkl} Y_{kl}[n-1] \quad (2)$$

$$U_{ij}[n] = F_{ij}[n] (1 + \beta L_{ij}[n]) \quad (3)$$

$$\theta_{ij}[n] = e^{-\tau_{\theta_{ij}}} \theta_{ij}[n-1] + V_{\theta} Y_{ij}[n-1] \quad (4)$$

$$Y_{ij}[n] = \begin{cases} 1 & U_{ij}[n] > \theta_{ij}[n] \\ 0 & U_{ij}[n] \leq \theta_{ij}[n] \end{cases} \quad (5)$$

where $F_{ij}[n]$ denotes the n th feedback input for the (i, j) neuron; S_{ij} , U_{ij} , and Y_{ij} represent the external stimulation, internal behavior, and output of neuron N_{ij} , respectively; L_{ij} , F_{ij} are the two input channels for the link domain and the feedback domain of the neuron N_{ij} ; M and W are the connection weight coefficient matrix of feedback domain and link domain; θ_{ij} and V_{θ} are the output and threshold amplification factor and the variable threshold function; β denotes synaptic link coefficient; τ_L , τ_F , τ_{θ} are the time attenuation constants of link domain, feedback domain, and variable threshold function, respectively.

From the perspective of simulation, the PCNN neuron consists of three parts: receiving domain, modulation domain, and pulse generation domain. In real application, PCNN has the advantage that the data processing does not depend on precise mathematics model. That is to say, in the pretreatment of denoising, once the network interface of PCNN receives the input signal, the receiving field transmits it through two channels, F and L . The impulse response function of F channel changes slowly with time compared to L channel. The modulation part combines the signal L_{ij} from channel L with an offset and multiplies the signal F_{ij} from channel F to generate the internal signal U_{ij} . Then, θ_{ij} and U_{ij} will be compared to control the firing of signal neurons. If $\theta_{ij} > U_{ij}$, the neurons will be activated. Otherwise, the neurons may be deleted from the structure of PCNN.

According to the link coefficient of L channel and F channel, PCNN can be divided into two cases: coupled and uncoupled. When $\beta = 0$, each neuron was separately operated and unaffected by the pulse output of other neurons around it. In addition, considering the friendly interface for end users, the basic structure of PCNN is shown as Figure 1.

Obviously, the original dataset may be used to identify the character of noises by training the PCNN network. Of course, the noise-polluted data may be cleaned through analyzing the PCNN firing matrix and then the noises may also be filtered from the original dataset. In general, the engineers may test the abnormal point in a long data sequence to better locate the defect of stacker running track.

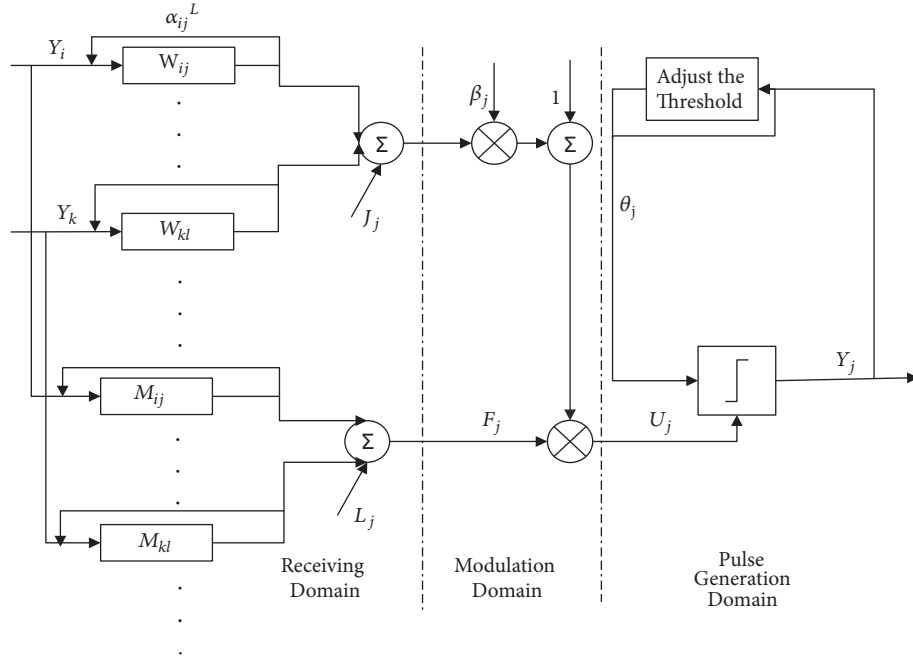


FIGURE 1: Basic structure of PCNN model diagram.

Unfortunately, although the basic structure of PCNN can clean the real dataset mixed with noise, the complexity of this topological structure can cause various issues that negatively impacts the engineer's operation play experience. In real scenario of ASRS, the difficulty in condition monitoring is to ensure the timeliness of locating the abnormal position of stacker running track. In particular, because the running process of stacker is complex and changeable, the original dataset signified the running state of the stacker including lots of noise. From an operational perspective, the traditional denoising method based on nominal model may hardly achieve the expected denoising performance. So, it is necessary to simplify network structure to meet the actual demand and it is a nontrivial problem to construct an improved denoising algorithm based on the existing PCNN model to meet the actual needs.

2.2. Modified PCNN Denoising Model for Vibration Signals of Stacker Running Track. In the industrial scenario, due to very poor measurement environment, the quality of the measurement signals may be affected by all kinds of factors. Meanwhile, the influential factors are connected with each other in vibration signals of stacker running track and they also have indirect effects. How to solve the coupling relations within the limits of real time control is very important to denoise the original dataset. In fact, considering that the basic topological structure of PCNN has the excessive parameters and the implementation is more complicated, it is not widely used in practice compared to the modified PCNN model. For a handy operation or statistics, the modified uncoupled model proposed in [21] is adopted to simplify the denoising process.

According to [21], the simplified PCNN model can be expressed by the following equation:

$$F_{ij}[n] = S_{ij}[n] \quad (6)$$

$$Y_{ij}[n] = \begin{cases} 1 & F_{ij}[n] > \theta_{ij}[n] \\ 0 & F_{ij}[n] \leq \theta_{ij}[n] \end{cases} \quad (7)$$

$$\theta_{ij}[n] = \begin{cases} V_{\theta} & Y_{ij}[n] = 1 \\ e^{-\tau_{\theta}} \theta_{ij}[n-1] & Y_{ij}[n] = 0 \end{cases} \quad (8)$$

$$B_{ij}[n] = \begin{cases} 1 & Y_{ij}[n] = 1 \\ 0 & Y_{ij}[n] = 0 \end{cases} \quad (9)$$

$$T_{ij}[n] = \begin{cases} n & Y_{ij}[n] = 1 \\ T_{ij}[n-1] & Y_{ij}[n] = 0 \end{cases} \quad (10)$$

where $F_{ij}[n]$ denotes the n th feedback input for the (i, j) neuron; S_{ij} denotes the external stimulation of neurons N_{ij} ; τ_{θ} denotes time attenuation constants of variable threshold function.

In this model, the signal from the channel L is not accepted by F_{ij} . As a result, F_{ij} is only affected by external input. The B matrix records whether the neuron fires at the n th input. And when the neuron fires, it will be assigned a larger threshold, so that it will not be fired again in a short time. Conversely, the threshold of the neuron that is not fired will decay over time. Therefore, the T matrix is used to record the time when each neuron is firstly fired. The noise point in the data can be filtered out by the value of T matrix.

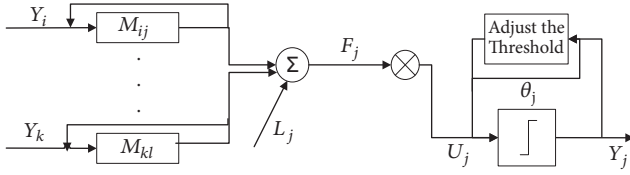


FIGURE 2: Modified PCNN model diagram.

The modified topological structure of simplified PCNN is shown as Figure 2.

Obviously, the modified model has advantages of less parameters and simple implementation. In other words, the simplified denoising system has operational simplicity and high efficiency for the denoising processing of the raw incoming data. For the sake of applying in industry, the simplified denoising process is more applicable. Thus, we can make use of the modified denoising model to denoise the vibration signals of stacker running track and finally realize the recognition of anomaly points.

3. Design and Analysis of Cooperative Anomaly Detection Method and Algorithm for Stacker Running Track of ASRS

In the above section, one valid dimensional data cleaning model and framework was discussed and analyzed. Once the original dataset measured from the track running system was processed by the modified PCNN, the errors, noises, or missing data that are contained in the dataset should be eliminated and removed. That is to say, the output dataset may be used to accurately locate the anomalous point for the stacker running track of ASRS. Obviously, the key stage of locating the abnormal defect of stacker running track is to find a reasonable model. The engineering practice shows that the energy of induction signal induced by the abnormal point of the stacker running track concentrates on the high frequency band. Of course, the fact has also provided a basis for determining anomaly point of stacker running stacker. Based on this, it is imperative to find a reasonable way to decompose the output dataset of modified PCNN into two parts: low frequency part and high frequency part.

Simultaneously, because the wavelet transform developing since 80's of last century has specific property of time-frequency localization, the method is especially fit for analyzing and detecting local signal mutation for the stacker running track of ASRS. Next step, the cooperative anomaly detection model of stacker running track will be constructed and analyzed based on wavelet transform.

3.1. Cooperative Anomaly Detection Method Based Wavelet Transform. In our experiments, the main feature of signal mutation is that the signal has local changes in time and space. To guarantee the accuracy of locating and identifying the defects of stacker running track, we have tried to design and construct a cooperative detection method combined with wavelet theory. The principle of using wavelet transform to detect the anomalous points is to decompose the signals

in different resolutions. When the signal is abrupt, the coefficient gotten by the wavelet transform has a modulus maximum value. Therefore, the location of the outliers can be filtered out through the detection of the maximum modulus point.

Without loss of generality, the basic principle of wavelet transform is clearly defined: Suppose $\phi(t) \in L^2(R)$ is a square integral function, if its Fourier transform satisfies the following condition.

$$\int_{\mathbb{R}} |\Psi(\omega)|^2 |\omega|^{-1} d\omega < +\infty \quad (11)$$

where $\psi(\omega)$ is wavelet transform of $\phi(t)$ and $\phi(t)$ is a wavelet function or base wavelet.

In fact, when the output dataset of modified PCNN was decomposed into high frequency and low frequency, the key factor is to carry the expansion or contraction, and the translation based on the base wavelet. If the expansion or contraction factor is supposed as a and the translation factor is supposed as b , then the wavelet function can be rewritten as follows.

$$\phi_{a,b}(t) = a^{-1/2} \phi\left(\frac{t-b}{a}\right) \quad a > 0, b \in \mathbb{R} \quad (12)$$

where a denotes the scaling factor (or scale factor) and b is translation factor. And $\phi_{a,b}(t)$ is wavelet base function which is concerned with a and b . It can be obtained by scaling or moving the parent function $\phi(t)$.

So, for an arbitrary signal $x(t) \in L^2(R)$, the wavelet transform can be expressed by the inner product of the signal and wavelet base function

$$\begin{aligned} W_x(a, b) &= \langle x, \phi_{a,b}(t) \rangle \\ &= a^{-1/2} \int_{\mathbb{R}} x(t) \phi_{a,b}\left(\frac{t-b}{a}\right) dt \end{aligned} \quad (13)$$

Notice that the actual measured signals indicating the changes of the running state of the stacker running track are discrete in the stacker running track in ASRS, and the wavelet transform should be rewritten in a discrete form to treat the output dataset provided by modified PCNN. In general, the scaling factor a and the translation factor b are put as follows.

$$\begin{aligned} a &= 2^{-j}, \\ b &= 2^{-j}k \end{aligned} \quad (14)$$

Thus, $W_x(a, b)$ became a discrete binary wavelet function as follows.

$$\phi_{j,k} = 2^{j/2} \phi_{j,k}(2^j t - k) \quad (15)$$

$$W_x(j, k) = 2^{j/2} \int_{\mathbb{R}} x(t) \phi(2^{-j} t - k) dt \quad (16)$$

where $j, k \in \mathbb{Z}$.

Then, the output dataset denoising by modified PCNN may be decomposed into high frequency and low frequency by the following formula.

$$W_x(j, k) = \sum_{j,k=-\infty}^{\infty} x(t) \phi_{j,k}(t) \quad (17)$$

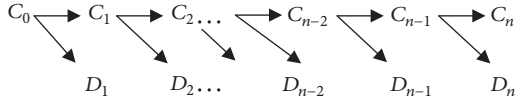


FIGURE 3: The wavelet decomposing process of output dataset.

Obviously, the wavelet series information may be used to show the changes of the running state of the stacker track. Moreover, to ensure that the energy of induction signal induced by the abnormal point of the stacker running track concentrates on the high frequency band, we have selected the orthogonal wavelet transform to decompose the output dataset into high frequency and low frequency. The basic decomposing mode is defined as follows.

$$\begin{aligned} C_{j+1} &= H * C_j \\ D_{j+1} &= D * C_j \end{aligned} \quad (18)$$

where C is the high frequency part and D is the low frequency part.

In our experiments, if the raw output signal $x(t)$ is described as C_0 , the wavelet decomposing process may be shown as Figure 3.

Obviously, according to the decomposing process in Figure 3, the high frequency band of the dataset, which indicates the energy of induction signal induced by the abnormal point of the stacker running track, can be gotten. To add extra flexibility, the high frequency band is described as C_j ($j = 0, 1, \dots$).

In practical project, the low-frequency coefficients reflect the contour of the original signal and the high-frequency coefficients describe the details of the signal. In particular, the singularity in the signals is often caused by a sudden change in frequency domain. For the engineers in health monitoring of stacker running state, it means that the high-frequency coefficients of wavelet transform can highlight singularity and can be used for detection and localization of the defect of the stacker running track. From the angle of engineering application, the damage of stacker running track will cause perturbations of measured signal at damage sites. Moreover, the measurement dataset is an aggregate of the running information, and the singularity of high frequency may depict the character of damage position on stacker running track. In other words, the damage concussion will cause the signal saltation. So, in practical engineering applications, it is very important to design a reasonable judgment rule of anomaly points.

To better locate the defects of stacker running track, the Lipschitz index is used to describe and design the judgment rule of singularity of the dataset. For the simplicity of analysis, the corresponding concept of Lipschitz index was defined as follows.

Definition 1. If there exists a constant $c > 0$ and h , such that $f(t)$ satisfies the following condition

$$|f(t_0 + h) - f(t_0)| \leq c|h|^\alpha \quad (19)$$

thus, α is the Lipschitz index of $f(t)$ at $t = t_0$. And then if $\alpha < 1$, $f(t)$ is singular at $t = t_0$.

In general, the size of Lipschitz index is related to the value of the singularity in actual project; i.e., the more severe the degree of mutation, the steeper the peak of the catastrophic point, and the smaller the singularity index, and vice versa. Based on this thesis, we can define the local singularity of high frequency signals decomposed by wavelet transform as follows.

Definition 2. $\forall x \in \delta x_0$, if there exists a constant $K > 0$ and s , the wavelet function $\phi(x)$ is continuous and differentiable and the wavelet transform has N vanishing moment (N is a positive integer); i.e.,

$$|Wf(s, x)| \leq Ks^\alpha \quad (20)$$

Thus, α is the local singularity at x_0 .

Notice that wavelet transform is applied to vibration signal analysis of stacker running track to detect the meshing abnormality of track with local defects, and the amplitudes of the vibration single will decrease or increase to some extent. So, by Definition 1, once there exists $\alpha < 1$ at one point, the engineers may judge that the position of the stacker running track may be damaged. Thus, the judgment rule of anomaly point is designed as follows.

Rule 1. $\forall x \in \delta x_0$, if the wavelet transform coefficient satisfies

$$|Wf(s, x)| \leq |Wf(x, x_0)| \quad (21)$$

thus, x_0 may be judged as the abnormal point of the stacker running stack.

Notice that the mutation information of flaws may be accumulated in running process of stacker's track, and the ability of a single high-frequency detail signal to reflect an abnormal point has limitations to locate the defect to stacker running track. To solve and overcome the problem, the product of the high-frequency coefficient, which can amplify the detail signal, is selected as the basis for the final judgment of the abnormal point in our experiments. To satisfy the need of engineering design, the accumulated information of track's flaws can be described by using the following formula.

$$C = C_j \times C_{j_{n-1}} \times C_{j_{n-2}} \quad (22)$$

where C is the product of high-frequency signal. C_j , $C_{j_{n-1}}$, $C_{j_{n-2}}$ are the n -order, $n - 1$ -order, and $n - 2$ -order high-frequency detail signals at the decomposition scale n , respectively.

Then, the basic rule is shown as follows.

Rule 2. If a mutation appears in the product of the high-frequency coefficient, it is an abnormal point.

Through the analysis and rules above, once the output dataset processed by modified PCNN has been decomposed into the low frequency and high frequency components of the signals, the high frequency components can be used to detect and locate the anomaly points of stacker running track.

3.2. Design and Analysis of Cooperative Anomaly Detection Algorithm Based on Modified PCNN and Wavelet Transform. Based on the above analysis and discussion, combining with the modified PCNN and wavelet transform, the cooperative anomaly detection algorithm of the stacker running track may be designed in detail as below.

Step 1. Normalize the data. Calculate the initial mean square error and initialize the network parameters by (1)-(9).

Step 2. Use the normalized data as input data. End the loop if matrix $B = 0$. Get matrix T when the loop ends.

Step 3. The noise points are determined according to the elements in the matrix, and then filter each data point.

Step 4. Calculate mean square error (MSE), and compare it with the mean square error before, if the mean square error is smaller than the mean square error before, back to Step 2. Input data into that model to continue to reduce noise. Otherwise, output the signal last time as the result.

Step 5. Select wavelet base function and determine the number of layers of wavelet decomposition.

Step 6. The wavelet transform coefficients of each layer are obtained by wavelet decomposition.

Step 7. Multiply the detail signal to amplify the mutation signal.

Step 8. Obtain the location of the outliers according to the location of the signal mutation.

The algorithm flow chart is shown as Figure 4.

4. Examples and Analysis

4.1. Simulation Examples

4.1.1. Simulation Results of Noise Reduction Effect of PCNN. To verify the noise reduction effect of modified PCNN, the simulation examples were first used to test the denoising ability of PCNN. In our simulation experiments, the sinusoidal signal was selected and adopted as the input data to train and test PCNN rule and the Gaussian white noise with a mean of zero and a variance of 1 is added to the sinusoidal signal as the experimental signal. The testing signal $x(t)$ was described as follows.

$$x(t) = \sin(t) + v \quad (23)$$

where v is the Gaussian white noise, and $v \sim N(0, 1)$.

In actual imitative preparation, v , n , and t were set up as below, respectively.

$$\begin{aligned} v(t) &= \text{normrnd}(0, 0.1, n) \\ t &= 0 : 0.1 : 100 \\ n &= \text{length}(\sin(t)) \end{aligned} \quad (24)$$

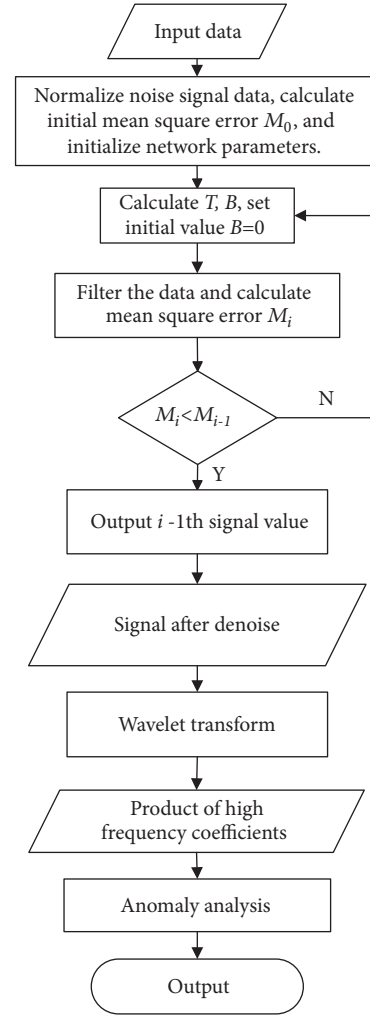


FIGURE 4: Flow chart of the algorithm.

By training the neural network of PCNN, the denoising results are shown as Figure 5.

Simultaneously, to explain the validity of PCNN denoising algorithm, the wavelet threshold denoising algorithm was used to compare with the presented algorithm in our simulation examples. The effect of wavelet threshold denoising algorithm is shown as Figure 6.

Obviously, although the comparison results between Figures 5 and 6 indicate the differences of the different denoising algorithm, the details of the differences are not obvious and significant. So, we must have a valid index selected to show the differences. To go through this process, the signal-to-noise ratio (SNR) and minimum mean square error (MSE) were used to compare the advantages of proposed denoising algorithm. The basic formulas were shown as follows.

(1) Signal-to-Noise Ratio

$$SNR = \frac{\hat{S}_t}{v} \quad (25)$$

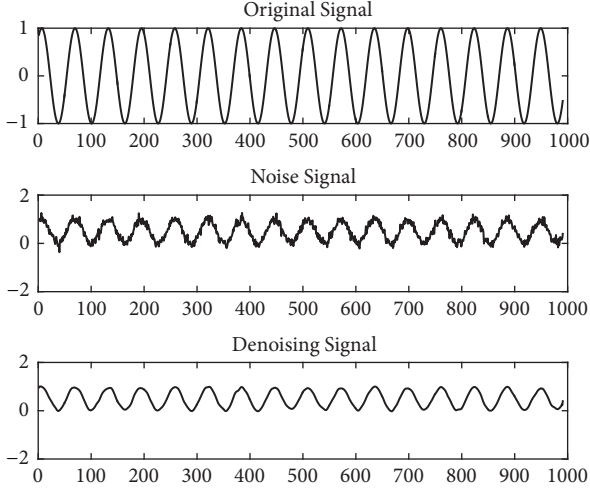


FIGURE 5: PCNN noise reduction results.

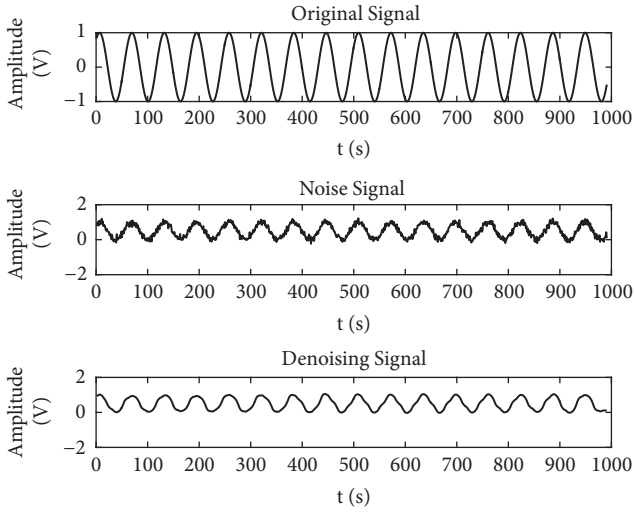


FIGURE 6: Wavelet threshold denoising results.

TABLE 1: Comparison of wavelet threshold denoising and PCNN noise reduction.

	Wavelet denoising	PCNN denoising
SNR	15.15	16.47
MSE	0.37	0.36

(2) Mean Square Error

$$MSE = \frac{1}{n} \sqrt{\sum_{t=1}^n (S_t - \hat{S}_t)^2} \quad (26)$$

where \hat{S}_t is denoising signal, S_t is the original signal, and v is the noise signal.

By (25) and (26), the corresponding comparison results are shown in Table 1.

It can be seen in Table 1 that PCNN can retain the characteristics of the original signal while getting good noise

reduction with higher SNR and lower MSE. So, it means that the denoising effect of modified PCNN is better than wavelet threshold denoising method.

4.1.2. Simulation Results of Anomaly Detection. In order to further verify the validity of cooperative anomaly detection method for singular point in signal dataset, a set of vibration signal with abnormal points is selected to test the effect of presented cooperative anomaly detection algorithm; i.e.,

$$x(t) = \begin{cases} \sin(0.02\pi t) & 0 \leq t \leq 400 \\ \sin(0.2\pi t) & 401 \leq t \leq 600 \end{cases} \quad (27)$$

In our simulation experiments, the simulation results are shown as Figure 7.

In fact, it can be seen from the simulation results that the sudden change of the signal appears at $t=400$ which can be observed from detail coefficients clearly. That indicates that the anomalies appear at $t=400$. It can be concluded that the presented cooperative anomaly detection can mark the location of the abnormal point of the vibration signal clearly. On the other hand, after testing the function, the presented cooperative algorithm may be applied to actual project.

4.2. Real Experiment Examples. Moreover, to further verify the validity of the proposed algorithm, the actual stacking machine vibration signal of ASRS, which has been developed and applied in State Grid Measuring Center of China, was selected to simulate the performance of the anomaly detection algorithm. The prototype systems of the stackers of State Grid Measuring Center of China is shown in Figure 8.

As can be seen in Figure 8, the main function is to grab, move, and stack goods from one goods shift to another. In actual project, the degree of unevenness of flaws (such as rusts, crack, the concavo-convex fluctuation, or any welding defects) will directly influence the safety and effectiveness of whole ASRS. In real engineering, the test rig of stacker running track is shown as Figure 9.

Figures 8 and 9 demonstrate that the crucial equipment of ASRS is the stacker running track. And then the operation track systems of the stacker contain the suspension transporting system (i.e., upper track) and road tracks (i.e., lower tracks). Thus, if outliers are presented and detected within the dataset, the defects of the stacker running track may be located and identified according to the precise geospatial data.

In real application, the sampling time is from March to April of 2018. The size of the sampling data source measured from stacker running track is 7370. The data may contain noise because of the interference of the site environment and collecting data equipment and other reasons. To the Management Department of State Grid Measuring Center of China, the engineers especially want to find the anomaly points and locate the defects of stacker running track from the experimental data. If the engineers can do this, the whole security of ASRS may be better ensured. So, the simulation results between the original signal and compounded signal with noise caused by the defects of stacker's running track

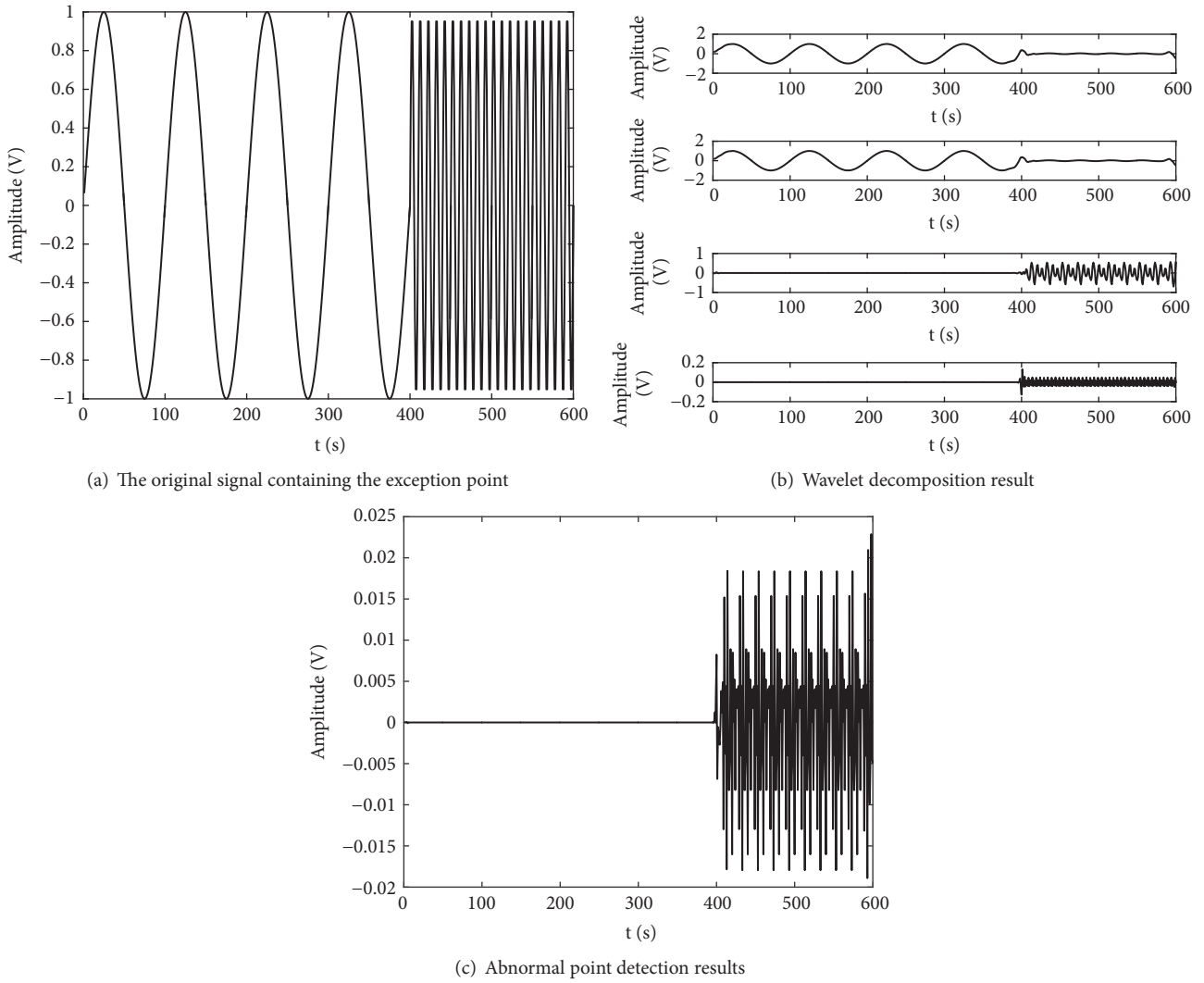


FIGURE 7: Simulation result of cooperative anomaly extraction.



FIGURE 8: Stackers in State Grid Measuring Center of China.



FIGURE 9: Basic structure of stacker running track.

were simulated in ASRS. In order to verify the effectiveness of the proposed model, wavelet transform and box-plot are chosen to compare with the result of PCNN-wavelet model. The results were shown as Figure 10.

As seen from Figure 10(a), due to the interference of noise points, it is impossible to accurately judge the abnormal points of the stacker by using only the wavelet transform. As can be seen from Figure 10(b), the abnormal

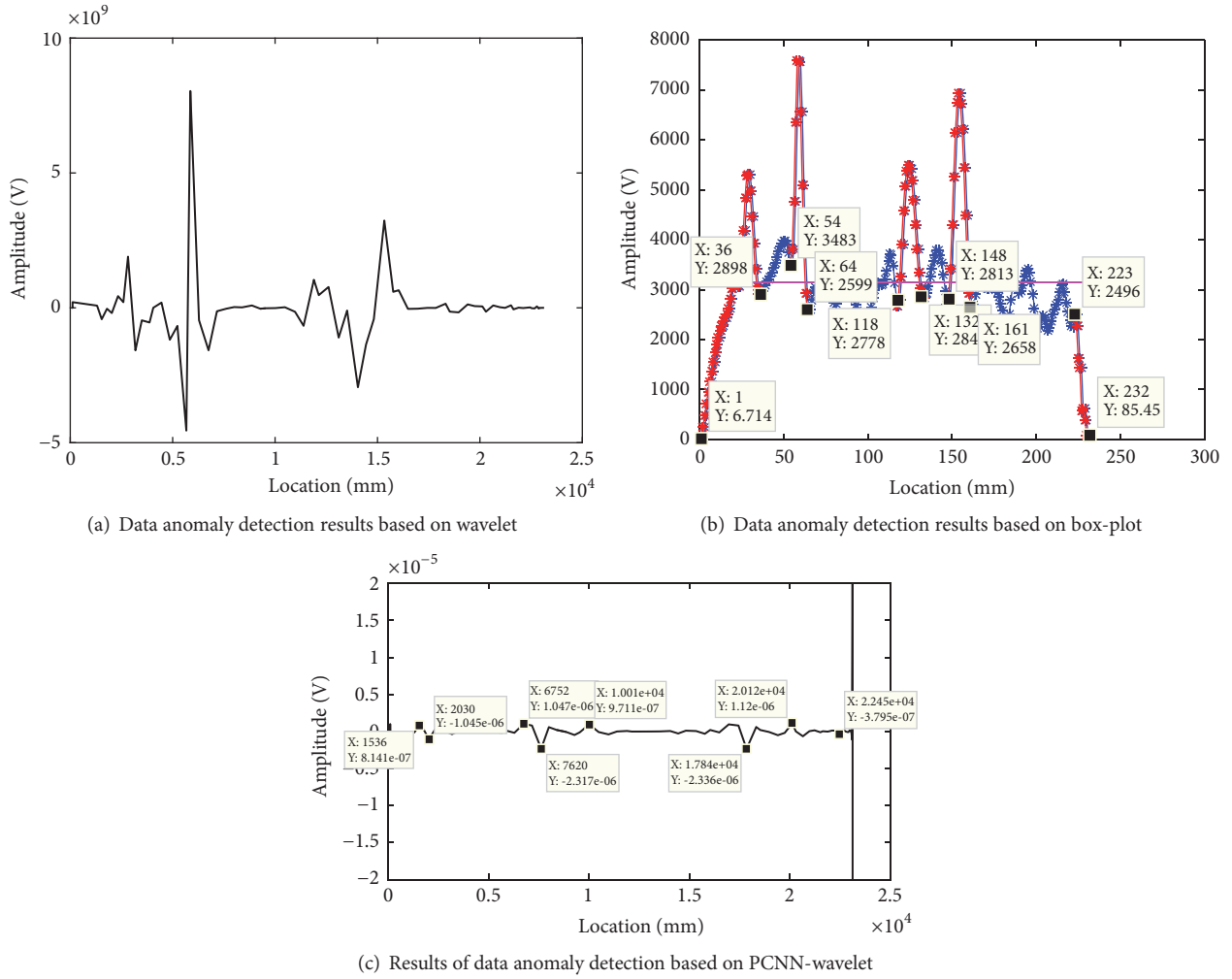


FIGURE 10: Comparison of abnormal point detection of three methods.

point determination interval is 1m-3.6m, 5.4m-6.4m, 11.8m-13.2m, 14.8m-16.1m, and 22.3m-23.2m. Correspondingly, the anomaly extensions may be at 1.5m-2.0m, 6.7m-7.6m, 10 m, 17.8m, 20 m, and 22.4m by the judgement rules in Figure 10(c). The results can be shown as Table 2.

Obviously, after the noise reduction of the input signal, the location of the abrupt change in the vibration signal may be depicted and described accurately by PCNN-wavelet. To ensure the operability in real engineering practice, some actual damage scenes of stacker running track were used to verify the effect of the presented algorithm. For instance, the actual testing and detecting sample photos at 1.5m, 7.2m, and 18 m are shown in Figure 11, respectively.

In addition, there are rail welds at 10 m, 20 m, and 22 m, respectively.

From the experimental simulation results and the actual situation verification, although the box diagram can roughly locate the abnormal point interval, the PCNN-wavelet is more accurate and closer to the actual situation. In Figure 10(c), the simulative curve appears to be changed suddenly in these places. In other words, the cooperative

TABLE 2: Comparison of abnormal point detection results.

Wavelet	Box-plot	PCNN-wavelet
\	1m-3.6m	1.5m-2.0m
\	5.4m-6.4m	6.7m-7.6m
\	11.8m-13.2m	10m
\	14.8m-16.1m	17.8m
\	\	20m
\	22.3m-23.2m	22.4m

anomaly detection method presented in this paper is effective.

In fact, the emergence of data mutation points may be caused by the depressions, cracks, and deformation at the interface in the tracks. On the other hand, the response information of the damage position may be developed to make different damage positions in different information range. And the administrators of the industrial system may locate damage positions according to numerical characteristics in the damage unit. Further, the relevant departments may

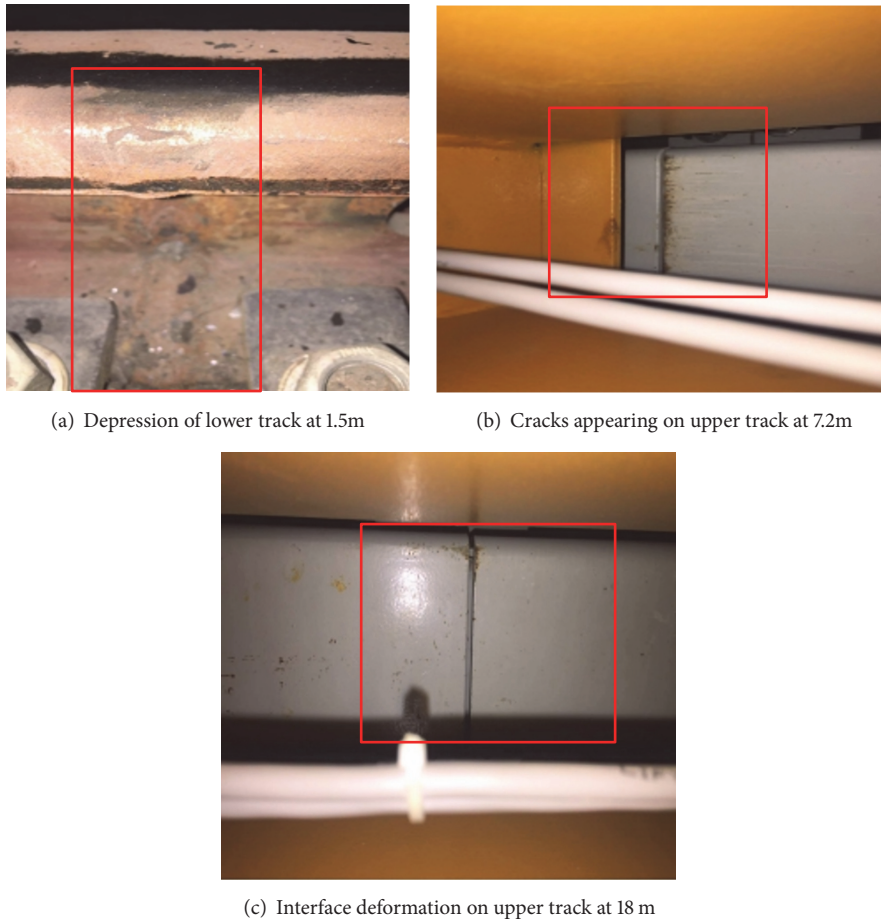


FIGURE 11: Testing and detecting sample photos from scene.

design the good maintenance strategies according to the monitoring curves. That means our algorithm may be applied to the real project.

5. Conclusion

In this paper, a cooperative anomaly detection method for the stacker running track in the industrial environment is presented, which is based on PCNN and wavelet transform. Firstly, the data denoising model is built based on PCNN. Then, the data is detected by wavelet transform. Finally, the rationality and validity of the proposed method are verified by example analysis and simulation. The main conclusions are as follows:

(1) In ASRS, under the influence of complex industrial environment, the data collected by the sensors will inevitably be interfered by noise, which will bring difficulties in data analysis. Simulation and real experiment examples prove that PCNN performs well in noise reduction. Moreover, it can eliminate noise interference as well as retain the original signal characteristics.

(2) After getting clean data, the wavelet transform can effectively locate the location of the abnormal point and has good applicability.

(3) After using PCNN to eliminate noise, the interference of noise-to-signal data is reduced, which is more conducive to the detection of signal data anomaly spot by wavelet transform. Through the comparison of the field and experimental data, it is shown that using PCNN and wavelet transform can realize the detection of the orbital anomaly spot of stacking machine.

Data Availability

The data used to support the findings of this study are available from the corresponding author upon request.

Conflicts of Interest

The authors declare that they have no conflicts of interest.

Acknowledgments

This work was supported by the National Natural Science Foundation of China under Grants 61703063, 61663008, 61573076, and 61004118; the Scientific Research Foundation for the Returned Overseas Chinese Scholars under Grant 2015-49; the Program for Excellent Talents of Chongqing

Higher School of China under Grant 2014-18; the petrochemical equipment fault diagnosis Key Laboratory in Guangdong Province Foundation of China under Grant GDUPKLAB201501; the Chongqing Natural Science Foundation of China under Grant CSTC2017jcyjA1665; Science and Technology Research Project of Chongqing Municipal Education Commission of China under Grants KJ1605002, KJ1705121, KJ1705139, and KJZD-K201800701; the Program of Chongqing Innovation and Entrepreneurship for Returned Overseas Scholars of China under Grant cx2018110.

References

- [1] V. Barnett and T. Lewis, *Outliers in Statistical Data*, John Wiley & Sons, New York, NY, USA, 1978.
- [2] M. E. Knorr and R. T. Ng, "Finding Intensional Knowledge of Distance-Based Outliers," *The VLDB Journal*, pp. 211–221, 1999.
- [3] M. Kontaki, A. Gounaris, A. N. Papadopoulos, K. Tsihlias, and Y. Manolopoulos, "Efficient and flexible algorithms for monitoring distance-based outliers over data streams," *Information Systems*, vol. 55, pp. 37–53, 2016.
- [4] L. Sheng, W. Zhang, and M. Gao, "Relationship between Nash equilibrium strategies and H_2/H_∞ control of stochastic Markov jump systems with multiplicative noise," *IEEE Transactions on Automatic Control*, 2014.
- [5] S. Ramaswamy, R. Rastogi, and K. Shim, "Efficient algorithms for mining outliers from large data sets," *SIGMOD Record*, vol. 29, no. 2, pp. 427–438, 2000.
- [6] A. Struyf and P. J. Rousseeuw, "High-dimensional computation of the deepest location," *Computational Statistics & Data Analysis*, vol. 34, no. 4, pp. 415–426, 2000.
- [7] S. Zhou and W. Xu, "Deviation-based local outlier detection algorithm," *Yi Qi Yi Biao Xue Bao/Chinese Journal of Scientific Instrument*, vol. 35, no. 10, pp. 2293–2298, 2014.
- [8] Z. Ge, Z. Song, S. X. Ding, and B. Huang, "Data Mining and Analytics in the Process Industry: The Role of Machine Learning," *IEEE Access*, vol. 5, pp. 20590–20616, 2017.
- [9] H. Liu, X. Li, and J. Li, "Efficient Outlier Detection for High-Dimensional Data," *IEEE Transactions on Systems Man & Cybernetics Systems*, no. 99, pp. 1–11, 2017.
- [10] M. Markou and S. Singh, "Novelty detection: a review—part 2: neural network based approaches," *Signal Processing*, vol. 83, no. 12, pp. 2499–2521, 2003.
- [11] J.-S. Wang and J.-C. Chiang, "A cluster validity measure with outlier detection for support vector clustering," *IEEE Transactions on Systems, Man, and Cybernetics, Part B: Cybernetics*, vol. 38, no. 1, pp. 78–89, 2008.
- [12] S. Mallat and W. L. Hwang, "Singularity detection and processing with wavelets," *IEEE Transactions on Information Theory*, vol. 38, no. 2, pp. 617–643, 1992.
- [13] W. P. Stuart-Bruges and V. Srinivasan, "Self-diagnostic control of a stacker crane," *Electronics and Power*, vol. 21, no. 2, pp. 108–111, 1975.
- [14] Z. Ge, "Review on data-driven modeling and monitoring for plant-wide industrial processes," *Chemometrics and Intelligent Laboratory Systems*, vol. 171, pp. 16–25, 2017.
- [15] LI. Xiaoping and YU. KangKang, "Research on Key Technology in Remote Fault Diagnosis of the Stacker," *Journal of Lanzhou Jiaotong University*, vol. 30, no. 4, pp. 15–20, 2011.
- [16] H. Darong, T. Jianping, and Z. Ling, "A fault diagnosis method of power systems based on gray system theory," *Mathematical Problems in Engineering*, vol. 2015, Article ID 971257, 2015.
- [17] K. Zhang, K. Peng, and J. Dong, "A Common and Individual Feature Extraction-Based Multimode Process Monitoring Method With Application to the Finishing Mill Process," *IEEE Transactions on Industrial Informatics*, vol. 14, no. 11, pp. 4841–4850, 2018.
- [18] K. Zhang, H. Hao, Z. Chen, S. X. Ding, and K. X. Peng, "A comparison and evaluation of key performance indicator-based multivariate statistics process monitoring approaches," *Journal of Process Control*, vol. 33, pp. 112–126, 2015.
- [19] H. Darong, K. Lanyan, M. Bo, Z. Ling, and S. Guoxi, "A New Incipient Fault Diagnosis Method Combining Improved RLS and LMD Algorithm for Rolling Bearings With Strong Background Noise," *IEEE Access*, vol. 6, pp. 26001–26010, 2018.
- [20] W. Jianguo, Y. Haipeng, and Z. Wenxing, "Data noise reduction method based on modified PCNN," in *China Measurement Test*, vol. 42, pp. 92–95, 2016.
- [21] Z. Wenxing, Y. Haipeng, and W. Jianguo, "Research on Data Noise Reduction Method Based on Modified PCNN," *Machinery Design Manufacture*, vol. 2, pp. 25–28, 2015.
- [22] R. Eckhorn, H. J. Reitboeck, M. Arndt, and P. Dicke, "Feature Linking via Synchronization among Distributed Assemblies: Simulations of Results from Cat Visual Cortex," *Neural Computation*, vol. 2, no. 3, pp. 293–307, 1990.

Research Article

Improvement of Low-Frequency Radiated Emission in Electric Vehicle by Numerical Analysis

Feng Gao ¹, Chengkai Ye ¹, Zilong Wang,² and Xu Li³

¹School of Automotive Engineering, Chongqing University, Chongqing 400044, China

²China Automotive Technology and Research Center, Tianjin 300300, China

³Chongqing Chang'an Automobile Corporation Limited, Chongqing 401120, China

Correspondence should be addressed to Feng Gao; gaofeng1@cqu.edu.cn

Received 22 March 2018; Revised 13 June 2018; Accepted 30 July 2018; Published 1 October 2018

Academic Editor: Daniela Proto

Copyright © 2018 Feng Gao et al. This is an open access article distributed under the Creative Commons Attribution License, which permits unrestricted use, distribution, and reproduction in any medium, provided the original work is properly cited.

In this paper, a methodology for improving vehicle-level radiated electromagnetic interference (EMI) in electric vehicle (EV) is proposed. This methodology predicts vehicle-level radiated EMI by using the multiport network theory, based on analyzing the contribution from each electronic component to find out the main EMI source. To validate its effectiveness, the proposed methodology is applied in an actual EV for low-frequency radiated emissions. Simulation in a commercially available electromagnetics software and measurement in the EV are combined to predict the vehicle-level emissions, and then the electronic component with the greatest EMI that causes failure to meet the EMC standard is identified. After improving this component, the vehicle-level radiated emission is reduced to comply with the EMC standard, proving that the presented numerical method is effective. The proposed methodology can also be used in other EMC issues, regardless of the amount of interference sources and sensitive equipment.

1. Introduction

In recent years, the problems of environmental pollution and energy crisis have aroused global concern. Compared to internal combustion engine vehicles, electric vehicles (EVs) have been rapidly developed because of such advantages as no pollution, no direct emission, and using renewable energy sources. However, high-voltage and current levels in EVs bring much more serious vehicle-level electromagnetic emission problems especially at low frequencies [1]. The electric traction system in EV is the source of high-voltage and high-current electromagnetic interference (EMI). It mainly consists of a high-voltage battery, a power distribution unit (PDU), a drive inverter, a direct-current/direct-current converter (DC/DC), an electric motor, and cables connecting the aforementioned components. The usage of power electronic devices in the drive inverter and the DC/DC causes large amounts of EMI because of high frequency switching [2]. Moreover, the cables connecting the components in the electric traction system carry the EMI and serve as the

transmitting antenna to radiate the EMI to the environment [3].

To avoid disturbing other equipment, the EMI generated by EV is restricted to a certain level. EVs are obliged to pass such standards as CISPR 12 and J551-5 before they are put on the market. The former is for the high frequency band and the latter is for the low-frequency band [4]. The compliance of EV to these standards only can be verified at a very late stage in the vehicle development process, because the electromagnetic compatibility (EMC) is greatly affected by the design changes in electronic/electrical components, electrical systems, and metal structures. The EMC problem discovered lately requires more time and cost to resolve. Moreover, when an EMC problem is found, it is difficult and time consuming to identify the actual source of EMI because (1) there are many sources causing radiated EMI in EV; (2) the parasitic parameters among structures cause many hidden transmission paths or antennas radiating/transmitting EMI. Compared to the experimental tests, the prediction technique using numerical simulation is an effective way to analyze and

improve the EMC of EV. Benefitting from the development of computer technologies and numerical solution algorithms for three-dimensional electromagnetic field with the coupling of cables, some commercial software packages for analysis of EMC have been presented, such as FEKO, CST Studio, and EMC Studio.

To improve low-frequency radiated emission in EV, automotive manufacturers usually troubleshoot the component with the greatest EMI and then improve the component-level EMC. Therefore, the present efforts in the literature on the improvement of radiated emission focus on component-level EMC. Di Piazza et al. developed a novel common-mode EMI active filter for automotive motor drives to mitigate the leakage high frequency common-mode currents, so as to reduce the radiated EMI [5]. Marczok et al. reworked the interference mechanisms of spark plugs and then improved its EMI properties so as to improve vehicle-level EMC [6]. Chun et al. proposed several solutions of switching noise reduction of DC/DC converter in HEV and EV for improvement of vehicle-level EMC [7]. These aforementioned works improve radiated emission through reduction of component-level emissions without consideration of the relationship between vehicle-level EMC and component-level EMC, so the degree of improvement is difficult to control. Numerical methods are efficient tools to analyze vehicle-level EMC issues. For analysis of vehicle-level radiated EMC issues using numerical methods, one widely used method is to establish the transfer function between EMI and the conducted interference current, which is measured in component test platforms or actual vehicles. Ala et al. predicted the radiated EMI generated by a 42V/14V DC/DC step-down converter [8]. The transfer function from the time-domain interference current to the near electromagnetic field strength was calculated by finite-difference time-domain method. Chen et al. also anticipated the vehicle-level radiated EMI by characterizing the transfer function between the interference current carried in wire harnesses and the voltage at receiving antenna terminal [9]. Zeng et al. established the vehicle-level simulation model by using a three-dimensional electromagnetic analysis software package to calculate the conversion factor from the conductor current at the outputs of inverter to the voltage of antenna terminal [10]. Dong et al. obtained the coefficient between the electric field strength and the conducted current by analyzing the generation mechanism of radiated emissions [11]. Summing up the aforementioned studies, the transfer function should be obtained under the condition which is the same as the actual one, because the transfer function is greatly influenced by the impedance of source and victim. This poses great restrictions on its application in practice.

To improve the low-frequency radiated emission in an EV with less number of experiments and cost, a new numerical analysis method is presented to find out the main source, which has the following advantages: (a) the vehicle-level model of EMI is described by algebraic equations in frequency domain, by which the cost of computation is reduced; (b) the interactions of impedance among sources, paths, and victims are decoupled to integrate more approaches to set up the vehicle-level model of EMI; (c) it can be applied at the whole vehicle development stage by integrating different

modeling approaches, test data, etc. This paper is organized as follows. Section 2 describes the studied EMC problem. Section 3 introduces the proposed numerical method used to model and analyze the problem. The application effect of this methodology on an EV is shown in Section 4. Finally, Section 5 concludes the paper.

2. Problem Description

SAE J551-5 limits the level of magnetic and electric emissions level from EVs over the frequency range from 150 kHz to 30 MHz. Figure 1 shows the test results of a four-seat sedan EV according to SAE J551-5. From Figure 1(b), it is found that the margin is sufficient at the low-frequency range, whereas it is narrow at the relative high frequency range and the magnetic field exceeds the limit about 10 dB μ A/m at 13.8 MHz.

Vehicle-level EMC is affected by many factors, among which the performance of components is very important. Furthermore, at this stage, compared with redesigning the electrical systems or arranging the components, it costs less to improve the component-level EMC. Automotive manufacturers usually attempt to find out the component with the greatest EMI by experimental tests. The widely used way of troubleshooting is to do standard tests after turning off different suspected electronic/electrical components, until the vehicle-level EMC gets better. Troubleshooting with this method costs more than the standard EMC test due to the high cost of long-hours EMC test facility and the need for hours of testing. Additionally, this troubleshooting method cannot quantify the contribution of the components which cannot be turned off during the experimental test, such as the motor and motor controller of an EV.

To improve the vehicle-level radiated emission more efficiently, a numerical method will be introduced to model and find out the main emission sources in the EV. This methodology combines numerical simulation using electromagnetic software and experimental modeling approaches to predict vehicle-level radiated EMI and analyze the contribution from each electronic/electrical component. In other words, the greatest source of radiated EMI can be found by this numerical method without multiple experimental tests.

3. Radiated EMI Modeling

The low-frequency radiated emission is mainly caused by high-voltage cables which carry common-mode conducted interference current. To improve the vehicle-level radiated EMI by numerical method, a mathematical model to describe the EMC problem should be obtained first. Considering the fact that the electrically small component can be equivalent to a circuit, which is more effective to be solved numerically, a new strategy to model the EMC problem is presented as shown in Figure 2. The electronic/electrical components, transmission paths, and the measuring instruments constitute a multiport network system, in which each electrically small component or measuring instrument acts as a terminal. The electrically large parts including high-voltage cables, vehicle body, and other large structures are considered as a network which serves as a black box to describe the

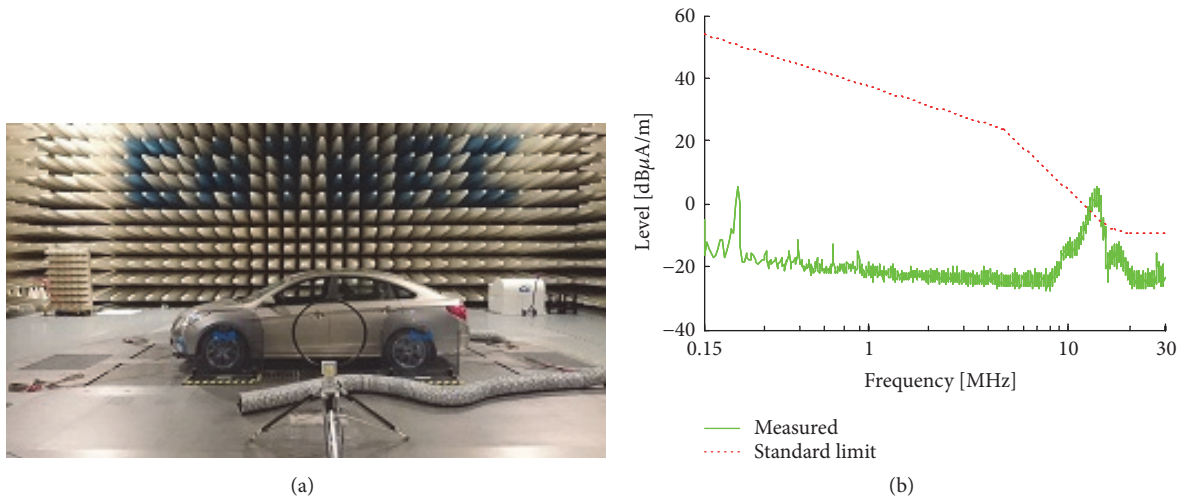


FIGURE 1: Experimental test of J551-5: (a) test setup; (b) test results.

transmission paths. The characteristics of the network can be calculated by existing commercial software or measured by network analyzer. Each terminal is characterized by Thevenin's equivalent circuit, whose circuit parameters can be measured in the EV.

The vehicle-level radiated emission is evaluated by the electromagnetic field strength measured by an antenna. Port 1 in Figure 2 denotes the measuring antenna while others (Indexed by $i = 2, \dots$) denote the on-board electronic components. Their Thevenin's equivalent circuits are described by the equivalent voltage source $V_{S,i}$ and Thevenin impedance $Z_{S,i}$. The port voltage and current are denoted by U_i and I_i , respectively. Note that the equivalent voltage sources of the devices without electromagnetic interference, including the measuring antenna, are equal to zero.

The open-circuit impedance parameter called \mathbf{Z} -parameter is used to characterize the electromagnetic coupling relationship among the ports:

$$\begin{bmatrix} U_1 \\ U_2 \\ \vdots \\ U_n \end{bmatrix} = \begin{bmatrix} Z_{11} & Z_{12} & \cdots & Z_{1n} \\ Z_{21} & Z_{22} & \cdots & Z_{2n} \\ \vdots & \vdots & \ddots & \vdots \\ Z_{n1} & Z_{n2} & \cdots & Z_{nn} \end{bmatrix} \begin{bmatrix} I_1 \\ I_2 \\ \vdots \\ I_n \end{bmatrix} \quad (1)$$

The vehicle-level emission is measured by the terminal voltage of the measuring antenna, and to distinguish the port of antenna from other on-board electronic/electrical components, (1) is rewritten using subscripts *ant* and *ele*:

$$\begin{bmatrix} U_{ant} \\ U_{ele} \end{bmatrix} = \begin{bmatrix} Z_{ant-ant} & Z_{ant-ele} \\ Z_{ele-ant} & Z_{ele-ele} \end{bmatrix} \begin{bmatrix} I_{ant} \\ I_{ele} \end{bmatrix} \quad (2)$$

Combining all Thevenin's equivalent circuits of the terminals together yields

$$\begin{bmatrix} U_{ant} \\ U_{ele} \end{bmatrix} = \begin{bmatrix} V_{S,ant} \\ V_{S,ele} \end{bmatrix} - \begin{bmatrix} Z_{S,ant} & \\ & Z_{S,ele} \end{bmatrix} \begin{bmatrix} I_{ant} \\ I_{ele} \end{bmatrix} \quad (3)$$

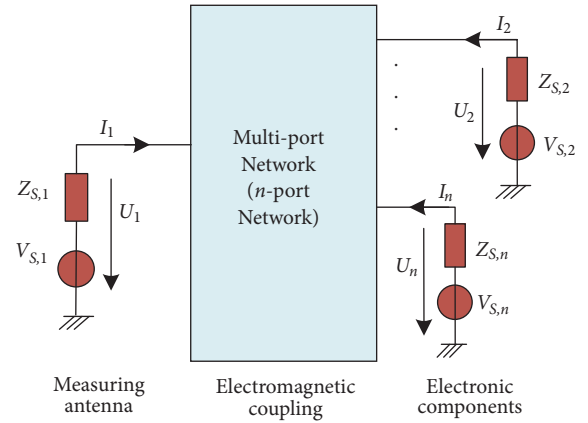


FIGURE 2: Model for pre-vehicle-level radiated EMI.

where $V_{S,ant} = 0$ and $Z_{S,ant} = Z_{S,1}$ are the equivalent voltage source and output impedances of measuring antenna. And $\mathbf{V}_{S,ele} = [V_{S,2}, \dots, V_{S,n}]^T$ and $\mathbf{Z}_{S,ele} = \text{diag}(Z_{S,2}, \dots, Z_{S,n})$ denote the equivalent voltage sources and output impedances of the on-board electronic components connected to the ports. Equations (2) and (3), respectively, describe the electromagnetic coupling relationship between the multiple ports and the equivalent characteristics of on-board electronic components.

Based on (2) and (3), the voltages at each port can be derived by

$$\begin{aligned} \begin{bmatrix} U_{ant} \\ U_{ele} \end{bmatrix} &= \begin{bmatrix} Z_{ant-ant} & Z_{ant-ele} \\ Z_{ele-ant} & Z_{ele-ele} \end{bmatrix} \begin{bmatrix} I_{ant} \\ I_{ele} \end{bmatrix} \\ &= \begin{bmatrix} Z_{ant-ant} & Z_{ant-ele} \\ Z_{ele-ant} & Z_{ele-ele} \end{bmatrix}^{-1} \begin{bmatrix} V_{S,ant} \\ V_{S,ele} \end{bmatrix} \end{aligned} \quad (4)$$

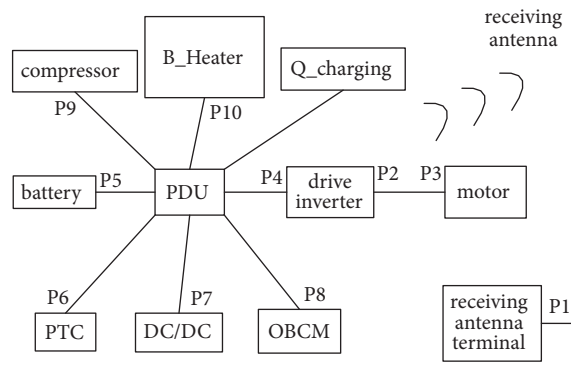


FIGURE 3: Multiport network of the EV.

Substituting the condition that $V_{S,ant} = 0$ to (4), the terminal voltage of measuring antenna is

$$U_{ant} = \frac{Z_{S,ant} Z_{ant-ele}}{Z_{ant-ant} + Z_{S,ant}} \left(Z_{S,ele} + Z_{ele-ele} - \frac{Z_{ele-ant} Z_{ant-ele}}{Z_{ant-ant} + Z_{S,ant}} \right)^{-1} \cdot V_{S,ele} \quad (5)$$

The conversion characteristics of measuring antenna are known in advance. The electromagnetic field strength at the specified position can be calculated by

$$|E| = |U_{ant}| \cdot AF_E \quad (6)$$

or $|H| = |U_{ant}| \cdot AF_H$

where $|H|$ and $|E|$ denote the electric and magnetic field strength, respectively. AF_E and AF_H are the electric antenna factor and magnetic antenna factor, respectively. From (5) and (6), the electromagnetic field strength, which measures the vehicle-level radiated EMI, can be figured out by three parts: Z -parameter of the entire network, the characteristics of electronic components, and measuring antenna. The above three parts can be obtained independently.

4. Prediction Model Validation

In this section, the predictive model is validated by applying it to predict the vehicle-level radiated EMI of the studied sedan EV. Figure 3 shows its equivalent multiport network for EMI prediction, which is a 10-port network. The main components relating to EMI emission are determined from the previous standard and troubleshooting test results. Note that it is concluded from the previous results that the low-frequency radiated EMI originates from the power electronic devices in the drive inverter and the DC/DC, so, in Figure 3, P2, P4, and P7 act as interference source.

4.1. Modeling of Port Coupling. As described in Section 3, Z -parameter is used to characterize the port coupling of the 10-port network. However, at the high frequency range, S -parameter representation is more precise and easily obtained.

In this paper, the S -parameter of the network is calculated by using FEKO, which is a commercial software package for numerical solving of three-dimensional electromagnetic field.

CAE preprocessing is necessary for EM simulation. It is widely accepted that the larger the EM energy is, the more detailed the EM model needs to be. Because the EMI source comes from drive inverter and the DC/DC and they are located at engine cabin, the EM energy mostly concentrates on engine cabin. In addition, the minor EM energy comes into the vehicle body because of the shielding effect of segregation board. So the EM model of engine cabin is detailed whereas the vehicle body can be highly simplified. The result of CAE preprocessing is shown in Figure 4(a). Figure 4(b) shows the calculation model in FEKO, which includes the main parts of EV and the measuring antenna arranged in the position required by SAE J551-5.

After calculating the S -parameter of the network, the required Z -parameter can be calculated by [9].

$$\begin{bmatrix} Z_{ant-ant} & Z_{ant-ele} \\ Z_{ele-ant} & Z_{ele-ele} \end{bmatrix} = Z_0 \left(\begin{bmatrix} 1 & \\ & \mathbf{E}_{ele} \end{bmatrix} - \begin{bmatrix} S_{ant-ant} & S_{ant-ele} \\ S_{ele-ant} & S_{ele-ele} \end{bmatrix} \right)^{-1} \cdot \left(\begin{bmatrix} 1 & \\ & \mathbf{E}_{ele} \end{bmatrix} + \begin{bmatrix} S_{ant-ant} & S_{ant-ele} \\ S_{ele-ant} & S_{ele-ele} \end{bmatrix} \right) \quad (7)$$

where Z_0 denotes port reference impedance when calculating the S -parameter, which is usually set to 50Ω . And \mathbf{E}_{ele} denotes the 9×9 identity matrix. Furthermore each part of Z -parameter can be obtained:

$$\begin{aligned} Z_{ant-ant} &= Z_0 \frac{1 + S_{ant-ant}}{1 - S_{ant-ant}} + 2Z_0 \\ &\quad \cdot S_{ant-ele} [(1 - S_{ant-ant}) (\mathbf{E}_{ele} - S_{ele-ele}) \\ &\quad - S_{ele-ant} S_{ant-ele}]^{-1} \cdot S_{ele-ant} \\ Z_{ant-ele} &= 2Z_0 \cdot S_{ant-ele} [(1 - S_{ant-ant}) (\mathbf{E}_{ele} - S_{ele-ele}) \\ &\quad - S_{ele-ant} S_{ant-ele}]^{-1} \end{aligned}$$

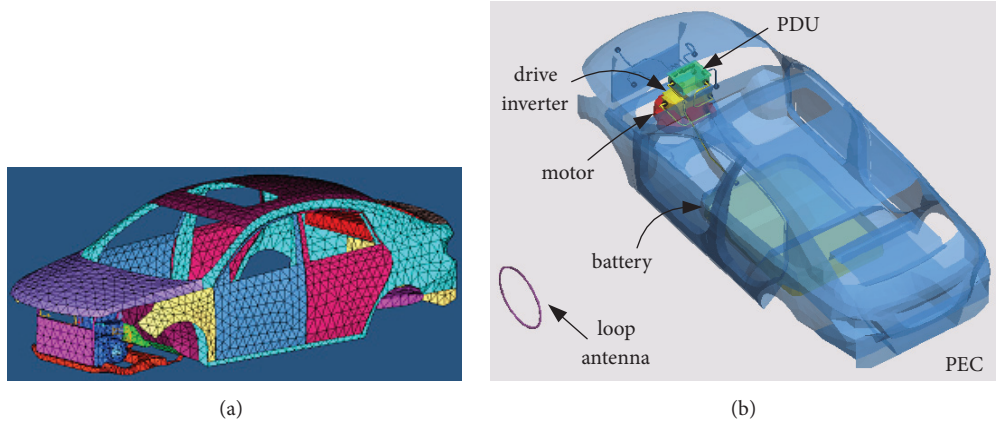


FIGURE 4: Simulation model: (a) CAE preprocessing result; (b) EM model in FEKO.

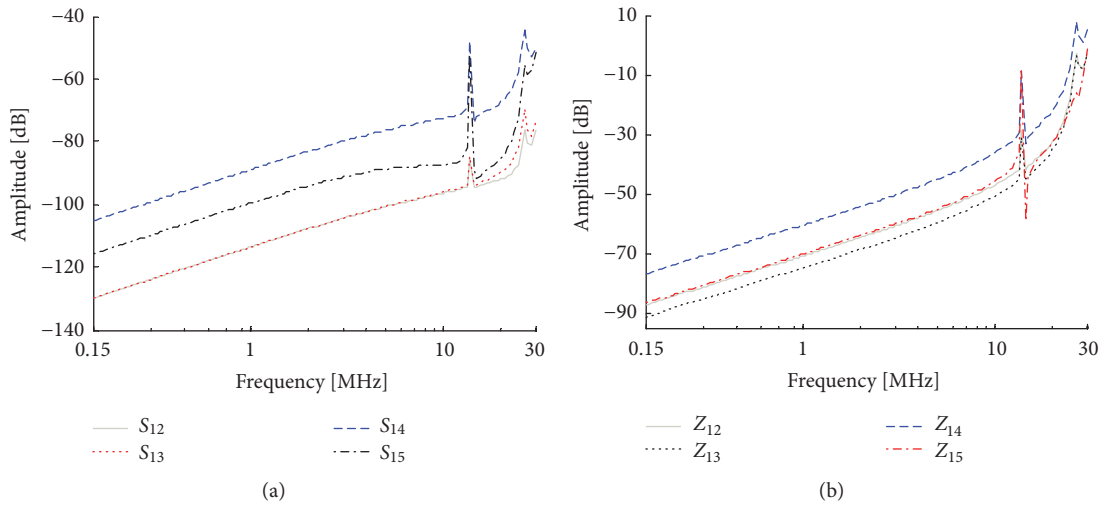


FIGURE 5: Network parameters: (a) S-parameter; (b) Z-parameter.

$$\begin{aligned}
 \mathbf{Z}_{ele-ant} &= 2Z_0 [(1 - S_{ant-ant}) (\mathbf{E}_{ele} - \mathbf{S}_{ele-ele}) \\
 &\quad - \mathbf{S}_{ele-ant} \mathbf{S}_{ant-ele}]^{-1} \cdot \mathbf{S}_{ele-ant} \\
 \mathbf{Z}_{ele-ele} &= Z_0 [(1 - S_{ant-ant}) (\mathbf{E}_{ele} - \mathbf{S}_{ele-ele}) \\
 &\quad - \mathbf{S}_{ele-ant} \mathbf{S}_{ant-ele}]^{-1} \cdot [(1 - S_{ant-ant}) (\mathbf{E}_{ele} + \mathbf{S}_{ele-ele}) \\
 &\quad + \mathbf{S}_{ele-ant} \mathbf{S}_{ant-ele}]
 \end{aligned} \tag{8}$$

Equation (8) is essentially the conversion formula from S-parameter to Z-parameter for vehicle-level radiated EMI prediction. Figure 5 shows the S-parameter and Z-parameter curves which describe the relationship between the measuring antenna (Port 1) and some of the component ports (Port 2 to 5) as an example.

4.2. *Equivalent Model of Components.* The parameters of Thevenin's equivalent circuits for electronic/electrical components are measured in the actual EV, which is explained in Figure 6. Note that it is concluded from previous results

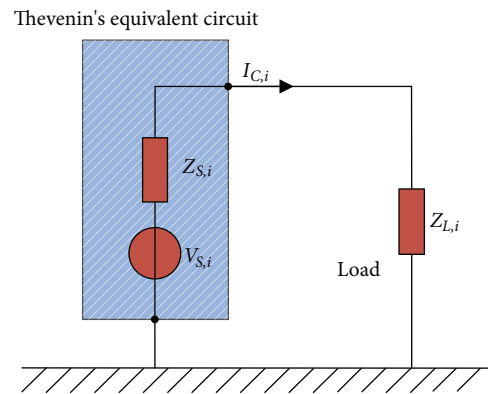


FIGURE 6: Measuring of electronic components.

that the radiated EMI is mainly caused by common-mode interferences. And so the positive and negative lines are equivalent to one.

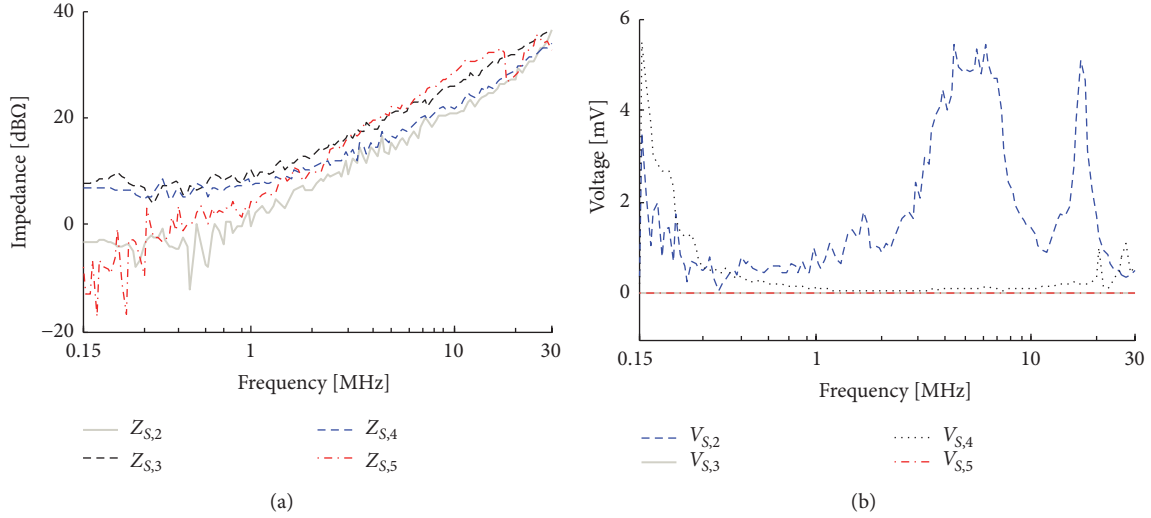


FIGURE 7: Thevenin's equivalent circuit parameters: (a) Thevenin impedance; (b) equivalent interference voltage.

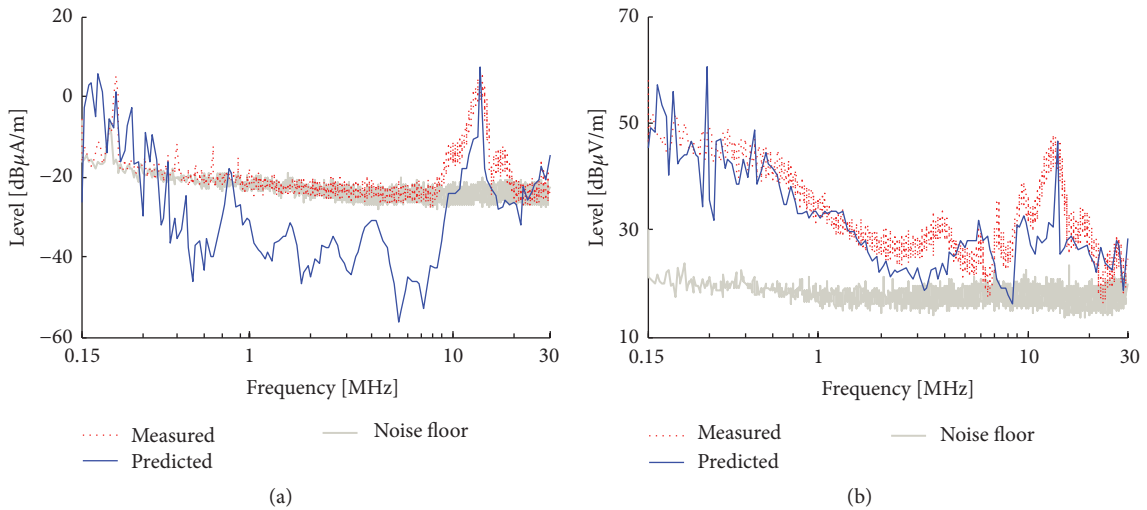


FIGURE 8: Predicted and measured EMI: (a) magnetic field; (b) electric field.

According to Figure 6, the parameters of Thevenin's equivalent circuit and the external load are formulated by

$$V_{S,i} = I_{C,i} \cdot (Z_{S,i} + Z_{L,i}) \quad (9)$$

where $I_{C,i}$ is the common-mode interference current, $V_{S,i}$ and $Z_{S,i}$ are the parameters of Thevenin's equivalent circuit, and $Z_{L,i}$ is the load impedance relative to ground. The interference current and impedance can be measured by a current clamp and a network analyzer, respectively. For the demonstration purpose, Figure 7 shows the output impedances and equivalent interference voltages of ports 2 to 5.

4.3. Prediction Results and Analysis. With the derived parameters of the coupling characteristic between ports and Thevenin's equivalent circuit for components, the voltage at the measuring antenna terminal is calculated by (5). Furthermore, after calibrating the antenna property in FEKO, the

radiated EMI is obtained using (6), which is compared with the measurement results as shown in Figure 8. The trend of the predicted and measured results agrees with each other. Moreover, the peak point of magnetic field at around 18.83 MHz, which exceeds the limit, is predicted precisely. In the frequency range 0.3 kHz-8 MHz of the magnetic field, the predicted EMI is much smaller than the measured value on the whole. Comparing the measured value with the noise floor of EMC laboratory, we find that in the inaccurate frequency range the antenna only measures the noise floor, which implies that the emission generated by EV is much smaller.

5. Main EMI Analysis and Improvement

For the EV failing the requirements of SAE J551-5, a numerical model has been set up to predict its radiated low-frequency EMI and validated by comparison with the

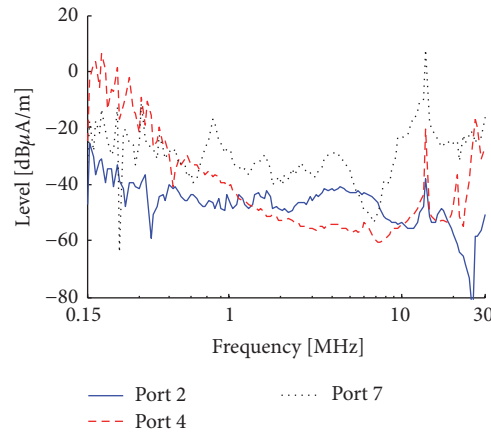


FIGURE 9: EMI from the three maximum components.

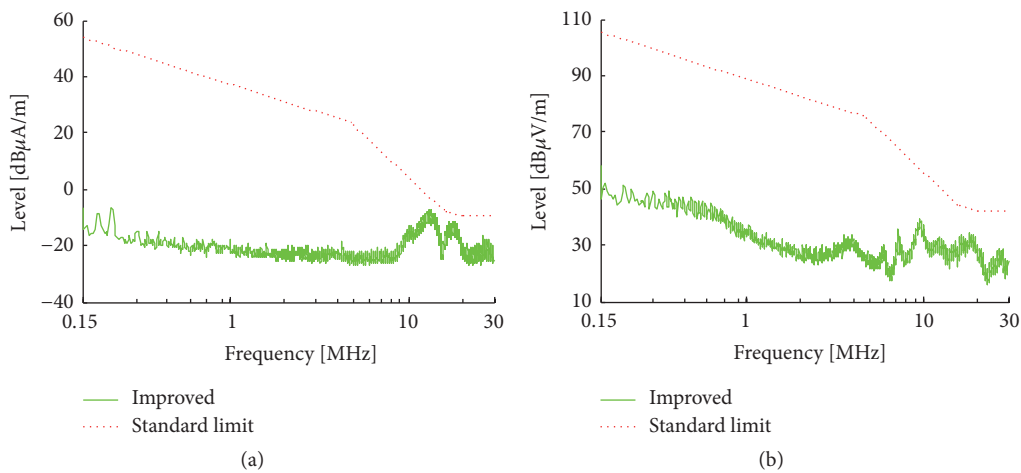


FIGURE 10: Test result after improvement: (a) magnetic field; (b) electric field.

measurement results. Instead of identifying the main source of EMI by expensive experimental testing, this predictive model is used to analyze the contribution to vehicle-level radiated EMI from each electronic component. Equation (5) shows that the vehicle-level radiated EMI is a sum of the induced interferences from every source. Then the generated interference magnetic field of each component can be derived, which is shown in Figure 9. Note that only the three maximum EMI sources are plotted to show clearly.

It is found that at the lower frequency range the greatest EMI is the drive inverter, whereas the EMI generated by the DC/DC is much higher than others especially at around the frequency where the EMI exceeds the limit. Therefore, this predictive model indicates that the DC/DC is the main source leading to excess vehicle-level magnetic field emission.

Although the radiated emission are also influenced by the coupling paths, from the standpoint of automotive enterprises, the easiest way is to improve EMC of the DC/DC converter because the vehicle may be required to be rearranged to reduce the coupling between components. This is because S -parameter and Z -parameter are affected by many factors like the structure of vehicle body, the layout of

cables, and so on, and it is difficult to control the variation of them. Note that improvement of EMC is at the last stage of vehicle development process, so we should consider the easiest method first. If it failed, redesigning the electric system or vehicle body is the last resort.

After redesigning the DC/DC, the new test results of vehicle-level low-frequency emission according to SAE J551-5 are shown in Figure 10, which show that the EV can pass SAE J551-5. This implies that the troubleshooting result obtained by the presented numerical method is correct and effective. Compared with the original experimental method, the cost of both time and money is greatly reduced.

6. Conclusion

This paper proposes a methodology for improving vehicle-level radiated emission by numerical analysis. This methodology combines both simulation in electromagnetic numerical solving software and measurement in actual vehicle to predict the vehicle-level radiated emission. Then this model is applied to find out the main EMI source. The experimental application results show that the radiated emission of the EV is improved successfully with reduced cost.

This methodology can be used not only in the improvement of vehicle-level radiated EMI, but also in other kinds of EMC issues, which can be equivalent to a multiport network. However, there are some open problems that need to be further studied:

(1) The characteristics of electronic/electrical components may vary with working conditions. Theoretically, the parameters of the equivalent circuit should be obtained under the condition, which is the same with the studied EMC problem.

(2) The transmission path of the presented application is approximated to be linear. How to model and solve the nonlinear interactions is to be studied.

Data Availability

We can provide the following data in the article: (1) the experimental test results of the original studied vehicle according to J551-5; (2) the data used to predict the low-frequency EMI including tested impedance data of components, the more common interference current of the EMI source port, the S-parameters of the equivalent network calculated by FEKO, and the factors of measuring antennas; (3) the experimental test results of the improved vehicle whose DC/DC is modified. The data are available from the corresponding author upon request. Unfortunately, we cannot provide the original FEKO project used to calculate the S-parameters, because it includes the vehicle model belonging to some OEM.

Conflicts of Interest

The authors declare that they have no conflicts of interest.

Acknowledgments

This research was supported the National Key R&D Program of China under grant 2017YFB0102504 and Scientific Technological Plans of Chongqing under grant cstc2017zdcy-zdxx0042. Thanks are due to the China Automotive Technology and Research Center, who provided the EV and the EMC laboratory.

References

- [1] D. Hamza and M. Pahlevaninezhad, "Integrated capacitor for common-mode EMI mitigation applicable to high frequency planar transformers used in electric vehicles DC/DC converters," in *Proceedings of the 2014 IEEE Energy Conversion Congress and Exposition (ECCE'14)*, pp. 4809–4814, Pittsburgh, Pa, USA, 2014.
- [2] S. Jeschke, H. Hirsch, M. Trautmann et al., "EMI measurement on electric vehicle drive inverters using a passive motor impedance network," in *Proceedings of the 7th Asia-Pacific International Symposium on Electromagnetic Compatibility, AP EMC '16*, pp. 292–294, Shenzhen, China, 2016.
- [3] H. Shim, H. Kim, Y. Kwack et al., "Inverter modeling including non-ideal IGBT characteristics in Hybrid Electric Vehicle for accurate EMI noise prediction," in *Proceedings of the 2015 IEEE International Symposium on Electromagnetic Compatibility - EMC '15*, pp. 691–695, Dresden, Germany, 2015.
- [4] A. R. Ruddle and R. Armstrong, "Review of current EMC standards in relation to vehicles with electric powertrains," in *Proceedings of the 2013 International Symposium on Electromagnetic Compatibility, EMC Europe '13*, pp. 298–303, Brugge, Belgium, September 2013.
- [5] M. C. Di Piazza, M. Luna, A. Ragusa, and G. Vitale, "An improved common mode active filter for EMI reduction in vehicular motor drives," in *Proceedings of the 7th IEEE Vehicle Power and Propulsion Conference, VPPC '11*, pp. 1–8, Chicago, Ill, USA, 2011.
- [6] C. Marczok, U. Maaß, E. Hoene, I. Ndirp, K.-D. Lang, and D. Hasselberg, "Analysis and improvement of a spark plug for less radiated electromagnetic emissions," in *Proceedings of the 2014 International Symposium on Electromagnetic Compatibility, EMC Europe '14*, pp. 385–390, Gothenburg, Sweden, 2014.
- [7] H. Chun et al., "Converter Switching Noise Reduction for Enhancing EMC Performance in HEV and EV," in *Proceedings of the PCIM Europe 2016; International Exhibition and Conference for Power Electronics, Intelligent Motion, Renewable Energy and Energy Management*, pp. 1–8, Nuremberg, Germany, 2016.
- [8] G. Ala, M. C. Di Piazza, G. Tinè, F. Viola, and G. Vitale, "Evaluation of radiated EMI in 42-V vehicle electrical systems by FDTD simulation," *IEEE Transactions on Vehicular Technology*, vol. 56, no. 4 I, pp. 1477–1484, 2007.
- [9] C. Chen, "Predicting vehicle-level radiated EMI emissions using module-level conducted EMIs and harness radiation efficiencies," in *Proceedings of the 2001 International Symposium on Electromagnetic Compatibility (EMC '01)*, pp. 1146–1151, Montreal, Canada, 2001.
- [10] H. Zeng, I. Hoda, W. Ivan et al., "Vehicle-Level EMC Modeling for HEV/EV Applications," *SAE International Journal of Passenger Cars - Electronic and Electrical Systems*, vol. 8, no. 2, pp. 278–281, 2015.
- [11] M. Dong, L. Zhai, R. Gao, and X. Zhang, "Research on radiated electromagnetic interference (EMI) from power cables of a three-phase inverter for electric vehicles," in *Proceedings of the 2014 IEEE Transportation Electrification Conference and Expo Transportation Electrification Asia-Pacific*, pp. 1–5, Beijing, China, 2014.

Research Article

Robust H_∞ Output-Feedback Yaw Control for Vehicles with Differential Steering

Paul Oke ¹, Sing Kiong Nguang ¹, and Wentai Qu²

¹Department of Electrical and Computer Engineering, The University of Auckland, Auckland 1010, New Zealand

²School of Information Science and Engineering, Ningbo Institute of Technology, Zhejiang University, Ningbo Higher Educational Zone, China

Correspondence should be addressed to Sing Kiong Nguang; sk.nguang@auckland.ac.nz

Received 24 May 2018; Revised 12 August 2018; Accepted 26 August 2018; Published 9 September 2018

Academic Editor: Darong Huang

Copyright © 2018 Paul Oke et al. This is an open access article distributed under the Creative Commons Attribution License, which permits unrestricted use, distribution, and reproduction in any medium, provided the original work is properly cited.

This paper examines the problem of designing a robust H_∞ output-feedback yaw controller with both input and output constraints for four-wheel independently driven in-wheel electric vehicles (EVs) with differential steering. Specifically, the controller aims are to ensure the stability and improve the performance of the EV despite variations in the road adhesion coefficient, longitudinal velocity, and external disturbance. Based on the linear matrix inequalities approach, sufficient conditions for the existence of an H_∞ output-feedback controller for linear systems with polytopic uncertainties, and input and control output constraints, are derived. Then those sufficient conditions are utilized to design an H_∞ output-feedback yaw controller that guarantees the robust performance and stability of an EV over a wider range of road conditions. Finally, the capability of the developed controller is simulated on a vehicle model with uncertain road conditions and longitudinal velocities.

1. Introduction

Active vehicle control (AVC) is a system that continuously observes the vehicle's dynamic responses and implements a corrective control action when necessary to improve drivability and stability of the vehicle. These subtle corrective actions can be a blend of regulating the steering angle and optimizing the transmitted tyre forces to the road [1–4]. Examples of AVC systems are active four-wheel steering (4WS), direct yaw moment control (DYC), active roll-over protection, anti-lock brake system (ABS), electronic stability control (ESC), active front-wheel steering (AFS), and active suspension system [2, 5]. The main aim of AVC is to improve vehicle safety, vehicle handling, and ride comfort and reduce the driving stress on poor road conditions.

In recent years, studies addressing active yaw moment control for physically steerable wheels to maintain the vehicle stability are enormous. In [4], stability control strategies of the vehicle via DYC are studied. Braking forces and traction controls are used to establish the stability threshold of the vehicle. Similarly, robust controller design [6–9] and optimal

distribution of tyre forces [10–13] have been developed for steerable wheels. However, there are currently no studies, as far as we know, addressing the robust control of EVs without physically steerable wheels.

Vehicles are subject to uncertainties such as the crosswind disturbances, payload, vehicle's longitudinal velocity, and, most importantly, friction differences in the tyre-ground interaction among many other factors. Several authors have adopted robust controller design for yaw stability control in an independently driven electric vehicle. In [14], a μ -synthesis robust controller design improves the yaw motion and chassis sideslip. In a similar study, in [15], the authors designed a controller with the aim of achieving both a neutral steer and a reduction in the sideslip of a four-wheel EV. These studies do not consider the tire force saturation.

In [16, 17], the authors consider the tire force saturation, parametric uncertainties, and external disturbances in solving the lateral-plane motion and yaw stability problem of an independently driven electric vehicle. Reference [18] investigated an active steering failure mechanism in a differential assisted steering for an autonomous system. The

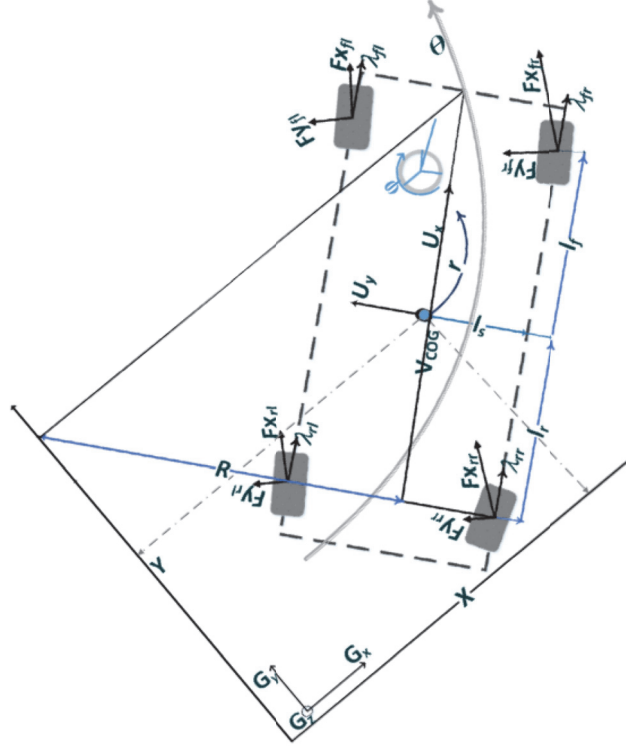


FIGURE 1: Differential Speed Steer EV maneuvering a curve.

authors consider the tyre force saturation and the use of a robust multiple-disturbances observer-based controller for a path following control.

In [19], a dynamic output-feedback controller is designed to realize a differential speed steering control strategy. However, in the previous design, the controller design was performed by linearizing the vehicle under a single operating condition tested for robustness. As one knows, the vehicle needs to operate over a wide range of guaranteed operating conditions, especially at different vehicle speed and road conditions. Based on the LMI approach, this paper designs a robust H_∞ dynamic output-feedback controller for four-wheel independently driven electric vehicles (FWIDEV) under bounded uncertainties and external environmental disturbance. The bounded uncertainties under consideration are the road coefficients of friction, vehicle's longitudinal speed, and the presence of lateral wind disturbances.

The main contributions of this paper are (1) the derivation of sufficient conditions for the existence of an H_∞ output-feedback controller for linear systems with polytopic uncertainties regarding input and output constraints and (2) the design of an H_∞ robust yaw controller that can achieve both robust stability and performance for EVs in the presence of uncertainties considering both input and output constraints.

The rest of the paper is organized as follows. Section 2 provides the mathematical model and the uncertain linear system of a four-wheel independently driven in-wheel electric vehicle. Section 3 presents the control problem and the robust controller design. Simulation results and discussion

are given in Section 4. Concluding remarks are given in Section 5.

2. Modelling of a Four-Wheel Independently Driven In-Wheel Electric Vehicle

The four-wheel independently driven in-wheel electric vehicle under consideration is shown in Figure 1. Each wheel in the EV is independently driven. Schematically, the longitudinal, lateral, and yaw equations of motion are as follows:

$$\dot{U}_x = U_y r + \left(\frac{1}{m}\right) (F_{xfl} + F_{xfr} + F_{xrl} + F_{xrr}) \quad (1)$$

$$\dot{U}_y = -U_x r + \left(\frac{1}{m}\right) (F_{yfl} + F_{yfr} + F_{yrl} + F_{yrr}) \quad (2)$$

$$J\dot{r} = l_f (F_{yfl} + F_{yfr}) - l_r (F_{yrl} + F_{yrr}) + l_s [F_{xfl} + F_{xrl} - F_{xfr} - F_{xrr}] + M_d \quad (3)$$

where U_x , U_y , and r are the vehicle's velocities along the longitudinal motion, lateral motion, and the yaw motion, respectively. m is the vehicle mass, l_f is the distance between the centre of gravity (COG) and the centre point of the front wheel, l_r is the distance between the COG and the rear wheel, l_s is half of the vehicle width, J is the yaw moment of inertia, and M_d is an external disturbance.

The tyre forces, F_{xi} and F_{yi} with $i = fl, fr, rl, rr$, are the result of the pneumatic deflections of the tire properties due to the weight of the vehicle, tyre pressure distribution,

and also the tyre-ground interaction. To determine the forces generated by the tyres as a result of the tyre-road interaction, the tyre nonlinear model for the combined lateral and longitudinal forces will be used as in [20–23].

The longitudinal and lateral forces components are

$$F_{xi} = \frac{\sigma_{xi}}{\sigma_i} F_{Ti}, \quad (4)$$

$$F_{yi} = \frac{\sigma_{yi}}{\sigma_i} F_{Ti}, \quad (5)$$

where

$$F_{Ti} = \begin{cases} \mu F_{zi} \left\{ 3\theta_c \sigma_i - \frac{1}{3} (3\theta_c \sigma_i)^2 + \frac{1}{27} (3\theta_c \sigma_i)^3 \right\} & \text{if } \sigma_i \leq \sigma_m \\ \text{or } \mu F_{zi} & \text{if } \sigma_i > \sigma_m, \end{cases} \quad (6)$$

where $\sigma_i = \sqrt{\alpha_{xi}^2 + \lambda_{yi}^2}$ is the total slip for each tyre and $\sigma_m = 1/\theta_c$ and $\theta_c = C_y/3\mu F_{zi}$ are the limiting values of slip.

Parameters C_y and μ are, respectively, tyre lumped lateral stiffness and the coefficient of tyre-road friction. The lateral tyre slip, σ_{yi} , is

$$\sigma_{yi} = \frac{U_y}{\bar{w}_i r_w} \tan(\lambda_i) \quad (7)$$

and the longitudinal tyre slip, σ_{xi} , is

$$\sigma_{xi} = \begin{cases} \frac{\bar{w}_i r_w - U_x}{\bar{w}_i r_w} & \text{during acceleration} \\ \text{or } \frac{\bar{w}_i r_w - U_x}{U_x} & \text{during braking.} \end{cases} \quad (8)$$

r_w is the effective wheel radius, \bar{w}_i is the angular velocity of each wheel, and λ_i is the tyre side slip angle. The normal load, F_{zi} , is based on the vehicle's geometry as

$$F_{zfl} = F_{zfr} = \frac{mgl_r}{2(l_f + l_r)} \quad (9)$$

$$F_{zfl} = F_{zfr} = \frac{mgl_f}{2(l_f + l_r)}.$$

Here a linear form of the combined tyre force modelled by (4) and (5) is used to describe the tyre frictional forces on each wheel [24]. We assume the vertical load of the vehicle is evenly distributed on each wheel. So that when the tyre side slip angle is small, by [21, 25], the tyre forces can be approximated as

$$F_{xi} = \mu C_{xi} \alpha_i, \quad (10)$$

$$F_{yi} = \mu C_{yi} \lambda_i, \quad (11)$$

where C_x is the longitudinal tyre stiffness; the tyre side slip angles, λ_i , are approximated as

$$\lambda_{fl} = - \left[\frac{U_y + rl_f}{U_x} \right],$$

$$\lambda_{fr} = - \left[\frac{U_y + rl_f}{U_x} \right],$$

$$\lambda_{rl} = - \left[\frac{U_y - rl_r}{U_x} \right],$$

$$\lambda_{rr} = - \left[\frac{U_y - rl_r}{U_x} \right],$$

(12)

And the longitudinal slip ratio, α_i , is

$$\alpha_i = \frac{r_w \bar{w}_i - U_x}{U_x}, \quad (13)$$

In this paper, we assume the longitudinal velocity, U_x , is an unknown constant but bounded as

$$\underline{U_x} < U_x < \bar{U_x}, \quad (14)$$

where $\underline{U_x}$ and $\bar{U_x}$, are, respectively, the lower and upper bounds of U_x . U_x is a constant; hence (1) is not considered here.

Moreover, we also assume that the coefficient of road friction, μ , is an unknown constant but bounded as

$$\underline{\mu} < \mu < \bar{\mu}, \quad (15)$$

where $\underline{\mu}$ and $\bar{\mu}$ are, respectively, the lower and upper bounds of μ .

We model the uncertainties in U_x and μ as polytopic uncertainties; hence (2) and (3) can be expressed as follows:

$$\begin{aligned} \dot{x}(t) &= A(\theta_u) x(t) + B_1 w(t) + B_2(\theta_u) u(t) \\ y(t) &= C_2 x(t) + D_2 w(t) \end{aligned} \quad (16)$$

where $x(t) = [U_y, r]^T$, $u(t) = \bar{w}_r - \bar{w}_l$, $w(t) = [M_d \ n_d]^T$, and n_d is the measurement noise. The uncertain matrices $A(\theta_u)$ and $B_2(\theta_u)$ belong to the polytopic uncertain domain

$$\Omega_p = \{A(\theta_u), B_2(\theta_u)\} = \sum_{i=1}^4 \theta_{ui} \{(A_i, B_{2i})\}, \quad (17)$$

where $\theta_{ui} \geq 0 \ \forall i$ and $\sum_{i=1}^m \theta_{ui} = 1$, and

$$A_1 = \begin{bmatrix} -\frac{C_y \underline{\mu}}{0.25m \underline{U_x}} & -\frac{C_y \underline{\mu} (l_f - l_r)}{0.5m \underline{U_x}} - \frac{\underline{U_x}}{0.5J \underline{U_x}} \\ \frac{C_y \underline{\mu} (l_r - l_f)}{0.5J \underline{U_x}} & -\frac{C_y \underline{\mu} (l_f^2 + l_r^2)}{0.5J \underline{U_x}} \end{bmatrix},$$

$$A_2 = \begin{bmatrix} -\frac{C_y \underline{\mu}}{0.25m \underline{U_x}} & -\frac{C_y \underline{\mu} (l_f - l_r)}{0.5m \underline{U_x}} - \frac{\underline{U_x}}{0.5J \underline{U_x}} \\ \frac{C_y \underline{\mu} (l_r - l_f)}{0.5J \underline{U_x}} & -\frac{C_y \underline{\mu} (l_f^2 + l_r^2)}{0.5J \underline{U_x}} \end{bmatrix},$$

$$\begin{aligned}
A_3 &= \begin{bmatrix} -\frac{C_y \bar{\mu}}{0.25m\bar{U}_x} & -\frac{C_y \bar{\mu}(l_f - l_r)}{0.5m\bar{U}_x} - \frac{\bar{U}_x}{0.5J\bar{U}_x} \\ \frac{C_y \bar{\mu}(l_r - l_f)}{0.5J\bar{U}_x} & -\frac{C_y \bar{\mu}(l_f^2 + l_r^2)}{0.5J\bar{U}_x} \end{bmatrix}, \\
A_4 &= \begin{bmatrix} -\frac{C_y \bar{\mu}}{0.25m\bar{U}_x} & -\frac{C_y \bar{\mu}(l_f - l_r)}{0.5m\bar{U}_x} - \frac{\bar{U}_x}{0.5J\bar{U}_x} \\ \frac{C_y \bar{\mu}(l_r - l_f)}{0.5J\bar{U}_x} & -\frac{C_y \bar{\mu}(l_f^2 + l_r^2)}{0.5J\bar{U}_x} \end{bmatrix}, \\
B_{2_1} &= \begin{bmatrix} 0 \\ \frac{r_w l_s C_x \bar{\mu}}{0.5J\bar{U}_x} \end{bmatrix}, \\
B_{2_2} &= \begin{bmatrix} 0 \\ \frac{r_w l_s C_x \bar{\mu}}{0.5J\bar{U}_x} \end{bmatrix}, \\
B_{2_3} &= \begin{bmatrix} 0 \\ \frac{r_w l_s C_x \bar{\mu}}{0.5J\bar{U}_x} \end{bmatrix}, \\
B_{2_4} &= \begin{bmatrix} 0 \\ \frac{r_w l_s C_x \bar{\mu}}{0.5J\bar{U}_x} \end{bmatrix}, \\
B_1 &= \begin{bmatrix} 0 & 0 \\ \frac{1}{J} & 0 \end{bmatrix}, \\
D_2 &= [0 \ 1]. \\
C_2 &= [0 \ 1]
\end{aligned} \tag{18}$$

In the next section, a robust H_∞ dynamic output-feedback controller design technique will be developed for general linear uncertain systems with polytopic uncertainties.

3. Robust Controller Design

Consider the following uncertain system:

$$\begin{aligned}
\dot{x}(t) &= A(\theta_u) x(t) + B_1 w(t) + B_2(\theta_u) u(t) \\
z(t) &= C_1 x(t) + D_1 u(t) \\
z_s(t) &= C_s(\theta_u) x(t) + D_{1s} w(t) + D_{2s}(\theta_u) u(t) \\
y(t) &= C_2 x(t) + D_2 w(t)
\end{aligned} \tag{19}$$

where $x(t)$ is the state vector, $u(t)$ is the control input, $w(t)$ is the disturbance, $z(t)$ is the performance output, $z_s(t)$ is the control output, $y(t)$ is the measured output, and θ_u exists in

a convex hull. The uncertain matrices $A(\theta_u)$, $B_2(\theta_u)$, $C_s(\theta_u)$, and $D_{2s}(\theta_u)$ belong to the polytopic uncertain domain

$$\begin{aligned}
\Omega_p &= \{A(\theta_u), B_2(\theta_u), C_s(\theta_u), D_{2s}(\theta_u)\} \\
&= \sum_{i=1}^m \theta_{ui} \{A_i, B_{2i}, C_{si}, D_{2si}\},
\end{aligned} \tag{20}$$

where $\theta_{ui} \geq 0 \forall i$ and $\sum_{i=1}^m \theta_{ui} = 1$. m is the number of vertices in the polytopic system. The matrices A_i , B_{2i} , C_{si} , and D_{2si} build the i -th vertex of the polytope.

Without loss of generality, we assume

$$\begin{aligned}
\int_0^\infty w^T(t) w(t) dt &\leq \rho \\
\text{and } \|w(t)\|^2 &\leq w_{\max}, \\
&\forall t > 0.
\end{aligned} \tag{21}$$

Since the sensors required to measure the lateral velocity are costly, in this paper, we will consider the dynamic output-feedback controller of the form

$$\begin{aligned}
\dot{\hat{x}}_c(t) &= A_c \hat{x}_c(t) + B_c y(t) \\
u(t) &= C_c \hat{x}_c(t)
\end{aligned} \tag{22}$$

where A_c , B_c , and C_c are the parameters of the controller.

Robust H_∞ Controller Formulation. Given γ , find a controller of the form (22) such that

- (1) system (19) with (22) is stable and satisfying the following inequality
- (2) under zero initial conditions, the following inequality is satisfied:

$$\int_0^\infty z^T(t) z(t) dt < \gamma \int_0^\infty w^T(t) w(t) dt \tag{23}$$

- (3) the following control output and input constraints are met:

$$\begin{aligned}
\|z_{sj}(t)\| &\leq z_{s,\max,j} \\
\text{and } \|u(t)\| &\leq u_{\max}, \\
&\forall t > 0
\end{aligned} \tag{24}$$

where $j = 1, 2, \dots, n_r$, and n_r is the number of rows in $z_s(t)$ and $z_{s,\max,j}^2 > (D_{1sj}^2 + D_{1sj}) w_{\max}$.

The closed-loop system of (19) with (22) is

$$\begin{aligned}
\dot{\tilde{x}}(t) &= A_{cl} \tilde{x}(t) + B_{cl} w(t) \\
z(t) &= C_{cl} \tilde{x}(t) \\
z_s(t) &= C_{scl} \tilde{x}(t) + D_{1s} w(t),
\end{aligned} \tag{25}$$

where

$$\begin{aligned}\bar{x}(t) &= \begin{bmatrix} x(t) \\ \hat{x}(t) \end{bmatrix}, \\ A_{cl} &= \begin{bmatrix} A(\theta_u) & B_2(\theta_u)C_c \\ B_c C_2 & A_c \end{bmatrix}, \\ B_{cl} &= \begin{bmatrix} B_1 \\ B_c D_2 \end{bmatrix}, \\ C_{cl} &= [C_1 \ D_1 C_c], \\ C_{scl} &= [C_s(\theta_u) \ D_{2s}(\theta_u)C_c].\end{aligned}\quad (26)$$

Theorem 1. Given γ , δ_1 , and δ_2 , suppose that there exist symmetric matrices W_{11}^i , W_{22}^i , Q_{1i} , Q_{2i} , and Y and matrices W_{12}^i , G , A_f , X , K , and L such that for $i = 1, \dots, m$ and $j = 1, \dots, n_r$ the following inequalities conditions hold:

$$W^i > 0, \quad (27)$$

$$\begin{bmatrix} -\frac{u_{\max}^2}{\gamma\rho} W^i & [0 \ L]^T \\ * & -I \end{bmatrix} < 0, \quad (28)$$

$$\begin{bmatrix} -\frac{\rho_{sj}}{\gamma\rho} W^i & [C_{sij}Y \ D_{2sij}L]^T \\ * & -(1 + \|D_{1sj}\|)^{-1} I \end{bmatrix} < 0, \quad (29)$$

$$\begin{bmatrix} -Q_{1i} & YA_i^T + L^T B_{2i}^T - G^T & 0 \\ * & -\delta_2 I & A_i Y + B_{2i} L - G \\ * & * & -Q_{2i} \end{bmatrix} < 0, \quad (30)$$

$$\begin{bmatrix} \phi_{11i} & \phi_{12i} & \phi_{13} & \phi_{14} & \phi_{15} \\ * & \phi_{22i} & \phi_{23} & 0 & 0 \\ * & * & -\gamma I & 0 & 0 \\ * & * & * & -I & 0 \\ * & * & * & * & -\delta_2 I \end{bmatrix} < 0, \quad (31)$$

where $\rho_{sj} = z_{s,\max,j}^2 - (\|D_{1sj}\|^2 + \|D_{2sj}\|)w_{\max}$

$$W^i = \begin{bmatrix} W_{11}^i & W_{12}^i \\ * & W_{22}^i \end{bmatrix},$$

$$\phi_{11i} = \begin{bmatrix} YA_i^T + L^T B_{2i}^T + & A_i + A_f \\ A_i Y + B_{2i} L + Q_{1i} & \\ * & A_i^T X + C_2^T K^T + \\ & XA + KC_2 \end{bmatrix}$$

$$\phi_{12i} = \begin{bmatrix} \delta_1 (A_i Y + B_{2i} L) - & \delta_1 A_i - I + W_{12}^i \\ Y + W_{11}^i & \\ -\delta_1 A_f^T - I + W_{12}^i & \delta_1 (XA_i + KC_2) \\ & -X + W_{22}^i \end{bmatrix}$$

$$\phi_{13} = \begin{bmatrix} B_1 \\ XB_1 + KD_2 \end{bmatrix}$$

$$\phi_{14} = \begin{bmatrix} YC_1^T + L^T D_1^T \\ C_1^T \end{bmatrix}$$

$$\phi_{15} = \begin{bmatrix} 0 \\ \delta_2 X \end{bmatrix}$$

$$\phi_{22i} = \begin{bmatrix} -2Y + Q_{2i} & -2I \\ -2I & -X - X^T \end{bmatrix}$$

$$\phi_{23} = \delta_1 \begin{bmatrix} B_1 \\ XB_1 + KD_2 \end{bmatrix}.$$

(32)

Then, system (19) with (22) is stable and the H_∞ performance (23) and the input and output constraints (24) hold. Moreover, the controller parameters are given as follows:

$$C_c = LY^{-1},$$

$$B_c = (Y^{-1} - X)^{-1} K,$$

(33)

$$A_c$$

$$= (Y^{-1} - X)^{-1} \{A_f - (Y^{-1} - X)B_c C_2 Y - XG\} Y^{-1}.$$

Proof. Refer to the Appendix for the proof. \square

4. Simulation Results

In this section, by using the parameters given in Table 1, the proposed control design is verified by stabilizing the EV along a straight path. The uncertainties in the coefficient of road friction and the longitudinal velocity are varying parameters from $0.2 \leq \mu \leq 1$ and $20 \leq U_x \leq 120$ km/hr, respectively. For comparison, the nominal operating points of 50 km/hr and $\mu = 0.8$ are selected for the H_∞ design. The uncertainty in μ and U_x , respectively, represents -75% to $+25\%$ and -60% to $+140\%$ of the nominal points.

In this simulation, the maximum speed of each wheel is assumed to be 219 rad/s or 260 km/hr in relation to vehicle's speed. Since the maximum operating speed of the vehicle is 120 km/hr (101 rad/s), the input constraint is given as

$$\|u(t)\| \leq u_{\max} = 118 \text{ rad/s}. \quad (34)$$

For the comfort of the driver and passengers, the output constraint for the yaw acceleration is chosen as $0.4g/l_c$; that is,

$$|\dot{r}(t)| \leq Z_{s,\max} = \frac{(0.4g)}{l_c}, \quad (35)$$

where $l_c = 1.36$ m is the centroid of the vehicle.

The disturbance term M_d used in the simulation is shown in Figure 2. The yaw rate measurement white noise's power density is 0.02 with a maximum amplitude of 0.1.

TABLE 1: Vehicle parameters.

Symbol	Parameters	Values
m	vehicle mass	1450 kg
l_f	distance from COG to front axle	1.013 m
l_r	distance from COG to rear axle	1.3 m
l_s	half of track width	0.7180 m
r_w	tire effective radius	0.33 m
g	acceleration of gravity	9.81 ms^{-2}
l_c	Midpoints of diagonals	1.36 m
J	yaw moment of inertia	2300 kg.m^2
μ	coefficient of friction	0.2 - 0.9
C_x	longitudinal tire stiffness	50000 N/rad
C_y	lateral tire stiffness	25000 N/rad

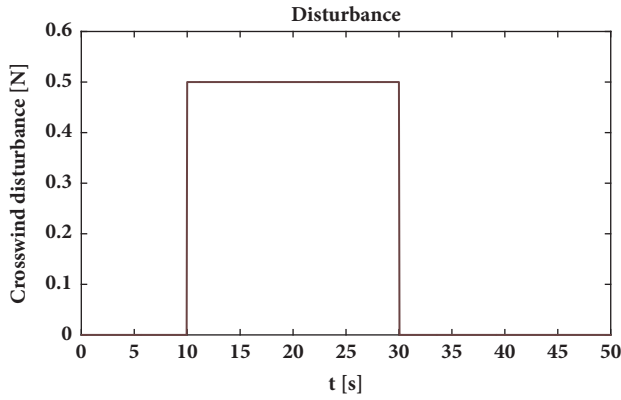


FIGURE 2: The disturbance.

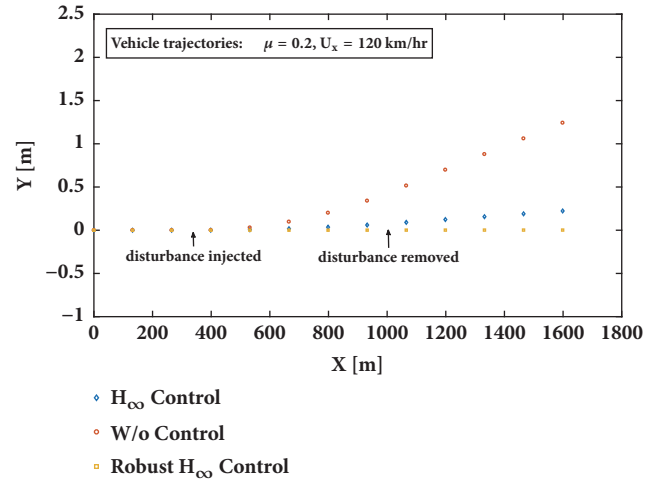
With this disturbance and the measurement noise, $\|w(t)\|^2 \leq 0.26$ and $\rho = 5$.

By Theorem 1, with $\delta_1 = 0.3$, $\delta_2 = 200$, and $\gamma = 1.2$, the following robust control parameters are obtained by solving the LMIs in (27), (28), (29), (30), and (31) using YALMIP toolbox (MOSEK solver) [26].

$$\begin{aligned}
 A_c &= \begin{bmatrix} -26.5443 & 4878.64 \\ 1.0912 & -218.41 \end{bmatrix}, \\
 B_c &= \begin{bmatrix} -4684.78 \\ 187.12 \end{bmatrix}, \\
 C_c &= [1.7951 \quad -33.0317].
 \end{aligned} \tag{36}$$

In comparison, we design an H_∞ with $\delta_1 = 0.5$, $\delta_2 = 8$, and $\gamma = 3.55$; the control parameters are

$$\begin{aligned}
 A_c &= \begin{bmatrix} -0.1668 & -4.09 \\ 4.2732 & -124.47 \end{bmatrix}, \\
 B_c &= \begin{bmatrix} -94.77 \\ 87.24 \end{bmatrix}, \\
 C_c &= [0.2111 \quad -2.0492].
 \end{aligned} \tag{37}$$

FIGURE 3: Vehicle trajectories: $\mu = 0.2$; vehicle speed: 120km/hr.

To test the effectiveness of the robust controller design and control strategy, different simulations are performed under multiple vehicle operating conditions. The nonlinear vehicle dynamic model in Section 2 is used in the final simulations. Each simulation ran for 50 seconds and generated 505 data points per second. The total displayed distance for the vehicle trajectory depends on the road condition (μ) and the vehicle's longitudinal velocity (U_x).

Figure 3 shows the trajectories of the EV with its longitudinal speeds at 120km/hr and coefficient of road friction at 0.2. The simulation starts with all the three vehicles operating without the crosswind disturbance, Figure 2; the trajectories of the vehicles can be seen to be on track. At the situation when the disturbance is injected from 10 sec to 30 sec, the vehicle without a controller begins to swerve off the desired path while the vehicles with a controller stay the course. The vehicle with the H_∞ controller shows a slight lateral deviation of less than 2 cm. After the vehicles exit the disturbance, the vehicles with a controller are still able to continue on the trajectory, but the vehicle with the robust controller shows an improved performance by maintaining a straight path.

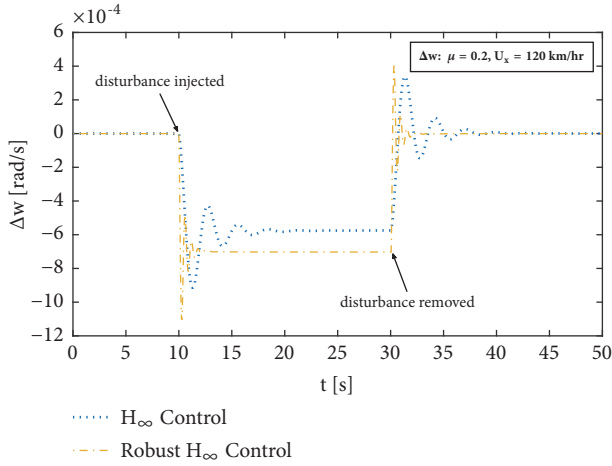


FIGURE 4: Δw : $\mu = 0.2$; vehicle speed: 120km/hr.

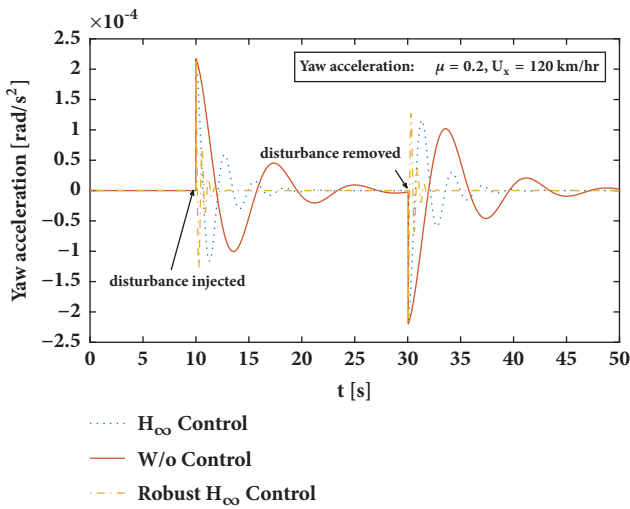


FIGURE 5: Yaw acceleration: $\mu = 0.2$; vehicle speed: 120 km/hr.

The controller output, Δw , and \dot{r} are shown in Figures 4 and 5, respectively. The robust controller shows a fast and good damping of the disturbance while still being within the constraints.

Figure 6 shows the vehicle's trajectories at the operating condition, $\mu = 0.8$ and $U_x = 20$ km/hr. Both of the vehicles with a controller indicated a strong performance, but an improvement can be seen with the robust controller as shown in the input, Figure 7, and control output, Figure 8. We can observe that the robust controller can quickly attenuate the disturbance upon entry and exit of the disturbance without violating the constraints. Figure 7 shows an improved performance of the robust controller. It is interesting to note the fast dynamics of the robust controller and its corresponding output constraint in Figure 8, for a straight-ahead driving, Figure 6. Figure 8 shows the vehicle's yaw acceleration at $\mu = 0.8$ and an entry speed of 20km/hr. The controllers are still able to stabilize the vehicle on the straight path with minimal lateral deviation.

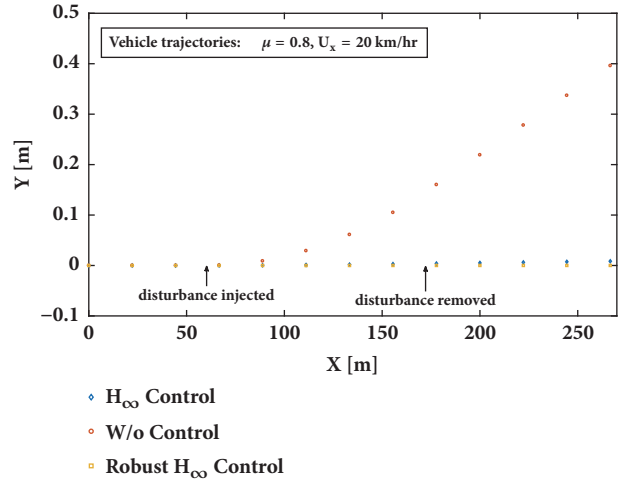


FIGURE 6: Vehicle trajectories: $\mu = 0.8$ and 20km/hr.

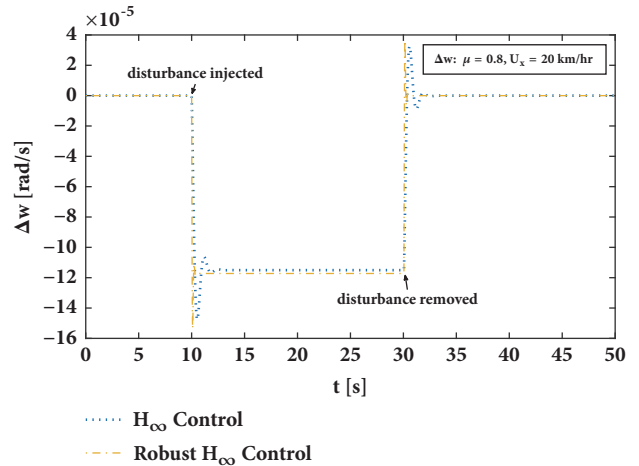


FIGURE 7: Control input: $\mu = 0.8$; vehicle speed: 20km/hr.

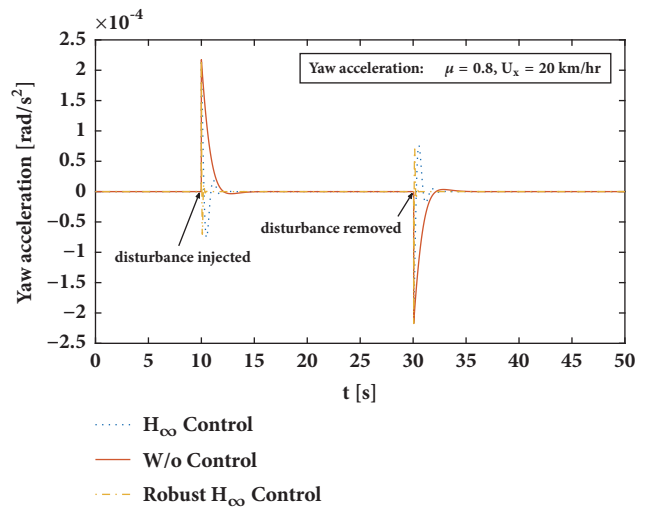


FIGURE 8: Yaw acceleration: $\mu = 0.8$; 20km/hr.

From the simulations, we observe that the vehicle with the robust controller is able to attenuates disturbance while satisfying both the input and output constraints.

5. Conclusion

This paper has designed a robust H_∞ dynamic output-feedback controller that attenuates external disturbances of four-wheel independently driven in-wheel electric vehicles. The electric vehicle has been modelled as an uncertain polytopic system with bounded uncertainties and external disturbance. We have developed sufficient conditions for the existence of a robust controller with input and output constraints that ensures the vehicle stays on course despite different road conditions and different longitudinal speeds. The performance of the robust controller has been tested on a complete nonlinear vehicle dynamic model. The simulation results have shown that despite significant differences in the operating conditions, the proposed robust controller ensures that the vehicle's trajectory stays on the desired path and satisfies both the input and control output constraints.

Appendix

Proof of Theorem 1. For the closed-loop system (25), consider the following parameter Lyapunov function:

$$V = \tilde{x}^T(t) \bar{P}(\theta_u) \tilde{x}(t), \quad (\text{A.1})$$

where

$$\bar{P}(\theta_u) = \sum_{i=1}^m \theta_{ui}(t) \bar{P}_i. \quad (\text{A.2})$$

Taking the time derivative of (A.1) along with (25) leads to

$$\dot{V} = \dot{\tilde{x}}^T(t) \bar{P}(\theta_u) \tilde{x}(t) + \tilde{x}^T(t) \dot{\bar{P}}(\theta_u) \tilde{x}(t) \quad (\text{A.3})$$

Adding

$$2 \left[\tilde{x}^T(t) P_1 + \dot{\tilde{x}}^T(t) P_2 \right] \left[A_{cl} \tilde{x}(t) - \dot{\tilde{x}}(t) + B_{cl} w(t) \right] = 0 \quad (\text{A.4})$$

to (A.3) by [27], for robust stability and performance, yields

$$\dot{V} = \varphi^T(t) Q \varphi(t) \quad (\text{A.5})$$

where $\varphi^T(t) = [\tilde{x}^T(t) \quad \dot{\tilde{x}}^T(t) \quad w^T(t)]$ and

$$Q = \begin{bmatrix} A_{cl}^T P_1^T + P_1 A_{cl} & \bar{P}(\theta) - P_1 + P_2 A_{cl} & P_1 B_{cl} \\ * & -P_2 - P_2^T & P_2 B_{cl} \\ * & * & 0 \end{bmatrix}. \quad (\text{A.6})$$

Adding and subtracting $(z^T(t)z(t) - \gamma w^T(t)w(t))$ to and from (A.5) results in

$$\dot{V} = \varphi^T \bar{Q} \varphi - z^T(t)z(t) + \gamma w^T(t)w(t), \quad (\text{A.7})$$

where

$$\bar{Q} = \begin{bmatrix} A_{cl}^T P_1^T + P_1 A_{cl} & \bar{P}(\theta) - P_1 + P_2 A_{cl} & P_1 B_{cl} \\ P_1 A_{cl} + C_{cl}^T C_{cl} & * & * \\ * & -P_2 - P_2^T & P_2 B_{cl} \\ * & * & -\gamma I \end{bmatrix}. \quad (\text{A.8})$$

Suppose the conditions in Theorem 1 hold; then $\phi_{22} < 0$. This condition implies that Y and X are nonsingular matrices. Without the loss of generality, let partition P_1 be

$$P_1 = \begin{bmatrix} X & Y^{-1} - X \\ Y^{-1} - X & X - Y^{-1} \end{bmatrix}. \quad (\text{A.9})$$

We assume $P_2 = \delta_1 P_1$. Define

$$J = \begin{bmatrix} Y & I \\ Y & 0 \end{bmatrix}. \quad (\text{A.10})$$

Multiplying the left-hand side of (A.8) by $\text{diag}\{J^T, J^T, I\}$ and its right-hand side by $\text{diag}\{J, J, I\}$ reads

$$\begin{aligned} & \text{diag}\{J^T, J^T, I\} \bar{Q} \text{diag}\{J, J, I\} \\ &= \begin{bmatrix} \Lambda_{11} & \Lambda_{12} & \Lambda_{13} \\ * & \Lambda_{22} & \Lambda_{23} \\ * & * & -\gamma I \end{bmatrix}, \end{aligned} \quad (\text{A.11})$$

where

$$\begin{aligned} \Lambda_{11} = & \begin{bmatrix} YA^T(\theta_u) + YC_c^T B_2^T(\theta_u) + \Gamma_1(\theta_u) \\ A(\theta_u)Y + B_2(\theta_u)C_c Y \\ * & \Gamma_2(\theta_u) \end{bmatrix} \\ & + \phi_{14} \phi_{14}^T, \end{aligned} \quad (\text{A.12})$$

with

$$\begin{aligned} \Gamma_1(\theta_u) &= A(\theta_u) + YA^T(\theta_u)X^T + YC_c^T B_2^T(Y^{-1} - X^T) \\ &+ YC_c^T B_2(\theta_u)^T X^T + YA_c^T(Y^{-1} - X^T), \\ \Gamma_2(\theta_u) &= A^T(\theta_u)X^T - C_2^T B_c^T(Y^{-1} - X^T) + XA(\theta_u) \\ &+ (Y^{-1} - X)B_c C_2 \end{aligned} \quad (\text{A.13})$$

Λ_{12}

$$= \begin{bmatrix} \delta_1 (A(\theta_u)Y + B_2(\theta_u)C_c Y) & \delta_1 A(\theta_u) - I + W_{12}(\theta_u) \\ -Y + W_{11}(\theta) & \\ \Gamma_3(\theta_u) & \delta_1 (XA(\theta_u) \\ & + (Y^{-1} - X)B_c C_2) \end{bmatrix}$$

with

$$\begin{aligned} \Gamma_3(\theta_u) &= \delta_1 (XA(\theta_u)Y + (Y^{-1} - X)B_c C_2 Y \\ &+ XB_2(\theta_u)C_c Y + (Y^{-1} - X)A_c Y) - I \\ &+ W_{12}(\theta_u), \end{aligned}$$

$$\begin{bmatrix} W_{11}(\theta_u) & W_{12}(\theta_u) \\ W_{21}(\theta_u) & W_{22}(\theta_u) \end{bmatrix} = J^T \bar{P}(\theta_u) J.$$

$$\Lambda_{13} = \begin{bmatrix} B_1 \\ XB_1 + (Y^{-1} - X)B_c D_2 \end{bmatrix},$$

$$\Lambda_{23} = \delta_1 \begin{bmatrix} B_1 \\ XB_1 + (Y^{-1} - X)B_c D_2 \end{bmatrix},$$

$$\Lambda_{22} = - \begin{bmatrix} 2Y & 2I \\ 2I & X + X^T \end{bmatrix}. \quad (\text{A.14})$$

With the notations given in Theorem 1, Λ_{11} can be rewritten as

$$\Lambda_{11} = \Lambda_{11}^1 + \Lambda_{11}^2 \quad (\text{A.15})$$

where

$$\Lambda_{11}^1 = \sum_{i=1}^m \theta_i \phi_{11i} + \phi_{14} \phi_{14}^T \quad (\text{A.16})$$

and

$$\Lambda_{11}^2 = \begin{bmatrix} -Q_1(\theta_u) & YA^T(\theta_u)X^T + (YC_c^T) \\ & B_2^T(\theta_u)X^T - G^T X^T \\ * & -\delta_2 XX^T \end{bmatrix}. \quad (\text{A.17})$$

Also rewrite Λ_{12} as

$$\Lambda_{12} = \sum_{i=1}^m \theta_{ui} \phi_{12i} + \begin{bmatrix} 0 & 0 \\ XA(\theta_u)Y + \\ XB_2(\theta_u)C_c Y - GX & 0 \end{bmatrix} \quad (\text{A.18})$$

$$= \Delta_{12}^1 + \Delta_{12}^2$$

and Λ_{22} as

$$\Lambda_{22} = \sum_{i=1}^m \theta_{ui} \phi_{22i} + \begin{bmatrix} -Q_2(\theta_u) & 0 \\ 0 & 0 \end{bmatrix} = \Delta_{22}^1 + \Delta_{22}^2. \quad (\text{A.19})$$

Then

$$\Lambda = \begin{bmatrix} \Lambda_{11}^1 & \Lambda_{12}^1 & \Lambda_{13} \\ * & \Lambda_{22}^1 & \Lambda_{23} \\ * & * & -\gamma I \end{bmatrix} + \begin{bmatrix} \Lambda_{11}^2 & \Lambda_{12}^2 & 0 \\ * & \Lambda_{22}^2 & 0 \\ 0 & 0 & 0 \end{bmatrix} \quad (\text{A.20})$$

$$= \Lambda^1 + \Lambda^2$$

Multiplying $\text{diag}\{I, X^{-1}, I\}$ to the left of Δ^2 and $\text{diag}\{I, X^{-T}, I\}$ to the right of Δ^2 , we obtain

$$\Lambda^2 = \begin{bmatrix} -Q_1(\theta_u) & S_{c12} & 0 & 0 & 0 \\ * & -\delta_2 I & S_{c22} & 0 & 0 \\ * & * & -Q_2(\theta_u) & 0 & 0 \\ * & * & * & 0 & 0 \\ * & * & * & * & 0 \end{bmatrix}, \quad (\text{A.21})$$

with

$$S_{c12} = YA^T(\theta_u) + L^T B_2^T(\theta_u) - G^T, \quad (\text{A.22})$$

$$S_{c22} = A(\theta_u)Y + B_2(\theta_u)L - G$$

The condition in (30) implies $\Lambda^2 \leq 0$. Applying Schur complement with respect to the last two rows of (31), it can be shown that $\Lambda^1 \leq 0$. Therefore,

$$\dot{V} < -z^T(t)z(t) + \gamma w^T(t)w(t). \quad (\text{A.23})$$

Integrating both sides and using the fact that $x(0) = \hat{x}(0) = 0$, we have

$$\int_0^\infty z^T(t)z(t)dt < \gamma \int_0^\infty w^T(t)w(t)dt. \quad (\text{A.24})$$

When $w(t)$ is zero,

$$\dot{V} < -z^T(t)z(t) < 0 \quad (\text{A.25})$$

This implies that (25) is stable.

For the control output and input constraints,

$$V(t) - V(0) < \gamma \int_0^t w^T(t)w(t)dt < \gamma \rho \quad (\text{A.26})$$

With the zero initial condition,

$$V(t) = \tilde{x}^T(t)\bar{P}(\theta_u)\tilde{x}(t) < \gamma \rho \quad (\text{A.27})$$

Note that $u(t) = C_c \hat{x}_c(t) = \bar{C}_c \tilde{x}$, where $\bar{C}_c = [0 \ C_c]$. Hence,

$$\|u(t)\|^2 = \|\bar{C}_c \tilde{x}(t)\|^2 \quad (\text{A.28})$$

$$\leq \tilde{x}^T \bar{P}(\theta_u) \tilde{x} \bar{P}^{-1/2}(\theta_u) \bar{C}_c^T \bar{C}_c \bar{P}^{-1/2}(\theta_u).$$

Using (A.27),

$$\|u(t)\|^2 \leq \gamma \rho \bar{P}^{-1/2}(\theta_u) \bar{C}_c^T \bar{C}_c \bar{P}^{-1/2}(\theta_u). \quad (\text{A.29})$$

From (A.29), $\|u(t)\| \leq u_{\max}$ if

$$\gamma \rho \bar{P}^{-1/2}(\theta_u) \bar{C}_c^T \bar{C}_c \bar{P}^{-1/2}(\theta_u) < u_{\max}^2. \quad (\text{A.30})$$

Applying the Schur complement on (A.30) gives

$$\begin{bmatrix} -\frac{u_{\max}^2}{\gamma \rho} & \bar{P}^{-1/2}(\theta_u) \bar{C}_c^T \\ * & -I \end{bmatrix} < 0. \quad (\text{A.31})$$

Multiplying left and right of (A.31) by $\begin{bmatrix} \bar{P}^{1/2}(\theta_u) & 0 \\ 0 & I \end{bmatrix}$ gives

$$\begin{bmatrix} -\frac{u_{\max}^2}{\gamma \rho} \bar{P}(\theta_u) & \bar{C}_c^T \\ * & -I \end{bmatrix} < 0. \quad (\text{A.32})$$

Then multiplying the left and right of (A.32) by

$$\begin{bmatrix} J^T & 0 \\ 0 & I \end{bmatrix} \quad (\text{A.33})$$

$$\text{and } \begin{bmatrix} J & 0 \\ 0 & I \end{bmatrix},$$

respectively, gives (28).

Note that $z_{sj} = C_{sclj}\tilde{x}(t) + D_{1sj}w(t)$, where $j = 1, \dots, n_r$. Therefore,

$$\begin{aligned} \|z_{sj}\|^2 &= \|C_{sclj}\tilde{x}(t) + D_{1sj}w(t)\|^2 \\ &\leq (1 + \|D_{1sj}\|) \|C_{sclj}\tilde{x}(t)\|^2 \\ &\quad + (\|D_{1sj}\|^2 + \|D_{1sj}\|) \|w(t)\|^2 \\ &\leq (1 + \|D_{1sj}\|) \|C_{sclj}\tilde{x}(t)\|^2 \\ &\quad + (\|D_{1sj}\|^2 + \|D_{1sj}\|) w_{\max} \end{aligned} \quad (\text{A.34})$$

Using (A.27),

$$\begin{aligned} \|z_s(t)\| &\leq (1 + \|D_{1sj}\|) \gamma\rho \|C_{sclj}\tilde{x}(t) \bar{P}^{-1/2}(\theta_u)\|^2 \\ &\quad + (\|D_{1sj}\|^2 + \|D_{1sj}\|) w_{\max} \end{aligned} \quad (\text{A.35})$$

From (A.35), $\|z_s(t)\| \leq z_{s,\max,j}^2$ if

$$(1 + \|D_{1sj}\|) \|C_{sclj}\tilde{x}(t) \bar{P}^{-1/2}(\theta_u)\|^2 \leq \frac{\rho_{sj}}{\gamma\rho} \quad (\text{A.36})$$

Applying the Schur complement on (A.36) gives

$$\begin{bmatrix} -\frac{\rho_{sj}}{\gamma\rho} & \bar{P}^{-1/2}(\theta_u) C_{sclj} \\ * & -(1 + \|D_{1sj}\|)^{-1} I \end{bmatrix} < 0. \quad (\text{A.37})$$

Multiplying left and right of (A.37) by $\begin{bmatrix} \bar{P}^{1/2}(\theta_u) & 0 \\ 0 & I \end{bmatrix}$ gives

$$\begin{bmatrix} -\frac{\rho_{sj}}{\gamma\rho} \bar{P}(\theta_u) & C_{sclj} \\ 0 & -(1 + \|D_{1sj}\|)^{-1} I \end{bmatrix} < 0. \quad (\text{A.38})$$

Then multiplying the left and right of (A.38) by

$$\begin{bmatrix} J^T & 0 \\ 0 & I \end{bmatrix} \quad (\text{A.39})$$

and $\begin{bmatrix} J & 0 \\ 0 & I \end{bmatrix}$,

respectively, gives (29). This completes the proof. \square

Data Availability

The data used to support the findings of this study are available from the corresponding author upon request.

Conflicts of Interest

The authors declare that they have no conflicts of interest.

Acknowledgments

This work was supported by the National Natural Science Foundation of China under Grant 61573315.

References

- [1] F. Yu, D.-F. Li, and D. A. Crolla, "Integrated vehicle dynamics control-state-of-the art review," in *Proceedings of the IEEE Vehicle Power and Propulsion Conference (VPPC '08)*, Harbin, China, September 2008.
- [2] Y. Furukawa and M. Abe, "Advanced chassis control systems for vehicle handling and active safety," *Vehicle System Dynamics*, vol. 28, no. 2-3, pp. 59–86, 1997.
- [3] P. Yih and J. C. Gerdes, "Modification of vehicle handling characteristics via steer-by-wire," *IEEE Transactions on Control Systems Technology*, vol. 13, no. 6, pp. 965–976, 2005.
- [4] N. Ding and S. Taheri, "An adaptive integrated algorithm for active front steering and direct yaw moment control based on direct Lyapunov method," *Vehicle System Dynamics*, vol. 48, no. 10, pp. 1193–1213, 2010.
- [5] A. Sigl and H. Demel, "ASR-traction control, state of the art and some prospects," *SAE Technical Papers*, 1990.
- [6] H. Du, N. Zhang, and G. Dong, "Stabilizing vehicle lateral dynamics with considerations of parameter uncertainties and control saturation through robust yaw control," *IEEE Transactions on Vehicular Technology*, vol. 59, no. 5, pp. 2593–2597, 2010.
- [7] A. Nasiri, S. Kiong Nguang, and A. Swain, "Adaptive sliding mode control for a class of MIMO nonlinear systems with uncertainties," *Journal of The Franklin Institute*, vol. 351, no. 4, pp. 2048–2061, 2014.
- [8] J. Zhang, P. Shi, J. Qiu, and S. K. Nguang, "A novel observer-based output feedback controller design for discrete-time fuzzy systems," *IEEE Transactions on Fuzzy Systems*, vol. 23, no. 1, pp. 223–229, 2015.
- [9] M. Shino and N. Masao, "Yaw-moment control of electric vehicle for improving handling and stability," *JSAE Review*, vol. 22, no. 4, pp. 473–480.
- [10] Y. Suzuki, Y. Kano, and M. Abe, "A study on tyre force distribution controls for full drive-by-wire electric vehicle," *Vehicle System Dynamics*, vol. 52, no. 1, pp. 235–250, 2014.
- [11] C.-C. Wang, S.-Y. Cheng, T. Hsiao, and W.-Y. Chou, "Application of optimum tire force distribution to vehicle motion control," in *Proceedings of the 2012 IEEE/ASME International Conference on Advanced Intelligent Mechatronics, AIM 2012*, pp. 538–543, Taiwan, July 2012.
- [12] E. Ono, Y. Hattori, Y. Muragishi, and K. Koibuchi, "Vehicle dynamics integrated control for four-wheel-distributed steering and four-wheel-distributed traction/braking systems," *Vehicle System Dynamics*, vol. 44, no. 2, pp. 139–151, 2006.
- [13] B. Li, H. Du, and W. Li, "Optimal distribution control of nonlinear tire force of electric vehicles with in-wheel motors," *Asian Journal of Control*, vol. 18, no. 1, pp. 69–88, 2016.
- [14] G. Yin, R. Wang, and J. Wang, "Robust control for four wheel independently-actuated electric ground vehicles by external yaw-moment generation," *International Journal of Automotive Technology*, vol. 16, no. 5, pp. 839–847, 2015.
- [15] G. Zhai, M. Naka, T. Kobayashi, and J. Imae, "Towards neutral steer and sideslip reduction for four-wheeled electric vehicles," *Frontiers of Mechanical Engineering*, vol. 7, no. 1, pp. 16–22, 2012.

- [16] R. Wang, H. Zhang, J. Wang, F. Yan, and N. Chen, "Robust lateral motion control of four-wheel independently actuated electric vehicles with tire force saturation consideration," *Journal of The Franklin Institute*, vol. 352, no. 2, pp. 645–668, 2015.
- [17] J.-S. Hu, Y. Wang, H. Fujimoto, and Y. Hori, "Robust yaw stability control for in-wheel motor electric vehicles," *IEEE/ASME Transactions on Mechatronics*, vol. 22, no. 3, pp. 1360–1370, 2017.
- [18] C. Hu, R. Wang, F. Yan, and H. R. Karimi, "Robust Composite Nonlinear Feedback Path-Following Control for Independently Actuated Autonomous Vehicles With Differential Steering," *IEEE Transactions on Transportation Electrification*, vol. 2, no. 3, pp. 312–321, 2016.
- [19] P. Oke, S. K. Nguang, and J. Wen, "H ∞ dynamic output feedback control for independently driven four-wheel electric vehicles with differential speed steering," in *Proceedings of the 2016 IEEE International Conference on Information and Automation, IEEE ICIA 2016*, pp. 567–572, China, August 2016.
- [20] J. Svendenius and M. Gäfvert, "A brush-model based semi-empirical tire-model for combined slips," *SAE Technical Paper*, vol. 01, no. 1064, 2004.
- [21] H. B. Pacejka, *Tire and Vehicle Dynamics*, SAE, USA, 2nd edition, 2005.
- [22] B. J. Olson, S. W. Shaw, and G. Stépán, "Nonlinear dynamics of vehicle traction," *Vehicle System Dynamics*, vol. 40, no. 6, pp. 377–399, 2003.
- [23] R. Rajamani, *Vehicle Dynamics and Control*, Springer, New York, NY, USA, 2012.
- [24] E. Bakker, L. Nyborg, and H. B. Pacejka, "Tyre modelling for use in vehicle dynamics studies," *SAE Technical Papers*, Article ID 870421, pp. 1–15, 1987.
- [25] G. Baffet, A. Charara, and J. Stephant, "Sideslip angle, lateral tire force and road friction estimation in simulations and experiments," in *Proceedings of the 2006 IEEE International Conference on Control Applications, CCA 2006*, pp. 903–908, Germany, October 2006.
- [26] J. Löfberg, "Automatic robust convex programming," *Optimization Methods & Software*, vol. 27, no. 1, pp. 115–129, 2012.
- [27] D. S. Bernstein and W. M. Haddad, "Robust stability and performance analysis for state-space systems via quadratic Lyapunov bounds," *SIAM Journal on Matrix Analysis and Applications*, vol. 11, no. 2, pp. 239–271, 1990.

Research Article

Event-Triggered Bipartite Consensus of Single-Integrator Multi-Agent Systems with Measurement Noise

Cui-Qin Ma ¹, Yun-Bo Zhao,² and Wei-Guo Sun¹

¹School of Mathematical Sciences, Qufu Normal University, Qufu 273165, Shandong, China

²College of Information Engineering, Zhejiang University of Technology, Hangzhou 310023, China

Correspondence should be addressed to Cui-Qin Ma; cuiqinma@amss.ac.cn

Received 29 May 2018; Accepted 22 July 2018; Published 6 August 2018

Academic Editor: Yong Chen

Copyright © 2018 Cui-Qin Ma et al. This is an open access article distributed under the Creative Commons Attribution License, which permits unrestricted use, distribution, and reproduction in any medium, provided the original work is properly cited.

Event-triggered bipartite consensus of single-integrator multi-agent systems is investigated in the presence of measurement noise. A time-varying gain function is proposed in the event-triggered bipartite consensus protocol to reduce the negative effects of the noise corrupted information processed by the agents. Using the state transition matrix, Itô formula, and the algebraic graph theory, necessary and sufficient conditions are given for the proposed protocol to yield mean square bipartite consensus. We find that the weakest communication requirement to ensure the mean square bipartite consensus under event-triggered protocol is that the signed digraph is structurally balanced and contains a spanning tree. Numerical examples validated the theoretical findings where the system shows no Zeno behavior.

1. Introduction

Recent years have witnessed the great achievements in studying the consensus problem of multi-agent systems (MASs) which has broad applications in various fields [1–8]. We notice that in these mentioned works interactions among agents are all assumed to be cooperative to achieve consensus. However, it is very natural to see, in many real examples, that in MASs some agents cooperate while others compete, and MASs with competitive interactions can introduce more complex behaviors. To quantitatively model such a scenario, the concept of bipartite consensus, i.e., agents agree on a certain quantity with the equal modulus but different signs, has been proposed [9], and many achievements have been made [9–18]. In [9], for single-integrator MASs, a linear feedback protocol is designed and under the assumption that the communication topology \mathcal{G} is strongly connected, the MAS is proved to achieve bipartite consensus if and only if \mathcal{G} is structurally balanced. Then, in [10], the communication condition in [9] is relaxed to containing a spanning tree. In [11], the communication topology in [9] is extended to the time-varying case.

It is worth noting that the above literatures mainly focus on continuous feedback protocols, where the agent state is monitored continuously and its controller is updated all the time. However, updating the controller in real-time easily increases the computational burden. Therefore, reducing the update frequency for a trade-off between the system performance and the resource usage is usually desired. This requirement then naturally brings event-triggered schemes into consideration, which updates only at some predetermined discrete time instants. Event-triggered techniques have already been widely used in traditional consensus problems of MASs [19–27]. For example, a self-triggered protocol is proposed in [19] and a decentralized event-triggered protocol ensuring average consensus is proposed in [20] for single-integrator MASs, time-dependent triggering functions are investigated in [24] for second-order MASs, and event-triggered consensus problems are considered in [25, 26] for general linear systems, just name a few. Despite these achievements, event-triggered protocols have not been well studied for bipartite consensus [28, 29], which thus motivates the present study.

In another parallel line, measurement noise is unavoidable in practice, making the investigation on

the event-triggered bipartite consensus of MASs with noise even interesting. In fact, studies on bipartite consensus with measurement noise can be found in [13, 16–18], which are however all with time-triggered controllers. Event-triggered bipartite consensus for MASs with measurement noise still remains to tackle.

In this paper, we investigate event-triggered bipartite consensus for single-integrator MASs with measurement noise. A time-varying control gain is introduced into the event-triggered protocols, leading to a time-varying closed-loop system. With the help of the state transition matrix and stochastic analysis theory, the closed-loop system is analyzed. Necessary and sufficient conditions for the system to achieve mean square bipartite consensus based on event-triggered protocols are given. We find that the communication topology being structurally balanced and containing a spanning tree are necessary and sufficient for ensuring a mean square bipartite consensus based on event-triggered protocols.

Organization. Section 2 gives the algebraic graph preliminaries and the problem in question. Section 3 contains the main results of the paper. Section 4 applies the results to examples of MASs with six agents. Section 5 closes this paper.

Notations. $R^{n \times m}$ represents the real matrix of $n \times m$ order. 0 denotes vector or matrix whose elements are 0 . $\mathbf{1}_n$ represents column vector whose elements are 1 . $\text{sgn}(\cdot)$ represents the sign function. \otimes represents Kronecker product. For a given matrix or vector X , X^T , and $\|X\|$ represent the transpose and European norm of X , respectively. $\|X\|_F$, $\|X\|_1$, and $\|X\|_\infty$ represent the Frobenius norm, 1-norm, and ∞ -norm, respectively. $\text{Re}(\lambda)$ is the real part of λ .

2. Problem Statement

The communication relations among N agents are described by the signed digraph $\mathcal{G} = (\mathcal{V}, \mathcal{E}, \mathcal{A})$, where $\mathcal{V} = \{1, \dots, N\}$ and $\mathcal{E} \subseteq \mathcal{V} \times \mathcal{V}$ represent the node set and the edge set, respectively. $\mathcal{A} = (a_{ij}) \in R^{N \times N}$, where $a_{ij} > 0$ and $a_{ij} < 0$ represent cooperation and competition between agents i and j , respectively. $a_{ij} \neq 0 \iff (j, i) \in \mathcal{E}$. We assume that $a_{ii} = 0$ and $a_{ij}a_{ji} \geq 0, \forall i, j \in \mathcal{V}$. $\mathcal{L} = \mathcal{C}_r - \mathcal{A}$ is the Laplacian matrix of \mathcal{G} , where $\mathcal{C}_r = \text{diag}(\sum_{j=1}^N |a_{1j}|, \dots, \sum_{j=1}^N |a_{Nj}|)$. A signed digraph $\mathcal{G} = (\mathcal{V}, \mathcal{E}, \mathcal{A})$ is said structurally balanced if \mathcal{V} can be divided into two subsets $\mathcal{V}_1, \mathcal{V}_2, \mathcal{V}_1 \cup \mathcal{V}_2 = \mathcal{V}, \mathcal{V}_1 \cap \mathcal{V}_2 = \emptyset$, such that $a_{ij} \geq 0, \forall i, j \in \mathcal{V}_p (p \in \{1, 2\})$, and $a_{ij} \leq 0, \forall i \in \mathcal{V}_p, j \in \mathcal{V}_q (p \neq q, p, q \in \{1, 2\})$. It is said structurally unbalanced otherwise.

Lemma 1 (see [12]). *If \mathcal{G} is structurally balanced, Laplacian \mathcal{L} of \mathcal{G} has at least one zero eigenvalue and all of the nonzero eigenvalues have positive real parts. Furthermore, \mathcal{L} has only one zero eigenvalue if and only if \mathcal{G} has a spanning tree.*

Consider a MAS described by

$$\dot{x}_i(t) = u_i(t), \quad i = 1, \dots, N, \quad (1)$$

where $x_i(t) \in R^n$ is the state of the i th agent and $u_i(t) \in R^n$ is the control input. A signed digraph $\mathcal{G} = (\mathcal{V}, \mathcal{E}, \mathcal{A})$ is used to describe interactions among the N agents.

Since communication is often disturbed by measurement noise, we assume the i th agent receives information from its neighbors with measurement noise $x_j(t) + \varphi_{ji}(t)$, $j \in \mathcal{N}_i$, $i = 1, \dots, N$. In order to reduce the frequency of controller updates, we design the following event-triggered protocol for the i th agent:

$$u_i(t) = b(t) \left[\sum_{j=1}^N |a_{ij}| \left(\text{sgn}(a_{ij}) x_j(t_k) - x_i(t_k) \right) + \sum_{j=1}^N a_{ij} \varphi_{ji}(t) \right], \quad \forall t \in [t_k, t_{k+1}), \quad (2)$$

where $i = 1, \dots, N$, $k = 0, 1, \dots, b(t) > 0$ is a piecewise continuous function. $\{\varphi_{ji}(t)\}$ is n dimensional independent standard white noise.

Remark 2. As far as we know the existing results [28, 29] for event-triggered bipartite consensus did not consider measurement noise. Here, we take noise into consideration. If we take $b(t) \equiv 1$, then (2) is reduced to the protocols in [28, 29] without measurement noise.

Let $X(t) = (x_1^T(t), \dots, x_N^T(t))^T$ and $J = \text{diag}(\zeta_1^T(t), \dots, \zeta_N^T(t))^T$ be $N \times N^2$ dimensional block diagonal matrix, where $\zeta_i^T(t) = (a_{i1}, \dots, a_{iN})$ is the i th row element of matrix \mathcal{A} . Then the closed-loop system is

$$dX(t) = -b(t) (\mathcal{L} \otimes I_n) X(t_k) dt + b(t) (J \otimes I_n) d\Lambda(t), \quad (3)$$

$$t \in [t_k, t_{k+1}), \quad k = 0, 1, \dots$$

where $\Lambda(t) = (\Lambda_1^T(t), \dots, \Lambda_N^T(t))^T$ and $\Lambda_i(t) = (\Lambda_{1i}^T(t), \dots, \Lambda_{Ni}^T(t))^T$, $i = 1, \dots, N$. For $i, j = 1, \dots, N$, $\int_0^t \varphi_{ji}(s) ds = \Lambda_{ji}(t)$ is n dimensional standard Brownian motion. Let $e(t) = (e_1(t), \dots, e_N(t))^T$ be the measurement error, where $e_i(t) = x_i(t_k) - x_i(t)$, $t \in [t_k, t_{k+1}), k = 0, 1, \dots$. Then (3) is changed to

$$dX(t) = -b(t) (\mathcal{L} \otimes I_n) (X(t) + e(t)) dt + b(t) (J \otimes I_n) d\Lambda(t), \quad (4)$$

$$t \in [t_k, t_{k+1}), \quad k = 0, 1, \dots$$

We present the following definition of event-triggered bipartite consensus for the stochastic system.

Definition 3. Let $\mathcal{U} = \{u_i, i = 1, \dots, N\}$ be an event-triggered protocol. If for any given $X(0) \in R^{nN}$, there exist $g = (g_1, \dots, g_N)^T \in R^N$, $g_i \in \{\pm 1\}$, $i = 1, \dots, N$ and n dimensional random vector v^* ,

$$\lim_{t \rightarrow \infty} E \|X(t) - g \otimes v^*\|^2 = 0, \quad (5)$$

where $E \|v^*\|^2 < \infty$, $E v^*$ is dependent on communication relations among agents and $X(0)$, which is deterministic.

Then, event-triggered protocol \mathcal{U} is called a mean square bipartite consensus protocol.

We introduce the event-triggered condition

$$\|e(t)\| \leq c_1 e^{-\alpha t}, \quad (6)$$

where $c_1 > 0, 0 < \alpha < \min_{\lambda(\mathcal{L}) \neq 0} \{\operatorname{Re}(\lambda(\mathcal{L}))\}$. When the measurement error $\|e(t)\|$ is over the threshold, the controller is triggered and updates itself.

To analyze the closed-loop system in (4), we make the following assumptions:

- (Q₁) $\mathcal{G} = (\mathcal{V}, \mathcal{E}, \mathcal{A})$ is structurally balanced.
- (Q₂) $\mathcal{G} = (\mathcal{V}, \mathcal{E}, \mathcal{A})$ contains a spanning tree.
- (Q₃) $\int_0^\infty b(s) ds = \infty$.
- (Q₄) $\int_0^\infty b^2(s) ds < \infty$.

The following lemma plays an important role in the following section.

Lemma 4 (see [16]). *Given linear time-varying system*

$$\frac{dY_l}{dt} = -b(t) F_l^\lambda Y_l, \quad l \in \mathbb{N}, \lambda \in \mathbb{C}, t \geq t_0 \geq 0, \quad (7)$$

where $Y_l = (y_{l1}, \dots, y_{lR_l})^T \in \mathbb{R}^{R_l}$ and F_l^λ is the $R_l \times R_l$ dimensional Jordan block, which λ is the diagonal element. Then the state transition matrix of (7) is $\Psi_{F_l^\lambda}(t, t_0) = e^{-\int_{t_0}^t b(s) ds F_l^\lambda}$. In addition, we can obtain $\lim_{t \rightarrow \infty} \Psi_{F_l^\lambda}(t, t_0) = 0$ if $\int_0^\infty b(s) ds = \infty$ and $\operatorname{Re}(\lambda) > 0$.

Lemma 5. *If the event-triggered protocol (2) is a mean square bipartite consensus protocol, then $\exists g = (g_1, \dots, g_N)^T \in \mathbb{R}^N$, $g_i \in \{\pm 1\}$, $i = 1, \dots, N$, and $\theta = (\theta_1, \dots, \theta_N)^T \in \mathbb{R}^N$, such that $\lim_{t \rightarrow \infty} \Psi(t, 0) = g\theta^T \otimes I_n$, where $\Psi(t, 0)$ is the state transition matrix of (4).*

Proof. From the above condition, Definition 3 implies that for any given initial state $X(0)$, there exist a vector g and a random vector v^* so that $\lim_{t \rightarrow \infty} E\|X(t) - g \otimes v^*\|^2 = 0$. Obviously,

$$\begin{aligned} X(t) &= \Psi(t, 0) X(0) \\ &- \int_0^t b(s) \Psi(t, s) (\mathcal{L} \otimes I_n) e(s) ds \\ &+ \int_0^t b(s) \Psi(t, s) (J \otimes I_n) d\Lambda(s). \end{aligned} \quad (8)$$

Without loss of generality, we assume $\int_0^t b(s) \Psi(t, s) (\mathcal{L} \otimes I_n) e(s) ds$ and $\int_0^t b(s) \Psi(t, s) (J \otimes I_n) d\Lambda(s)$ converge to Y^* and Z^* in mean square sense, respectively. Then,

$$\begin{aligned} g \otimes E v^* &= \lim_{t \rightarrow \infty} E X(t) \\ &= (\Psi_\infty \otimes I_n) X(0) - E Y^* + E Z^*, \end{aligned} \quad (9)$$

where $\lim_{t \rightarrow \infty} \Psi(t, 0) = \Psi_\infty \otimes I_n$. According to Definition 3 and the arbitrariness of $X(0)$, one obtains $(\Psi_\infty \otimes I_n) X(0) = g \otimes E v^*$, where $E v^* \in \mathbb{R}^N$.

Let $\Psi_\infty = (\varrho_1, \dots, \varrho_N)$. Then, all elements of ϱ_i have the same absolute value. The same applies for $\sum_{j=1}^N (\varrho_j \otimes \tau_j)$, where $\tau_j \in \mathbb{R}^n$, $j = 1, \dots, N$. If $\Psi_\infty = 0$, then by making $\theta = 0$, Lemma 5 holds. If Ψ_∞ has at least one nonzero column, without loss of generality, we assume $\varrho_1 \neq 0$. Then $\varrho_1 = \theta_1 g$. Without loss of generality, we assume $\theta_1 > 0$. For any $\alpha, \beta \in \mathbb{R}^n$, $a, b \in \mathbb{R}$, $a, b \neq 0$, $a\alpha + b\beta \neq \pm(a\alpha - b\beta)$. If $\varrho_j \neq 0$ for some $j \neq 1$, then all n dimensional components of $\varrho_j \otimes \alpha - \varrho_1 \otimes \beta$ have the same modulus if and only if $\varrho_j = \theta_j g$, $\theta_j > 0$. If $\varrho_j = 0$, we have $\varrho_j = \theta_j g$ by taking $\theta_j = 0$. Then $\Psi_\infty = (\varrho_1, \dots, \varrho_N) = (\theta_1 g, \dots, \theta_N g) = g(\theta_1, \dots, \theta_N)$. In addition, $\lim_{t \rightarrow \infty} \Psi(t, 0) = \Psi_\infty \otimes I_n$, so $\lim_{t \rightarrow \infty} \Psi(t, 0) = g(\theta_1, \theta_2, \dots, \theta_N) \otimes I_n = g\theta^T \otimes I_n$. \square

Lemma 6. *If (Q₁) – (Q₄) hold, then for any given initial state $X(0)$, there is a random vector X^* such that $X(t)$ converges to X^* in mean square sense, i.e., $\lim_{t \rightarrow \infty} E\|X(t) - X^*\|^2 = 0$.*

Proof. If (Q₁) and (Q₂) hold, then Laplacian \mathcal{L} has exactly one zero eigenvalue and all nonzero eigenvalues have positive real parts by Lemma 1. Thus, there exists an invertible matrix D , such that

$$D^{-1} \mathcal{L} D = F = \operatorname{diag}(0, F_2, \dots, F_\gamma), \quad (10)$$

where F_i ($i = 2, \dots, \gamma$) is the $R_i \times R_i$ dimensional Jordan block, which λ_i is the diagonal element, and $R_2 + \dots + R_\gamma = N - 1$. Obviously, $\lambda_2, \dots, \lambda_\gamma$ are eigenvalues of \mathcal{L} and $\operatorname{Re}(\lambda_i) > 0$, $i = 2, \dots, \gamma$.

Since $\Psi(t, t_0)$ ($t_0 \geq 0$) is the state transition matrix of (4), $\Psi(t, t_0) = e^{-\int_{t_0}^t b(s) ds \mathcal{L}} \otimes I_n$. From Lemma 4,

$$\begin{aligned} \Psi(t, t_0) &= (D \otimes I_n) \\ &\cdot \operatorname{diag}\left(I_n, \Psi_{F_2^{\lambda_2}}(t, t_0) \otimes I_n, \dots, \Psi_{F_\gamma^{\lambda_\gamma}}(t, t_0) \otimes I_n\right) \\ &\cdot (D^{-1} \otimes I_n). \end{aligned} \quad (11)$$

Combining this with (Q₃), one has

$$\lim_{t \rightarrow \infty} \Psi(t, t_0) = \left[D \operatorname{diag}(1, 0, 0, \dots, 0) D^{-1} \right] \otimes I_n. \quad (12)$$

Thus, there exists $T > 0$ so that for any $t \geq t_0 > 0$,

$$\max(\|\Psi(t, t_0)\|_1, \|\Psi(t, t_0)\|_\infty) \leq T < \infty. \quad (13)$$

By Itô formula, the solution of (4) is given by

$$\begin{aligned} X(t) &= \Psi(t, 0) X(0) \\ &- \int_0^t b(s) \Psi(t, s) (\mathcal{L} \otimes I_n) e(s) ds \\ &+ \int_0^t b(s) \Psi(t, s) (J \otimes I_n) d\Lambda(s). \end{aligned} \quad (14)$$

By (\mathbf{Q}_4) , one obtains that, $\forall \varepsilon > 0, \exists \Gamma_0 > 0, \int_{\Gamma_0}^{\infty} b^2(s) ds < \varepsilon$. By (12), $\exists \Gamma_1 > \Gamma_0$, such that $\max(\|\Psi(t_2, t_3) - \Psi(t_1, t_3)\|_1, \|\Psi(t_2, t_3) - \Psi(t_1, t_3)\|_{\infty}) < \varepsilon, t_2 \geq t_1 > \Gamma_1, \forall t_3 \in [0, \Gamma_0]$.

Let $X_2(t) = \int_0^t b(s)\Psi(t, s)(\mathcal{L} \otimes I_n)e(s)ds$, then by (10) and (11), one has

$$\begin{aligned} X_2(t) &= \int_0^t b(s)(D \otimes I_n) \\ &\cdot \text{diag}\left(I_n, \Psi_{F_2^{\lambda_2}}(t, s) \otimes I_n, \dots, \Psi_{F_v^{\lambda_v}}(t, s) \otimes I_n\right) \\ &\cdot (D^{-1}\mathcal{L} \otimes I_n)e(s) ds. \end{aligned} \quad (15)$$

By (6), (10), and direct calculation, one has $(D^{-1}\mathcal{L} \otimes I_n)e(s) = (0, \mathcal{D}_2^T(s), \dots, \mathcal{D}_N^T(s))^T$, where $\mathcal{D}_i(s)$ ($i = 2, \dots, N$) is the linear combination of $e_1(s), \dots, e_N(s)$. By L'Hospital and direct calculation, one obtains

$$\begin{aligned} \lim_{t \rightarrow \infty} \int_0^t b(s) e^{-\lambda_i \int_s^t b(\tau) d\tau} \left(\int_s^t b(\tau) d\tau \right)^m e^{-\alpha s} ds &= 0, \\ m &= 0, 1, \dots, R_i - 1; i = 2, \dots, \gamma. \end{aligned} \quad (16)$$

Noticing that $\Psi_{F_i^{\lambda_i}}(t, s) = \sum_{d=0}^{\infty} ((-\int_s^t b(\tau) d\tau)^d (F_i^{\lambda_i})^d / d!)$, one has $\lim_{t \rightarrow \infty} X_2(t) = 0$.

Let $X_3(t) = \int_0^t b(s)\Psi(t, s)(J \otimes I_n)d\Lambda(s)$, then

$$\begin{aligned} X_3(t_2) - X_3(t_1) &= \int_0^{t_2} b(s) [\Psi(t_2, s) - \Psi(t_1, s)] (J \otimes I_n) d\Lambda(s) \\ &+ \int_{t_1}^{t_2} b(s) \Psi(t_1, s) (J \otimes I_n) d\Lambda(s) \triangleq X_{31} + X_{32}. \end{aligned} \quad (17)$$

Therefore $E\|X_3(t_2) - X_3(t_1)\|^2 \leq 2E\|X_{31}\|^2 + 2E\|X_{32}\|^2$. It is easy to obtain

$$\begin{aligned} E\|X_{31}\|^2 &= \int_0^{t_2} b^2(s) \|\Psi(t_2, s) - \Psi(t_1, s)\|_F^2 ds. \end{aligned} \quad (18)$$

Noting

$$\begin{aligned} \int_0^{T_0} b^2(s) \|\Psi(t_2, s) - \Psi(t_1, s)\|_F^2 ds \\ \leq nN \|(J \otimes I_n)\|_1^2 \int_0^{\infty} b^2(s) ds \triangleq M_4 \varepsilon^2 \end{aligned} \quad (19)$$

and

$$\begin{aligned} \int_{\Gamma_0}^{t_2} b^2(s) \|\Psi(t_2, s) - \Psi(t_1, s)\|_F^2 ds \\ \leq 4nNL^2 \|(J \otimes I_n)\|_1^2 \varepsilon \triangleq M_5 \varepsilon, \end{aligned} \quad (20)$$

one has $E\|X_{31}\|^2 \leq M_4 \varepsilon^2 + M_5 \varepsilon$. Similarly, one obtains

$$\begin{aligned} E\|X_{32}\|^2 &= \int_{t_1}^{t_2} b^2(s) \|\Psi(t_1, s)(J \otimes I_n)\|_F^2 ds \\ &\leq nNL^2 \|(J \otimes I_n)\|_1^2 \varepsilon \triangleq \frac{M_5}{4} \varepsilon. \end{aligned} \quad (21)$$

So $E\|X_3(t_2) - X_3(t_1)\|^2 \leq 2M_4 \varepsilon^2 + (5/2)M_5 \varepsilon$. By Cauchy criterion and the arbitrariness of ε , there exists X_3^* such that $X_3(t)$ converges to X_3^* in mean square sense. So there exists X^* such that $X(t)$ converges to X^* in mean square sense. By (12), $X^* = [D \text{diag}(1, 0, \dots, 0)D^{-1} \otimes I_n]X(0) + X_3^*$. \square

3. Main Results

In this section, we give necessary and sufficient conditions for the proposed event-triggered protocols to guarantee a mean square bipartite consensus.

Theorem 7. *The event-triggered protocol in (2) is a mean square bipartite consensus protocol for the system in (1) if and only if (\mathbf{Q}_1) - (\mathbf{Q}_4) hold.*

Proof (sufficiency).

(S.1) *Construct a Bipartition for the MAS.* By (\mathbf{Q}_3) , \mathcal{V} can be decomposed into two disjoint subsets $\mathcal{V}_{v_1}, \mathcal{V}_{v_2}, \mathcal{V}_{v_1} \cup \mathcal{V}_{v_2} = \mathcal{V}, \mathcal{V}_{v_1} \cap \mathcal{V}_{v_2} = \emptyset$, and $a_{st} \leq 0$ for $s \in \mathcal{V}_f, t \in \mathcal{V}_g, f \neq g, f, g \in \{v_1, v_2\}$, and $a_{st} \geq 0$ for $s, t \in \mathcal{V}_p, p \in \{v_1, v_2\}$. Without loss of generality, we assume $\mathcal{V}_{v_1} = \{1, \dots, m\}, \mathcal{V}_{v_2} = \{m+1, \dots, N\}$. Let $g_i = 1$ for $i \in \mathcal{V}_{v_1}$ and $g_j = -1$ for $j \in \mathcal{V}_{v_2}$. By definition, one has $\mathcal{L}g = 0$, where $g = (g_1, \dots, g_N)^T$.

(S.2) *Prove $\lim_{t \rightarrow \infty} E\|X(t) - g \otimes v^*\|^2 = 0$.* From Lemma 6, $\exists X^*, \lim_{t \rightarrow \infty} E\|X(t) - X^*\|^2 = 0$. Without loss of generality, we assume $\lim_{t \rightarrow \infty} E\|x_1(t) - v^*\|^2 = 0$. Next, we will prove $\lim_{t \rightarrow \infty} E\|x_i(t) - g_i v^*\|^2 = 0, i = 2, \dots, N$.

Let $\phi(t) = (\phi_2^T(t), \dots, \phi_N^T(t))^T$, where $\phi_i(t) = x_i(t) - g_i x_1(t), i = 2, \dots, N$. Now we prove that $\lim_{t \rightarrow \infty} E\|\phi(t)\|^2 = 0$. For this purpose, We assume $\tilde{\phi}(t) \triangleq (Q \otimes I_n)X(t)$, where

$$\begin{aligned} Q &\triangleq \left(\begin{array}{c|cc} \frac{1}{N} & \frac{1}{N} \dots \frac{1}{N} & -\frac{1}{N} \dots -\frac{1}{N} \\ -\mathbf{1}_{m-1} & I_{m-1} & 0 \\ -\mathbf{1}_{N-m} & 0 & -I_{N-m} \end{array} \right) \\ &= \begin{pmatrix} \frac{1}{N} g^T \\ Q_2 \end{pmatrix}. \end{aligned} \quad (22)$$

Then $\tilde{\phi}(t) = (\chi^T(t), \phi^T(t))^T$, where $\chi(t) \triangleq (1/N)(g^T \otimes I_n)X(t)$. Since

$$Q\mathcal{L}Q^{-1} = \begin{pmatrix} 0 & \omega^T \\ 0 & L_2 \end{pmatrix}, \quad (23)$$

by (4), one has

$$\begin{aligned} d\phi(t) = & -b(t)(L_2 \otimes I_n)\phi(t) dt \\ & - b(t)(Q_2L \otimes I_n)e(t) dt \\ & + b(t)(Q_2J \otimes I_n)d\Lambda(t). \end{aligned} \quad (24)$$

By (23), $S^{-1}L_2S = \text{diag}(F_2, \dots, F_\gamma)$, where S is invertible and F_2, \dots, F_γ are given in (10). The state transition matrix of the system in (24) is

$$\begin{aligned} \Psi_2(t, t_0) = & (S \otimes I_n) \\ & \cdot \left[\text{diag} \left(\Psi_{F_2^{\lambda_2}}(t, t_0) \otimes I_n, \dots, \Psi_{F_\gamma^{\lambda_\gamma}}(t, t_0) \otimes I_n \right) \right] \\ & \cdot (S^{-1} \otimes I_n), \end{aligned} \quad (25)$$

where $\Psi_{F_q^{\lambda_q}}(t, t_0)$, $q = 2, \dots, \gamma$ are defined as in Lemma 4. Hence, $\lim_{t \rightarrow \infty} \Psi_2(t, t_0) = 0$, i.e., $\forall \varepsilon > 0, \exists T_2 > T_1$, such that $\|\Psi_2(t, t_0)\| < \varepsilon, \forall t > T_2$. Furthermore, $\exists T_{L_2} > 0$, such that, $\forall t > t_0 \geq 0, \max(\|\Psi_2(t, t_0)\|_1, \|\Psi_2(t, t_0)\|_\infty) \leq T_{L_2} < \infty$.

By Itô formula, it can be seen that the state of the system in (24) can be described as

$$\begin{aligned} \phi(t) = & \Psi_2(t, 0)\phi(0) \\ & - \int_0^t b(s)\Psi_2(t, s)(Q_2L \otimes I_n)e(s) ds \\ & + \int_0^t b(s)\Psi_2(t, s)(Q_2J \otimes I_n)d\Lambda(s). \end{aligned} \quad (26)$$

Therefore,

$$\begin{aligned} E\|\phi(t)\|^2 = & \|\Psi_2(t, 0)\phi(0)\|^2 - 2\phi^T(0)\Psi_2^T(t, 0) \\ & \cdot \int_0^t b(s)\Psi_2(t, s)(Q_2L \otimes I_n)e(s) ds \\ & + \left\| \int_0^t b(s)\Psi_2(t, s)(Q_2L \otimes I_n)e(s) ds \right\|^2 \\ & + \int_0^t b^2(s)\|\Psi_2(t, s)(Q_2J \otimes I_n)\|_F^2 ds, \end{aligned} \quad (27)$$

and hence,

$$\begin{aligned} E\|\phi(t)\|^2 \leq & 2\|\Psi_2(t, 0)\phi(0)\|^2 \\ & + 2\left\| \int_0^t b(s)\Psi_2(t, s)(Q_2L \otimes I_n)e(s) ds \right\|^2 \\ & + \int_0^t b^2(s)\|\Psi_2(t, s)(Q_2J \otimes I_n)\|_F^2 ds. \end{aligned} \quad (28)$$

Since

$$\begin{aligned} \left\| \int_0^t b(s)\Psi_2(t, s)(Q_2L \otimes I_n)e(s) ds \right\|^2 \\ \leq \int_0^t b^2(s)\|\Psi_2(t, s)\|^2 ds \int_0^t \|(Q_2L \otimes I_n)\|^2 \|e(s)\|^2 ds \end{aligned} \quad (29)$$

and

$$\begin{aligned} \int_0^t \|(Q_2L \otimes I_n)\|^2 \|e(s)\|^2 ds \\ \leq \|(Q_2L \otimes I_n)\|^2 \int_0^t c_1^2 e^{-2\alpha s} ds \leq \frac{c_1^2}{2\alpha} \|(Q_2L \otimes I_n)\|^2, \end{aligned} \quad (30)$$

there exists $\beta_3 > 0$ such that $\int_0^t \|(Q_2L \otimes I_n)\|^2 \|e(s)\|^2 ds \leq \beta_3$. Then

$$\begin{aligned} \left\| \int_0^t b(s)\Psi_2(t, s)(Q_2L \otimes I_n)e(s) ds \right\|^2 \\ \leq \beta_3 \int_0^{\Gamma_0} b^2(s)\|\Psi_2(t, s)\|^2 ds \\ + \beta_3 \int_{\Gamma_0}^t b^2(s)\|\Psi_2(t, s)\|^2 ds. \end{aligned} \quad (31)$$

Since $\int_0^{\Gamma_0} b^2(s)\|\Psi_2(t, s)\|^2 ds = \|\Psi_2(t, \eta)\|^2 \int_0^{\Gamma_0} b^2(s) ds \leq \|\Psi_2(t, \eta)\|^2 \int_0^{\infty} b^2(s) ds$, where $\eta \in (0, \Gamma_0)$ and $\int_{\Gamma_0}^{\infty} b^2(s) ds < \varepsilon$, one has $\int_{\Gamma_0}^t b^2(s)\|\Psi_2(t, s)\|^2 ds \leq T_{L_2}^2 \varepsilon \triangleq M_6 \varepsilon$. Therefore, $\forall t > T_2$

$$\begin{aligned} \left\| \int_0^t b(s)\Psi_2(t, s)(Q_2L \otimes I_n)e(s) ds \right\|^2 \\ \leq \beta_3 \|\Psi_2(t, \eta)\|^2 \int_0^{\infty} b^2(s) ds + M_6 \beta_3 \varepsilon \\ \leq \varepsilon^2 \beta_3 \int_0^{\infty} b^2(s) ds + M_6 \beta_3 \varepsilon. \end{aligned} \quad (32)$$

From $\int_{\Gamma_0}^{\infty} b^2(s) ds < \varepsilon$, one gets

$$\begin{aligned} \int_{\Gamma_0}^t b^2(s)\|\Psi_2(t, s)(Q_2J \otimes I_n)\|_F^2 ds \\ < nNT_{L_2}^2 \|(Q_2J \otimes I_n)\|_1^2 \varepsilon \triangleq M_7 \varepsilon. \end{aligned} \quad (33)$$

Combining this with

$$\begin{aligned} \int_0^{\Gamma_0} b^2(s)\|\Psi_2(t, s)(Q_2J \otimes I_n)\|_F^2 ds \\ \leq nN\|\Psi_2(t, \xi)\|_1^2 \|(Q_2J \otimes I_n)\|_1^2 \int_0^{\infty} b^2(s) ds, \\ \xi \in (0, \Gamma_0), \end{aligned} \quad (34)$$

one has

$$\begin{aligned} E\|\phi(t)\|^2 \leq & 2\|\phi(0)\|^2 \varepsilon^2 + 2\beta_3 \varepsilon^2 \int_0^{\infty} b^2(s) ds \\ & + nN \varepsilon^2 \|(Q_2J \otimes I_n)\|_1^2 \int_0^{\infty} b^2(s) ds \\ & + 2M_6 \beta_3 \varepsilon + M_7 \varepsilon. \end{aligned} \quad (35)$$

By the arbitrariness of ε , one gets $\lim_{t \rightarrow \infty} E\|\phi(t)\|^2 = 0$. Hence, $\lim_{t \rightarrow \infty} E\|X(t) - g \otimes v^*\|^2 = 0$.

(S.3) *Analyze the Statistical Characteristics of v^* .* By Lemma 6, $g \otimes v^* = X^* = [D \text{diag}(1, 0, 0, \dots, 0)D^{-1} \otimes I_n]X(0) + X_3^*$. So $g \otimes Ev^* = EX^* = [D \text{diag}(1, 0, 0, \dots, 0)D^{-1} \otimes I_n]X(0)$.

We assume m_r, m_1^T represent the first column of D and the first row of D^{-1} , respectively. Then, $g \otimes Ev^* = (m_r m_1^T \otimes I_n)X(0)$. Since $D^{-1}\mathcal{L}D = F$, $\mathcal{L}D = DF$, and $D^{-1}\mathcal{L} = FD^{-1}$, $\mathcal{L}m_r = 0$ and $m_1^T \mathcal{L} = 0$. By (S.1), $\mathcal{L}g = 0$. Therefore, $m_r = \kappa g$ ($\kappa \in \mathbb{R}$ and $\kappa \neq 0$) and $g \otimes Ev^* = g \otimes [\kappa(m_1^T \otimes I_n)X(0)]$. Then $Ev^* = \kappa(m_1^T \otimes I_n)X(0)$. Clearly, m_1 is concerned with communication topology. Thus, Ev^* is determined by $X(0)$ and communication topology of MASs.

It is easy to obtain that $\Psi(\cdot)$ is uniformly bounded. Therefore, $\forall \varepsilon > 0, \exists \Gamma_3 > \Gamma_2$,

$$\begin{aligned} & \int_{\Gamma_3}^{\infty} b^2(s) \left\| \Psi(t, s) (J \otimes I_n) (J \otimes I_n)^T \Psi^T(t, s) \right\| ds < \varepsilon, \\ & \int_{\Gamma_3}^{\infty} b^2(s) \left\| (m_r m_1^T \otimes I_n) (J \otimes I_n) (J \otimes I_n)^T \right. \\ & \quad \left. \cdot (m_r m_1^T \otimes I_n)^T \right\| ds < \varepsilon. \end{aligned} \quad (36)$$

Let $X_4(t) = \int_0^{\Gamma_3} b^2(s) \Psi(t, s) (J \otimes I_n) (J \otimes I_n)^T \Psi^T(t, s) ds$. Then for any $t > \Gamma_4$, $\|X_4(t) - \int_0^{\Gamma_3} b^2(s) (m_r m_1^T \otimes I_n) (J \otimes I_n) (J \otimes I_n)^T (m_r m_1^T \otimes I_n)^T ds\| < \varepsilon$. This together with (36) leads to $\lim_{t \rightarrow \infty} \int_0^t b^2(s) \Psi(t, s) (J \otimes I_n) (J \otimes I_n)^T \Psi^T(t, s) ds = \int_0^{\infty} b^2(s) (m_r m_1^T J J^T m_1 m_r^T \otimes I_n) ds = \Theta (g g^T \otimes I_n)$, where $\Theta = \kappa^2 (m_1^T J J^T m_1) \int_0^{\infty} b^2(s) ds$. Combining this with $D(X^*) = \lim_{t \rightarrow \infty} \int_0^t b^2(s) \times \Psi(t, s) (J \otimes I_n) (J \otimes I_n)^T \Psi^T(t, s) ds$, one gets $D(v^*) = \Theta I_n$. Therefore, $E\|v^*\|^2 < \infty$. By Definition 3, the sufficiency is established.

Necessity.

(B.1) *Prove (Q₃), Namely, $\int_0^{\infty} b(s) ds = \infty$.* By contradiction, we assume that (Q₃) does not hold. Then, $\exists \bar{\varepsilon} > 0$, $\int_0^{\infty} b(s) ds = \bar{\varepsilon}$, and $\lim_{t \rightarrow \infty} e^{-\int_0^t b(s) ds \mathcal{L}} = e^{-\bar{\varepsilon} \mathcal{L}}$. Therefore, $\text{rank}(\lim_{t \rightarrow \infty} \Psi(t, 0)) = \text{rank}(e^{-\bar{\varepsilon} \mathcal{L}} \otimes I_n) = nN$. However, by Lemma 5, $\lim_{t \rightarrow \infty} \Psi(t, 0) = g \theta^T \otimes I_n$ and $\text{rank}(\lim_{t \rightarrow \infty} \Psi(t, 0)) \leq n$. This is a contradiction. So (Q₃) holds.

(B.2) *Prove That Laplacian Matrix \mathcal{L} Has Exactly One Zero Eigenvalue.* By contradiction, we assume that 0 is not an eigenvalue of \mathcal{L} . Then all the eigenvalues of \mathcal{L} have positive real part and $-\mathcal{L}$ is a Hurwitz matrix. By (Q₃) and Lemma 4, $\lim_{t \rightarrow \infty} \Psi(t, 0) = 0$. Combining this with Lemma 5, one has $g \otimes Ev^* = EZ^* - EY^*$. Since EZ^* and EY^* are independent of $X(0)$, Ev^* is independent of $X(0)$. This contradicts Definition 3. So 0 is an eigenvalue of \mathcal{L} .

Let F_1^0 be a Jordan block with eigenvalue 0. Then it is 1 dimensional. Otherwise, we assume F_1^0 is R_1 dimensional and $R_1 > 1$. Then, by (Q₃) and the definition of matrix exponent

function, one gets that $\lim_{t \rightarrow \infty} e^{-\int_0^t b(s) ds F_1^0}$ does not exist, and hence, $\lim_{t \rightarrow \infty} \Psi(t, 0)$ does not exist. This contradicts Lemma 5. So F_1^0 is 1 dimensional.

Let algebra multiplicity of eigenvalue 0 be w . Then $w = 1$. Otherwise, $w > 1$. Take $w = 2$ as an example. Since each Jordan block corresponding to eigenvalue 0 is 1 dimensional,

$$\begin{aligned} \Psi_{\infty} \otimes I_n & \triangleq \lim_{t \rightarrow \infty} \Psi(t, 0) = \lim_{t \rightarrow \infty} e^{-\int_0^t b(s) ds \mathcal{L}} \otimes I_n \\ & = D \text{diag}(1, 1, 0, \dots, 0) D^{-1} \otimes I_n. \end{aligned} \quad (37)$$

Thus, $\text{rank}(\Psi_{\infty}) = 2$. This contradicts $\text{rank}(\Psi_{\infty}) \leq 1$ from Lemma 6. So Laplacian \mathcal{L} has exactly one zero eigenvalue.

(B.3) *Prove (Q₁) and (Q₂).* By (B.2) and (Q₃), one has (12). By Lemma 5, one gets

$$D \text{diag}(1, 0, 0, \dots, 0) D^{-1} = g \theta^T. \quad (38)$$

Noticing that m_r is the first column of D , one has $\mathcal{L}m_r = 0$. By (38), one obtains $m_r = g \kappa^*$, where $\kappa^* = \theta^T m_r \in \mathbb{R}$. Then, $\mathcal{L}g = 0$. By the definition of \mathcal{L} , for any j , we obtain $g_j \sum_{k \neq j} |a_{jk}| = \sum_{k \neq j} g_k a_{jk}$, $j = 1, \dots, N$. Since $g_j = \pm 1$ and $g_j^2 = 1$, $j = 1, 2, \dots, N$, $\sum_{k \neq j} |a_{jk}| = \sum_{k \neq j} g_j g_k a_{jk}$. So $g_j g_k a_{jk} = |a_{jk}| \geq 0$. Let $V_1 = \{j \mid g_j = 1\}$ and $V_2 = \{j \mid g_j = -1\}$, then $V_1 \cap V_2 = \emptyset$, $V_1 \cup V_2 = V$. If $j \in \mathcal{V}_p$, $p \in \{1, 2\}$, then $a_{jk} \geq 0$, $k \in \mathcal{V}_p$ or $a_{jk} \leq 0$, $k \in \mathcal{V}_r$, $r \neq p$, $r \in \{1, 2\}$. By definition, \mathcal{G} is structurally balanced, that is, (Q₁) holds.

By (B.2) and (Q₁), Lemma 1 implies that (Q₂) holds.

(B.4) *Prove (Q₄).* Assume $\int_0^{\infty} b^2(s) ds = \infty$. Due to the first row of D^{-1} which is m_1^T , $m_1^T \mathcal{L} = 0$. By (4), we obtain $d((m_1^T \otimes I_n)X(t)) = b(t)(m_1^T \otimes I_n)(J \otimes I_n)d\Lambda(t)$, i.e.,

$$\begin{aligned} & (m_1^T \otimes I_n) X(t) \\ & = (m_1^T \otimes I_n) X(0) \\ & \quad + (m_1^T \otimes I_n) (J \otimes I_n) \int_0^t b(s) d\Lambda(s). \end{aligned} \quad (39)$$

From Definition 3, it is known that $X(t)$ converges to $g \otimes v^*$ in mean square sense, where $E\|v^*\|^2 < \infty$. Thus, when $t \rightarrow \infty$, $(m_1^T \otimes I_n)(J \otimes I_n) \int_0^t b(s) d\Lambda(s)$ converges to a random variable X_m in mean square sense with $E\|X_m\|^2 < \infty$. Then $\lim_{t \rightarrow \infty} E\|(m_1^T \otimes I_n)(J \otimes I_n) \int_0^t b(s) d\Lambda(s)\|^2 = \lim_{t \rightarrow \infty} \text{tr}(m_1^T J J^T m_1 \otimes I_n) \int_0^t b^2(s) ds = \infty$. This leads to a contradiction. So (Q₄) holds. \square

Remark 8. From Theorem 7 it can be seen that under (Q₁)-(Q₄) the event-triggered protocol in (2) ensures agents converging to v^* or $-v^*$ under measurement noise.

Remark 9. From Theorem 7 one sees that to guarantee the mean square bipartite consensus, (Q₁)-(Q₂) are requirements for time-varying gain $b(t)$ while (Q₃)-(Q₄) are the weakest connectivity assumptions.

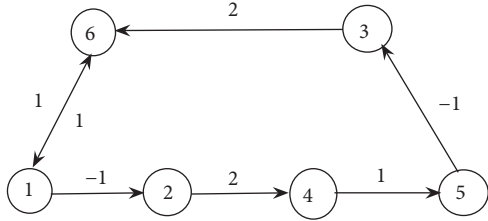
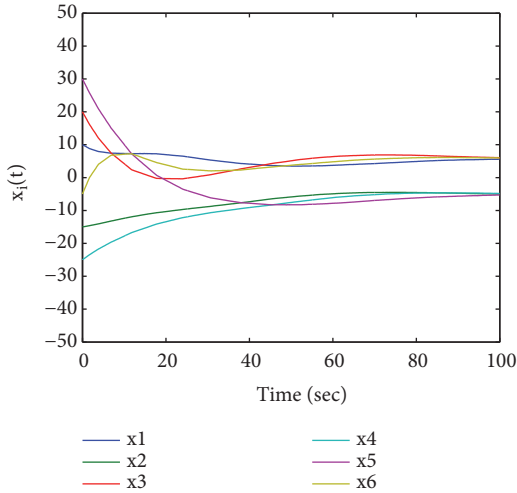
FIGURE 1: Communication graph \mathcal{G} among the 6 agents.

FIGURE 2: State trajectories of six agents.

4. Numerical Simulation

To demonstrate the developed result in the preceding, we consider an MAS of six agents, whose dynamics satisfy the system in (1). The communication graph that connects the six agents is illustrated in Figure 1. Clearly, $\mathcal{V} = \{1, \dots, 6\}$, $\mathcal{A} = (a_{ij})$, $a_{16} = a_{61} = a_{54} = 1$, $a_{21} = a_{35} = -1$, and $a_{42} = a_{63} = 2$ in $\mathcal{G} = (\mathcal{V}, \mathcal{E}, \mathcal{A})$. From Figure 1, \mathcal{G} satisfies (Q_1) and (Q_2) . Furthermore, all eigenvalues of Laplacian \mathcal{L} are $\lambda_1 = 0$, $\lambda_2 = 0.6733 + 0.9192j$, $\lambda_3 = 0.6733 - 0.9192j$, $\lambda_4 = 2.0887 + 0.7157j$, $\lambda_5 = 2.0887 - 0.7157j$, and $\lambda_6 = 3.4760$ ($j^2 = -1$). Obviously, $\min_{\lambda(\mathcal{L}) \neq 0} \{\text{Re } \lambda(\mathcal{L})\} = 0.6733$. The initial state of the MAS is given by $X(0) = (10, -15, 20, -25, 30, -5)$. Choose $b(t) = \ln(t+1)/(t+1)$. By direct calculation we know that $b(t)$ satisfies (Q_3) - (Q_4) . Assume event-triggered condition (6) is satisfied by taking $c_1 = 1.2$ and $\alpha = 0.6$. Applying protocol (2) to the system in (1), we get the six agents' state trajectories. As shown in Figure 2 one can see that the states of agents 1, 3, and 6 converge to 5 in mean square sense while the states of agents 2, 4, and 5 converge to -5 in mean square sense. Thus, mean square bipartite consensus is achieved with event-triggered protocol (2). On the other hand, from Figure 3 we know that the inputs are constants between the event triggering time interval. Moreover, from Figure 4, it can be seen that

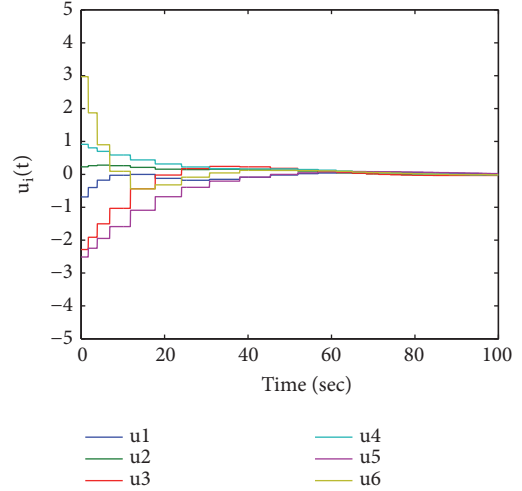


FIGURE 3: Control inputs of six agents.

the absolute value of the measurement error of each agent converges to zero. This means that the MAS does not exhibit Zeno behavior.

5. Conclusion

Mean square bipartite consensus problem of single-integrator MASs is investigated in the context of event-triggered control and measurement noise. By using time-varying gain, an event-triggered bipartite consensus protocol is proposed under measurement noise, with which the controller update frequency is reduced. With given necessary and sufficient conditions on protocol gain and communication topology, the MAS is proved to achieve event-triggered bipartite consensus. The simulation shows that the system will not show Zeno behavior.

Data Availability

The Matlab based models used to support the findings of this study are available from the corresponding author upon request.

Conflicts of Interest

The authors declare that they have no conflicts of interest.

Acknowledgments

This work was supported by the National Natural Science Foundation of China under Grants 61104136 and 61673350, Postgraduate Education Innovation Program of Shandong Province under Grant no. SDYY16088, and the Young Teacher Capability Enhancement Program for Domestic Study, Qufu Normal University.

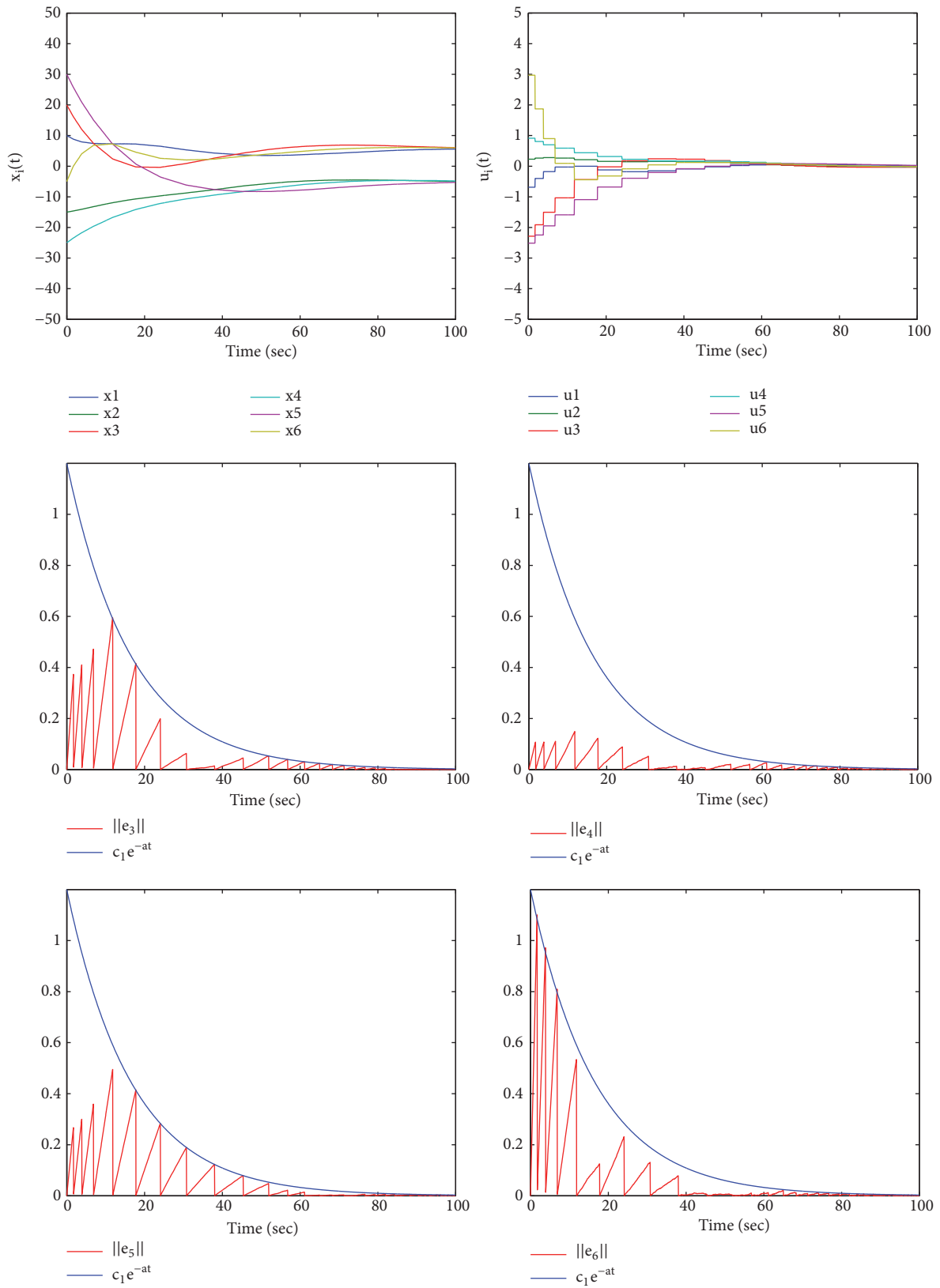


FIGURE 4: The evolution of error norm.

References

- [1] R. Olfati-Saber and R. M. Murray, "Consensus problems in networks of agents with switching topology and time-delays," *IEEE Transactions on Automatic Control*, vol. 49, no. 9, pp. 1520–1533, 2004.
- [2] W. Ren and R. W. Beard, "Consensus seeking in multiagent systems under dynamically changing interaction topologies," *IEEE Transactions on Automatic Control*, vol. 50, no. 5, pp. 655–661, 2005.
- [3] C. Q. Ma and J. F. Zhang, "Necessary and sufficient conditions for consensusability of linear multi-agent systems," *IEEE Transactions on Automatic Control*, vol. 55, no. 5, pp. 1263–1268, 2010.
- [4] K. You and L. Xie, "Network topology and communication data rate for consensusability of discrete-time multi-agent systems," *IEEE Transactions on Automatic Control*, vol. 56, no. 10, pp. 2262–2275, 2011.
- [5] C. Q. Ma, T. Li, and J. F. Zhang, "Consensus control for leader-following multi-agent systems with measurement noises," *Journal of Systems Science and Complexity*, vol. 23, no. 1, pp. 35–49, 2010.
- [6] Z. Li, Z. Duan, G. Chen, and L. Huang, "Consensus of multiagent systems and synchronization of complex networks: a unified viewpoint," *IEEE Transactions on Circuits and Systems I: Regular Papers*, vol. 57, no. 1, pp. 213–224, 2010.
- [7] C. Q. Ma and J. F. Zhang, "On formability of linear continuous multi-agent systems," *Journal of Systems Science and Complexity*, vol. 25, no. 1, pp. 13–29, 2012.
- [8] X. Dong and G. Hu, "Time-varying formation control for general linear multi-agent systems with switching directed topologies," *Automatica*, vol. 73, pp. 47–55, 2016.
- [9] C. Altafini, "Consensus problems on networks with antagonistic interactions," *IEEE Transactions on Automatic Control*, vol. 58, no. 4, pp. 935–946, 2013.
- [10] J. Hu and W. X. Zheng, "Emergent collective behaviors on cooperation networks," *Physics Letters A*, vol. 378, no. 26–27, pp. 1787–1796, 2014.
- [11] A. V. Proskurnikov, A. S. Matveev, and M. Cao, "Opinion dynamics in social networks with hostile camps: consensus vs. polarization," *Institute of Electrical and Electronics Engineers Transactions on Automatic Control*, vol. 61, no. 6, pp. 1524–1536, 2016.
- [12] D. Meng, M. Du, and Y. Jia, "Interval bipartite consensus of networked agents associated with signed digraphs," *Institute of Electrical and Electronics Engineers Transactions on Automatic Control*, vol. 61, no. 12, pp. 3755–3770, 2016.
- [13] C. Q. Ma and Z. Y. Qin, "Bipartite consensus on networks of agents with antagonistic interactions and measurement noises," *IET Control Theory & Applications*, vol. 10, no. 17, pp. 2306–2313, 2016.
- [14] J. Hu and Y. Wu, "Interventional bipartite consensus on cooperation networks with unknown dynamics," *Journal of The Franklin Institute*, vol. 354, no. 11, pp. 4438–4456, 2017.
- [15] H. Zhang and J. Chen, "Bipartite consensus of multi-agent systems over signed graphs: state feedback and output feedback control approaches," *International Journal of Robust and Nonlinear Control*, vol. 27, no. 1, pp. 3–14, 2017.
- [16] C. Q. Ma, Z. Y. Qin, and Y. B. Zhao, "Bipartite consensus of integrator multi-agent systems with measurement noise," *IET Control Theory & Applications*, vol. 11, no. 18, pp. 3313–3320, 2017.
- [17] C. Q. Ma, W. Zhao, and Y. B. Zhao, "Bipartite linear χ -consensus of double-integrator multi-agent systems with measurement noise," *Asian Journal of Control*, vol. 20, no. 1, pp. 577–584, 2018.
- [18] C. Q. Ma and L. Xie, "Necessary and sufficient conditions for leader-following bipartite consensus with measurement noise," *IEEE Transactions on Systems, Man, and Cybernetics: Systems*, pp. 1–6, 2018.
- [19] D. V. Dimarogonas, E. Frazzoli, and K. H. Johansson, "Distributed event-triggered control for multi-agent systems," *IEEE Transactions on Automatic Control*, vol. 57, no. 5, pp. 1291–1297, 2012.
- [20] G. S. Seyboth, D. V. Dimarogonas, and K. H. Johansson, "Event-based broadcasting for multi-agent average consensus," *Automatica*, vol. 49, no. 1, pp. 245–252, 2013.
- [21] B. Wang, X. Meng, and T. Chen, "Event based pulse-modulated control of linear stochastic systems," *Institute of Electrical and Electronics Engineers Transactions on Automatic Control*, vol. 59, no. 8, pp. 2144–2150, 2014.
- [22] B. Wang and M. Fu, "Comparison of periodic and event-based sampling for linear state estimation," *IFAC Proceedings Volumes*, vol. 47, no. 3, pp. 5508–5513, 2014.
- [23] S. Liu, D. E. Quevedo, and L. Xie, "Event-triggered distributed constrained consensus," *International Journal of Robust and Nonlinear Control*, vol. 27, no. 16, pp. 3043–3060, 2017.
- [24] E. Garcia, Y. Cao, and D. W. Casbeer, "Decentralised event-triggered consensus of double integrator multi-agent systems with packet losses and communication delays," *IET Control Theory & Applications*, vol. 10, no. 15, pp. 1835–1843, 2016.
- [25] D. Yang, W. Ren, X. Liu, and W. Chen, "Decentralized event-triggered consensus for linear multi-agent systems under general directed graphs," *Automatica*, vol. 69, pp. 242–249, 2016.
- [26] W. Hu and L. Liu, "Cooperative output regulation of heterogeneous linear multi-agent systems by event-triggered control," *IEEE Transactions on Cybernetics*, vol. 47, no. 1, pp. 105–116, 2017.
- [27] A. Hu, J. Cao, M. Hu, and L. Guo, "Event-triggered consensus of multi-agent systems with noises," *Journal of The Franklin Institute*, vol. 352, no. 9, pp. 3489–3503, 2015.
- [28] Y. Zhou and J. Hu, "Event-based bipartite consensus on signed networks," in *Proceedings of the 2013 IEEE 3rd Annual International Conference on Cyber Technology in Automation, Control, and Intelligent Systems (CYBER)*, pp. 326–330, China, May 2013.
- [29] J. Zeng, F. Li, J. Qin, and W. X. Zheng, "Distributed event-triggered bipartite consensus for multiple agents over signed graph topology," in *Proceedings of the 2015 34th Chinese Control Conference (CCC)*, pp. 6930–6935, Hangzhou, China, July 2015.

Research Article

PID Control for Electric Vehicles Subject to Control and Speed Signal Constraints

Amanda Danielle O. da S. Dantas ¹

André Felipe O. de A. Dantas ², João Tiago L. S. Campos ²,

Domingos L. de Almeida Neto ² and Carlos Eduardo T. Dórea ¹

¹Department of Automation and Computing, CT, Federal University of Rio Grande do Norte, 59078-970 Natal, RN, Brazil

²Master of Engineering in Oil and Gas, Potiguar University, 59054-180 Natal, Brazil

Correspondence should be addressed to André Felipe O. de A. Dantas; andre.dantas@unp.br

Received 1 June 2018; Accepted 19 July 2018; Published 1 August 2018

Academic Editor: Darong Huang

Copyright © 2018 Amanda Danielle O. da S. Dantas et al. This is an open access article distributed under the Creative Commons Attribution License, which permits unrestricted use, distribution, and reproduction in any medium, provided the original work is properly cited.

A PID control for electric vehicles subject to input armature voltage and angular velocity signal constraints is proposed. A PID controller for a vehicle DC motor with a separately excited field winding considering the field current constant was tuned using controlled invariant set and multiparametric programming concepts to consider the physical motor constraints as angular velocity and input armature voltage. Additionally, the integral of the error, derivative of the error constraints, and λ were considered in the proposed algorithm as tuning parameters to analyze the DC motor dynamic behaviors. The results showed that the proposed algorithm can be used to generate control actions taking into account the armature voltage and angular velocity limits. Also, results demonstrate that a controller subject to constraints can improve the electric vehicle DC motor dynamic; and at the same time it protects the motor from overvoltage.

1. Introduction

Some researchers state that electric vehicles can be one of the renewable solutions to energy and environmental problems caused by oil based vehicles due to the various advantages associated with the use of electric energy, such as low cost [1–5]. In this scenario, direct current (DC) motors are one of the most used actuators in the construction of electric vehicles [6]. This type of actuator has numerous advantages, such as low cost, high reliability, easy maintenance, and simple control for both speed and position variables with PID being one of the main used controllers [7, 8].

The Proportional Integral Derivative Controller (PID) has been widely used for most industrial process, due to its simplicity and effectiveness in control [9, 10]. This type of controller is commonly used in level, flow, temperature, and vehicular systems, as well as electric motors [10–12]. In addition, the design of the PID controller is considered easy

to implement, since it is only necessary to tune three parameters K_p , K_i , and K_d and tuning methods can be performed automatically [13]. Some of most used PID tuning methods in control engineering literature are Ziegler and Nichols, Cohen and Conn, Relay method, and Relatus Apparatus. These methods are effective and achieve excellent results when controlling unconstrained monovariate systems although some of these ones are also applicable for multivariate systems [9].

Despite all advantages of PID controllers, most of tuning methods do not consider the process constraints. Thus, many researches tried to consider these conditions in the control loop using antireset windup, control signal saturation, and integrator constraints. These techniques aim to limit the control action to suit the controller to constrained processes [14, 15]. However, these methods still do not take into account the constraints while tuning the controller and, therefore, such methods are not totally appropriate; i.e., they do not lead to an optimal control signal for the constrained system.

In order to solve the optimal constrained problem many controllers are being proposed. One solution consists of maintaining the system trajectory within λ -contractive controlled invariant polyhedron set defined in the state space. This set contains all states for which there is a state feedback control law that maintains the trajectory of the dynamic system within Ω [16, 17]. The state feedback control law can be calculated online, from the solution of a linear programming (LP) problem, or offline, by solving a multiparametric linear programming problem (mp-LP) [17]. This optimal solution represents an explicit PWA (PieceWise Affine) state feedback control law defined under a set of polyhedral regions in state space [14]. In a complementary way to feedback control recent research has shown that there is a state space form that allows the tuning of PID controllers using the Linear Quadratic Regulator (LQR) [13, 18], and this may allow us to combine both strategies making a new tuning method that considers constraints.

Within this context, in this paper a design of a new type of gain-scheduling PID controller to control angular velocity of electric vehicle DC motors subject to constraints in angular velocity and input voltage and PID states is proposed. To this end, the formulations in the state space of the PID controller are used, as well as the concept of controlled invariant sets together with the solution of a multiparametric programming problem [6, 9, 19, 20]. In this case, we use the same techniques applied to obtain explicit controllers (which take into account system constraints) to tune similar PID controllers (mp-PID) to constrained systems.

This work is organized as follows: At first, we will approach the concept of the λ -contractive controlled invariant set. In sequence, the problem of linear multiparametric programming will be described. After that, we will introduce how to tune PID controllers from multiparametric linear programming technique. An overview of electrical vehicle DC motors will be discussed later. Finally, a set of simulations will be carried out with the objective of proving the functionality of the proposed algorithm and the concept of mp-PID in the control of electrical vehicle DC motors, i.e., specified to work with electric cars.

2. Controlled Invariant Sets

The concept of controlled invariant sets has become important in the design of controllers for linear discrete-time systems subject to constraints since it represents a fundamental condition to maintain system stability ensuring that the constraints are not violated [21].

Consider the linear time-invariant discrete-time system described by

$$x(k+1) = Ax(k) + Bu(k), \quad (1)$$

where $k \in \mathbb{N}$ is the sample time, $x \in \mathbb{R}^n$ is the state of the system with $x \in \Omega = \{x : Gx \leq \rho\}$ (where $G \in \mathbb{R}^{g \times n}$ and $\rho \in \mathbb{R}^g$), and $u(k) \in \mathbb{R}^m$ is the control input subject to the constraints $u(k) \in \mathcal{U} = \{u : Vu \leq \varphi\}$.

A nonempty closed set $\Omega \subset \mathbb{R}^n$ is controlled invariant with respect to the system described in (1), if there exists a control signal u such that $x(k+1)$ remains inside it for

every $x(k)$ belonging to the closed set. Moreover, if a given contraction rate $0 < \lambda < 1$ is considered, a set $\Omega \subset \mathbb{R}^n$ is said to be λ -contractive controlled invariant set with respect to system (1) if there exists a control signal u such that $x(k+1)$ belongs to the set $\lambda\Omega$, for every $x(k)$ belonging to the closed set [16, 21]. In general, the set of constraints Ω defined in state space is not a controlled invariant set; i.e., there is not necessarily a control law ($u(k) \in \mathcal{U}$) which maintains the trajectory of the state vector completely contained in the set of constraints. However, it is possible to compute a controlled invariant set Ω_c , to be as large as possible, contained within the set of constraints Ω [22]. Therefore, before starting the controller synthesis process, it is necessary to define a controlled invariant set and then to compute a suitable control law that is able to restrict the state vector to a controlled invariant set $\forall x \in \Omega_c$.

By defining the maximal contractive controlled invariant set ($\Omega_c = \{G_c x \leq \rho_c\}$) [16, 22], a state feedback control law ($u(k) \in \mathcal{U}$), capable of maintaining the system dynamics (1), contained in Ω_c , can be computed online by solving the linear programming problem (LP) as described in [16] or offline from the solution of the following multiparametric programming problem (mp-LP) [23]:

$$\min_v \quad c^T v + d^T x, \quad (2)$$

$$\text{subject to: } Dv \leq W + Ex,$$

where

$$c^T = [0 \quad 1],$$

$$D = \begin{bmatrix} G_c B & -\rho_c \\ V & 0 \end{bmatrix},$$

$$v = \begin{bmatrix} u \\ \varepsilon \end{bmatrix}, \quad (3)$$

$$W = \begin{bmatrix} 0 \\ \varphi \end{bmatrix},$$

$$E = \begin{bmatrix} GA \\ 0 \end{bmatrix},$$

where $0 < \varepsilon \leq \lambda$ is the contraction rate to be minimized at each time step, $u(k)$ is the control action to be computed, and $x(k)$ is set of states contained inside Ω_c . The expression $G_c(Ax(k) + Bu(k)) \leq \varepsilon\rho$ represents a convex polyhedron in the space \mathbb{R}^{n+m} , and $\mathcal{U} = \{u : Vu \leq \varphi\}$ is a convex polytope that represents the constraints in the control variable.

In the design of controllers under constraints, the solution of the mp-LP (problem (2)) results in a PWA state feedback control law over the polyhedral regions in the space of parameters $x(k)$ as follows [24]:

- (1) The set Ω_c (controlled invariant polyhedral) is partitioned into N_q different polyhedral regions:

$$R_j = \{x \in \mathbb{R}^n \mid P_j x \leq b_j\} \quad j = 1, \dots, N_q, \quad (4)$$

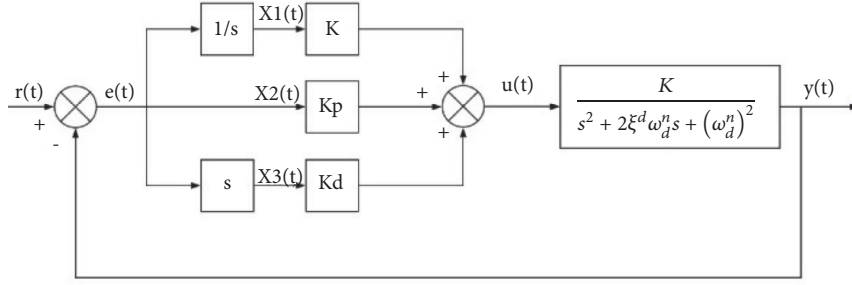


FIGURE 1: System controlled by a PID.

(2) The optimal solution $u^*(x(k)) : \Omega_c \rightarrow \mathbb{R}^m$ is a PWA function over R_j :

$$u^*(x(k)) = F^j x(k) + g^j \quad \text{for } x(k) \in R_j. \quad (5)$$

As the system is in the state space form it is possible to find the largest λ -contractive invariant set and, in sequence, the parameters of the control law are computed which maintain the dynamics of the states within the λ -contractive invariant set. In order to associate with the PID controller, we will call this “the tuning step”, because we find the controller’s parameters that guarantee positive invariance and λ -contractivity. That is, by using this process we will be able to find a PID control law, PWA, that allows the controller to synthesize control actions capable of controlling the process under constraints.

2.1. Tuning of Gain-Scheduling PID Control Design (mp-PID). Based on formulation that allows the reorganization of a second-order systems in state space form, described in [20], whose states are the tracking error, integral of the error, and derivative of the error, we propose the tuning of a type of gain-scheduling PID controller by using the PWA state feedback control law computed by multiparametric linear programming, described in (2).

2.1.1. PID Controllers. Consider now the system presented in (1) is described by

$$\frac{Y(s)}{U(s)} = \frac{K}{s^2 + 2\xi^{ol} \omega_n^{ol} s + (\omega_n^{ol})^2}. \quad (6)$$

Because the external setpoint does not affect the controller design, we assume $r(t) = 0$ for the system of Figure 1 [20].

The relation $y(t) = -e(t)$ is valid for the standard regulation problem. Thus, it is possible to place the system in function of the error and control signal, as presented in [20]

$$\left[s^2 + 2\xi^{ol} \omega_n^{ol} s + (\omega_n^{ol})^2 \right] E(s) = -KU(s), \quad (7)$$

$$\Rightarrow \ddot{e} + 2\xi^{ol} \omega_n^{ol} \dot{e} + (\omega_n^{ol})^2 e = -Ku. \quad (8)$$

Use the following definitions:

$$\begin{aligned} x_1 &= \int_0^t e(t) dt, \\ x_2 &= e(t), \\ x_3 &= \frac{de(t)}{dt}. \end{aligned} \quad (9)$$

Equation (8) can be rewritten as

$$\ddot{x}_3 + 2\xi^{ol} \omega_n^{ol} \dot{x}_3 + (\omega_n^{ol})^2 x_2 = -Ku. \quad (10)$$

Considering the state space, the formulation becomes [20]

$$\begin{bmatrix} \dot{x}_1 \\ \dot{x}_2 \\ \dot{x}_3 \end{bmatrix} = \begin{bmatrix} 0 & 1 & 0 \\ 0 & 0 & 1 \\ 0 & -(\omega_n^{ol})^2 & -2\xi^{ol} \omega_n^{ol} \end{bmatrix} \begin{bmatrix} x_1 \\ x_2 \\ x_3 \end{bmatrix} + \begin{bmatrix} 0 \\ 0 \\ -K \end{bmatrix} u. \quad (11)$$

In this case, we assume the reference signal equal to zero and because the system is regulatory it is organized in a way that the states tend to zero and tend to eliminate the disturbance. When applied in electrical vehicle motor control, we intend to make changes in the reference, so some considerations must be realized:

- (i) The external reference does not affect the controller design.
- (ii) It is possible to work step-type references in two ways, by using model illustrated in Figure 1 or by forcing changes in the operational point, so the new system’s reference is forced to be at the origin likewise linearizing a nonlinear system in the operational point.

Concerning the direct change of reference, it is possible to verify that as the system is stable in closed loop, it tends to converge to the reference. However, in this case, only the error and derivative of the error states will converge to zero and the integral of the error will become a value that maintains the necessary control action to force the output to zero, in the same way conventional PID does.

The second way to control the system is using the linearization idea and it can be observed in Figure 2.

- 1: Convert the continuous system into a state space system, where the states are the errors and the input is the control action, according to equation (11);
- 2: Compute the maximal λ -contractive controlled invariant set contained in the set of constraints, which must be reexplained in terms of the new state representation;
- 3: Solve the mp-LP problem described in equation (2);
- 4: Compute the integral of error, error, and derivative of error;
- 5: Identify which polyhedral region the computed state $x(k)$ belongs to.
- 6: Use the affine control law to control the system with $F^j = [K_i \ K_p \ K_d]^T$ and g^j being the mp-PID parameters, corresponding to the j -th polyhedral region;
- 7: If the control routine is not interrupted, return to step 4.

ALGORITHM 1

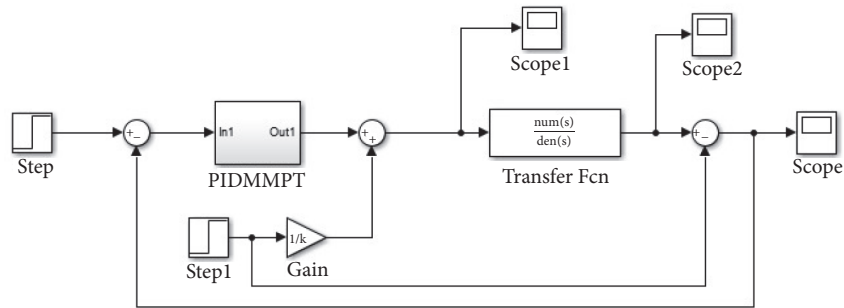


FIGURE 2: System controlled by a PID.

Figure 2 considers the reference equal to zero (step) and, to make changes in reference, we are changing the operational point using step 1. The concept is very simple; by changing the reference (step 1) in this system, the operational point will change. Thus, the zero will be shifted; i.e., the entered reference will be recognized as an instantaneous error disturbance on the system's states. The system was designed to force the error, integral of the error, and the derivative of the error to the origin, so the system will work to stabilize states in this "new zero", which is the operational point. In this way, the system's output will be forced toward the reference using the same considerations as depicted in Figure 2. In this scheme when there is a reference change the invariant set moves along with it; i.e., if the error limit is equal to 1, for example, and the reference is 5, the output will be limited between the values 6 and 4. However, if the reference is changed to 4, the output will be limited to the interval between 3 and 5. This is particularly useful when it is desirable to constrain the error around a variable reference. However, it is needed to be careful not to vary the reference above the limits of the invariant set and not to exceed the physical limitations of the system. When the operator wants to limit the output between 4 and 6 and use the operating points 4 and 5, because of this, the constraints on the magnitude of the error would be within ± 1 in the first example and in the second one between 2 and 0 ($error = -y$). This means that, for these examples, it would be necessary to modify the system's constraints by making a set of constraints for each operational point.

Given the main considerations about the state space system, it is necessary to tune and use the controller. In this case the concept of invariant sets will be used to find an optimum tuning for a PWA PID control law, which we call mp-PID. Thus, the λ -contractive controlled invariant set is computed by using the algorithms proposed by [22]; then, mp-LP problem (2) is solved to compute the parameters F^j and g^j of the affine law $u(x) = F^j x + g^j$, where F_i multiplies the state $X = [x_1 \ x_2 \ x_3]$ corresponding to integral of the error, the error, and the derivative of the error. This means that the parameters of the proposed PID controller are defined by $F^j = [K_i \ K_p \ K_d]^T$ plus affine term g^j which is associated with a polyhedral region R_j , forming a gain-scheduling PID control (mp-PID). Such approach can be obtained from the implementation of Algorithm 1.

As described in Algorithm 1, the proposed PID control design is performed from a sequence of steps, where at first the system must be rearranged in state space form, so that the input is the control action and the states are the integral of the error, error, and derivative of the error, according to (11). Then, the new system is discretized with the desired sampling period and, then given the new state space extended system, the maximal λ -contractive controlled invariant set is computed as well as the multiparametric linear programming problem (mp-LP) (2). The solution of the mp-LP problem represents a PWA control law over polyhedral regions R_j associated with a PID controller. At the end of these steps, the control law is inserted into the control loop, where the error tends to zero and the constraints are not violated as long as the

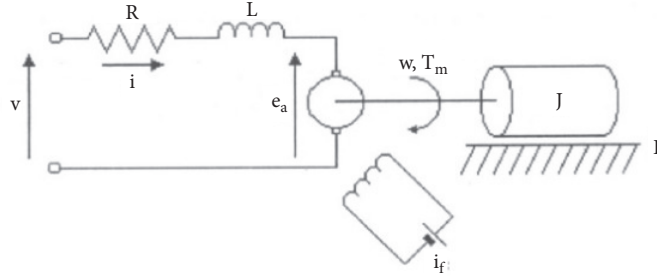


FIGURE 3: DC motor with separated winding field with constant current ($i_f(t)$) [25].

initial state is inside the λ -contractive controlled invariant set.

3. DC Motors Overview

After the definition of the PID tuning method the application must be studied in order to have mp_PID applied to it, so in this section we present an overview of electric vehicle DC motors.

Recently, electric vehicles are gaining popularity among the population resulting in more demand for these types of car. Electric vehicles are efficient and need less maintenance than fuel-based cars and they do not pollute the environment [15]. However, the electric car depends heavily on battery systems that are finite and have fewer storage capabilities. Therefore, strategies to reduce and use more efficiently the energy stored in the batteries are needed.

The consuming of the electric vehicles depends heavily on the used motor type and adopted control strategy. Actually, DC motors and induction motors are being proposed to be used in the electric vehicle industry, with DC motor type being a good candidate to be used in electric vehicle applications [26, 27]. DC motors are efficient, presenting high reliability and easy maintenance. They are easy to control resulting in smooth acceleration and efficient battery usage [7, 8]. Although brushed DC motor suffers from the brush maintenance, the aforementioned advantages turn the DC motor to be applicable for use in electric cars.

DC motors have the advantage of being easy to control resulting in several control techniques for velocity control using PID type control. Techniques using metaheuristic PID [28, 29], multivariate PID [30], genetic algorithm method with PID [12], and Adaptive PID Dynamic, Fuzzy, and Neurofuzzy Controller [19] were proposed to control DC motors.

DC motors have different configurations as compound, shunt, series, permanent magnetic DC and separated field winding where each of them has advantages and disadvantages. DC motors in series configuration are the type of motors that can be used in electric cars due to their instantaneous torque and smooth acceleration. However, these types of motors need a minimal load not to be damaged, which is a condition that occurs in electric car applications. One way to limit the damage in the DC motor series control is

to limit the maximum velocity in the adopted control strategy [31]. DC motors with separated field are the most versatile because they allow controlling torque and velocity separately using the armature current and field current separately with more options for control applications. In this paper, DC motor with separated field was chosen to test the control algorithm because it allows more restrictions options to be tested by the proposed control algorithm.

In sequence, we present the DC motor modelling with excited separately field and afterwards we present the numerical examples controlling the motor and testing the performance of the tuned controllers.

A DC motor controlled by current armature with independent field is depicted in Figure 3.

The torque induced (T_m) in the motor is given by

$$T_m(t) = J \frac{dw(t)}{dt} + Bw(t), \quad (12)$$

$$T_m(t) = K_a i(t), \quad (13)$$

where $i(t)$ is the armature current, J is the inertia moment, w is the angular velocity, B is the friction coefficient, and K_a is the torque constant.

The armature induced voltage ($e_a(t)$) with constant field current (i_f) is given by

$$e_a(t) = K_b w(t), \quad (14)$$

where K_b is the velocity constant.

As the DC motor has separated field, the voltage applied ($v(t)$) in the armature windings is given by

$$v(t) = L \frac{di(t)}{dt} + Ri(t) + e_a(t), \quad (15)$$

where L is the armature inductance, and R is the armature resistance.

The following second-order transfer function resulted:

$$\frac{W(s)}{V(s)} = \frac{K_a}{(Js + B)(Ls + R) + K_a K_b}. \quad (16)$$

4. Numerical Examples

- (i) The parameters of a motor suitable for use in electric cars are determined.

TABLE 1: Motor parameters.

V_n	48 V
R	0.1 Ω
L	0.005 H
K_b	0.004 V.s/rad
K_a	0.0036 N.m/A
J	0.1 N.m ²
B	0.05 N.m.s/rad

- (ii) The mp_PID controllers are tuned.
- (iii) The proposed tuning algorithm is performed using different parameters and, then, the results are compared.
- (iv) The influence of each parameter on the final process performance is analyzed.

4.1. DC Motor Parameters. At first, in order to control an electric vehicle DC motor we specify its parameters (the motor) in such a way that it is able to move the vehicle. The voltage armature, resistance and inductance armatures, moment of inertia, velocity constant, torque constant, and friction coefficient motor parameters presented in Table 1 were used to test the proposed control algorithm performance.

Replacing the motor parameters in (17),

$$\frac{W(s)}{V(s)} = \frac{0.0036}{(s + 0.05)(0.005s + 0.1) + 1.44e^{-5}}, \quad (17)$$

then, the simplified transfer function of the used motor becomes

$$G(s) = \frac{7.2}{s^2 + 20.5s + 10.03}. \quad (18)$$

In the model of (18) the output is the angular velocity (*rad/s*) in the range of $\pm 34.56 \text{ rad/s}$ and the input is the voltage that will vary in the range of $\pm 48 \text{ V}$. Note that as this type of motor allows two-direction movement, we will have both positive and negative voltages and positive and negative speeds considered in the controller constraints.

4.2. Tuning of the Controllers mp_PID. This section presents the general tuning process of the mp_PID controllers. Some important aspects to emphasize are described as follows:

- (i) The output constraints can be transformed into constraints on the error, especially when assuming the operating point at zero. The output constraints for the electric vehicle DC motor case will be the maximum speed allowed at a voltage of 48V.
- (ii) The control signal constraints must be limited to $\pm 48 \text{ V}$, since we need to limit motor damage from overcurrent as the armature current is directly dependent on the applied load and armature voltage, so the algorithm is able to optimize the system within this set of constraints, unlike other techniques which only

insert constraint on control action without taking in account the constraints at tuning phase resulting in lower dynamic performance of the vehicle DC motor.

- (iii) The integral and derivative of the error values will be appropriately chosen; i.e., they will be used as a tuning parameter and the influence of these constraints will be evaluated in order to emphasize how the final performance of the system is changed, in aspects such as overshooting and stabilization time.
- (iv) The main tuning parameter of the mp_PID controller is the value of λ . It is related to the contractivity and will also be an observed parameter.
- (v) In a specific case we observe the difference between varying the operating point and varying the reference.

4.3. Set of Tests. Based on these considerations, tests are performed varying the constraints on the integral of the error, derivative of the error, and the λ parameter. After that, a comparison between changing the reference and changing the operating point will be made.

4.3.1. Test 1: Integral of the Error Constraints Change Effect. In this first test the objective is to observe the influence, in system's performance, of integral of the error constraints change. Despite the direct relationship between error and the output of the motor (angular velocity), the integral of the error is an internal state of the system in state space and influences the motor dynamic performance but not necessarily forces physically the system outside its limits. Therefore, by hypothesis we assume that we can freely modify these parameters. In this way, the test conditions presented in Table 2 were chosen. In these test conditions, the integral of the error limits was varied and the derivative of the error limits and λ were maintained constant.

The system's outputs and the control actions for test condition 1 are depicted in Figures 5 and 6. Also, Figure 4 presents the polyhedron formed by the first test case (test 1).

As seen, Figure 4 presents the polyhedron formed by the first test case (test 1), where the default value is 34.56 so $MaxIe = 1$ means 1 times 34.56 and $MaxDe = 5$ means 5 times 34.56 and this concept is applicable to all the others figures. Because this polyhedron changes its shape for each test in all tests we present only the quantity of sets generated within the invariant set that in this case are 10, 8, and 10. The number of regions within the invariant set reveals the computational cost difference (in Algorithm 1 we need to search the region to find which PID controller parameters will be used to compute the control signal). In this case, as observed, the quantity is very similar; for a reference, there may be cases in which the amount of computed regions may be greater than 400, which in this case points out that the control signal computation will be inexpensive.

Figure 5 shows the output, i.e., the angular velocity in the 3 performed tests. We observe that, with lower constraint values in the integral of the error signal, the system tends to converge faster; on the other hand, with more relaxed restriction in the integral of the error signal, the system tends to stabilize slower. Another important factor to be analyzed is

TABLE 2: Table with the 3 tests, varying integral of error.

Simulations	λ	Integral of the Error Limits	Derivative of the Error Limits
1	0.999	± 34.56	± 172.80
2	0.999	± 172.80	± 172.80
3	0.999	± 1728	± 172.80

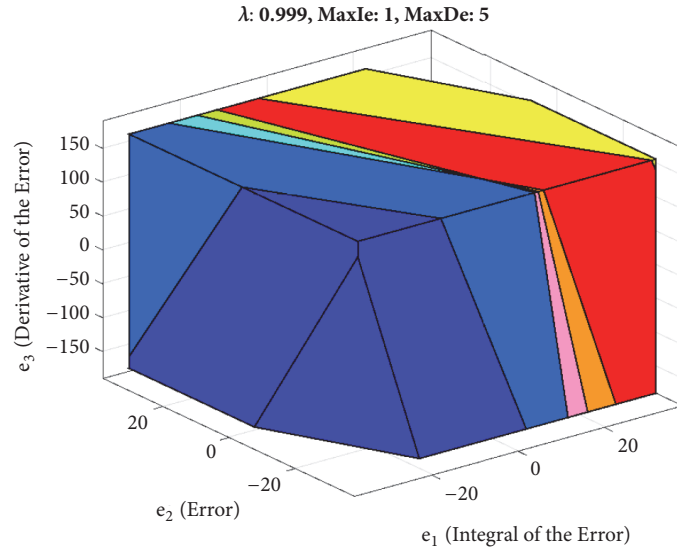
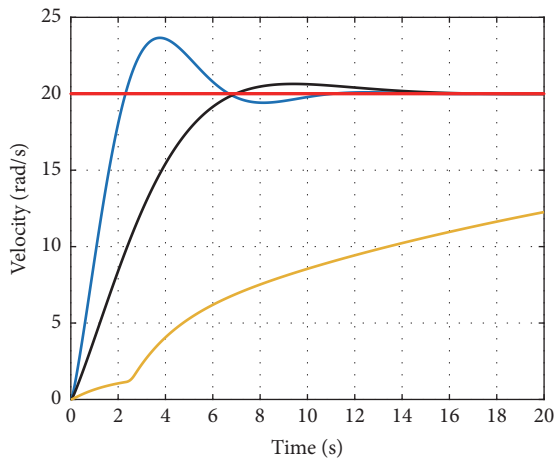
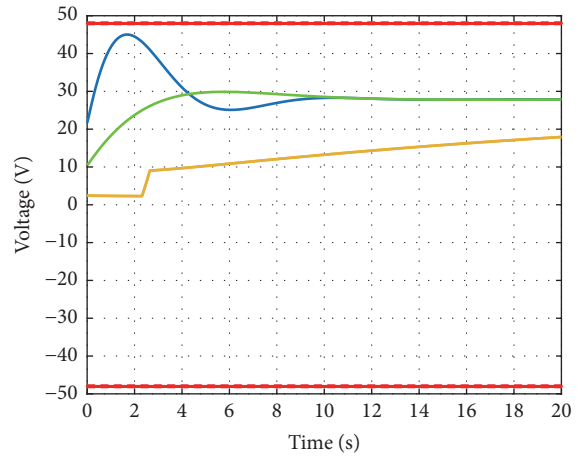


FIGURE 4: Polyhedron test 1 for test condition 1.



— $\lambda: 0.999, \text{MaxIe}: 1, \text{MaxDe}: 5$
 — $\lambda: 0.999, \text{MaxIe}: 5, \text{MaxDe}: 5$
 — $\lambda: 0.999, \text{MaxIe}: 50, \text{MaxDe}: 5$

FIGURE 5: System's outputs for test condition 1.



— $\lambda: 0.999, \text{MaxIe}: 1, \text{MaxDe}: 5$
 — $\lambda: 0.999, \text{MaxIe}: 5, \text{MaxDe}: 5$
 — $\lambda: 0.999, \text{MaxIe}: 50, \text{MaxDe}: 5$

FIGURE 6: Control actions for test condition 1.

that the lower the restriction value in the integral of the error is, the greater the overshooting system tends to present.

Figure 6 corresponds to the behavior of the control signal. Here, the similarity in behavior with respect to the output signal is evident; i.e., the smaller the restriction value in the integral of the error is, the closer to the limits the signal will be, which in this case is ± 48 .

4.3.2. *Test 2: Derivative of the Error Constraints Parameters Change Effect.* Similarly to the first test, in this second test our objective is to observe the influence in the performance of the system, when the derivative of the error constraints is changed. This also happened to the integral of the error constraint, the derivative of the error is an internal state of the system in state space and influences the performance but not

TABLE 3: Table with the 3 tests, varying derivative of error.

Simulations	λ	Integral of the Error Limits	Derivative of the Error Limits
1	0.999	± 172.80	± 17.28
2	0.999	± 172.80	± 172.80
3	0.999	± 172.80	± 1728.0

TABLE 4: Table with the 3 tests, varying λ .

Simulations	λ	Integral of Error Limits	Derivative of Error Limits
1	0.99	± 172.80	± 172.80
2	0.90	± 172.80	± 172.80
3	0.60	± 172.80	± 172.80

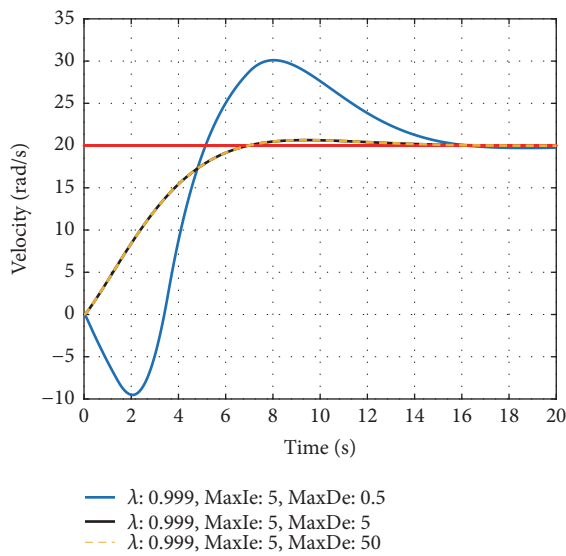


FIGURE 7: System's outputs for test condition 2.

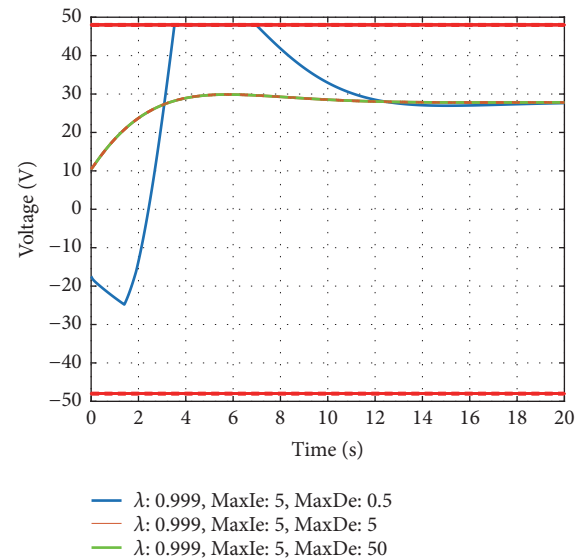


FIGURE 8: Control actions for test condition 2.

necessarily physically forces the system outside its limits (we are not considering variation effects in this case, although in some cases they are included in problems with restrictions). Therefore, by hypothesis we assume that we can freely modify these parameters. In this way, the test conditions presented in Table 3 were chosen. In these test conditions, the derivative of the error limits was varied and the integral of the error limits and λ were maintained constant.

The system's outputs and the control signals for test condition 2 are depicted in Figures 7 and 8.

Figure 5 shows the output, i.e., the angular velocity in the 3 performed tests. We observe that as the derivative of the error limits increases the system begins to present nonminimum phase and it is more difficult to stabilize it in smaller times; this means that in the case in which the limits are relaxed the integral of the error values can be larger and consequently the system tends to have a better transient.

In these tests the quantity of sets generated within the controlled invariant set is 8, 8, and 12. Similarly to the previous test we emphasize that it will be very inexpensive to compute the control action.

The figure of this second test (Figure 6) corresponds to the behavior of the control signal. Here, the similarity in behavior with respect to the output action is evident; i.e., the smaller the constraint value in the derivative of the error is, the closer the control signal will be to its limit. A second important factor to be highlighted here is that in the case where the system tends to exceed the control action it is evident that there is a saturation and because the controller was obtained from a constrained optimization problem its performance will be optimal.

4.3.3. Test 3: Effect of Changing λ . Unlike the first 2 tests, this one will not present the effect in constraints, but in the tuning parameter (λ) of the optimization problem. What should be highlighted here is that this parameter is associated with the contraction rate, which makes the invariant set smaller at each iteration and it is related to the system's convergence speed. In this way, the test conditions presented in Table 4 were chosen. In these test conditions, λ was varied and the integral and derivative of the error limits were maintained constant.

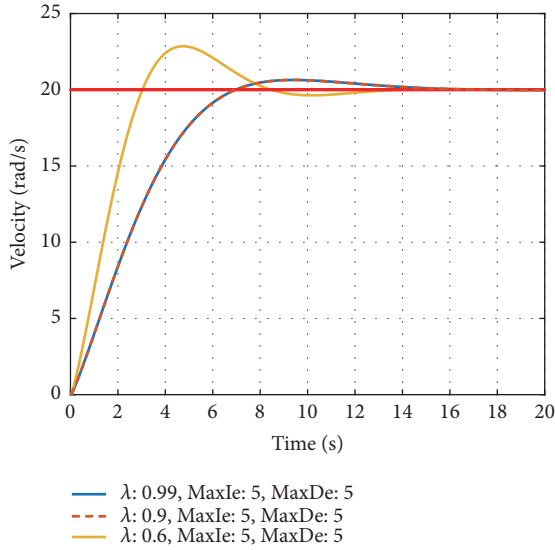


FIGURE 9: System's output for test condition 3.

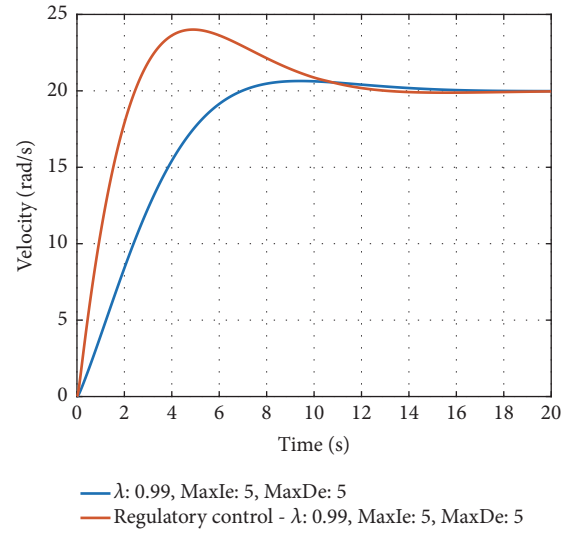


FIGURE 11: System's output.

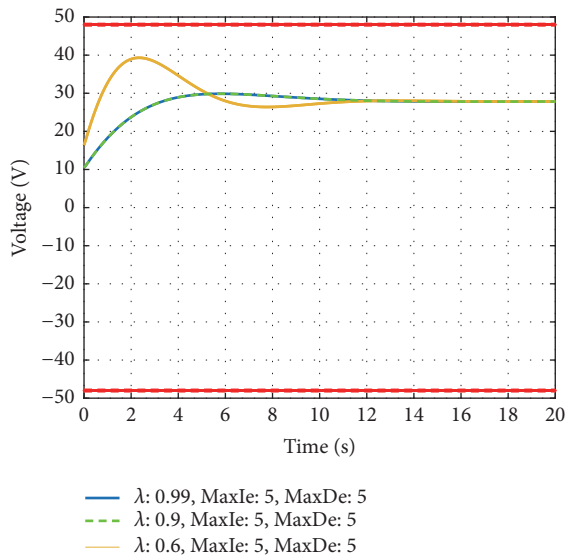


FIGURE 10: Control actions for test condition 3.

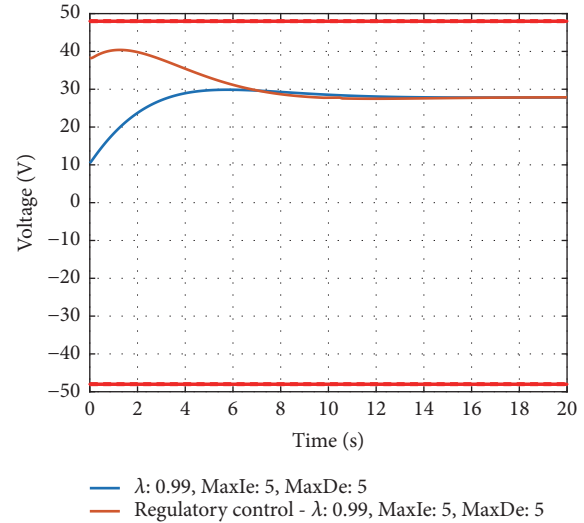


FIGURE 12: Control action.

The system's outputs and the control actions for the test condition 3 are depicted in Figures 9 and 10.

This third test resulted as the quantities of sets within the invariant sets 8, 14, and 12. Also, Figure 9 shows the output, i.e., the angular velocity in the 3 performed tests. We observe that the lower the λ value is the more aggressive the system's behavior is, forcing the stabilization to happen before, but reflecting in greater overshooting. This also means that by increasing the value of this parameter we have less aggressive systems, but with slower responses.

The last figure of this third test (Figure 10) corresponds to the behavior of the control signal. Here, the similarity to the output signal is evident; i.e., the smaller the value of λ is the closer to its limits it is.

4.3.4. *Test 4: Reference Changes versus Setpoint Changes.* The first three tests aimed to show the results related to the controllers tuning when the systems are subject to reference variations (step). This means that the controlled invariant set remained unchanged as well as the operating point of the system. In this fourth test, the objective is to present the changes related to the operating point. Note that there is a possibility of differences in behaviors, because although it has the same amount of variation, this test directly affects the activated regions in the control process, which consequently changes the response of the system. Thus, the test condition is to change the setpoint by 20 units and compare it with the changed operating point (setpoint 1) by 20.

The system's outputs and the control actions for the test condition 4 are depicted in Figures 11 and 12.

Figure 11 shows the output, i.e., the angular velocity in the 3 performed tests. We observe that the system's response,

which had its setpoint changed, was less aggressive (observing the overshooting). Despite the presented output, it is not enough to emphasize that in any and every change of operating point the response will behave accordingly, since this difference is related to the fact that different regions of the invariant set are activated in both cases. Another important fact to note is that, depending on the stabilization criteria, we observe the operating point change case stabilizing before the response to the setpoint change case; this is mainly due to a faster reaction of this response.

Figure 12 of the fourth test corresponds to the behavior of the control signal. Here, the similarity in behavior with respect to the output signal is evident. We observe that the initial value of control action in operating point change case is greater than that of the reference change case; this impacts on the initial response and the possibility of faster stabilization. Note that additionally to the performed tests other possibilities were investigated, i.e., the change of the objective function to minimize the integral of the error and the derivative of the error (as alternatives to changing constraints). However, the results were not satisfactory, impacting directly on the size of the set of constraints and affecting the performance of the process.

5. Conclusion

This paper presented a PID controller for electric vehicle DC motors based on proving the functionality of the proposed algorithm from a set of simulations. The algorithm proved that it is possible to generate control actions that consider the 48V limits of the motor, as well as forcing the output speed of the motors to be limited to their specified values. In addition, it was verified that the integral and derivative of the error constraints make tuning parameters “constrain” the performance of the process output. In other words, we found a direct relationship between error constraints and the DC motor dynamics. Another important point to note is that changes in λ also interfere with system’s performance and the output behavior also depends on how the error is changed. In this second case, we verify the behavior of the system to reference and setpoint variations.

In conclusion, control of electric vehicle DC motors under constraints and tuning controllers adjusting the behavior of the system’s output is possible by using the proposed algorithm. In this sense, important improvements can be proposed. The first one would be to use a methodology to automatically tune parameters, since there are no tuning rules for these constraints (in the integral of the error and in the derivative of the error). A second improvement would be to extend the tests by verifying that the behavior presented to the DC motors, i.e., verified, can be extended to other processes.

6. Future Works

Although DC motor with excited separately field can be used in an electric vehicle, new types of motors as permanent magnet synchronous motor (PMSM) are being used recently [11, 32, 33]. The usage of the proposed algorithm in this type of motors will be investigated.

Data Availability

The [algorithms] data used to support the findings of this study have not been made available because scientific research is still being carried out using the presented algorithms.

Conflicts of Interest

The authors declare that they have no conflicts of interest.

Acknowledgments

The authors would like to mention the institutions that contributed to the development of this project: UFRN (Federal University of Rio Grande do Norte), DCA (Department of Computation and Automation), CNPQ (National Council for Scientific and Technological Development), UnP (Potiguar University), and LAUT (Laboratory of Automation in Petroleum).

References

- [1] S. Chu and A. Majumdar, “Opportunities and challenges for a sustainable energy future,” *Nature*, vol. 488, no. 7411, pp. 294–303, 2012.
- [2] X. Zhu, H. Zhang, D. Cao, and Z. Fang, “Robust control of integrated motor-transmission powertrain system over controller area network for automotive applications,” *Mechanical Systems and Signal Processing*, vol. 58, pp. 15–28, 2014.
- [3] Z. Shuai, H. Zhang, J. Wang, J. Li, and M. Ouyang, “Combined AFS and DYC control of four-wheel-independent-drive electric vehicles over CAN Network with time-varying delays,” *IEEE Transactions on Vehicular Technology*, vol. 63, no. 2, pp. 591–602, 2014.
- [4] X. Wang, W. Kong, D. Zhang, and L. Shen, “Active disturbance rejection controller for small fixed-wing UAVs with model uncertainty,” in *Proceedings of the 2015 IEEE International Conference on Information and Automation, ICIA 2015 - In conjunction with 2015 IEEE International Conference on Automation and Logistics*, pp. 2299–2304, China, August 2015.
- [5] Y. Luo, T. Chen, and K. Li, “Multi-objective decoupling algorithm for active distance control of intelligent hybrid electric vehicle,” *Mechanical Systems and Signal Processing*, vol. 64–65, pp. 29–45, 2015.
- [6] Z. Has, A. H. Muslim, and N. A. Mardiyah, “Adaptive-fuzzy-PID controller based disturbance observer for DC motor speed control,” in *Proceedings of the 2017 4th International Conference on Electrical Engineering, Computer Science and Informatics (EECSI)*, pp. 1–6, Yogyakarta, September 2017.
- [7] N. Matsui, “Sensorless PM brushless DC motor drives,” *IEEE Transactions on Industrial Electronics*, vol. 43, no. 2, pp. 300–308, 1996.
- [8] J. S. Ko, J. H. Lee, S. K. Chung, and M. J. Youn, “A robust digital position control of brushless DC motor with dead beat load torque observer,” *IEEE Transactions on Industrial Electronics*, vol. 40, no. 5, pp. 512–520, 1993.
- [9] H. Jeongheon and R. Skelton, “An LMI optimization approach for structured linear controllers,” in *Proceedings of the 42nd IEEE International Conference on Decision and Control*, pp. 5143–5148, Maui, HI, USA, 2003.

- [10] A. Kalangadan, N. Priya, and T. K. S. Kumar, "PI, PID controller design for interval systems using frequency response model matching technique," in *Proceedings of the International Conference on Control, Communication and Computing India, ICCCI 2015*, pp. 119–124, India, November 2015.
- [11] S. Hu, Z. Liang, W. Zhang, and X. He, "Research on the integration of hybrid energy storage system and dual three-phase PMSM Drive in EV," *IEEE Transactions on Industrial Electronics*, vol. 65, no. 8, pp. 6602–6611, 2018.
- [12] M. Jaiswal, M. Phadnis, and H. O. D. Ex, "Speed control of DC motor using genetic algorithm based PID controller," *International Journal of Advanced Research in Computer Science and Software Engineering*, vol. 3, no. 7, pp. 2277–128, 2013.
- [13] E. Vinodh Kumar and J. Jerome, "LQR based optimal tuning of PID controller for trajectory tracking of magnetic levitation system," in *Proceedings of the 2013 International Conference on Design and Manufacturing, IConDM 2013*, pp. 254–264, India, July 2013.
- [14] M. Kvasnica, P. Grieder, M. Baotić, and M. Morari, "Multi-parametric toolbox (MPT)," *Lecture Notes in Computer Science (including subseries Lecture Notes in Artificial Intelligence and Lecture Notes in Bioinformatics): Preface*, vol. 2993, pp. 448–462, 2004.
- [15] S.-M. Lu, "A review of high-efficiency motors: specification, policy, and technology," *Renewable & Sustainable Energy Reviews*, vol. 59, pp. 1–12, 2016.
- [16] F. Blanchini, "Ultimate boundedness control for uncertain discrete-time systems via set-induced Lyapunov functions," *Institute of Electrical and Electronics Engineers Transactions on Automatic Control*, vol. 39, no. 2, pp. 428–433, 1994.
- [17] A. D. O. d. S. Dantas, C. E. T. Dorea, and A. F. O. d. A. Dantas, "Projeto de controladores para sistemas lineares sujeitos a restrições utilizando análise de agrupamento de dados," *Simpósio Brasileiro de Automação Inteligente - SBAI*, 2015.
- [18] S. Das, I. Pan, K. Halder, S. Das, and A. Gupta, "LQR based improved discrete PID controller design via optimum selection of weighting matrices using fractional order integral performance index," *Applied Mathematical Modelling: Simulation and Computation for Engineering and Environmental Systems*, vol. 37, no. 6, pp. 4253–4268, 2013.
- [19] A. K. Hassan, M. S. Saraya, M. S. Elksasy, and F. F. Areed, "Brushless DC motor speed control using PID controller, fuzzy controller, and neuro fuzzy controller," *International Journal of Computer Applications*, vol. 180, no. 30, pp. 47–52, 2018.
- [20] J.-B. He, Q.-G. Wang, and T.-H. Lee, "PI/PID controller tuning via LQR approach," *Chemical Engineering Science*, vol. 55, no. 13, pp. 2429–2439, 2000.
- [21] F. Blanchini and S. Miani, *Set-theoretic methods in control, Systems & Control: Foundations & Applications*, Birkhauser Boston, Inc., Boston, MA, USA, 2008.
- [22] C. E. Dórea and J. C. Hennet, "(a, b)-invariant polyhedral sets of linear discrete-time systems," *Journal of Optimization Theory and Applications*, vol. 35, pp. 521–542, 1999.
- [23] G. P. Weinkeller, J. L. Salles, and T. F. B. Filho, "Controle preditivo via programação multiparamétrica aplicado no modelo cinemático de uma cadeira de rodas robótica," in *Proceedings of the DINCON 2013—Conferência Brasileira de Dinâmica, Controle e Aplicações*, 2008.
- [24] A. Bemporad, F. Borrelli, and M. Morari, "Model predictive control based on linear programming—the explicit solution," *IEEE Transactions on Automatic Control*, vol. 47, no. 12, pp. 1974–1985, 2002.
- [25] A. A. R. Coelho and L. S. Coelho, "Identificação de sistemas dinâmicos lineares," *Didáctica (Editora da UFSC)*, 2004.
- [26] S. Lixin, "Electric vehicle development: the past, present & future," in *Proceedings of the 2009 3rd International Conference on Power Electronics Systems and Applications, PESA 2009*, China, May 2009.
- [27] C. Chan, "The past, present and future of electric vehicle development," in *Proceedings of the IEEE 1999 International Conference on Power Electronics and Drive Systems. PEDS'99 (Cat. No.99TH8475)*, pp. 11–13 vol.1, Hong Kong, July 1999.
- [28] D. Puangdownreong, "Optimal PID controller design for DC motor speed control system with tracking and regulating constrained optimization via cuckoo search," *Journal of Electrical Engineering & Technology*, vol. 13, no. 1, pp. 460–467, 2018.
- [29] P. Payakkawan, K. Klomkarn, and P. Sooraksa, "Dual-line PID controller based on PSO for speed control of DC motors," in *Proceedings of the 2009 9th International Symposium on Communications and Information Technology, ISCIT 2009*, pp. 134–139, Republic of Korea, September 2009.
- [30] B. Gasbaoui and A. Nasri, "A novel multi-drive electric vehicle system control based on multi-input multi-output PID controller," *Serbian Journal of Electrical Engineering*, vol. 9, no. 2, pp. 279–291, 2012.
- [31] Z. Bitar, S. Al Jabi, and I. Khamis, "Modeling and simulation of series DC motors in electric car," in *Proceedings of the International Conference on Technologies and Materials for Renewable Energy, Environment and Sustainability, TMREES 2014 - EUMISD*, pp. 460–470, Lebanon, April 2014.
- [32] R. Xiao, Z. Wang, H. Zhang, J. Shen, and Z. Chen, "A Novel Adaptive Control of PMSM for Electric Vehicle," in *Proceedings of the 2017 IEEE Vehicle Power and Propulsion Conference (VPPC)*, pp. 1–8, Belfort, France, December 2017.
- [33] C. Shi, Y. Tang, and A. Khaligh, "A three-phase integrated onboard charger for plug-in electric vehicles," *IEEE Transactions on Power Electronics*, vol. 33, no. 6, pp. 4716–4725, 2018.

Research Article

An Electrical Insulator Defects Detection Method Combined Human Receptive Field Model

Li Guo , Yu Liao , Hongying Yao, Jinhao Chen, and Manran Wang

Hubei University for Nationalities, Hubei, Enshi 445000, China

Correspondence should be addressed to Yu Liao; 23262837@qq.com

Received 29 March 2018; Accepted 4 June 2018; Published 3 July 2018

Academic Editor: Darong Huang

Copyright © 2018 Li Guo et al. This is an open access article distributed under the Creative Commons Attribution License, which permits unrestricted use, distribution, and reproduction in any medium, provided the original work is properly cited.

Nondestructive inspection of electrical insulators subjected to the high electrical stress and environmental damage is fundamental for reliable operation of a transmission lines. The breakage and defect of the insulator have great influence on the safe of transmission lines, and insulator defect detection with difference types is a complex work. This paper proposed an insulator defect detection method inspired by human receptive field model, which meets the requirements for detecting defect insulator in a simple background. In this method, the defect detection combined human receptive field model of human visual system is constructed and applied on the different insulators, so as to achieve accurate detection of the insulator defected parts. Experimental results show that the method can accurately and robustly detect the defect (such as cracks and damage) of electrical insulator in case of noise affect.

1. Introduction

High-voltage transmission lines and transmission towers in China are usually in a harsh environment where their components are often eroded by rain or damaged by unpredictable foreign objects. When an electrical insulator is in operation at the high-voltage transmission line systems, those devices are subjected to a strong electrical stress and also damaged by the severely environmental conditions [1]. It is well known that the presence of voids and inclusions are introduced in the manufacturing process, or generation and propagation of defects, such as holes and cracks inside and outside of the electrical insulators, when those devices are in operation under high-voltage stress, a partial discharge begins as localized dielectric breakdown. Furthermore, partial discharge can also occur along the boundary between different insulating materials, ultimately leading to electrical breakdown and, eventually, explosion with stop of energy transportation [2–4]. Therefore, the defect of electrical insulator is an important reason causing electrical network accident, so it is a crucial work to detect the defect of insulator periodically and minimize interruption of energy accidents. The traditional way of monitoring and troubleshooting is to conduct manual inspection of the videos and images of

the transmission lines photographed by the helicopter. But it is too time-consuming and labor-intensive to get efficient defect detection, usually easy to make wrong judgements because of the large amount of data. At present work, D. Zuo et al. used SVM classification to detect missing insulators [5]. Qaddoumi et al. introduced artificial neural network-based near-field microwave to accurately test damage of outdoor insulators [6]. Armando et al. detected the cracks and operation defects in the insulators and breaker by a portable low cost computed radiography systems [7]. Chen et al. extract single insulator disk in infrared image of insulator string [8]. Huang et al. proposed some back propagation neural network method for equipment fault diagnosis [9, 10]. However, the above methods are operated in the special imaging situation to achieve the insulator defect detection, it has great limitation to the natural captured insulator images in damage detection. With the developing of high-speed digital imaging and processing technique, intelligent identification technology began to be used in high-voltage safe operation and long-distance power transmission lines inspection [11–16]. Figure 1 is the illustration of electrical safe operation and transmission inspection, the electrical insulator (glass/ceramic material) image is captured by UAV (unmanned aerial vehicle), which is suitable for several



FIGURE 1: Electrical safe inspection captured by UAV Imaging [2].

kinds electrical safe inspection. In view of the above details, this paper proposed an electrical insulator defect detection method inspired by human brain receptive field (RF) model, aiming to achieve accurate detection including defect, crack even dirty of different damaged insulators, so as to improve safety and reliability of high-voltage transmission line. Experimental results show that this method can quickly and accurately detect whether the insulator is broken or damaged.

The paper is organized as follows. In Section 2, we detailed the biology basis of human brain RF and the proposed method combined RF model. Section 3 discussed important parameter selection and experimental performance evaluation. Finally, we give a brief summary and draw a conclusion in Section 4.

2. Defect Detection Method Combined RF Model

2.1. Biology Basis of the RF Model. A large number of biological experiments show that the primary visual pathway of the human brain can obtain the main information of the object and play a key role in the overall perception of the object [17, 18]. In Figure 2(a), visual information reaches the eye through the cornea and pupil, passes through the photoelectric conversion of photoreceptor cells in the retina, then passes into the lateral geniculate nucleus (LGN), and projects to V1 area, finally creating visual perception of the brain [19, 20]. LGN is an important step to V1 area of HVS, Figure 2(b) represents two types of LGN RF model, that is, center-on (“+”) and center-off (“-”) cells. In these cells, the central region is excitatory (marked by red in center-on and blue in center-off) and the surrounding is inhibitory (color opposite to excitatory area), respectively. From Figure 2(b), it can be seen that the center of the on-type is surrounded by off-type and the center off-type around is surrounded by on-type. Both of these cells are arranged and their total number is substantially equal and detect contrast changes. Some researchers have proved that the on-type and off-type channels are located between the LGN and the visual cortex is fully parallel separation [21, 22]. The process of LGN receptive field is defined as a 2D Gaussian function in the following:

$$\begin{aligned} DOG_{\sigma}^{\delta}(x, y) \\ = A \left[\exp\left(-\frac{x^2 + y^2}{\sigma^2}\right) - \exp\left(-\frac{x^2 + y^2}{k\sigma^2}\right) \right] \end{aligned} \quad (1)$$

In this equation, x and y represent spatial variables respectively, δ represents the type of cell (that is sensitivity of excitatory and inhibition area of RF), which is “+” or “-”, A is a mapping function of δ , when δ is “+”, a center-on RF cell is defined as $A(x) = x$, else $A(x)$ is defined as the negative of $A(x)$, that is $A(x) = -x$, so a center-off RF cell is $DOG_{\sigma}^{-}(x, y) = -DOG_{\sigma}^{+}(x, y)$. σ is the standard deviation of the outer Gaussian function, which represents the size of excitatory and inhibitory area of RF, usually is set by 0.5σ , which is in accordance with electron-physiological findings of LGN cells in mammals.

2.2. Construction of the Detection Method with RF Model. For the above details, the proposed electrical insulator defect detection method is inspired by human brain RF model, which is followed in [21]. Figure 3 shows the relationship of above described LGN cell and the main information of an image (object). In Figure 3, center-on LGN RF cell is marked by green and center-off LGN RF cell is marked by red, V1 simple cell RF is marked by blue circle. The center of RF is positioned on an edge (marked by points) which gives rise to model LGN cell responses rendered in the left two columns of Figure 3. The eight small points represent the RF centers of eight subunits, four of center-on (in green), and four of center-off (in red) type. For the considered example, it results in the inclusion of eight subunits in the model. The number of subunits depends on the number of circles we considered and the specific input pattern presented at the time of configuration. In this insulator defect detection method, each subunit included is represented in parametric form by a tuple $(\delta, \sigma, \rho, \phi)$, where the parameters δ represent the polarity of subunit, σ is the scale of the involved model LGN cells, the radius ρ , and the polar angle ϕ of the RF center of the subunit relative to the RF center of the model cell [21, 23], respectively.

We denote by $S = \{(\delta_i, \sigma_i, \rho_i, \phi_i) \mid i = 1 \dots n\}$ 4-tuples of the configured subunits of model. According to the right three subparts in Figure 3, we explain the general configuration process of the proposed detection method in more detail below. A cell group computes the sum of the weighted responses of the model LGN cells it receives input from. These models LGN cells have the same polarity (on or off), RF size and neighboring RFs. In this way, a subunit detects contrast changes, similar to a model LGN cell. A subunit can be thought of as a dendrite branch of a simple cell which receives input from a pool of adjacent LGN cells.

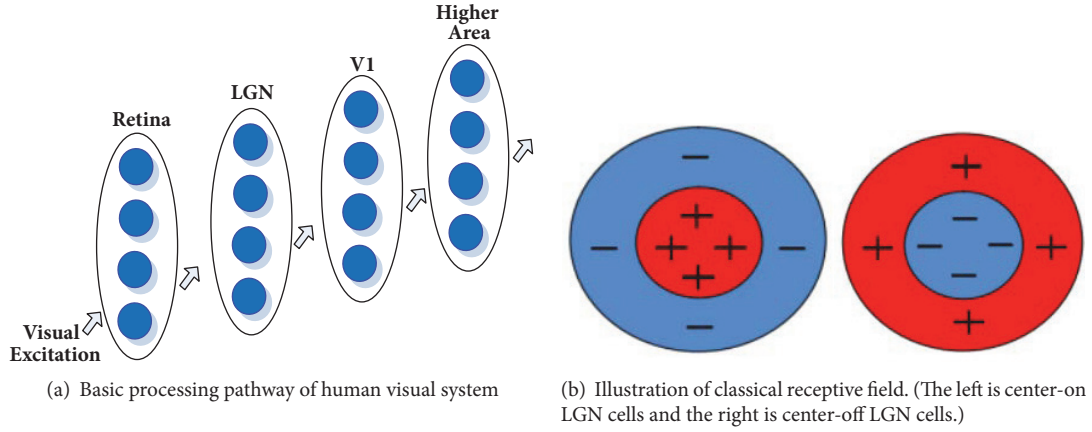


FIGURE 2: Illustration of Basic Human Receptive Field (RF).

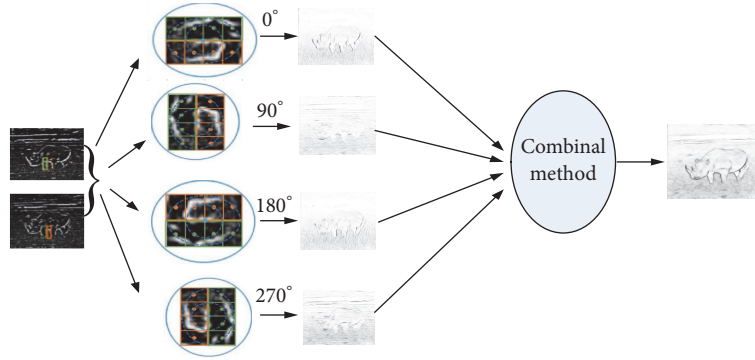


FIGURE 3: The process of detection and illustration of constructed model.

In Figure 3, input image passes through LGN cell and gets their responses, several LGN cells with same polarity form a cell group. Afterwards, a plurality of LGN cells of the same attribute forms a cell group, a certain number of same polarity cell groups are arranged colinearly and different attribute cell groups are arranged in parallel, the interaction forms a V1 simple cell with different preference directions, and each output is simple cell response. Finally, different simple cell responses were integrated by weighted summation to obtain the overall responses of V1 simple cells. Figure 3 is the construction process with a simple image from RUG dataset [21, 23], with only specific cells preferentially oriented at 0, 90, 180, and 270 degrees.

The concentric receptive field of a single LGN cell can be characterized as (1). For an LGN cell that located at coordinate (x, y) , the response can be obtained by convolving the intensity distribution function of the image with the cell receptive field, that is represented by the following:

$$l_{\sigma}^{\delta}(x, y) = I * DOG_{\sigma}^{\delta} \quad (2)$$

Considering the different δ may lead to $l_{\sigma}^{\delta}(x, y)$ being negative value, but the self-firing rate is positive in biology, the

nonnegative half-wave operation [22, 24] is adopted to obtain single LGN cell response as follows:

$$D_{\sigma}^{\delta}(x, y) = \max \{0, l_{\sigma}^{\delta}(x, y)\} \quad (3)$$

All the feature characteristic LGN cells can be combined to a group, which is defined as follows similar to [25].

$$S = \{(\delta_i, \sigma_i, \rho_i, \phi_i) \mid i = 1, 2, \dots, m\} \quad (4)$$

In (4), m represents the quality of cell group included in each cell group. For each specified $(\delta_i, \sigma_i, \rho_i, \phi_i)$, ρ and ϕ represent the single cell relative to the center of cell group. For the LGN cell group located at (x, y) , the response is described as follows:

$$\begin{aligned} & Z_{\delta_i, \sigma_i, \rho_i, \phi_i}(x, y) \\ &= \sum_{x'} \sum_{y'} \{D_{\sigma_i}^{\delta_i}(x - \Delta x_i - x', y - \Delta y_i - y') \\ &\quad \cdot G_{\sigma_i}(x', y')\} \end{aligned} \quad (5)$$

The parameters satisfied the following conditions:

$$\begin{aligned} \Delta x_i &= -\rho_i \cos \phi_i \\ \Delta y_i &= -\rho_i \sin \phi_i \end{aligned} \quad (6)$$

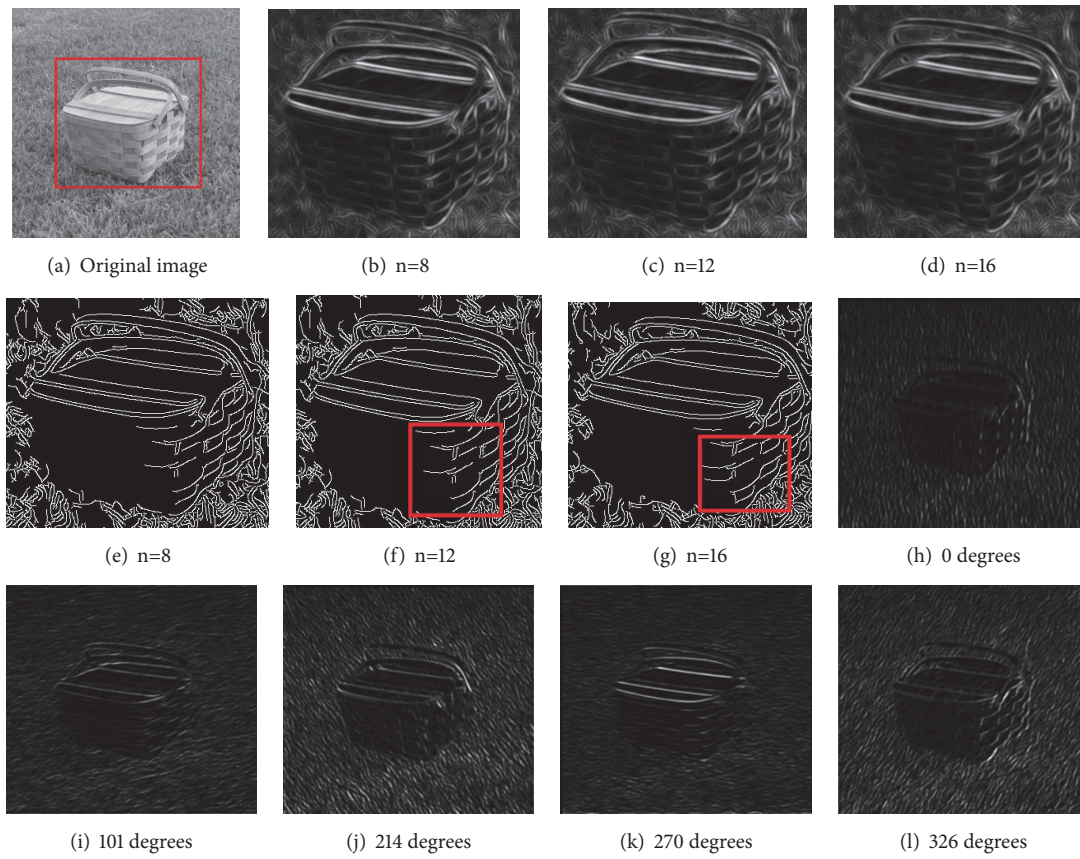


FIGURE 4: Selection of the appropriate parameter n and orientation comparison.



FIGURE 5: Some electrical insulator images in our dataset.

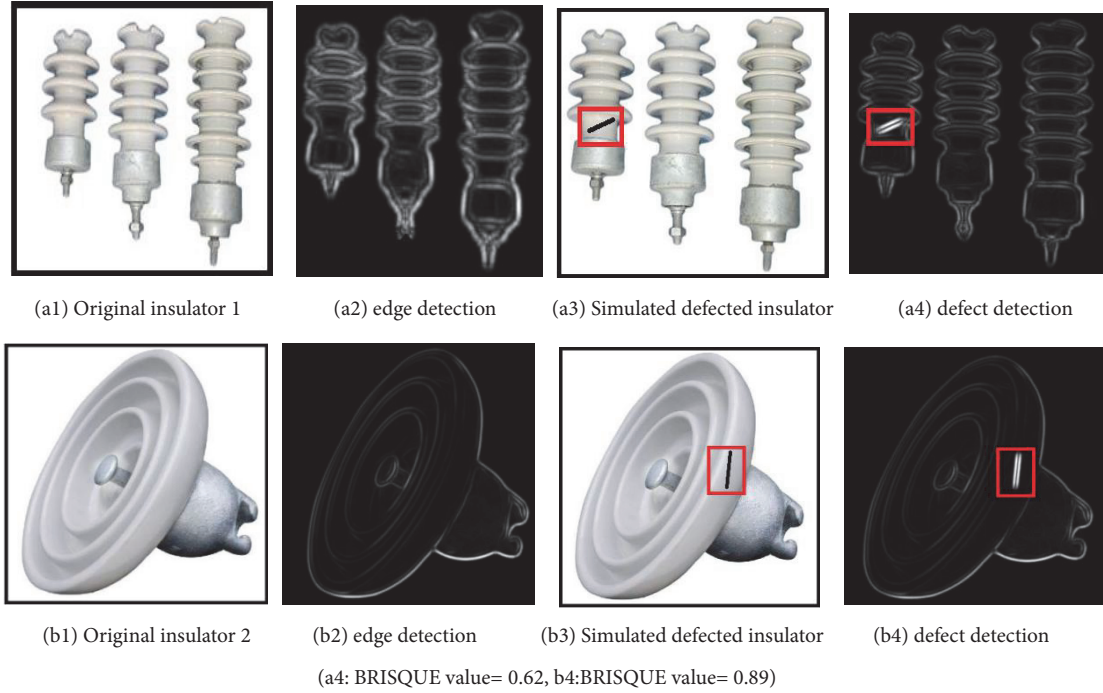


FIGURE 6: Simulated defect detection of ceramic electrical insulator.

Define Q_{S,ϕ_i} as the simple cell response of the direction ϕ_i , which is determined by all cell group response in the defined region. In Hubel-Wiesel's work, only the response of all LGN cell group included in given region can excite simple cell. In order to show the biological nature, all of the cell group responses are multiplied to get geometry average, so as to represent the simple cell response, which is mathematical explained in the following:

$$Q_{S,\phi_i}(x, y) = \left[\prod_{i=1}^{|S|} (Z_{\delta_i, \sigma_i, \rho_i, \phi_i}(x, y))^{w_i} \right]^{1/\sum_{i=1}^{|S|} w_i} \quad (7)$$

In the above equation, it is satisfied as $w_i = e^{-\rho_i/2\sigma'^2}$ and $\sigma' = (1/3)\max_{i \in \{1, 2, \dots, |S|\}} \{\rho_i\}$, the direction function is defined as $\beta = \{(2\pi/n)i \mid 0 \leq i < n\}$, $i = 0, 1, \dots, n$, all of these simple cell responses are combined to get the overall response of V1 area in the following:

$$Q_{all}(x, y) = \sum_{\phi \in \beta} Q_{S,\phi}(x, y) \quad (8)$$

3. Performance Evaluation of the Method

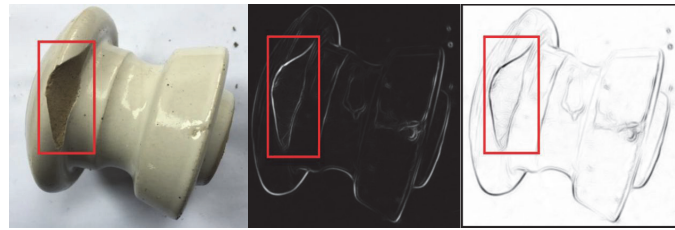
3.1. Key Parameter Selection. The appropriate selection of parameter n is a key step in the proposed detection method, because the structure of the electrical insulator is relatively simple, in order to show the detection efficiency by different parameters on insulator defect detection. In order to verify the parameter selection difference, we choose the image as an example from RUG (university of Groningen) image dataset [20]. Because the texture of the natural image (such as basket) is more complex and more detailed than a simple insulator

image, as shown in Figure 1. Figure 4(a) is the original image, Figures 4(b)–4(d) are the basic contour of original image in various parameters condition, and Figures 4(e)–4(g) are the binary detection result by different parameters, which takes 8, 12, and 16, respectively.

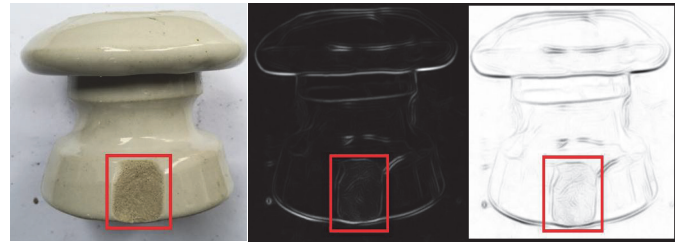
The configured detection model cell response to a natural image is illustrated in Figure 4. When $n=4$, there are a large number of missed detections of the model and it is difficult to recognize the basic appearance of the object from the output information. The basic appearance of the object can already be basically resolved when $n=8$, but the included edge information is still incomplete. The output of the model contains relatively complete edges when $n=12$, which can clearly identify the appearance of the object. The last one in Figure 4(g) is $n=16$, the model will get more complete local contour information. As the above analysis, the parameter is selected as $n=16$ in our experiment. When the orientation selection is $n=16$, some simple cell with different orientations are shown in Figures 4(h)–4(l). This illustration proved that a single simple cell just sensitive to the specific orientation, different orientation cell groups can better describe various redundant detailed features.

3.2. Experimental Results. In this section, the evaluation performance of the proposed model in the electrical insulator defect detection task is shown. Although several types of insulators are used in China, this paper only showed two main types of insulators: one type is the white ceramic insulator and the other is the dark red insulator.

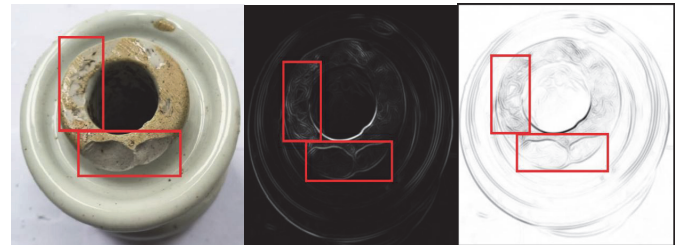
For the reason of lacking public electrical insulator dataset, all of the electrical insulators used in our experiment are from our team's captured dataset. The dataset includes



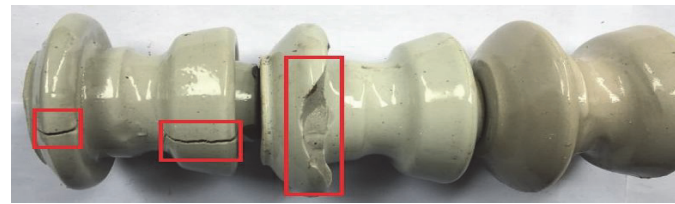
(a1) Real defected insulator 1 (a2) Defect detection result (a3) Illumination reversed of (a2)
(a2:BRISQUE value= 0.71, a3:BRISQUE value=0.74)



(b1) Real defected insulator 2 (b2) Defect detection result (b3) Illumination reversed of (b2)
(b2:BRISQUE value=0.64, b3:BRISQUE value= 0.67)



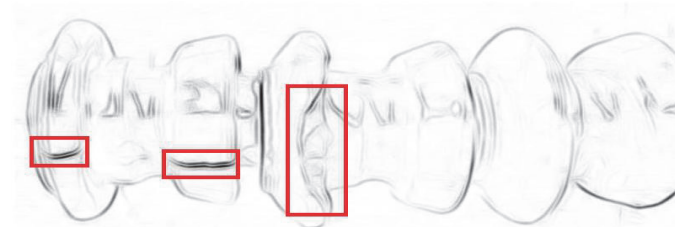
(c1) Real defected insulator 3 (c2) Defect detection result (c3) Illumination reversed of (c2)
(c2:BRISQUE value= 0.62, c3:BRISQUE value= 0.67)



(d1) Real defected insulator 4

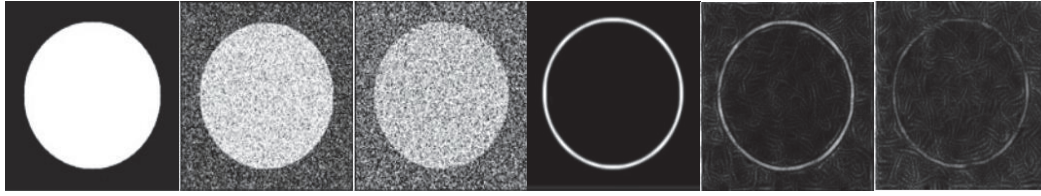


(d2) Defect detection result (BRISQUE value=0.64)



(d3) Illumination reversed of (d2) (BRISQUE value=0.58)

FIGURE 7: Real defected detection of ceramic electrical insulator.



(a1-f1) Comparable detection result of original circle image and corresponding noisy version



(a2-c2) Robust detection of noisy ceramic insulator image 1 (variance is 0.01)



(a3-c3) Robust detection of noisy ceramic insulator image 1 (variance is 0.05)

FIGURE 8: Robust detection test of original circle and different noisy insulator.

300 images, there are 34 images are good electrical insulator images, and others are defect electrical insulator images. Figure 5 shows some ceramic electrical insulators in our dataset. The first row includes good ceramic electrical insulators and some broken/damaged ones are shown in the second row.

There are three experiments are adopted in this paper, which include simulated defect detection, real defect detection, and robust feature detection. All of these experimental results can sufficiently show the efficiency of the proposed detection method.

(A) *Simulated Defect Detection.* Figure 6 shows defect detection result of electrical insulator with simulated crack. Figures 6(a1) and 6(b1) are real original ceramic electrical insulators. Figures 6(a2) and 6(b2) give the edge detection of original ceramic electrical insulators without crack. In Figures 6(a3) and 6(b3), there is a simulated crack located on the surface of real ceramic electrical insulator respectively. Figures 6(a4) and 6(b4) clearly show the crack and achieve accurate defect detection.

(B) *Real Defect Detection.* In Figure 7, four real damaged ceramic electrical insulators are used in our experiment. Figures 7(a1)–7(d1) are real original damaged insulator images from our dataset, we can see that there are obviously damaged on the surface of electrical insulators. Figures 7(a2)–7(d2)

is the defect detection result of these damaged electrical insulators. In order to further provide the efficiency of the proposed method, the results of Figures 7(a2)–7(d2) are reversed operation to show accurate detection result, which is shown in Figures 7(a3)–7(d3) and marked in red rectangle. In addition, except for the subjective experimental result, objective evaluation result such as BRISQUE metric [26] is also provided here. Objective experimental evaluation value reflects that the insulator defect detection is more acceptable, it is easy to achieve further fault judgement.

3.3. *Robust Detection.* Experiments in Section 3.2 are electrical insulator captured in a good natural condition, the image is clear and clean. However, the electrical insulator has been exposed in outdoor electricity transmission line for a long time in normal situation, so the captured insulator image including noise. In order to verify the robust of our method, the experiment is added in this section. Figures 8(a1)–8(c1) represent the original clean circle image, the noisy circle image additive with standard deviation is 0.01, and the noisy circle image additive with standard deviation is 0.05. The damaged part of the insulator is marked by red rectangle. The type of noise is Gaussian noise. In Figures 8(d1)–8(f1), we can see the detection result of fore-referred circle images. Figures 8(a2) and 8(a3) are noisy version of the same electrical ceramic insulator (the standard deviation is 0.01 and 0.05,

respectively). Experimental results shown in Figures 8(b2) and 8(b3) are the detection results; the damaged part of the noisy defect electrical insulator is accurately detected and it is very clear. For the purpose of further show the robust detection result, Figures 8(c2) and 8(c3) are operated reversely in order to show more clear damaged part of the electrical insulator.

4. Conclusion

The application of image processing and machine learning method is a popular development trend in future electricity power transmission line inspections. Inspired by human brain visual pathway LGN and V1 simple cell RF characteristic, this paper proposed an electrical insulator defect detection method combined computational model in area V1 of visual cortex, different feature orientation selectivity is achieved by combining operation of a collection of LGN cells with center-surround RF. Demonstration of different experimental results shown that the proposed method can achieve accurate electrical insulator defect detection, even complete robust detection of noisy insulators. Because the background of the insulator image acquired by aerial photography is complicated and there is more than one insulator type, defects are difficult to detect, so that our further work will focus on optimizing this method, identifying and locating the insulator defect by segmentation, and extending it to more wide application. The aim is greatly improving the efficiency of electricity power transmission line and easy to find defect or fault in the system, so as to provide completely and timely guarantee for electricity grid dispatching and electrical equipment maintenance.

Data Availability

Because the original datasets are captured by our research group, the datasets generated during and/or analysed during the current study are available from the corresponding author on reasonable request.

Conflicts of Interest

The authors declare that they have no conflicts of interest.

Acknowledgments

This work is supported by National Natural Science Foundation of China (61663008), Natural Science Foundation of Hubei Province (2015CFC781, 2014CFB612), and Ph.D. Technology Program of Hubei University for Nationalities (MY2014B018).

References

- [1] W. Angelika, "Vision diagnostics of power transmission lines: approach to recognition of insulators," in *Improvements to Segmentation Method of Stained Lymphoma Tissue Sections Images*, 440, p. 431, Springer, 2016.
- [2] T. Alshaketheep, K. Murakami, and N. Sekimura, "Effect of insulator environment on thermal ageing estimations for ethylene propylene rubber insulated nuclear power plant cables," *Journal of Nuclear Science and Technology*, vol. 53, no. 9, pp. 1366–1370, 2016.
- [3] H. Zou, X. Lei, and S. Ma, "Motion feature extraction of random video sequence based on visual cortex V1 model," *Journal of Computer Applications*, vol. 36, no. 6, pp. 1677–1681, 2016.
- [4] D. Huang, C. Chen, G. Sun, and L. Zhao, "Recognition and diagnosis method of objective entropy weight for power transformer fault," *Dianli Xitong Zidonghua/Automation of Electric Power Systems*, vol. 41, no. 12, pp. 206–211, 2017.
- [5] D. Zuo, H. Hu, R. Qian, and Z. Liu, "An insulator defect detection algorithm based on computer vision," in *Proceedings of the 2017 IEEE International Conference on Information and Automation (ICIA)*, pp. 361–365, China, July 2017.
- [6] N. N. Qaddoumi, A. H. El-Hag, and Y. Saker, "Outdoor insulators testing using artificial neural network-based near-field microwave technique," *IEEE Transactions on Instrumentation and Measurement*, vol. 63, no. 2, pp. 260–266, 2014.
- [7] H. Armando, Shinohara, and M. Danilo, "Defects detection in electrical insulators and breaker for high voltage by low cost computed radiography systems," in *Proceedings of the International Conference of symposium on digital industrial radiology and computed tomography*, vol. 6, pp. 25–27, France, 2007.
- [8] F. Chen and J. Yao, "Extraction method of single insulator disk in infrared image of insulator string," *Power System Technology*, vol. 34, no. 5, pp. 220–224, 2010.
- [9] D.-R. Huang, C.-S. Chen, G.-X. Sun, L. Zhao, and B. Mi, "Linear discriminant analysis and back propagation neural network cooperative diagnosis method for multiple faults of complex equipment bearings," *Acta Armamentarii*, vol. 38, no. 8, pp. 1649–1657, 2017.
- [10] H. Darong, T. Jianping, and Z. Ling, "A fault diagnosis method of power systems based on gray system theory," *Mathematical Problems in Engineering*, vol. 2015, Article ID 971257, 11 pages, 2015.
- [11] X. Mei, T. Lu, X. Wu, and B. Zhang, "Insulator surface dirt image detection technology based on improved watershed algorithm," in *Proceedings of the 2012 Asia-Pacific Power and Energy Engineering Conference, APPEEC 2012*, March 2012.
- [12] M. Oberweger, A. Wendel, and H. Bischof, "Visual recognition and fault detection for power line insulators," in *Proceedings of the 19th Computer Vision Winter Workshop, Krtiny*, vol. 2, pp. 3–5, Czech Republic, 2014.
- [13] S. Liao and J. An, "A robust insulator detection algorithm based on local features and spatial orders for aerial images," *IEEE Geoscience and Remote Sensing Letters*, vol. 12, no. 5, pp. 963–967, 2015.
- [14] L. Junfeng, L. Min, and W. Qinruo, "A novel insulator detection method for aerial images," in *Proceedings of the the 9th International Conference*, vol. 2, pp. 18–21, Sydney, Australia, February 2017.
- [15] J. Zhao, X. Liu, and J. Sun, "Detecting insulators in the image of overhead transmission line," in *Proceedings of the of International Conference on Intelligent Computing*, pp. 442–450, 2012.
- [16] H. Darong, K. Lanyan, C. Xiaoyan, Z. Ling, and M. Bo, "Fault diagnosis for the motor drive system of urban transit based on improved Hidden Markov Model," *Microelectronics Reliability*, vol. 82, pp. 179–189, 2018.

- [17] M. Bartolucci and A. T. Smith, "Attentional modulation in visual cortex is modified during perceptual learning," *Neuropsychologia*, vol. 49, no. 14, pp. 3898–3907, 2011.
- [18] S. Grossberg, E. Mingolla, and W. D. Ross, "Visual brain and visual perception: how does the cortex do perceptual grouping?" *Trends in Neurosciences*, vol. 20, no. 3, pp. 106–111, 1997.
- [19] J. Carl and B. Bassi, "Parallel processing in the human visual system," in *New Methods of Sensory Visual Testing*, 59, p. 53, Springer, New York, NY, USA, 1989.
- [20] C. Grigorescu, N. Petkov, and M. A. Westenberg, "Contour detection based on nonclassical receptive field inhibition," *IEEE Transactions on Image Processing*, vol. 12, no. 7, pp. 729–739, 2003.
- [21] G. Azzopardi and N. Petkov, "A CORF computational model of a simple cell that relies on LGN input outperforms the Gabor function model," *Biological Cybernetics*, vol. 106, no. 3, pp. 177–189, 2012.
- [22] C. Grigorescu, N. Petkov, and M. A. Westenberg, "Contour and boundary detection improved by surround suppression of texture edges," *Image and Vision Computing*, vol. 22, no. 8, pp. 609–622, 2004.
- [23] Q. Sang, B. Cai, and H. Chen, "Contour detection improved by context-adaptive surround suppression," *PLoS ONE*, vol. 12, no. 7, Article ID e0181792, 2017.
- [24] D. G. Albrecht, R. L. De Valois, and L. G. Thorell, "Visual cortical neurons: are bars or gratings the optimal stimuli?" *Science*, vol. 207, no. 4426, pp. 88–90, 1980.
- [25] C. Lv, Y. Xu, and S. Li, "An edge detection model by brain-inspired," *Computer Engineering and Application*, vol. 53, no. 24, pp. 142–146, 2017.
- [26] T. Sun, X. Zhu, J. Pan, J. Wen, and F. Meng, "No-reference image quality assessment in spatial domain," *Genetic and Evolutionary Computing*, vol. 21, no. 12, pp. 4695–4708, 2012.

Research Article

Backstepping Control with Disturbance Observer for Permanent Magnet Synchronous Motor

Yong-Hong Lan  and Lei-Zhou

College of Information Engineering, Xiangtan University, Xiangtan, Hunan 411105, China

Correspondence should be addressed to Yong-Hong Lan; 961501563@qq.com

Received 26 February 2018; Revised 9 April 2018; Accepted 22 May 2018; Published 2 July 2018

Academic Editor: Darong Huang

Copyright © 2018 Yong-Hong Lan and Lei-Zhou. This is an open access article distributed under the Creative Commons Attribution License, which permits unrestricted use, distribution, and reproduction in any medium, provided the original work is properly cited.

For the speed tracking control problem of Permanent Magnet Synchronous Motor (PMSM), a disturbance observer-based (DOB) backstepping speed tracking control method is presented in this paper. First, to reconstruct the load disturbance, a slowly time-varying disturbance observer for PMSM is constructed. Next, by stability theory, the norm of the observation error and disturbance observer design method are obtained. On the basis of these, through the designing of the virtual control input that include the reconstruction disturbances, and using backstepping control strategy, the DOB controller of the closed-loop system is proposed. The obtained controller can achieve high precision speed tracking and disturbance rejection. Finally, some results of evaluative experiments verified the effectiveness of the proposed method for high-performance control and disturbance rejection for the PMSM drive.

1. Introduction

Permanent magnet synchronous motor (PMSM) is receiving increasing attention in high-performance industrial servo applications due to its advantages such as high torque to current ratio, super power density, and fast response, as well as low noise [1, 2]. However, PMSM is a typical high nonlinear, multivariable coupled system. It is sensitive to load disturbance, unmodeled dynamics, nonlinear uncertainties, and parameter uncertainties.

Over the last decades, various design methods have been developed for PMSM control systems, such as adaptive control [3], robust control [4], neural network control [5], predictive control [6], and so on. Recently, to improve the control performances in PMSM systems, much attention has been given to disturbance reject-based control method [7], which are insensitive to parameter variations and external disturbances. In [8, 9], the fractional order sliding-mode control (SMC) scheme has been proposed. The proposed control system not only obtained high control performance but also was robust against to external load disturbance and parameter variations.

To further improve the disturbance rejection performance of SMC, extended sliding-mode disturbance observer was proposed in [10, 11], and the estimated system disturbance is considered as the feed forward compensation part to compensate sliding-mode speed controller. In [12], an improved SMC scheme to solve time-varying parameters and disturbances for PMSM drive system was proposed. The new speed controller was designed by the nonsingular terminal SMC strategy with the disturbance observer. In [13], a new speed controller is designed by the nonsingular terminal SMC strategy with disturbance observer. The controller can make the motor speed reach the reference value in finite time, accompanied with a faster convergence and a better tracking precision. It is worth noting that one obvious disadvantage of SMC method is the chattering phenomenon, which is caused by discontinuous control law and frequent switching action near sliding surface. Besides, as the upper bound of lumped disturbances is not easy to be determined in advance, which could cause a large amount of chattering of SMC strategy in PMSM system.

Recently, disturbance observer-based (DOB) [14] control methods have been applied to PMSM system for better

robustness against system disturbance. In [15], a DOB state feedback controller was designed for PMSM system. By using the same disturbance observer, a sensorless control method for PMSM drive was developed in [16]. The proposed DOBC method involved the use of a back electromotive force observer and a torque observer to estimate rotor position and compensate for load torque disturbance, respectively. For the mismatched disturbance, in [17], a DOB integral sliding-mode control approach for linear systems with mismatched disturbances was presented. The disturbance observer is proposed to generate the disturbance estimate, which can be incorporated in the controller to counteract the disturbance.

Backstepping is a well-known recursive and systematic design methodology for the feedback control of uncertain nonlinear system with matched uncertainties [18]. The key point is to use the virtual control variable to make the original high-order system simple; thus the final controller can be derived through Lyapunov stable theorem. In [19], an adaptive backstepping speed controller was proposed for the speed control of PMSM. The controller is robust against stator resistance, viscous friction uncertainties, and load torque disturbance. However, this approach uses the feedback linearization. By means of a nonlinear and adaptive backstepping design method, a speed and current control scheme for PMSM was presented in [20], in which all the parameters in both PMSM and load dynamics were considered unknown. In [21], a new nonlinear and full adaptive backstepping speed tracking control scheme was developed for an uncertain PMSM. Except for the number of pole pairs, all the other parameters in both PMSM and load dynamics were assumed unknown. Taking into account the unobservable of the systems states, a backstepping control method for speed sensorless PMSM based on slide model observer was proposed in [22], in which the slide model observer was designed by using slide model control technique and phase loop lock (PLL) method. In [23], a backstepping control algorithm based on disturbance observer was proposed. The minimum-order observer was established to observe the disturbance value of load inertia. Furthermore, the estimated disturbance value was used to identify the load inertia. Based on the identification results, the backstepping controller was designed. However, the above observer and controller are designed separately.

Motivated by the discussions above, in this paper, we mainly investigate backstepping speed control for PMSM based on disturbance observer. A nonlinear disturbance observer is first constructed to estimate the external slowly time-varying disturbance. Then, based on the backstepping control theory, the PMSM rotor speed and current tracking backstepping controllers are designed. Meanwhile, global asymptotic stability is guaranteed by Lyapunov stability analysis.

The rest of this paper is structured as follows. In Section 2, the mathematic model of PMSM and problem formulation are presented. The nonlinear disturbance observer design and stability analysis are derived in Section 3. In Section 4, the DOB backstepping controller design method is obtained. Section 5 presents the numerical simulation and experimental results. Finally, some conclusions are drawn in Section 6.

2. Mathematic Model of PMSM and Problem Formulation

Assume that magnetic circuit is unsaturated and hysteresis and eddy current loss are ignored. With above standard assumptions, the mathematical model of a conventional surface mounted PMSM with mismatched external disturbances can be given in the $d-q$ frame as follows [20, 22]:

$$\begin{aligned} \frac{d\omega}{dt} &= \frac{3p\phi_f}{2J}i_q - \frac{B}{J}\omega - \frac{T_L}{J}, \\ \frac{di_q}{dt} &= -\frac{R}{L}i_q - p\omega i_d - \frac{p\phi_f}{L}\omega + \frac{1}{L}u_q + \frac{1}{L}d_1, \\ \frac{di_d}{dt} &= -\frac{R}{L}i_d + p\omega i_q + \frac{1}{L}u_d + \frac{1}{L}d_2, \end{aligned} \quad (1)$$

where ω is the rotor speed, i_d and i_q are the $d-q$ axis currents, u_d and u_q are the $d-q$ axis voltages, and d_i ($i = 1, 2$) are external disturbances. R and L denote the stator resistance and inductance per phase, respectively, p is the number of pole pairs, ϕ_f is the permanent magnet flux, J is the rotor moment of inertia, B is the viscous friction factor, and T_L also represents the applied load torque disturbance.

To formulate the design problem, according to system (1), the state space model of the PMSM can be rewritten as the following nonlinear system:

$$\begin{aligned} \dot{x}(t) &= Ax(t) + f(x(t)) + Bu(t) + \eta + Bd(t), \\ y(t) &= Cx(t), \end{aligned} \quad (2)$$

where $x(t) = [\omega \ i_q \ i_d]^T$, $u = [u_q \ u_d]^T$ and

$$A = \begin{bmatrix} -\frac{B}{J} & \frac{3p\phi_f}{2J} & 0 \\ \frac{p\phi_f}{L} & -\frac{R}{L} & 0 \\ 0 & 0 & -\frac{R}{L} \end{bmatrix},$$

$$B = \begin{bmatrix} 0 & 0 \\ \frac{1}{L} & 0 \\ 0 & \frac{1}{L} \end{bmatrix},$$

$$C = [1, 0, 0],$$

$$f(x(t)) = \begin{bmatrix} 0 \\ -p\omega i_d \\ -p\omega i_d \end{bmatrix},$$

$$\eta = \begin{bmatrix} -\frac{T_L}{J} \\ 0 \\ 0 \end{bmatrix}$$

$$d(t) = \begin{bmatrix} 0 \\ d_1 \\ d_1 \end{bmatrix}. \quad (3)$$

For the PMSM control system (2), we give the following assumptions.

Assumption 1. The external disturbance $d(t)$ is assumed that $d(t) \leq \alpha$, $\dot{d}(t) = 0$, where α is a positive constant.

Assumption 2. For all $x_1, x_2 \in \Omega_1$ the nonlinear term $f(x(t))$ in system (2) satisfies

$$\|f(x_1) - f(x_2)\| \leq \gamma \|x_1 - x_2\|, \quad (4)$$

where γ is Lipschitz constant.

The main control objective is to design a DOB backstepping controller to keep all the signals in the closed-loop system bounded and ensures global asymptotic convergence of the desired speed and current tracking errors to zero eventually.

3. Nonlinear Disturbance Observer and Stability Analysis

Motivated by the disturbance observers in [14–16], the following disturbance observer for system (2) can be employed:

$$\begin{aligned} \dot{v}(t) &= \Lambda \hat{d}(t) + \Lambda B^\dagger (Ax(t) + f(x(t)) + Bu(t) + \eta), \\ \hat{d}(t) &= v(t) - \Lambda B^\dagger x(t), \end{aligned} \quad (5)$$

where $B^\dagger = (B^T B)^{-1} B^T$, $\hat{d}(t)$ is the estimation of $d(t)$, $v(t)$ is the internal variable vector of the observer, and Λ is a Hurwitz matrix chosen by designer. For simplicity, we assume $\hat{d}(0) = 0$. Define the disturbance estimation error $\tilde{d}(t)$ as

$$\tilde{d}(t) = d(t) - \hat{d}(t). \quad (6)$$

To show that the disturbance can be observed asymptotically by observer (5), we first give the following lemma.

Lemma 3. For nonlinear system (2), suppose that the disturbance observer holds form (5); then the disturbance can be observed asymptotically.

Proof. It can be obtained that

$$\dot{v}(t) = \Lambda \hat{d}(t) + \Lambda B^\dagger \dot{x}(t) - \Lambda d(t), \quad (7)$$

which implies that $\dot{\tilde{d}}(t) = -\Lambda \tilde{d}(t)$. Therefore, we have

$$\dot{\tilde{d}}(t) = \Lambda \tilde{d}(t). \quad (8)$$

Define a monochromatic Lyapunov function as

$$V_o(t) = \frac{1}{2} \tilde{d}^T(t) \tilde{d}(t). \quad (9)$$

Clearly,

$$\dot{V}_o(t) \leq \tilde{d}^T(t) (\Lambda + \Lambda^T) \tilde{d}(t). \quad (10)$$

Since Λ is Hurwitz, then

$$\dot{V}_o(t) \leq 2\lambda_{\max}(\Lambda) \|\tilde{d}(t)\|^2 = -\beta \|\tilde{d}(t)\|^2, \quad \beta > 0, \quad (11)$$

which implies the error dynamics (8) is asymptotically stable. This completes the proof. \square

Remark 4. It follows from Lemma 3 that parameter Λ in the disturbance observer (5) can change the rate of convergence of the observer and should be selected as large enough.

4. DOB Backstepping Controller Design

In the backstepping procedure, a virtual control state is firstly defined and then it is forced to become a stabilizing function. By defining a corresponding error variable and using Lyapunov stability theory, the related control input can be obtained to stabilize the error dynamics [21]. In this paper, the overall control design can be established by three steps in the following order.

Step 1. In the first step of the backstepping control design, a fictitious control input for the rotor speed ω has to be determined. Let ω_r^* be the desired trajectory. Furthermore, the trajectory of ω_r^* is sketched to be smooth and $\dot{\omega}_r^* = 0$. Define the speed tracking error $e_\omega = \omega_r^* - \omega$. The speed tracking error dynamics can be obtained as

$$\dot{e}_\omega = \dot{\omega}_r^* - \dot{\omega} = \frac{1}{J} \left(B\omega + T_L - \frac{3p\phi_f}{2} i_q \right). \quad (12)$$

The first positive definite Lyapunov function can be defined as

$$V_1(t) = \frac{1}{2} e_\omega^2 + V_o(t). \quad (13)$$

Differentiating $V_1(t)$ with respect to time and using the results of (11) and (12), the time derivative of $V_1(t)$ is given as

$$\begin{aligned} \dot{V}_1(t) &= e_\omega \dot{e}_\omega + \dot{V}_o(t) \\ &\leq \frac{e_\omega}{J} \left(B\omega + T_L - \frac{3p\phi_f}{2} i_q \right) - \beta \|\tilde{d}(t)\|^2. \end{aligned} \quad (14)$$

In order to stabilize the speed tracking error dynamics, define the stabilizing virtual control input:

$$i_q = \frac{2}{3p\phi_f} (B\omega + T_L + k_1 J e_\omega), \quad (15)$$

where $k_1 > 0$ is a real constant. Therefore, this definition leads to

$$\dot{V}_1(t) \leq -k_1 e_\omega^2 - \beta \|\tilde{d}(t)\|^2 \leq 0, \quad (16)$$

which guarantees that the tracking error for rotor speed will converge asymptotically.

Step 2. In order to realize the complete decoupling and speed tracking of PMSM, the virtual input current can be chosen as

$$i_q^* = \frac{2}{3p\phi_f} (B\omega + T_L + k_1 J e_\omega), \quad i_d^* = 0. \quad (17)$$

Define the tracking error of q axis current as $e_q = i_q^* - i_q$. The time derivative of e_q is

$$\begin{aligned} \dot{e}_q &= \frac{di_q^*}{dt} - \frac{di_q}{dt} = \frac{2}{3p\phi_f} \left(B \frac{d\omega}{dt} + k_1 J \frac{de_\omega}{dt} \right) - \frac{di_q}{dt} \\ &= \frac{2(B - k_1 J)}{3p\phi_f J} \left(\frac{3p\phi_f J}{2} i_q - B\omega - T_L \right) + \frac{Ri_q}{L} + p\omega i_d \\ &\quad - \frac{u_q}{L} + \frac{p\phi_f}{L} \omega - \frac{\widetilde{d}_1}{L} - \frac{\widehat{d}_1}{L}, \end{aligned} \quad (18)$$

where $\widetilde{d}_1 + \widehat{d}_1 = d_1$.

Choose the second Lyapunov function to stabilize q axis current tracking error dynamics as

$$V_2(t) = V_1(t) + \frac{1}{2} e_q^2. \quad (19)$$

By some mathematical manipulation, the time derivative of $V_2(t)$ is given by

$$\begin{aligned} \dot{V}_2(t) &= \dot{V}_1(t) + e_q \dot{e}_q \leq -k_1 e_\omega^2 \\ &\quad + e_q \left[\frac{2(B - k_1 J)}{3p\phi_f J} \left(\frac{3p\phi_f J}{2} i_q - B\omega - T_L \right) + \frac{Ri_q}{L} \right. \\ &\quad \left. + p\omega i_d - \frac{u_q}{L} + \frac{p\phi_f}{L} \omega - \frac{\widehat{d}_1}{L} \right] - \frac{\widetilde{d}_1}{L} e_q - \beta \|\widetilde{d}(t)\|^2. \end{aligned} \quad (20)$$

Setting

$$\begin{aligned} \frac{2(B - k_1 J)}{3p\phi_f J} \left(\frac{3p\phi_f J}{2} i_q - B\omega - T_L \right) + \frac{Ri_q}{L} + p\omega i_d \\ - \frac{u_q}{L} + \frac{p\phi_f}{L} \omega - \frac{\widehat{d}_1}{L} = -k_2 e_q, \end{aligned} \quad (21)$$

where $k_2 > 0$ and using the generic inequality $\pm ab \leq \varepsilon_1 a^2 + (1/4\varepsilon_1)b^2$ ($\varepsilon_1 > 0$), it yields

$$\begin{aligned} \dot{V}_2(t) &\leq -k_1 e_\omega^2 - k_2 e_q^2 - \frac{\widetilde{d}_1}{L} e_q - \beta \|\widetilde{d}(t)\|^2 \\ &\leq -k_1 e_\omega^2 - k_2 e_q^2 + \frac{1}{L} \left(\varepsilon_1 e_q^2 + \frac{1}{4L\varepsilon_1} \|\widetilde{d}_1(t)\|^2 \right) \\ &\quad - \beta \|\widetilde{d}(t)\|^2 = -k_1 e_\omega^2 - C_1 e_q^2 - C_2 \|\widetilde{d}(t)\|^2, \end{aligned} \quad (22)$$

where

$$\begin{aligned} C_1 &= k_2 - \frac{\varepsilon_1}{L}, \\ C_2 &= \beta - \frac{1}{4L\varepsilon_1}. \end{aligned} \quad (23)$$

If parameters k_2 and ε_1 are properly selected such that $C_1 > 0$ and $C_2 > 0$, then $\dot{V}_2(t) < 0$, which indicates the tracking error for q -axis stator current will converge asymptotically to zero.

On the other hand, from (21), the stabilizing control law u_q can be designed to stabilize q axis current tracking error dynamics as follows:

$$\begin{aligned} u_q^* &= L \left[\left(\frac{B}{J} + \frac{R}{L} \right) i_q - \frac{2B^2}{3p\phi_f J} \omega + \frac{p\phi_f}{L} \omega - \frac{2BT_L}{3p\phi_f J} \right. \\ &\quad \left. + p\omega i_d - \frac{2k_1^2 J}{3p\phi_f} e_\omega + k_2 e_q - \frac{\widehat{d}_1}{L} \right]. \end{aligned} \quad (24)$$

Step 3. As to design of command input for u_d , define the tracking error

$$e_d = i_d^* - i_d \quad (25)$$

with $\widehat{i}_d^* = 0$ being the desired stator current of d axis. The time derivative of e_d is

$$\dot{e}_d = \frac{di_d^*}{dt} - \frac{di_d}{dt} = \frac{R}{L} i_d - p\omega i_d - \frac{1}{L} u_d - \frac{\widetilde{d}_2}{L} - \frac{\widehat{d}_2}{L}, \quad (26)$$

where $\widetilde{d}_2 + \widehat{d}_2 = d_2$.

Choose the last Lyapunov function candidate as

$$V_3(t) = V_2(t) + \frac{1}{2} e_d^2, \quad (27)$$

which results in

$$\begin{aligned} \dot{V}_3(t) &= \dot{V}_2(t) + e_d \dot{e}_d \\ &\leq -k_1 e_\omega^2 - C_1 e_q^2 - C_2 \|\widetilde{d}(t)\|^2 \\ &\quad + e_d \left(\frac{R}{L} i_d - p\omega i_d - \frac{1}{L} u_d - \frac{\widehat{d}_2}{L} \right) - \frac{\widetilde{d}_2}{L} e_d. \end{aligned} \quad (28)$$

If the stabilizing control law for u_d is defined as

$$u_d^* = Ri_d - pL\omega i_q + Lk_3 e_d - \frac{\widehat{d}_2}{L}, \quad k_3 > 0, \quad (29)$$

then the following result is obtained:

$$\dot{V}_3(t) \leq -k_1 e_\omega^2 - C_1 e_q^2 - C_2 \|\widetilde{d}(t)\|^2 - k_3 e_d^2 - \frac{\widetilde{d}_2}{L} e_d. \quad (30)$$

Again, based on the generic inequality, inequality (30) can be rewritten as follows:

$$\begin{aligned} \dot{V}_3(t) &\leq -k_1 e_\omega^2 - C_1 e_q^2 - C_2 \|\widetilde{d}(t)\|^2 - k_3 e_d^2 + \frac{\varepsilon_2}{L} e_d^2 \\ &\quad + \frac{1}{4L\varepsilon_2} \|\widetilde{d}_2(t)\|^2 \\ &= -k_1 e_\omega^2 - C_1 e_q^2 - \left(k_3 - \frac{\varepsilon_2}{L} \right) e_d^2 \\ &\quad - \left(C_2 - \frac{1}{4L\varepsilon_2} \right) \|\widetilde{d}(t)\|^2. \end{aligned} \quad (31)$$

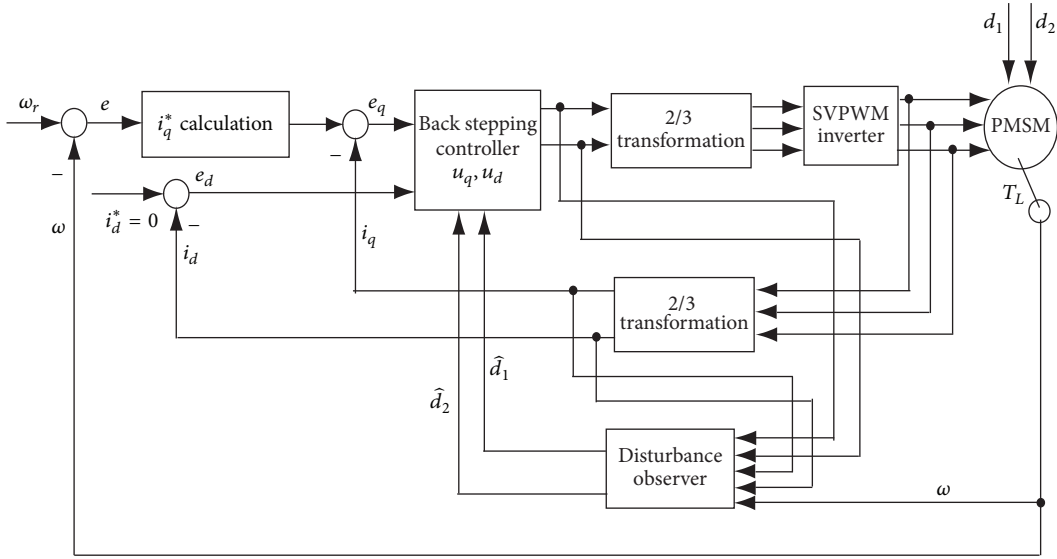


FIGURE 1: Block diagram of the proposed DOB backstepping PMSM control system.

If parameters k_1, k_2, k_3 and $\varepsilon_1, \varepsilon_2$ are properly chosen to make the following conditions hold:

$$\begin{aligned}
 k_1 &> 0, \\
 \left(k_2 - \frac{\varepsilon_1}{L}\right) &= C_1 > 0, \\
 \left(\beta - \frac{1}{4L\varepsilon_1}\right) &= C_2 > 0, \\
 \left(k_3 - \frac{\varepsilon_2}{L}\right) &> 0, \\
 \left(C_2 - \frac{1}{4L\varepsilon_2}\right) &> 0,
 \end{aligned} \tag{32}$$

then $\dot{V}_3(t) < 0$. Consequently, the tracking error for d -axis stator current will tend to zero eventually. The objective of tracking control of PMSM is completed.

5. Numerical Simulation and Experimental Results

In this section, the numerical example and experimental results are presented to demonstrate the validity of the proposed method.

(1) *Numerical Simulation Results.* The motor parameters used are listed in Table 1. The MATLAB/Simulink model of the proposed DOB backstepping PMSM control system is shown in Figure 1. The initial rotation speed of the motor is 1200 r/min, and the rotation speed is 1000 r/min at 0.6s. The initial load torque of the motor is 0N·m and the load disturbance torque is 10N·m at 0.8s. The parameters of the DOB-backstepping controller are selected as $\Lambda = -180I_2$, $\varepsilon_1 = \varepsilon_2 = 0.153$, $k_1 = 250$, $k_2 = 500$, $k_3 = 160$.

In this simulation, to illustrate the effectiveness of the proposed method, the phase traces by the conventional

TABLE 1: The parameters of PMSM.

Parameter	numerical value
Pole Pairs p	3
Friction factor B ($N \cdot m \cdot s/rad$)	0.001
Stator Inductance L (H)	0.0153
Rotor moment of inertia J ($kg \cdot m^2$)	0.0021
Permanent magnet flux ϕ_f (wb)	0.82
Stator Resistance R (Ω)	0.56

backstepping (BS) method [22] and the proposed DOB backstepping (DOB-BS) method are simulated and compared. The numerical simulation results are shown in Figures 2–4. Figure 2(a) indicates the actual rotation speed of the motor with BS method and the proposed DOB-BS method in the presence of the above disturbances load, respectively. Figure 2(b) shows the rotation speed response between [0.008s, 0.012s], during which the PMSM motor just started. Figure 2(c) shows the rotation speed response between [0.585s, 0.625s]. In this time period, the reference rotation speed has a sudden change at $t = 0.6s$. Figure 2(d) shows rotation speed response between [0.785s, 0.825s], in which the external disturbance load is added at $t = 0.8s$. From Figure 2, it can be seen that the rotation speed of the proposed DOB-BS method can rapidly track the reference rotation speed with smaller stability error, faster response, and smaller overshoot than that of the conventional BS method.

Figure 3 shows the three-phase current of the stator. The current amplitude is proportional to the rotation torque and changes rapidly as the load torque varies. The current frequency is inversely proportional to the rotation speed. Figure 4 shows the variation of electromagnetic torque as the load torque changes. Obviously, the DOB-BS method gives less load torque fluctuations.

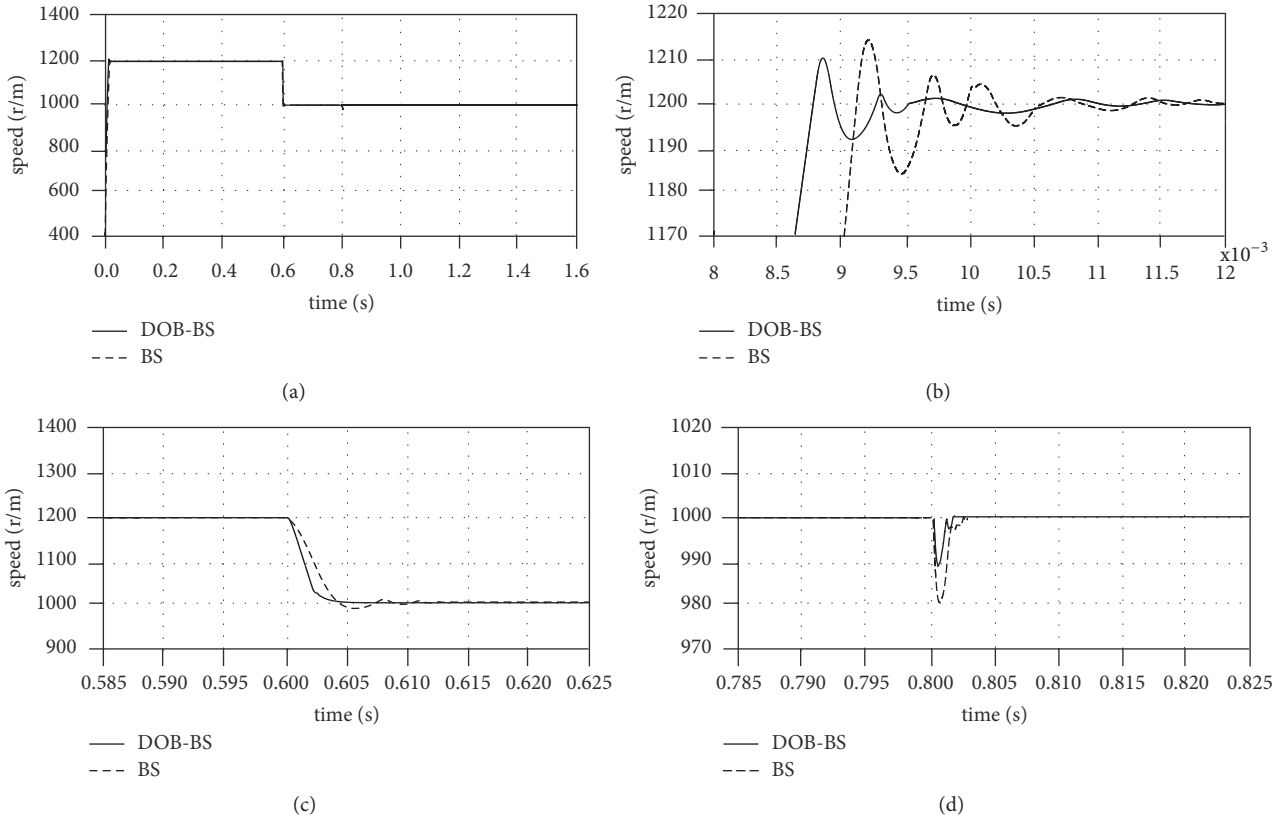


FIGURE 2: Rotation speed responses.

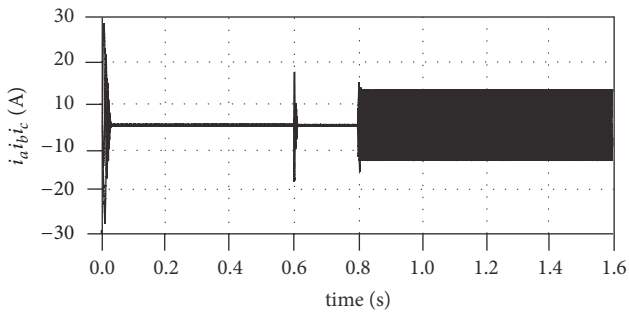


FIGURE 3: Three-phase stator current.

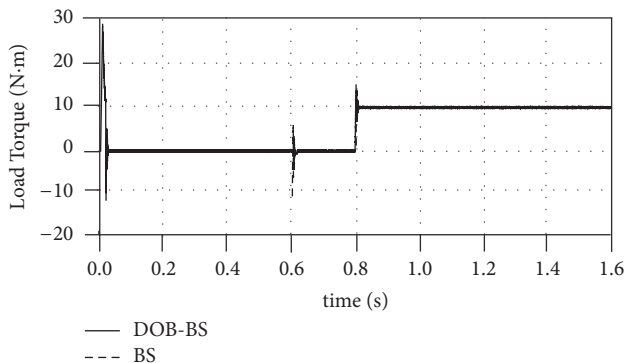


FIGURE 4: Load torque responses.

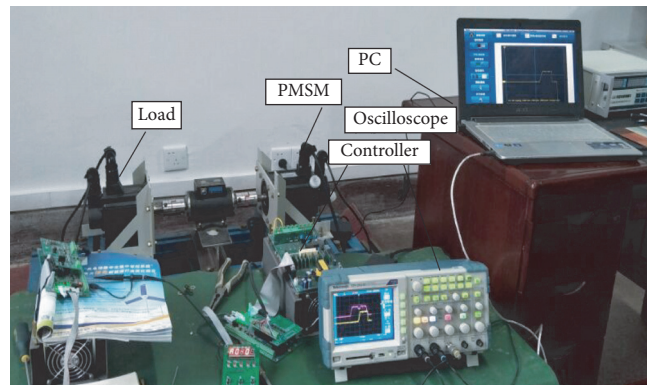


FIGURE 5: Load torque responses.

(2) *Experimental Results.* To evaluate the performance of the proposed method, a three-phase PMSM control system is set up. The experimental platform configuration is shown in Figure 5. The main chip of the inverter adopts the TMS320F28335 digital signal processor (DSP). The initial rotation speed of the motor is 1600 r/min, and the rotation speed is 600 r/min at 0.6s. The initial load torque of the motor is 0N·m and the load disturbance torque is 5N·m at 0.8s.

The results of the experiment are shown in Figures 6–8. Figure 6(a) shows the speed response of the closed-loop system under the BS and DOB-BS schemes. It can be seen

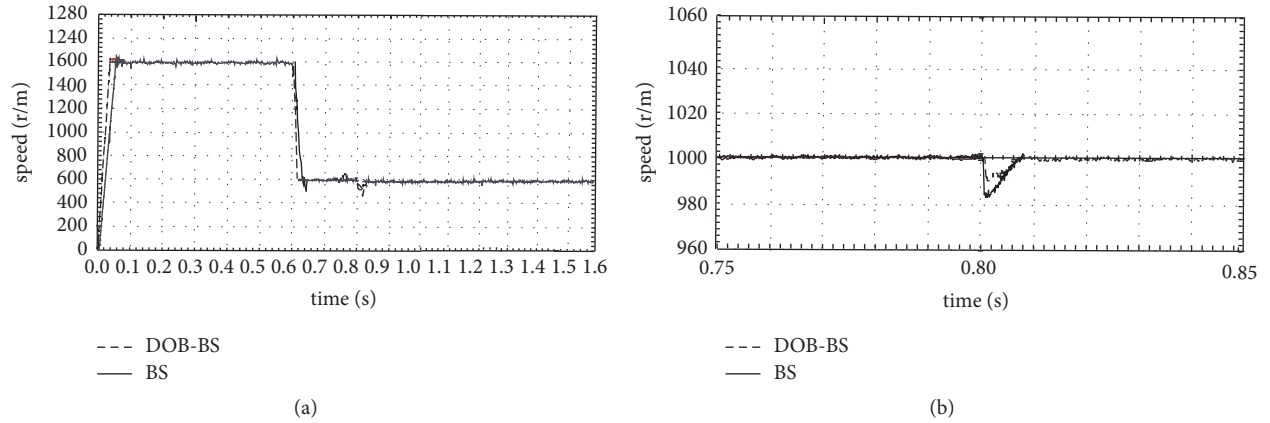


FIGURE 6: Rotation speed responses.

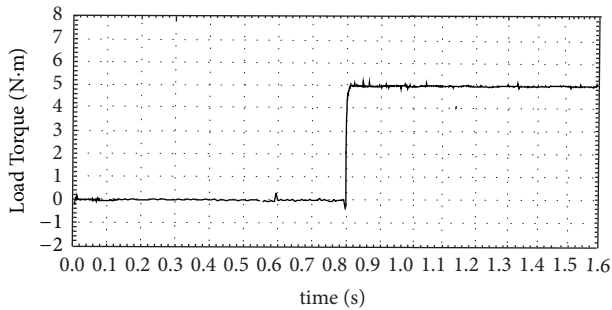


FIGURE 7: Load torque response.

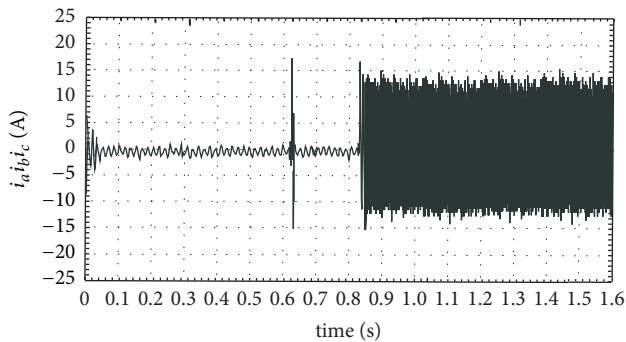


FIGURE 8: Three-phase stator current.

that the settling time of the DOB-BS method is shorter than that of the BS method. The experimental results of antiload disturbance of the two control schemes are shown in Figure 6(b). After the speed output of PMSM system (without load) is in the steady state, a step disturbance load, i.e., a rated torque of 10N.m at 0.8s, is added suddenly. Clearly, the DOB-BS method has a less speed drop, i.e., a better disturbance rejection capacity when the disturbance load is added.

The load torque and current responses of DOB-BS method is shown in Figures 7 and 8, which illustrates the quick response and low ripple.

From these results, it can be observed that the proposed DOB-BS method is effective under different operating

conditions and has a better performance at most conditions than that of BS method.

6. Conclusion

In this paper, a disturbance observer-based (DOB) backstepping speed tracking control method has been presented for the speed tracking control PMSM. Through disturbance estimation, the DOB backstepping control strategy can achieve high precision speed tracking and disturbance rejection performance. Both simulation and experimental results have shown the effectiveness of the proposed method.

Data Availability

The data used to support the findings of this study are available from the corresponding author upon request.

Conflicts of Interest

The authors declare that there are no conflicts of interest regarding the publication of this paper. There have no financial and personal relationships with other people or organizations that will influence our work, there is no professional or other personal interest of any nature or kind in any product, service, and/or company that could be construed as influencing the position presented in or the review of the manuscript.

Acknowledgments

This work was supported in part by the National Natural Science Foundation of China (61573298), Scientific Research Fund of Hunan Provincial Education Department (15B238), and the Key Laboratory of Intelligent Computing and Information Processing of Ministry of Education.

References

- [1] S. Bolognani, R. Oboe, and M. Zigliotto, "Sensorless full-digital pmsm drive with ekf estimation of speed and rotor position,"

- IEEE Transactions on Industrial Electronics*, vol. 46, no. 1, pp. 184–191, 1999.
- [2] Z. Chen, M. Tomita, S. Doki, and S. Okuma, “New adaptive sliding observers for position-and velocity-sensorless controls of brushless dc motors,” *IEEE Transactions on Industrial Electronics*, vol. 47, no. 3, pp. 582–591, 2000.
- [3] Y. Yi, D. M. Vilathgamuwa, and M. A. Rahman, “Implementation of an artificial-neural-network-based real-time adaptive controller for an interior permanent-magnet motor drive,” *IEEE Transactions on Industry Applications*, vol. 39, no. 1, pp. 96–104, 2003.
- [4] G. Lei, T. Wang, J. Zhu, Y. Guo, and S. Wang, “System-level design optimization method for electrical drive systems—robust approach,” *IEEE Transactions on Industrial Electronics*, vol. 62, no. 8, pp. 4702–4713, 2015.
- [5] M.-S. Wang, I. N. Syamsiana, and F.-C. Lin, “Sensorless speed control of permanent magnet synchronous motors by neural network algorithm,” *Mathematical Problems in Engineering*, vol. 2014, pp. 1–7, 2014.
- [6] X. Wu, H. Wang, X. Yuan, S. Huang, and D. Luo, “Design and implementation of recursive model predictive control for permanent magnet synchronous motor drives,” *Mathematical Problems in Engineering*, vol. 2015, pp. 1–10, 2015.
- [7] H. Wang, R. Zhao, F. Cheng, and H. Yang, “Active disturbance rejection control for PMSM servo system applied in industrial sewing machines,” in *Proceedings of the International Conference on Electrical and Control Engineering, ICECE 2010*, pp. 3249–3252, China, May 2010.
- [8] B. Zhang, Y. Pi, and Y. Luo, “Fractional order sliding-mode control based on parameters auto-tuning for velocity control of permanent magnet synchronous motor,” *Isa Transactions*, vol. 51, no. 5, pp. 649–656, 2012.
- [9] J. Huang, H. Li, Y. Chen, and Q. Xu, “Robust position control of PMSM using fractional-order sliding mode controller,” *Abstract and Applied Analysis*, vol. 2012, no. 4, pp. 473–505, 2014.
- [10] J. Yang, S. Li, and X. Yu, “Sliding-mode control for systems with mismatched uncertainties via a disturbance observer,” *IEEE Transactions on Industrial Electronics*, vol. 60, no. 1, pp. 160–169, 2013.
- [11] D. Ginoya, P. D. Shendge, and S. B. Phadke, “Sliding mode control for mismatched uncertain systems using an extended disturbance observer,” *IEEE Transactions on Industrial Electronics*, vol. 61, no. 4, pp. 1983–1992, 2014.
- [12] X. G. Zhang, L. Z. Sun, K. Zhao, and L. Sun, “Nonlinear speed control for PMSM system using sliding-mode control and disturbance compensation techniques,” *IEEE Transactions on Power Electronics*, vol. 28, no. 3, pp. 1358–1365, 2013.
- [13] W. Xu, Y. J. Jiang, and C. X. Mu, “Novel composite sliding mode control for PMSM system based on disturbance observer,” *IEEE Transactions on Applied Superconductivity*, vol. 26, no. 7, pp. 12905–12910, 2016.
- [14] W.-H. Chen, “Disturbance observer based control for nonlinear systems,” *IEEE/ASME Transactions on Mechatronics*, vol. 9, no. 4, pp. 706–710, 2004.
- [15] A. A. Apte, V. A. Joshi, R. A. Walambe, and A. A. Godbole, “Speed control of PMSM using disturbance observer,” *IFAC-Papers OnLine*, vol. 49, no. 1, pp. 308–313, 2016.
- [16] L. Xiaoquan, L. Heyun, and H. Junlin, “Load disturbance observer-based control method for sensorless PMSM drive,” *IET Electric Power Applications*, vol. 10, no. 8, pp. 735–743, 2016.
- [17] J. Zhang, X. Liu, Y. Xia, Z. Zuo, and Y. Wang, “Disturbance observer-based integral sliding-mode control for systems with mismatched disturbances,” *IEEE Transactions on Industrial Electronics*, vol. 63, no. 11, pp. 7040–7048, 2016.
- [18] P. V. Kokotovic, “The joy of feedback: nonlinear and adaptive,” *IEEE Control Systems Magazine*, vol. 12, no. 3, pp. 7–17, 1992.
- [19] J. Zhou and Y. Wang, “Real-time nonlinear adaptive backstepping speed control for a PMSM,” *Control Engineering Practice*, vol. 13, no. 4, pp. 1259–1269, 2005.
- [20] M. Karabacak and H. I. Eskikurt, “Speed and current regulation of a permanent magnet synchronous motor via nonlinear and adaptive backstepping control,” *Mathematical and Computer Modelling*, vol. 53, no. 9-10, pp. 2015–2030, 2011.
- [21] M. Karabacak and H. I. Eskikurt, “Design, modelling and simulation of a new nonlinear and full adaptive backstepping speed tracking controller for uncertain PMSM,” *Applied Mathematical Modelling: Simulation and Computation for Engineering and Environmental Systems*, vol. 36, no. 11, pp. 5199–5213, 2012.
- [22] C.-X. Chen, Y.-X. Xie, and Y.-H. Lan, “Backstepping control of speed sensorless permanent magnet synchronous motor based on slide model observer,” *International Journal of Automation and Computing*, vol. 12, no. 2, pp. 149–155, 2015.
- [23] Y. Chen, X. Wang, M. Li, and X. Liu, “Disturbance observer-based backstepping control for permanent magnet synchronous motor,” in *Proceedings of the 2017 Chinese Automation Congress (CAC)*, pp. 1–5, Jinan, China, October 2017.

Research Article

Performance Analysis and Comparison for High Maneuver Target Track Based on Different Jerk Models

Qinghai Meng,¹ Bowen Hou,² Dong Li,¹ Zhangming He,^{1,3} and Jiongqi Wang ²

¹PLA 91550, Dalian 116024, China

²College of Liberal Arts and Science, National University of Defense Technology, Changsha 410073, China

³Beijing Institute of Spacecraft System Engineering, China Academy of Space Technology, Beijing 100086, China

Correspondence should be addressed to Jiongqi Wang; wjq_gfkd@163.com

Received 29 March 2018; Accepted 14 May 2018; Published 11 June 2018

Academic Editor: Darong Huang

Copyright © 2018 Qinghai Meng et al. This is an open access article distributed under the Creative Commons Attribution License, which permits unrestricted use, distribution, and reproduction in any medium, provided the original work is properly cited.

The Jerk model is widely used for the track of the maneuvering targets. Different Jerk model has its own state expression and is suitable to different track situation. In this paper, four Jerk models commonly used in the maneuvering target track are advanced. The performances of different Jerk models for target track with the state variables and the characters are compared. The corresponding limit conditions in the practical applications are also analyzed. Besides, the filter track is designed with UKF algorithm based on the four different models for the high-maneuvering target. The simplified dynamic model is used to gain the standard trajectory with Runge-Kutta numerical integration method. The mathematical simulations show that Jerk model with self-adaptive noise variance has the best robustness while other models may diverge when the initial error is much larger. If the process noise level is much lower, the track accuracy for four Jerk models is similar and stationary in the steady track situation, but it will be descended greatly in the much highly maneuvering situation.

1. Introduction

Target tracking refers to estimating the motion parameters, such as the position and the velocity for a target through the noise-containing measurement data acquired by the measurement device in real time. Because of the uncertainty of the maneuvering target motion, the measurement process uncertainty, and the difficulty of estimating the nonlinear system, the maneuvering target tracking has always been a research focus for more than half a century and there are a lot of proposed algorithms. To sum up, the track algorithms study has been focused on two parts, *i.e.*, maneuver target modeling and nonlinear filter design [1, 2].

For the nonlinear filter design, there are three main methods, including Extended Kalman filter (EKF), Unscented Kalman filter (UKF), and Particle filter (PF) [3, 4]. Many articles have sufficiently studied the three algorithms in the nonlinear fitness, filter accuracy, filter stability, computational complexity, and other aspects [5, 6]. The conclusion is that

UKF has the best performance in much practical applications [7].

For the maneuver target modeling, there are lots of motion model describing the maneuver process of the target. The accuracy of the target modeling directly affects the tracking performance of maneuvering target, detection of the target [8, 9], and the fault diagnosis of the target [10, 11]. According to their modeling state dimensions, they can be divided into second-order model, three-order model and four-order model. Two-order models contain CV (Constant Velocity) model and CT (Constant Turn) model; three-order models contain CA (Constant Acceleration) model, Singer model, CS (Current Statistic) model, semi-Markov model, and so on [12, 13]. Four-order models contain Jerk (Jerk denotes the rate of the acceleration change) model and its corresponding improved version. The higher the order of maneuvering model is, the higher the order of the target is described. Jerk model extends the target maneuvering form via estimating the acceleration changing rate in real time.

Theoretically, it can be applied on the highly maneuvering target tracking much better [14, 15].

Therefore, in this paper, we mainly focused on the maneuvering target track with Jerk model and UKF filter algorithm.

The references related to Jerk model has shown the good simulation results. However, due to the simple and the special simulation background, the trajectory is different from the true target. Therefore, the results cannot be convincing. This paper summarizes the various Jerk models in the references. Firstly, the advantages and disadvantages are analyzed in theory. Then every model is applied on the near-space high-speed maneuvering target, and the simulation results are compared. The track trajectory is generated through the integral of the simplified dynamic equation, which is close to the true target. Therefore, it is convictive to some extent.

2. Description for Different Jerk Model

Jerk denotes the acceleration changing rate. Jerk model is a model which describes the target Jerk mathematically. The models in the references mainly contain the following different kinds.

2.1. SJ Model. The earliest Jerk model is proposed by Mehrota, etc. [16]. They used Singer model for reference and modeled the Jerk model of the target as a zero-mean and first-order time related process. To distinguish other Jerk models, it is marked as SJ (Singer Jerk) model. Taking a one-dimension linear motion as an example, SJ model is expressed as

$$\dot{j}(t) = -\alpha j(t) + w(t) \quad (1)$$

where $j(t) = \ddot{x}(t)$ denotes the target Jerk, the α denotes "Jerk" frequency (the reciprocal of the "Jerk" constant), $w(t)$ denotes zero-mean Gaussian white noise, and the covariance is $\sigma_w^2 = 2\alpha\sigma_j^2$, σ_j^2 denotes the covariance of target Jerk.

2.2. CSJ Model. Qiao [15] used the analyzing method which is also applied on Singer model tracking accuracy in [17] to analyze the SJ model. He proposed that SJ model shows a steady-state deterministic error in the tracking step Jerk signals. Therefore, the Jerk model with nonzero mean and first-order time correlation is built using CS model for reference. According to the same analyzing process, the new model has eliminated the steady-state deterministic error. The model is marked as CSJ (Current Statistic Jerk) model. Taking the one-dimension model as an example, CSJ model is expressed as

$$\begin{aligned} \ddot{x}(t) &= \bar{j}_{CSJ}(t) + j_{CSJ}(t) \\ \dot{j}_{CSJ}(t) &= -\alpha j_{CSJ}(t) + w(t) \end{aligned} \quad (2)$$

where $\bar{j}_{CSJ}(t)$ denotes the nonzero mean of Jerk. $j_{CSJ}(t)$ denotes the covariance of the zero-mean colored Jerk noise, and $w(t)$ denotes zero-mean Gaussian white noise. Other parameters are defined as SJ model.

The model should set α and σ_j^2 previously before the practical application. Therefore, Pan proposed a novel CSJ algorithm to describe the probability density of Jerk according to truncated normal distribution and construct the connection between σ_j^2 and current Jerk estimation. It is

$$\sigma_j^2(k) = \frac{[J_{\max} - |\hat{x}(k|k)|]^2}{9} \quad (3)$$

In this way, the probable extreme Jerk can be predefined as J_{\max} . That is the covariance of the state noise can be self-adapted according to the Jerk estimation during the filter process to adapt to different maneuvering situations. The model is marked as MCSJ (Modified CSJ) model.

2.3. αJ Model. The Jerk models above cannot avoid the problem that the Jerk frequency α should be predefined. However, α cannot be directly measured and it is constantly changing in the target practical motion process. For this reason, Luo [7] considered α in SJ model as an estimated parameter and took it as the extension variable. Therefore, it can be estimated in real time during the filter process. α is modeled as nonzero-mean Gaussian white noise and the derivative of it is zero mean Gaussian white noise which can be considered as

$$\dot{\alpha} = \varepsilon(t) \quad (4)$$

where $\varepsilon(t)$ denotes the zero-mean input noise, whose variance is σ_ε^2 . This is called αJ (Alpha Jerk) model. αJ model can estimate α in real time, but σ_j^2 and σ_ε^2 need to be predefined carefully. If the values of them are not proper, the estimation accuracy of α will be decreased severely and even cause the divergence of the filter.

Take the one-dimension motion as an example. (Three-dimension situation has the same principle as the one-dimension motion.) The state variable, state equation, and the characteristic of the four models are shown in Table 1. The specific form of the matrices in Table 1 can be found in the related references [14, 16].

3. Performance Comparison

3.1. Trajectory State Equation. Tracking target is the near-space and high-speed target whose true trajectory comes from the integral of the dynamic equation. To simplify the dynamic equation of the target, the earth is assumed as an irrational ball and the influence on the center of mass motion of the target of the controlling force is neglected. The target has nonliteral movement and the simple dynamic equation in the launching frame is expressed as

$$\begin{bmatrix} \dot{v}_x \\ \dot{v}_y \end{bmatrix} = \frac{\rho VS}{2m} \begin{bmatrix} -C_x v_x - C_y v_y \\ C_y v_x - C_x v_y \end{bmatrix} + \frac{g_0 R_0^2}{r^3} \begin{bmatrix} x - R_{0x} \\ y - R_{0y} \end{bmatrix} \quad (5)$$

where ρ denotes the atmosphere density which is used as American 1976 standard atmosphere model. V denotes the resultant velocity; S denotes the aerodynamic reference area

TABLE 1: Description for four different Jerk models.

Model	State Variable	Continuous State Equation	Discrete State Equation	Characteristic
SJ	$[x, \dot{x}, \ddot{x}, \ddot{x}]^T$	$\dot{\mathbf{X}}(t) = \mathbf{F}_S \mathbf{X}(t) + \mathbf{B}w(t)$	$\mathbf{X}_{k+1} = \Phi_S \mathbf{X}_k + \mathbf{W}_k$ $\mathbf{Q}_k = 2\alpha\sigma_j^2 \mathbf{Q}_0$	Tracking step Jerk signal shows deterministic error. α and σ_j^2 need to be predefined. Parameters are constant.
CSJ	$[x, \dot{x}, \ddot{x}, \ddot{x}]^T$	$\dot{\mathbf{X}}(t) = \mathbf{F}_S \mathbf{X}(t) + \mathbf{A} \bar{J}_{CSJ}(t) + \mathbf{B}w(t)$	$\mathbf{X}_{k+1} = \Phi_S \mathbf{X}_k + \mathbf{U}^j_{k+1} + \mathbf{W}_k$ $\bar{J}_{k+1} = \ddot{x}_k$ $\mathbf{Q}_k = 2\alpha\sigma_j^2 \mathbf{Q}_0$	Tracking step Jerk signal does not show steady-state deterministic error. α and σ_j^2 need to be predefined. Parameters are constant.
MCSJ	$[x, \dot{x}, \ddot{x}, \ddot{x}]^T$	Ditto	Ditto, but σ_j^2 is self-adaption	Tracking step Jerk signal does not show steady-state deterministic error. α and J_{\max} need to be predefined. σ_j^2 is self-adaption.
αJ	$[x, \dot{x}, \ddot{x}, \ddot{x}, \alpha]^T$	$\dot{\mathbf{X}}_a(t) = \mathbf{F}_a \mathbf{X}_a(t) + \mathbf{B}_a w_a(t)$ $\mathbf{F}_a = \text{diag}(\mathbf{F}_S, 0)$ $w_a(t) = [w(t), \varepsilon(t)]^T$	$\mathbf{X}_a(k+1) = \Phi_a \mathbf{X}_a(k) + \mathbf{W}_a(k)$ $\Phi_a = \text{diag}(\Phi_S, 1)$ $\mathbf{Q}_k = \text{diag}(2\alpha_k \sigma_j^2 \mathbf{Q}_0, T\sigma_\varepsilon^2)$	Tracking step Jerk signal shows steady-state deterministic error. σ_j^2 and σ_ε^2 need to be predefined. α needs to be estimated in real time.

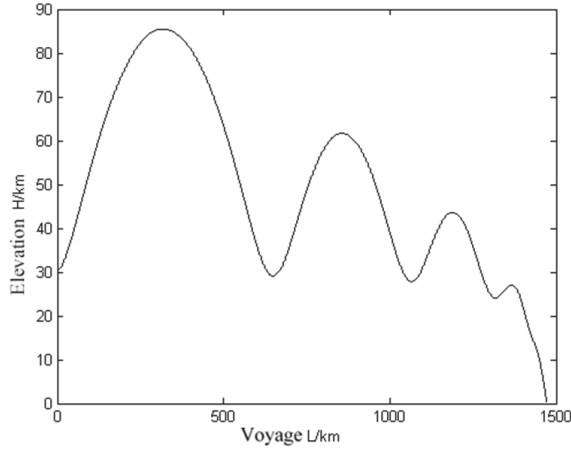


FIGURE 1: Target trajectory.

of the target; m denotes the mass of the target; C_x and C_y denote the resistance coefficient and the lift coefficient, respectively (they are the function of the attack angle the Mach number Ma); g_0 denotes the gravitational acceleration on the sea level; R_0 denotes the radius of the earth; R_{0x} and R_{0y} denote the coordinates of the earth center in the launching frame; r denotes the geocentric distance of the target.

The target parameter S and m and the aerodynamic parameters C_x and C_y use the public values in American high-performance general air vehicle (CAV-H). The longitude, the latitude, the height, and the launching angle are 0° , 0° , $0m$, and 90° . The initial longitude, the latitude, and the height of the target are 0° , 0° , and 30 km , respectively. The initial Mach number is 10. The local velocity angle is -1° , and the velocity drift angle is 0° . The controlled quantity is the attacking angle α and is constant with 15° . The integral method of the trajectory is fourth-order Runge-Kutta numerical integration. The height and the voyage are shown in Figure 1.

3.2. Measurement Setting Condition. The measurement device is a pulse radar and the measurement elements are the distance R , the azimuth angle A , the pitch angle E , and the radial velocity V . The measure error standard deviations of the distance, the angle, and the velocity are 10m, 0.5mrad, and 1m/s, respectively. The longitude, the latitude, and the height of the radar station are 14°E , 1°N , and $0m$, respectively. The sampling period is 0.05s and the tracking period is 70~790s. To compare the tracking performance of the models (including the tracking accuracy, the filter robustness, and the computation complexity), the simulation results cannot be compared as the general references setting a parameter. Mehrotra proposed that ‘‘Jerk’’ frequency α has a good robustness in [7] via the simulation. That is, the filter performance can maintain stable when α changes in a large range. Therefore, the paper focuses on the standard deviation of Jerk and the robustness of the filter initial value error. The initial position and velocity in filter are equal to the true value adding the random error. The standard deviations of

TABLE 2: Filter parameters.

Parameters	P1	P2	P3
α		0.1	
α_0		α	
σ_j	1	1	0.1
J_{\max}		$3\sigma_j$	
σ_{p0}	1000	100	100
σ_{v0}	100	10	10
σ_ε		0.1	

the position and the velocity are σ_{p0} and σ_{v0} , respectively. The acceleration and the Jerk are 0. α J model needs to set the initial value of α and the standard deviation σ_ε of the input noise $\varepsilon(t)$. MCSJ model needs to set the extreme Jerk value J_{\max} . The parameter sets of the three filters are expressed as P1, P2, and P3, respectively. The specific parameter values are shown in Table 2. The Monte Carlo simulation number is 100.

3.3. Simulation Results. The filter root mean square error (RMSE) of the position and the velocity under the parameter sets is shown in Figures 2, 3, and 4, respectively. Because of the different values of P1 and P2, the initial value robustness of the four models can be compared. Comparing Figures 2 and 3, when the filter initial value is large, only the self-adaption state noise of MCSJ model can maintain the convergence and the initial value robustness is much better. But the other three models will present filter divergence performance during the 100 Monte Carlo steps and the convergence is influenced by the initial value which is not proper for the practical tracking application. On the other hand, because the only difference between P2 and P3 is σ_j . The parameter robustness of the four models can be compared. When comparing Figures 3 and 4, when σ_j is small, the tracking accuracy of the four models in the steady period of the target motion can be improved. However, the filter error has a large jump when the target has a severe maneuvering motion. The computation complexity ratio of SJ, CSJ, MCSJ, and α J is 8:8:9:12.

4. Conclusion

The paper summarizes the proposed Jerk models which are applied on the high-maneuvering target tracking. The tracking accuracy, the filter robustness, and the computation complexity of the models are compared in the theoretical analysis and the tracking simulation. The tracking simulation trajectory is created by the integral of the dynamic equation which is similar to the true process and is pretty persuasive. The simulation results demonstrate that the self-adaptive noise variance method has the best tracking performance. However, in the highly maneuvering period, all models have the error jumping problem. Controlling the filter jumping error is the key to improve the near-space and high-speed target tracking performance in the future.

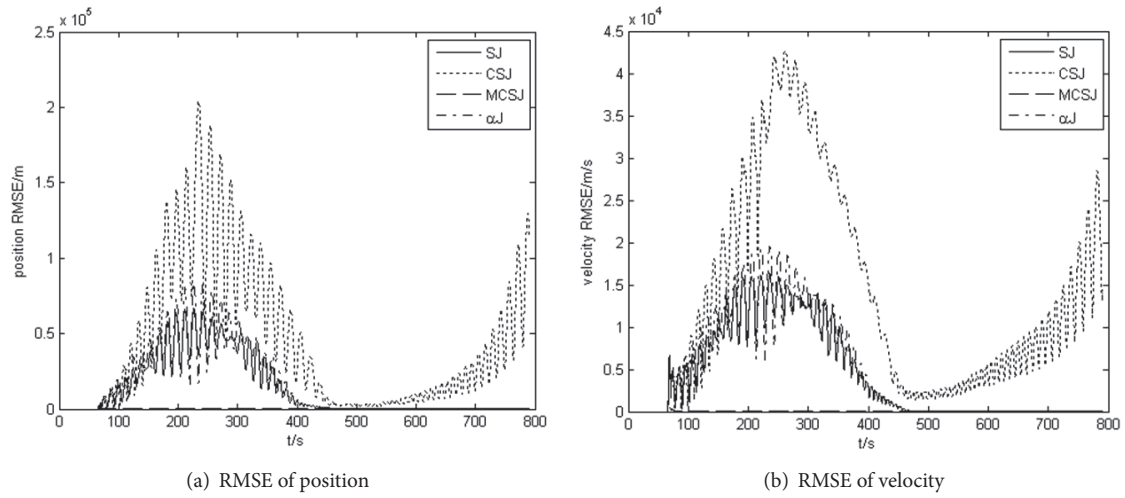


FIGURE 2: Filtering RMSE for four models in P1 parameter.

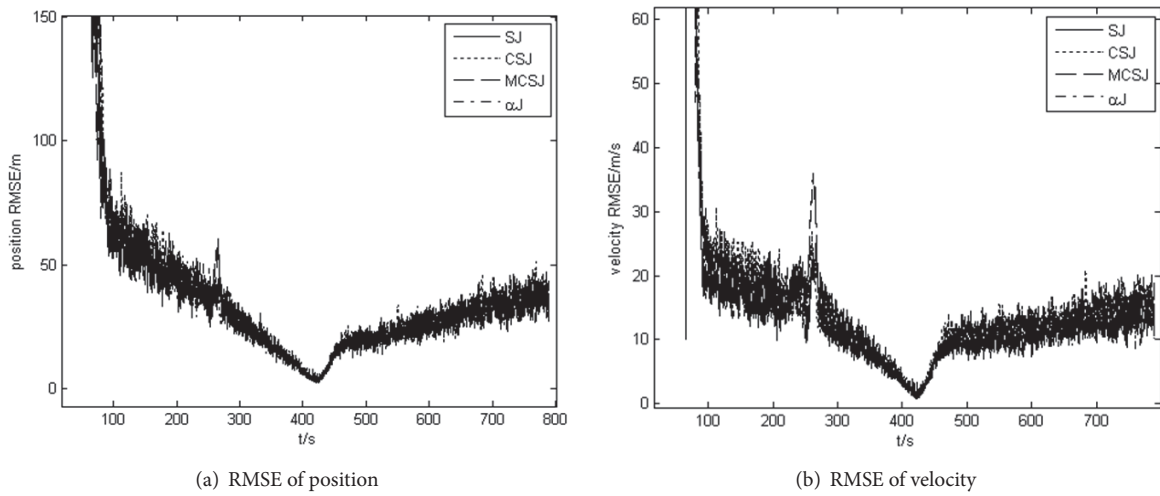


FIGURE 3: Filtering RMSE for four models in P2 parameter.

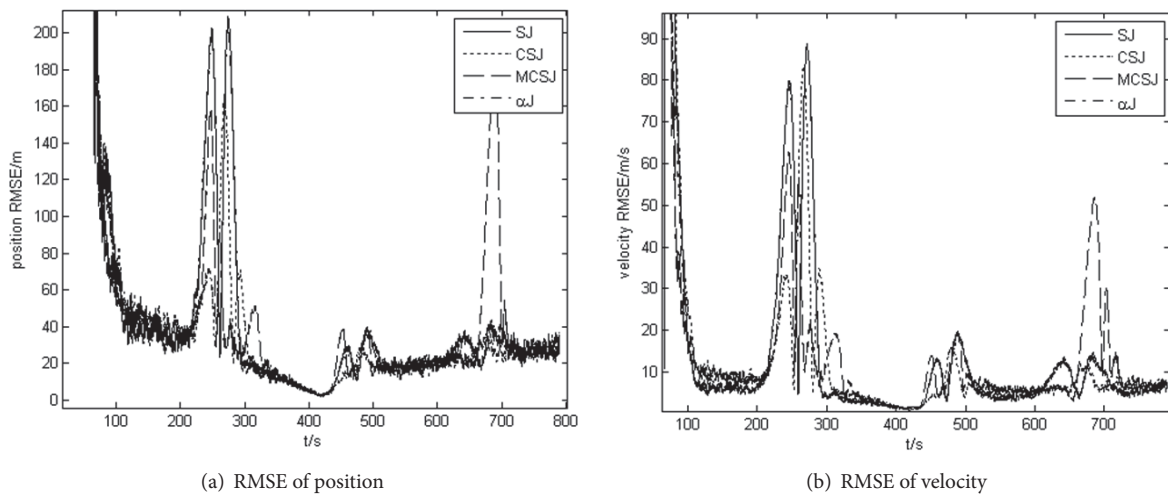


FIGURE 4: Filtering RMSE for four models in P3 parameter.

Data Availability

The data used to support the findings of this study are available from the corresponding author upon request.

Conflicts of Interest

The authors declare that they have no conflicts of interest.

Acknowledgments

This work was supported in part by National Natural Science Foundation of China (NSFC) under Grants no. 61773021 and no. 61703408 and National Defense Technology Foundation of China under Grant no. 3101065.

References

- [1] Y. Bar-Shalom and K. Birmiwal, "Variable dimension filter for maneuvering target tracking," *IEEE Transactions on Aerospace and Electronic Systems*, vol. 18, no. 5, pp. 621–629, 1982.
- [2] X. R. Li and V. P. Jilkov, "Survey of maneuvering target tracking—part I: dynamic models," *IEEE Transactions on Aerospace and Electronic Systems*, vol. 39, no. 4, pp. 1333–1364, 2003.
- [3] M. S. Arulampalam, S. Maskell, N. Gordon, and T. Clapp, "A tutorial on particle filters for online nonlinear/non-Gaussian Bayesian tracking," *IEEE Transactions on Signal Processing*, vol. 50, no. 2, pp. 174–188, 2002.
- [4] N. J. Gordon, D. J. Salmond, and A. F. M. Smith, "Novel approach to nonlinear/non-gaussian Bayesian state estimation," *IEE proceedings F*, vol. 140, no. 2, pp. 107–113, 1993.
- [5] D. Zhao, S. X. Ding, Y. Wang, and Y. Li, "Krein-space based robust H_∞ mathContainer Loading Mathjax fault estimation for two-dimensional uncertain linear discrete time-varying systems," *Systems & Control Letters*, vol. 115, pp. 41–47, 2018.
- [6] Y. Li, "State estimation for stochastic discrete-time systems with multiplicative noises and unknown inputs over fading channels," *Applied Mathematics Computation*, vol. 320, pp. 116–130, 2018.
- [7] S. J. Julier and J. K. Uhlmann, "Unscented filtering and nonlinear estimation," *Proceedings of the IEEE*, vol. 92, no. 3, pp. 401–422, 2004.
- [8] D. R. Huang, C. S. Chen, G. X. Sun, Z. Ling, and M. I. Bo, "Linear Discriminant Analysis and Back Propagation Neural Network Cooperative Diagnosis Method for Multiple Faults of Complex Equipment Bearings," *Acta Armamentarii*, vol. 38, pp. 1649–1657, 2017.
- [9] D. Huang, C. Chen, G. Sun, and L. Zhao, "Recognition and Diagnosis Method of Objective Entropy Weight for Power Transformer Fault," *Dianli Xitong Zidonghua/Automation of Electric Power Systems*, vol. 41, no. 12, pp. 206–211, 2017.
- [10] Y. Li, H. R. Karimi, Q. Zhang, and D. Zhao, "Fault Detection for Linear Discrete Time-Varying Systems Subject to Random Sensor Delay: A Riccati Equation Approach," *IEEE Transactions on Circuits Systems I Regular Papers*, pp. 1–10, 2017.
- [11] H. Darong, T. Jianping, and Z. Ling, "A fault diagnosis method of power systems based on gray system theory," *Mathematical Problems in Engineering*, vol. 2015, Article ID 971257, 2015.
- [12] Y. Li, H. R. Karimi, C. K. Ahn, Y. Xu, and D. Zhao, "Optimal residual generation for fault detection in linear discrete time-varying systems with uncertain observations," *Journal of The Franklin Institute*, vol. 355, no. 7, pp. 3330–3353, 2018.
- [13] H. Darong, K. Lanyan, C. Xiaoyan, Z. Ling, and M. Bo, "Fault diagnosis for the motor drive system of urban transit based on improved Hidden Markov Model," *Microelectronics Reliability*, vol. 82, pp. 179–189, 2018.
- [14] X. B. Luo, "A α -jerk Model for Tracking Maneuvering Targets," *Signal Processing*, 2007.
- [15] K. Mehrotra and P. R. Mahapatra, "A jerk model for tracking highly maneuvering targets," *IEEE Transactions on Aerospace and Electronic Systems*, vol. 33, no. 4, pp. 1094–1105, 1997.
- [16] C. F. Yang, S. L. Wang, and F. Zhou, "Interacting Multiple Model UKF Algorithm Based on Jerk Model with Adaptive Parameter," *Techniques of Automation & Applications*, 2010.
- [17] X. D. Qiao, B. S. Wang, L. I. Tao, and G. W. Hua, "A CS-Jerk model for tracking highly maneuvering targets," *Journal of Xidian University*, 2002.

Research Article

An Equivalent Circuit Model for Lithium Battery of Electric Vehicle considering Self-Healing Characteristic

Zhaodi Pei ¹, Xiaoxu Zhao,¹ Huimei Yuan,¹ Zhen Peng,² and Lifeng Wu ^{1,3,4}

¹College of Information Engineering, Capital Normal University, Beijing 100048, China

²Information Management Department, Beijing Institute of Petrochemical Technology, Beijing 102617, China

³Beijing Engineering Research Center of High Reliable Embedded System, Capital Normal University, Beijing 100048, China

⁴Beijing Advanced Innovation Center for Imaging Technology, Capital Normal University, Beijing 100048, China

Correspondence should be addressed to Lifeng Wu; wulifeng@cnu.edu.cn

Received 30 March 2018; Accepted 10 May 2018; Published 10 June 2018

Academic Editor: Darong Huang

Copyright © 2018 Zhaodi Pei et al. This is an open access article distributed under the Creative Commons Attribution License, which permits unrestricted use, distribution, and reproduction in any medium, provided the original work is properly cited.

Considering the self-healing phenomenon of lithium batteries during intermittent discharge, a self-healing characteristic-based equivalent circuit model of lithium batteries is proposed. The mathematical description of the lithium battery in the self-healing process is obtained through the analysis of the equivalent circuit model. Based on experimental platform, an experiment considering self-healing characteristic was performed. Result shows that the self-healing characteristic-based lithium battery equivalent circuit model can describe the voltage of the lithium battery accurately during the self-healing process.

1. Introduction

Energy is the foundation of the society progress and development and it is vital to develop a new energy storage that is efficient and environmentally friendly and more necessarily put it to effect [1]. Electric vehicles have received extensive attention due to their features such as cleanliness and high efficiency [2, 3]. The lithium-ion battery is one of the best choices for electric vehicle battery because of its small volume, light weight, and low self-discharge rate [4]. However, power batteries have become an important factor that influences the performance and stability of electric vehicles [5]. Therefore, the research on the safety and reliability of lithium-ion batteries has become the focus of attention [6–8]. Huang et al. [9] proposed a new method to estimate the state of charge (SOC) and state of health (SOH) of a battery by using the amount of voltage change per unit time during the discharge process of battery. Based on the battery cycle-life test data, it is found that the state of health has a linear relationship with the reciprocal of the unit time voltage drop, which is a function of the state of charge. This method realizes the online estimation of SOC and SOH and the model is proved to have robustness. Zou

et al. [10] proposed a combined SOC and SOH estimation method through the lifetime of a lithium-ion battery. Two Extended Kalman Filters of two time scales are used to estimate SOC in real time and update SOH offline, which provides accurate SOC and SOH estimations. Xiong et al. [11] used adaptive extended Kalman filter (AEKF) to estimate the state of charge of lithium batteries. The AEKF algorithm improves the traditional KF and solves the defect of inaccuracy on nonlinear problems. Besides, the AEKF algorithm can improve the prediction accuracy by adaptively updating the process and measurement noise covariance. However, the above researches focus on the ideal working condition and do not take the intermittent discharge of the lithium battery in the actual operation into account. In fact, self-healing phenomenon could be found during the intermittent discharge of lithium batteries [12]. In other words, the capacity of the battery will rebound when standing. There is no doubt that the self-healing phenomenon could be a benefit to prolong the useful life of lithium batteries [6]. Therefore, further research is needed under this condition.

Currently, the models of batteries can be divided into two categories: electrochemical models and equivalent circuit models [13]. Based on the electrochemical theory,

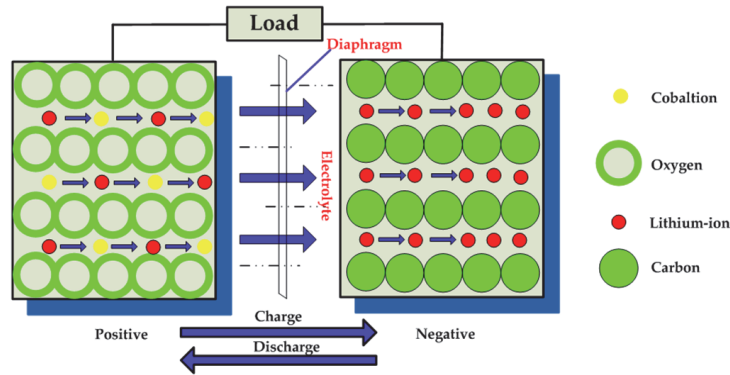


FIGURE 1: Lithium battery charge and discharge microscopic diagram.

the electrochemical model uses mathematical methods to describe the reaction process inside the battery. By using this model, the relationship between the cell performance and microscopic quantities can be established. However, this method is computationally complex and difficult to determine the value of parameters [14, 15]. The equivalent circuit model based on the external characteristics of the battery can avoid analyzing the internal reactions and complex parameter calculations. Comprehensively considering the accuracy and practicality of the battery model, equivalent circuit model is widely used in battery performance estimation of battery management systems [16, 17]. He et al. [18] proposed a model-based online estimation method for LiFePO_4 battery, which uses the Thevenin equivalent circuit model to simulate the LiFePO_4 battery and gives the corresponding mathematical expression equation. Feng et al. [19] proposed a new lithium battery equivalent circuit model by adding a moving average noise to the first-order resistor-capacitor circuit model. This new model simplifies the computational complexity of model parameters in a much more accurate way. Sun et al. [20] proposed a model-based dynamic multiparameter method for peak power estimation of lithium-ion batteries. This method refines the ohmic resistance of the Thevenin model for the lithium-ion battery, which improves the accuracy of the model. It is indicated that the model-based dynamic multiparameter method can be used to calculate the available power more accurately, whereas the above models cannot describe the change in self-healing phenomenon of lithium batteries. Therefore, in order to better describe the state of lithium battery in self-healing process, an equivalent circuit model of lithium battery is proposed based on self-healing characteristics.

The remainder of the paper is organized as follows. Section 2 introduces the self-healing phenomenon, which is very common in the actual use of electric vehicles. In Section 3, the equivalent circuit model based on self-healing characteristic is proposed and the analysis of the model is given. Section 4 describes the experiment platform and the experiment schedule based on LabView. In Section 5, the parameters of the model are identified and the simulation results are compared with the experiment. In addition, the

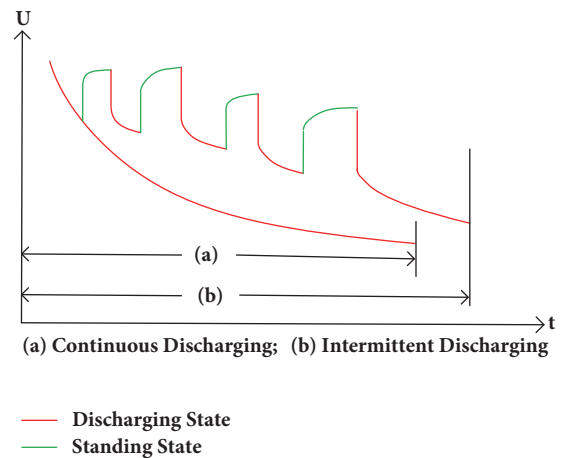


FIGURE 2: Comparison of lithium battery continuous discharge and intermittent discharge.

error between the simulation and experiment is analyzed. In the final section, some conclusions are given.

2. Self-Healing Process

In practice, three states are often used in the lithium battery. They are charging state, discharging state and standing state. As is shown in Figure 1, when the battery is charged, the positive electrode of the battery will generate lithium ions and at the same time lithium ions will pass through the electrolyte. Finally the lithium ions, generated at the positive electrode of the battery, arrive at the negative cathode of the battery and combine with graphite. And the capacity of the battery is related to the amount of lithium ions arriving at the cathode of the battery. When the battery is discharged, lithium ions in the negative electrode of the battery are separated from the graphite and returned to the positive electrode of the battery. The capacity of the battery is decreased.

In actual use, after each charge is completed, the lithium battery is repeatedly switched between discharging state and standing state, that is, intermittent discharging, as shown in Figure 2. When standing, the battery will self-heal. This

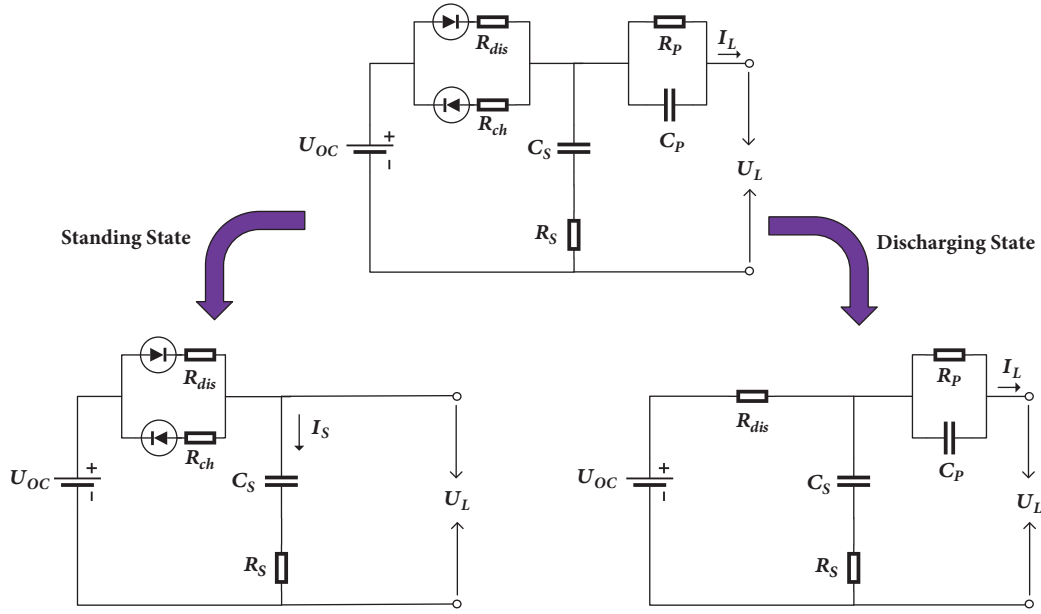


FIGURE 3: Lithium battery equivalent circuit model circuit diagram.

phenomenon is the reverse process of battery discharge, which is similar to the charging process of the battery, and the battery's state of charge will increase [21]. And, in the long term, this phenomenon will finally influence the state of health of lithium battery [22]. Mostly the electric vehicle is in a running and stagnant state, and the lithium battery is in a discharging and standing state so self-healing phenomenon is very common. The strength of self-healing is related to the time the battery is in standing state and it will change as the battery cycle times increase. Besides, the self-healing phenomenon will affect the remaining useful life of the battery. Therefore, it is essential to establish a battery model which could be used to describe the self-healing phenomenon of lithium-ion batteries. This paper will introduce a lithium battery equivalent circuit model based on self-healing characteristic.

3. Battery Model

3.1. Proposal of the Model. In order to better describe the voltage change of the lithium battery in the standing state, a lithium battery equivalent model based on self-healing characteristics is proposed. As shown in Figure 3, the self-healing characteristic-based model includes the open-circuit voltage U_{OC} , the internal resistance R_i of the battery, a capacitor C_S , a resistor R_S , and a RC network. The internal resistance R_i , respectively, includes a resistor R_{dis} in discharging state and a resistor R_{ch} in charging state. And I_S is the current pass through the capacitance C_S , I_L is the load current (positive for discharging state and negative for charging state), and U_L is the terminal voltage. Among them, the open-circuit voltage U_{OC} describes the voltage characteristics of the battery, and the capacitance C_S describes the capacity characteristics of the battery. The model can be divided into two parts. One

part is mainly to describe the voltage of the lithium battery in discharging state and the other part is mainly to describe the voltage of self-healing phenomenon of the lithium battery in standing state.

3.2. Description of the Model. When the battery reaches a stable state, the battery voltage no longer changes. At this time, the terminal voltage is equal to the open-circuit voltage U_{OC} of the battery, which is also equal to the voltage of the capacitor C_S , as shown in

$$U_L = U_{OC} = U_{C_S} \quad (1)$$

3.2.1. Description of the Model in Discharging State. The Hybrid Pulse Power Characteristic test is conducted to describe the discharging state of the lithium battery equivalent circuit model. When the battery passes the pulse current, the voltage of the battery undergoes two stages, faster voltage conversion and slower voltage conversion. Figure 4 shows the battery voltage changes when the HPPC test is carried out.

In the faster voltage conversion, the rapid drop in voltage is mainly affected by the internal resistance R_i of the battery. The value of internal resistance R_i is related to the change in voltage, as show in (2). The slower voltage conversion in voltage is assigned to the part of the RC network including diffusion resistance R_p . And (3) describe the voltage change of the slower conversion.

$$\Delta U_{L1} = U_{OC} - U_{L-F} = U_{OC} * \frac{R_i}{R_L // R_S + R_i} \quad (2)$$

$$\begin{aligned} \Delta U_{L2} &= U_{L-F} - U_{L-S} \\ &= U_{OC} * \left(\frac{R_L // R_S}{R_L // R_S + R_i} - \frac{R_L}{R_L + R_p + R_i} \right) \end{aligned} \quad (3)$$

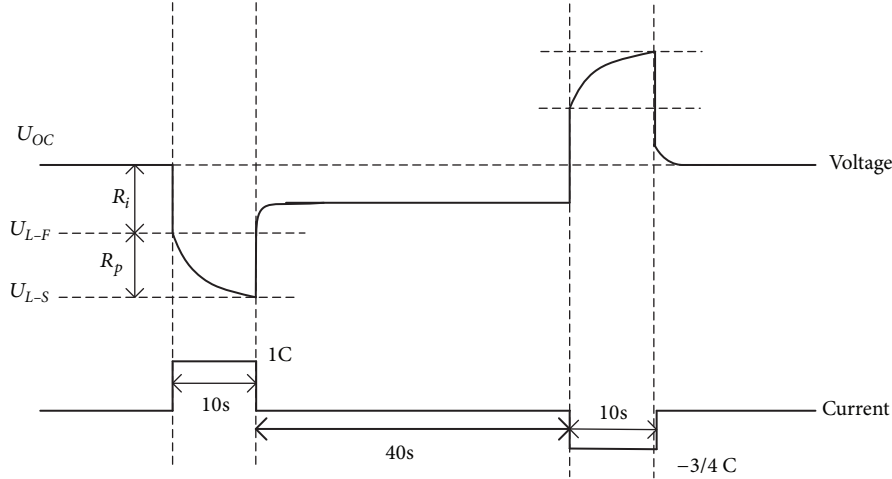


FIGURE 4: The lithium battery voltage and current changes in the HPPC test.

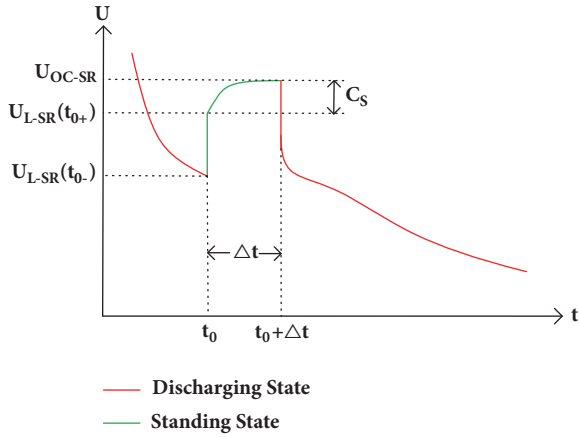


FIGURE 5: Self-healing test profile.

3.2.2. *Description of the Model in Standing State.* In order to describe the self-healing phenomenon of the battery, it is necessary to perform the self-healing test of the battery. And the self-healing test profile is shown in Figure 5. One self-healing test is performed within a single charge and discharge cycle of a lithium battery. When the charging process is completed, the lithium battery will start to discharge. At the point of t_0 when the voltage reaches the level of U_{L-SR} , the battery will be switched into the standing state. And the self-healing process with time interval Δt is performed. When the battery is in the standing state, no current flows through the RC network (resistance R_p and capacitance C_p), so the model can be simplified to the form in Figure 3.

At $t_0(-)$, the lithium battery is still in the state of discharging, the voltage over the capacitor C_S can be expressed by (4); at $t_0(+)$, the battery has been switched to the standing state, and the voltage of the capacitor C_S can be expressed by (5). Because the voltage of the capacitor cannot be abruptly

changed, the voltage of capacitor C_S at time $t_0(-)$ is equal to the voltage at time $t_0(+)$, as shown in

$$U_{C_S}(t_{0-}) = U_{L-SR}(t_{0-}) + I_L * R_p = U_{OC-SR} - U_i(t_{0-}) \quad (4)$$

$$U_{C_S}(t_{0+}) = U_{L-SR}(t_{0+}) - U_{R_S}(t_{0+}) \quad (5)$$

$$U_{C_S}(t_0) = U_{C_S}(t_{0-}) = U_{C_S}(t_{0+}) \quad (6)$$

From (4), (5), and (6), how the voltage changes when the battery is switched from the discharging state to the standing one can be deduced.

$$\Delta U_{L-SR} = U_{R_S}(t_{0+}) + I_L * R_p \quad (7)$$

When the battery is still for an enough long period of time, the battery is in a stable state. It can be obtained by (1) that the voltage of the capacitor C_S will be equal to the open-circuit voltage of the battery U_{OC-SR} , while the voltage of capacitor C_S at t_0 is less than U_{OC-SR} . Comparing (4) and (8), it can be concluded that the lithium battery is charged by the ideal voltage source U_{OC} during the interval time Δt when the battery is in the standing state. Where the current flowing through capacitor C_S is marked as I_S , the time constant is τ and the quantity of the battery is Q_{C_S} :

$$U_{C_S}(\Delta t \rightarrow \infty) = U_{OC-SR} \quad (8)$$

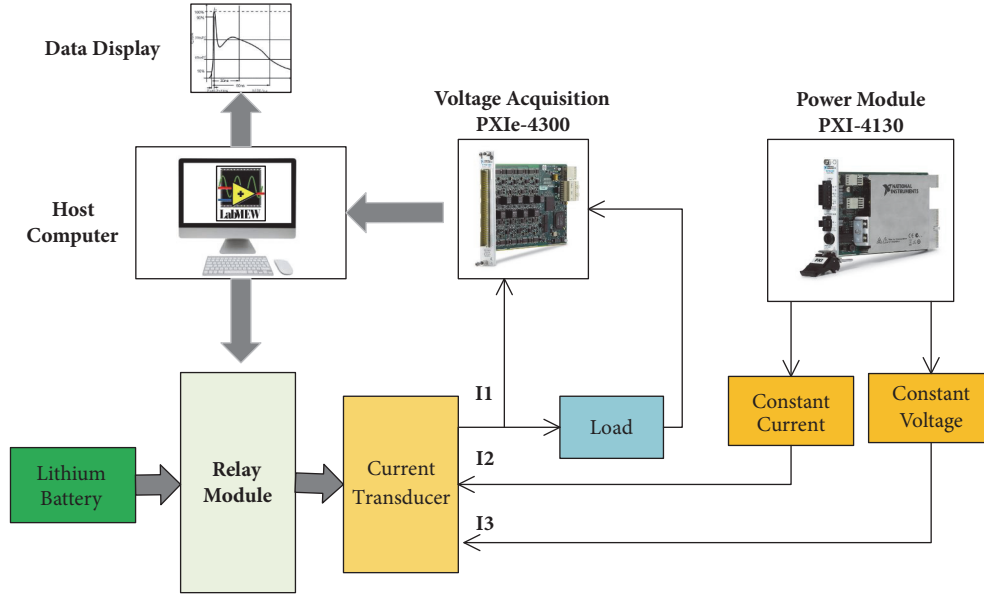
$$I_S = C_S * \frac{dU_{C_S}}{dt} \quad (9)$$

$$\tau = C_S * (R_i + R_S) \quad (10)$$

$$Q_{C_S} = U_{C_S} * C_S \quad (11)$$

When the lithium battery is switched from the discharging state to the standing state, the voltage of capacitor C_S satisfies

$$U_{C_S} = U_{OC-SR} - [U_{OC-SR} - (U_{L-SR}(t_{0-}) + I_L * R_p)] * \exp\left[-\frac{t/C_S}{(R_S + R_i)}\right] \quad (12)$$

FIGURE 6: Lithium battery monitoring system based on *LabView*.

Meanwhile, the relationship between the terminal voltage U_{L-SR} and the voltage of capacitor U_{Cs} accords with (5). So from (5), (7), (9), and (12), the function of the terminal voltage U_{L-SR} can be derived as follows:

$$U_{L-SR} = U_{Cs} + \frac{R_S * C_S}{C_S * (R_i + R_S)} * [U_{OC-SR} - U_{L-SR}(t_{0-}) - I_L * R_P] * \exp\left(-\frac{t}{\tau}\right) \quad (13)$$

4. Experiments

4.1. Experiment Platform. In order to monitor the discharging state and the standing state of the battery, a lithium battery charge/discharge monitoring system based on *LabView2012* is established, as shown in Figure 6. The system uses *LabView 2012* as a software development platform, including upper computer, *NI* data acquisition cards, power supply modules, and relay modules. The system realizes the programming control of the discharge process of the lithium battery, simulates the transition from the discharging state to the standing state during the actual use of the lithium battery, and monitors the self-healing phenomenon of the lithium battery. The upper computer can accomplish the real-time monitoring of the lithium battery and is responsible for switching the state of the circuit. Voltage acquisition card *PXIe-4300* contains 8 analog input channels; each channel is equipped with an independent analog-to-digital converter of 16-bit resolution and can be simultaneously sampled to ensure the efficiency of data acquisition. The current sensor has a measurement range of 50 mA to 10A and is responsible for transmitting the current signal to a channel of the voltage

acquisition card. The voltage, current, and other information of the battery are transmitted to the upper computer through the *PXI* bus, ensuring the accuracy and high efficiency of data transmission. *PXI-4130* is used to charge lithium batteries. It is a programmable power module that can control output constant voltage and constant current.

4.2. Experiment Schedule. In order to analyze the self-healing phenomenon during the intermittent discharge process, a set of experiments are carried out on the 18650 lithium battery and the experiment schedule is shown in Figure 7. For the purpose of obtaining the initial capacity of the lithium battery, the SCT test was performed and repeated three times. After that, the battery is discharged and the HPPC test is performed. At the same time, the test data is recorded. The key to the experiment schedule is to conduct self-healing characteristic test on the lithium battery. Among them, U^* represents the state transition voltage. When the voltage drops to U^* for the first time, the working state of the battery changes, switching from the discharging state to the standing state. The value of the state transition voltage represents the depth of discharge, which could affect the strength of the self-healing phenomenon. So, for an evident observation of the self-healing phenomenon, the state transition voltage is selected to be 3 V in this experiment. That is, when the battery voltage drops to 3 V for the first time, the battery enters the standing state and performs the self-healing test. The value of the SOC at this time can be obtained by the method of coulomb counting by the data logger of the experimental system. Experiments of three times scales are performed, respectively, 15minutes, 60 minutes, and 90 minutes. In other words, the period in the standing state is 15 min, 60 min, and 90 min. And each self-healing test is repeated three times.

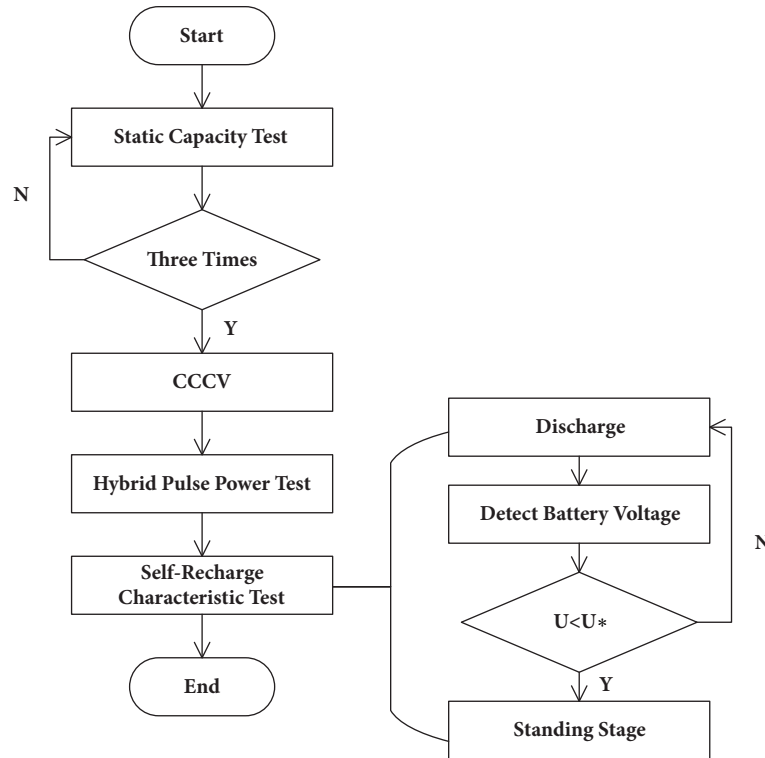


FIGURE 7: Experiment schedule.

TABLE 1: Parameter Identification Results at $U^* = 3$ V.

SOC	R_{dis}	R_{ch}	R_p	C_s	R_s
12.23%	82.3 m Ω	81.7 m Ω	16.1 m Ω	400.851 F	0.506 Ω

5. Results and Discussion

In order to make clear the relationship between self-healing characteristics and self-healing time, this paper selects the first test data with self-healing time of 60 minutes to identify the model parameters and compares the simulated value of the battery model with measured value during the standing state. In the meantime, the parameters obtained from this experiment are applied to the other experiments with the same self-healing time and also to multiple sets of experiments with different self-healing times. The results are as follows.

5.1. Parameter Identification. Using the test data to identify the unknown parameters of the battery model is the basis for analysis and discussion of the results. MATLAB 2018 provides a variety of methods to achieve the fitting functions, one of which is Cftool. Cftool has a visual interactive interface and provides numbers of fitting functions, so this paper selects Cftool as the fitting tool. The parameter identification results are shown in Table 1.

5.2. Evaluation on the Battery Model. After the model parameters are obtained from the first experiment test data with self-healing time of 60 minutes, the simulated value of the model

is compared with the measurements. Figures 8(a), 8(b), and 8(c) represent the results of the comparison between the simulations and the experiment measurements of three times, of which the self-healing time is 60 min. After the lithium battery is switched from the discharging state to the standing state, the model is able to describe the rising status of the lithium battery voltage. And when the standing time is long enough, the simulation value is still very close to the terminal voltage of the lithium battery. Repeat the experiment with a standing time of 60 min and compare the test data with the simulated values of the model. Result shows that the model can simulate the process of the other experiments with the same self-healing time, as shown in Figures 8(b) and 8(c).

Figure 9 shows the error characteristic curve between model simulation values and experiment measurements when the self-healing time is 60 min. When the battery starts to switch from the discharging state to the standing state, the battery voltage suddenly changes. In this short period, the model has a larger error. But, after a brief change in voltage, the model can better describe the status of the lithium battery. And as the battery voltage tends to be flat, the model error decreases and approaches the level of zero.

In order to prove that this model can describe the state of lithium batteries with different self-healing time, experiments with self-healing time of 15 min and 90 min are designed. And the parameters obtained from the experiment with a self-healing time of 60 min are applied to experiments with self-healing time of 15 min and 90 min. As is shown in Figures 10 and 11, the model can also describe the status of the battery.

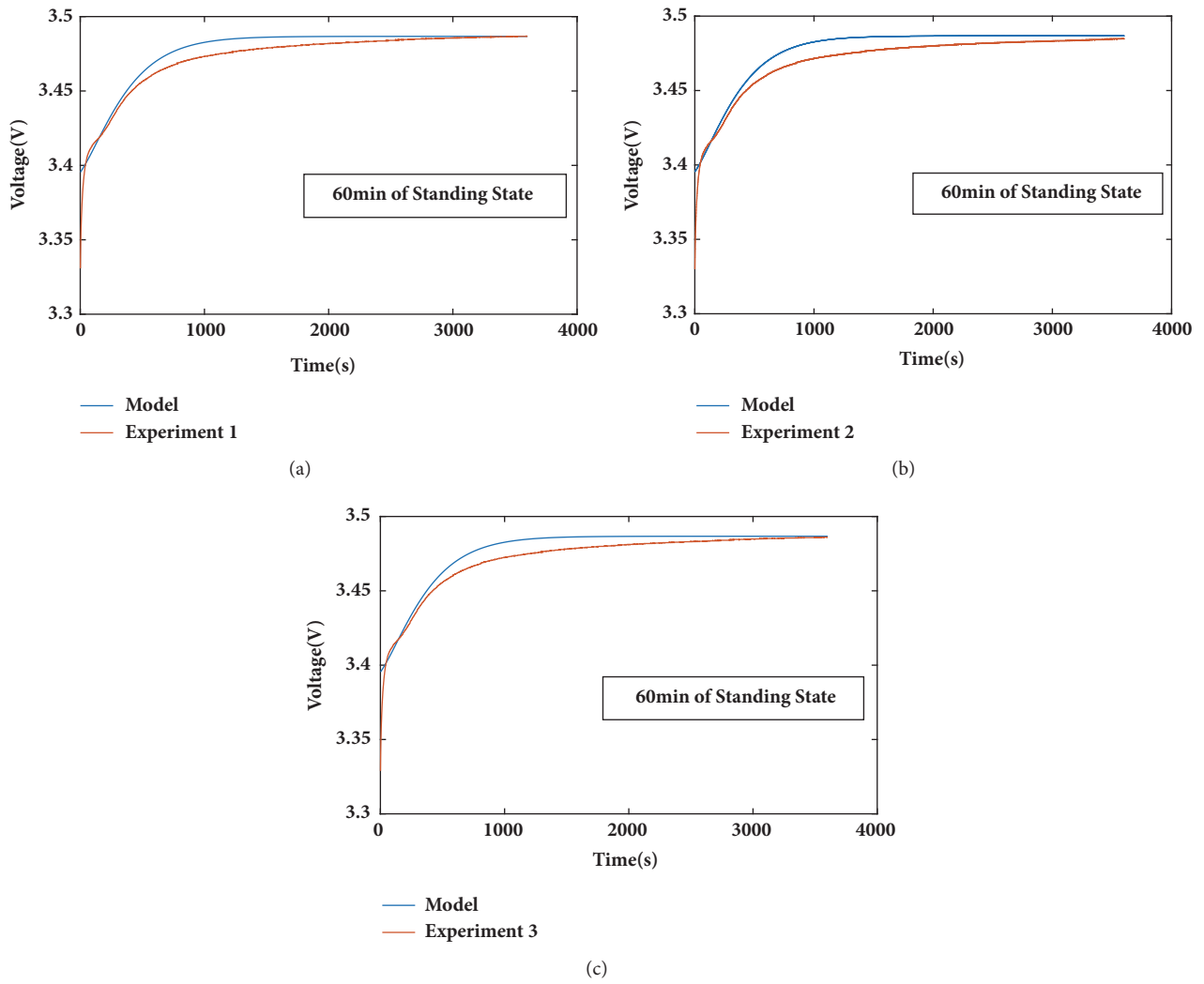


FIGURE 8: Comparison of model simulations and measurements at self-healing time of 60 minutes: (a) experiment 1, (b) experiment 2, and (c) experiment 3.

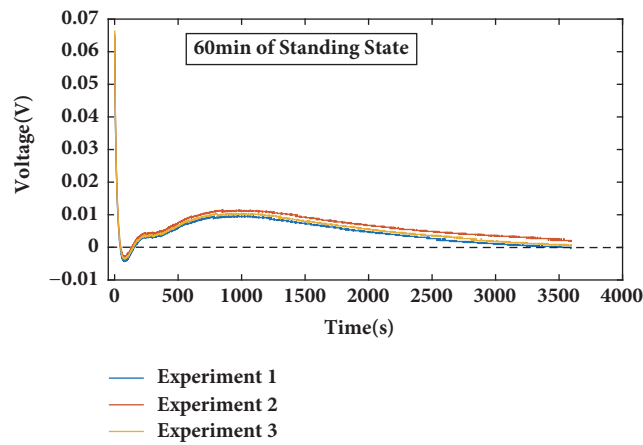


FIGURE 9: Comparison of the error between the model simulations and experiments measurements at self-healing time of 60 minutes.

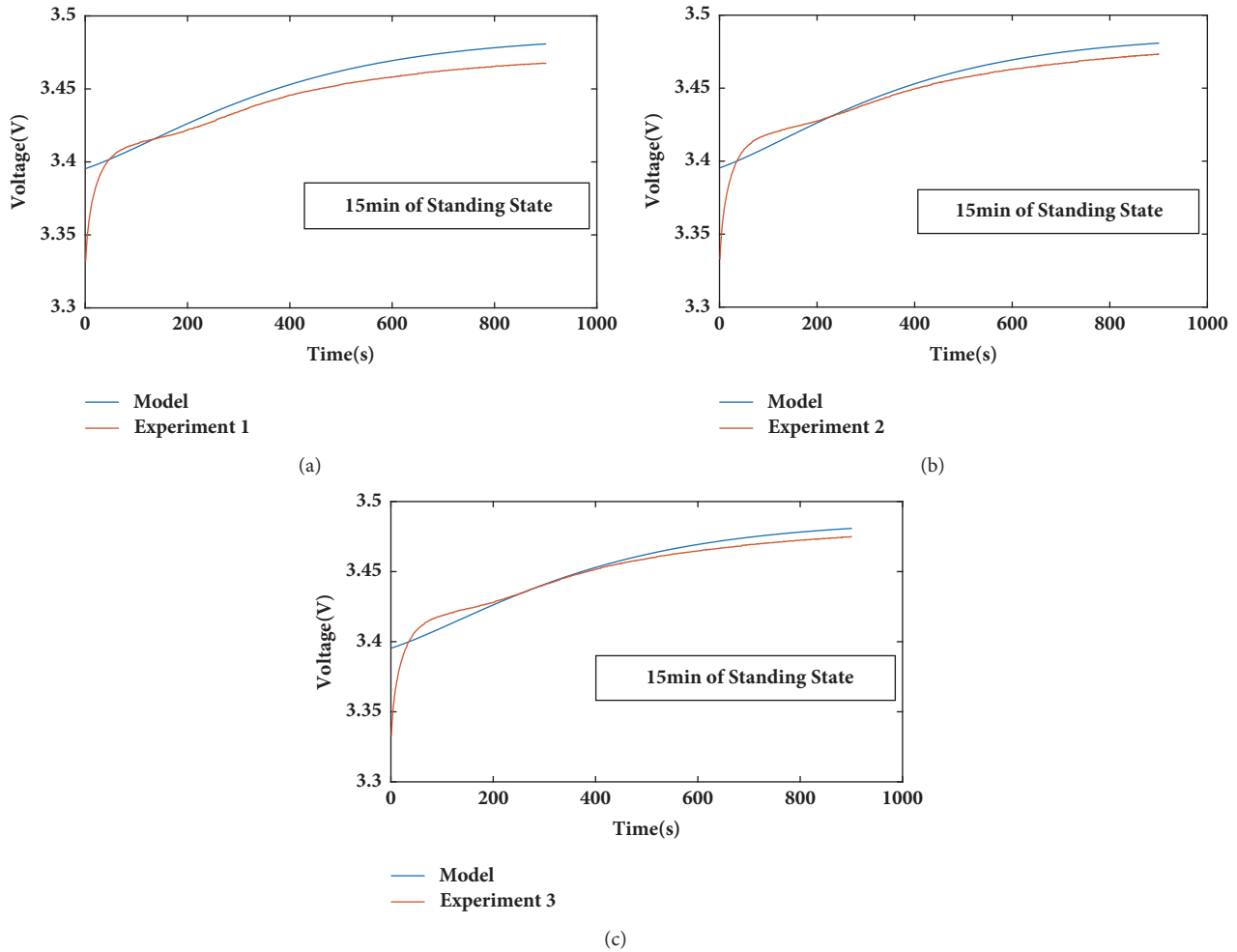


FIGURE 10: Comparison of model simulations and measurements at self-healing time of 15 minutes, (a) experiment 1, (b) experiment 2, and (c) experiment 3.

Figures 12 and 13 are the error curves between the model simulations and the experiment measurements when the self-healing time is 15 min and 90 min, respectively. In the state transition stage, there is a large error between the model and the measurement but the error between the model and the measurement gradually decreases along with time, and the error tends to be stable, which is similar to the result at self-healing time of 60 min.

5.3. Accuracy Analysis of the Battery Model. The accuracy of the lithium battery model will be analyzed by the maximum error (the maximum value of the voltage error), the mean error (the average value of the voltage error), and the RMSE (the root-mean-square error of the voltage). Three experiment test datasets for self-healing time of 15 min, 60 min, and 90 min are analyzed. The results are shown in Table 2.

In the three experiments with self-healing time of 60 minutes, the maximum error is less than 70 mV, the maximum error rate is also less than 2%, and the root-mean-square error is less than 8 mV. When using this model for accuracy analysis of test data with self-healing time of 15 min and 90 min,

the maximum error does not exceed 70 mV. Except that the maximum error rate of the third group of experiments with self-healing time of 90 minutes is slightly more than 2%, the maximum error rate of the rest of the tests is less than 2%. And the root-mean-square error is less than 13 mV. Therefore, the model has high accuracy and efficiency.

6. Conclusion

This paper discusses the working state of lithium battery in actual cases, which aims at the self-healing phenomenon in the process of intermittent discharge and proposes an equivalent circuit model for self-healing phenomenon. The function of the model is obtained when the lithium battery is switched to the standing state from the discharging state. By using a LabView-based lithium battery test system, the self-healing characteristic-based experiment is designed, and the parameters of the model are identified through test data. Experiment results prove that the model can accurately describe the voltage change of the battery in the standing state with different self-healing time. The error between

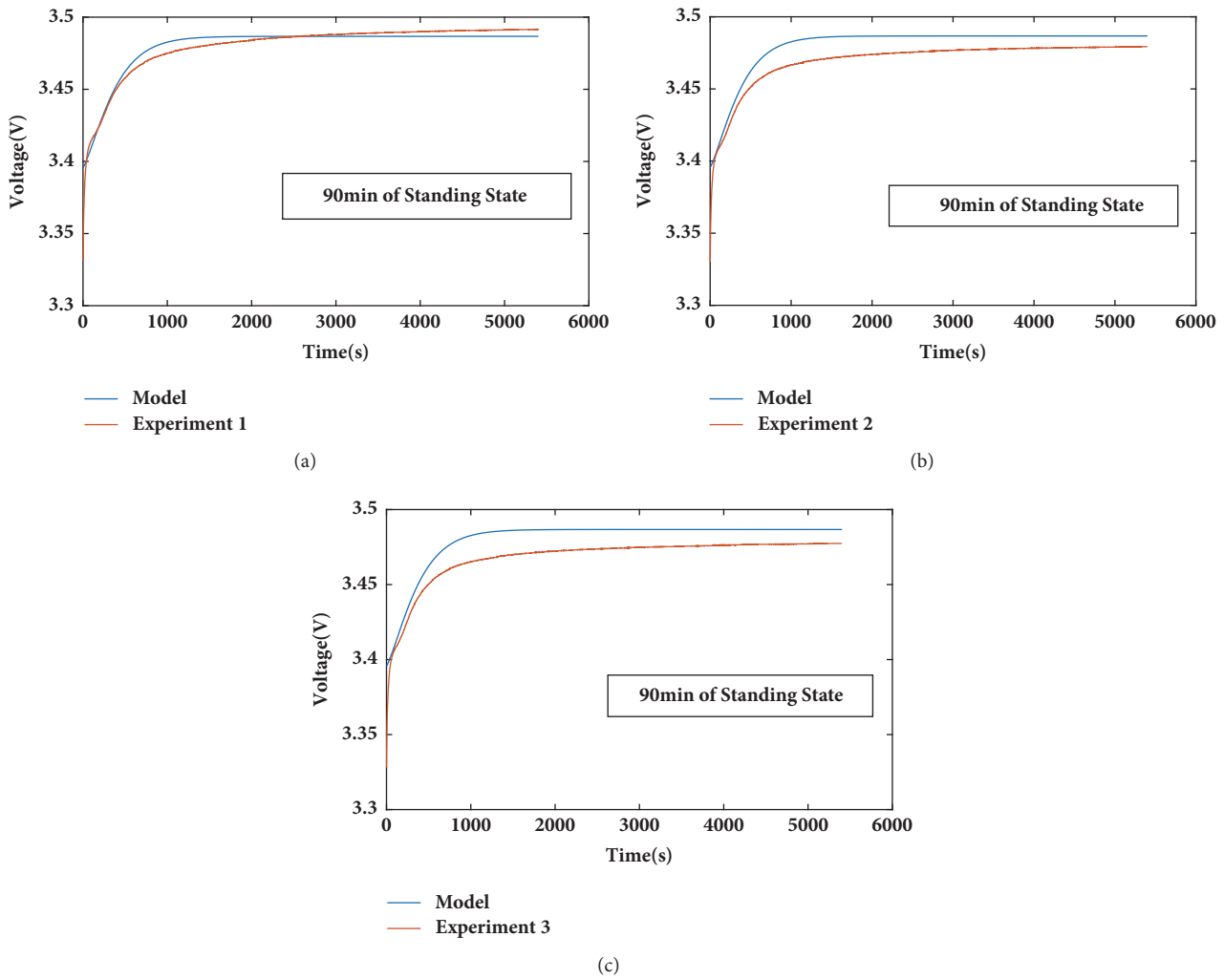


FIGURE 11: Comparison of model simulations and measurements at self-healing time of 90 minutes, (a) experiment 1, (b) experiment 2, and (c) experiment 3.

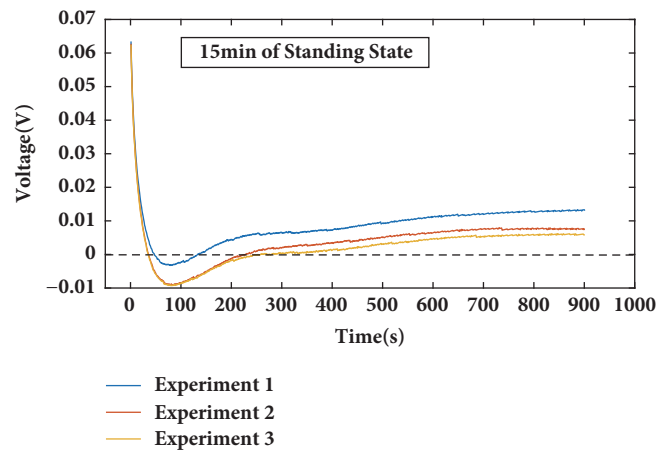


FIGURE 12: Comparison of the error between the model simulations and experiments measurements at self-healing time of 15 minutes.

TABLE 2: Model error analysis.

Time of Standing State	Number of Experiments	Maximum/V	Mean/V	RMSE/V	Max.Error Rate(%)
60 min	1	0.06464	0.004535	0.006093	1.94
	2	0.06556	0.006485	0.007588	1.97
	3	0.06655	0.005302	0.006689	1.99
15 min	1	0.06342	0.008516	0.010537	1.91
	2	0.06277	0.003718	0.007682	1.88
	3	0.06241	0.002196	0.006796	1.87
90 min	1	0.06466	0.000354	0.004623	1.94
	2	0.06555	0.010587	0.011145	1.97
	3	0.06746	0.012269	0.012731	2.03

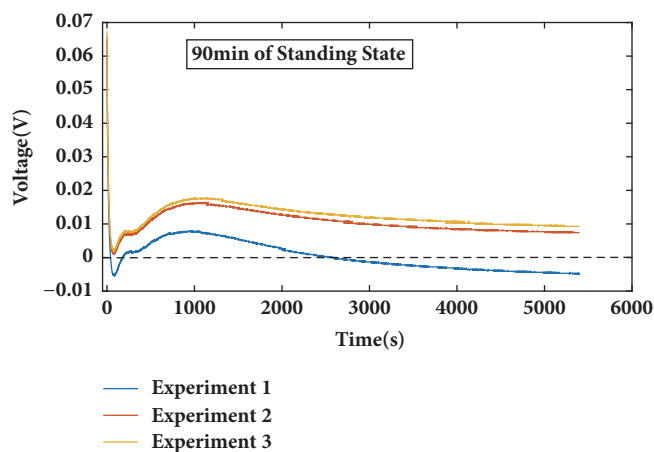


FIGURE 13: Comparison of the error between the model simulations and experiments measurements at self-healing time of 90 minutes.

the simulations and measurements is maintained within a stable range and the model is highly accurate. In spite of the advantages of the equivalent circuit model for self-healing characteristic, the description for the working state of lithium batteries is complicated to some degree and the identification of battery parameters needs more experiments. Future works aim at the optimization of the model and parameter identifications.

Data Availability

The data used to support the findings of this study are available from the corresponding author upon request.

Conflicts of Interest

All authors declare they have no conflicts of interest.

Acknowledgments

This work received financial support from the National Natural Science Foundation of China (no. 71601022), the Natural Science Foundation of Beijing (4173074), and the Key Project B Class of Beijing Natural Science Fund (KZ201710028028). And the work is supported by Youth Innovative Research Team of Capital Normal University.

References

- [1] J. B. Dunn, L. Gaines, J. C. Kelly, C. James, and K. G. Gallagher, "The significance of Li-ion batteries in electric vehicle life-cycle energy and emissions and recycling's role in its reduction," *Energy & Environmental Science*, vol. 8, no. 1, pp. 158–168, 2015.
- [2] J. Hu, H. Morais, T. Sousa, and M. Lind, "Electric vehicle fleet management in smart grids: a review of services, optimization and control aspects," *Renewable & Sustainable Energy Reviews*, vol. 56, pp. 1207–1226, 2016.
- [3] D. Huang, J. Tang, and L. A. Zhao, "A fault diagnosis method of power systems based on gray system theory," *Mathematical Problems in Engineering*, vol. 2015, Article ID 971257, 11 pages, 2015.
- [4] J. Jaguemont, L. Boulon, and Y. Dubé, "A comprehensive review of lithium-ion batteries used in hybrid and electric vehicles at cold temperatures," *Applied Energy*, vol. 164, pp. 99–114, 2016.
- [5] A. Fotouhi, D. J. Auger, K. Propp, S. Longo, and M. Wild, "A review on electric vehicle battery modelling: from lithium-ion toward lithium-sulphur," *Renewable & Sustainable Energy Reviews*, vol. 56, pp. 1008–1021, 2016.
- [6] L. Wu, X. Fu, and Y. Guan, "Review of the remaining useful life prognostics of vehicle lithium-ion batteries using data-driven methodologies," *Applied Sciences*, vol. 6, no. 6, p. 166, 2016.
- [7] W. Yan, B. Zhang, W. Dou, D. Liu, and Y. Peng, "Low-cost adaptive lebesgue sampling particle filtering approach for real-time li-ion battery diagnosis and prognosis," *IEEE Transactions*

- on Automation Science and Engineering*, vol. 14, no. 4, pp. 1601–1611, 2017.
- [8] M. E. Orchard, P. Hevia-Koch, B. Zhang, and L. Tang, “Risk measures for particle-filtering-based state-of-charge prognosis in lithium-ion batteries,” *IEEE Transactions on Industrial Electronics*, vol. 60, no. 11, pp. 5260–5269, 2013.
- [9] S.-C. Huang, K.-H. Tseng, J.-W. Liang, C.-L. Chang, and M. G. Pecht, “An online SOC and SOH estimation model for lithium-ion batteries,” *Energies*, vol. 10, no. 4, 2017.
- [10] Y. Zou, X. Hu, H. Ma, and S. E. Li, “Combined State of Charge and State of Health estimation over lithium-ion battery cell cycle lifespan for electric vehicles,” *Journal of Power Sources*, vol. 273, pp. 793–803, 2015.
- [11] R. Xiong, F. Sun, X. Gong, and H. He, “Adaptive state of charge estimator for lithium-ion cells series battery pack in electric vehicles,” *Journal of Power Sources*, vol. 242, pp. 699–713, 2013.
- [12] A. Eddahech, O. Briat, and J.-M. Vinassa, “Lithium-ion battery performance improvement based on capacity recovery exploitation,” *Electrochimica Acta*, vol. 114, pp. 750–757, 2013.
- [13] X. S. Hu, S. B. Li, and H. Peng, “A comparative study of equivalent circuit models for Li-ion batteries,” *Journal of Power Sources*, vol. 198, pp. 359–367, 2012.
- [14] X. Lai, Y. Zheng, and T. Sun, “A comparative study of different equivalent circuit models for estimating state-of-charge of lithium-ion batteries,” *Electrochimica Acta*, vol. 259, pp. 566–577, 2018.
- [15] H. He, R. Xiong, and J. Fan, “Evaluation of lithium-ion battery equivalent circuit models for state of charge estimation by an experimental approach,” *Energies*, vol. 4, no. 4, pp. 582–598, 2011.
- [16] X. Chen, W. Shen, Z. Cao, A. Kapoor, and I. Hijazin, “Adaptive gain sliding mode observer for state of charge estimation based on combined battery equivalent circuit model in electric vehicles,” in *Proceedings of the IEEE 8th Conference on Industrial Electronics and Applications (ICIEA '13)*, pp. 114–123, IEEE, June 2013.
- [17] H. W. He, R. Xiong, H. Q. Guo, and S. C. Li, “Comparison study on the battery models used for the energy management of batteries in electric vehicles,” *Energy Conversion and Management*, vol. 64, no. 4, pp. 113–121, 2012.
- [18] H. He, R. Xiong, and H. Guo, “Online estimation of model parameters and state-of-charge of LiFePO₄ batteries in electric vehicles,” *Applied Energy*, vol. 89, no. 1, pp. 413–420, 2012.
- [19] T. Feng, L. Yang, X. Zhao, H. Zhang, and J. Qiang, “Online identification of lithium-ion battery parameters based on an improved equivalent-circuit model and its implementation on battery state-of-power prediction,” *Journal of Power Sources*, vol. 281, pp. 192–203, 2015.
- [20] F. Sun, R. Xiong, H. He, W. Li, and J. E. E. Aussems, “Model-based dynamic multi-parameter method for peak power estimation of lithium-ion batteries,” *Applied Energy*, vol. 96, no. 3, pp. 378–386, 2012.
- [21] T. Qin, S. Zeng, J. Guo, and Z. Skaf, “A rest time-based prognostic framework for state of health estimation of lithium-ion batteries with regeneration phenomena,” *Energies*, vol. 9, no. 11, p. 896, 2016.
- [22] T. Qin, S. Zeng, J. Guo, and Z. Skaf, “State of health estimation of li-ion batteries with regeneration phenomena: a similar rest time-based prognostic framework,” *Symmetry*, vol. 9, no. 1, p. 4, 2016.

Research Article

Estimating Remaining Useful Life for Degrading Systems with Large Fluctuations

Dang-Bo Du, Jian-Xun Zhang , Zhi-Jie Zhou , Xiao-Sheng Si, and Chang-Hua Hu 

High-Tech Institute of Xi'an, Xi'an, Shaanxi 710025, China

Correspondence should be addressed to Chang-Hua Hu; hch_reu@sina.com

Received 16 March 2018; Accepted 3 April 2018; Published 14 May 2018

Academic Editor: Darong Huang

Copyright © 2018 Dang-Bo Du et al. This is an open access article distributed under the Creative Commons Attribution License, which permits unrestricted use, distribution, and reproduction in any medium, provided the original work is properly cited.

Remaining useful life (RUL) prediction method based on degradation trajectory has been one of the most important parts in prognostics and health management (PHM). In the conventional model, the degradation data are usually used for degradation modeling directly. In engineering practice, the degradation of many systems presents a volatile situation, that is, fluctuation. In fact, the volatility of degradation data shows the stability of system, so it could be used to reflect the performance of system. As such, this paper proposes a new degradation model for RUL estimation based on the volatility of degradation data. Firstly the degradation data are decomposed into trend items and random items, which are defined as a stochastic process. Then the standard deviation of the stochastic process is defined as another performance variable because standard deviation reflects the system performance. Finally the Wiener process and the normal stochastic process are used to model the trend items and random items separately, and then the probability density function (PDF) of the RUL is obtained via a redefined failure threshold function that combines the trend items and the standard deviation of the random items. Two practical case studies demonstrate that, compared with traditional approaches, the proposed model can deal with the degradation data with many fluctuations better and can get a more reasonable result which is convenient for maintenance decision.

1. Introduction

With the development of industrial system, the technology of intelligent vehicle has become more and more mature, and its safety and reliability have become the key factor which restricts its development. An intelligent driving system of a vehicle is a complicated system, which usually needs to monitor the running state, position, and environment [1]. The navigation system is one of its monitoring systems. It can provide information about the position, direction, speed, and acceleration. With the development of intelligent driving technology, navigation system is more and more important. As a key part of the navigation system, the performance of the gyroscope will directly affect the performance of the whole system, and then influence the safety of the entire vehicle system. Therefore, it is necessary to forecast its remaining useful life for better maintenance or health management strategies, using the available condition monitoring information [2, 3].

Generally, the current methods for estimating RUL can usually be divided into two types: physics of failure based

methods and data driven methods. Physics of failure based methods rely on the physics of the failure mechanisms. However, with advances in design and production technologies, engineering systems become more complex and large-scale, so it is difficult to obtain the physical failure mechanisms in advance. In contrast, data driven methods achieve RUL estimation via data fitting mainly including machine learning and statistics-based approaches. Therefore, data driven methods attempt to derive models directly from collected CM data and life data and have gained much attention in variety of industrial assets [4, 5]. Considering that the life data may not be available for cost-expensive or highly reliable products, we mainly focus on the statistical data driven approaches for RUL estimation in this paper.

Under a recognized definition of lifetime, that is, first hitting time (FHT) [6, 7], many RUL estimation approaches have been reported in literature [8–10]. References [6, 11] provide a detailed overview of the degradation modeling and RUL predicting method. It can be founded that these models mainly concern the system degrading with a soothing wave.

However, some degradation processes have high dynamics and the observed degradation data exhibit many fluctuations. In this case, it is difficult to model those degradation data for estimating the RUL via traditional approaches [12, 13], while the fluctuation of degradation can reflect the stability of the system. With the deterioration of the system, the stability of the system may worsen gradually, which causes the fluctuation's degree of the degradation data to usually increase over time. Such large fluctuating characteristics can be described by a stochastic degradation process with time-varying mean and variance. Hence, in order to simplify the expression, we use "large fluctuation" to describe the characteristics of these degradation data with time-varying mean and variance. Therefore, the issue of how to model those data with many fluctuations is of practical significance.

In this paper, it is assumed that the degradation process of the system is a stochastic process with time-dependent expectation and standard deviation at each time. Considering that the fluctuation can be represented by a stochastic degradation of standard deviation, which is a new key performance factor, then the whole system RUL can be estimated by considering the stochastic degradation data and the fluctuation. The model parameters can be estimated by maximum likelihood estimation method. Finally, a numbering validation method and INS gyro study are provided to show the superiority of our approach.

The remaining parts are organized as follows. In Section 2, the problem of failure prognosis is formulated and defined. In Section 3, a degradation model for prognosis is developed based on the degradation data and the standard deviation. Section 4 provides two case studies to illustrate the application and usefulness of the developed model. Section 5 draws the main conclusions.

2. Problem Formulation

In this section, based on the fluctuation and the stochastic degradation data, a new model for RUL estimation is proposed. Firstly, we introduce the variables used in this paper.

2.1. Notations. The notations that will be used in this paper are listed as follows:

- t_i : time of the i th CM point (can be irregularly spaced)
- ξ : failure threshold
- $X(t)$: random variable representing the degradation at time instant t
- x_i : degradation observation at t_i
- $\mathbf{X}_{0:i}$: history of degradation observations for the system up to t_i
- $R(t)$: trend item
- $C(t)$: fluctuation item
- μ_c : expectation of $C(t)$
- σ_c : standard deviation of $C(t)$
- $\psi(\cdot)$: failure function

- $\sigma_c(t)$: standard deviation function at the time instant t
- T : lifetime
- $\mathfrak{D}, \lambda_\mu, \lambda_\sigma, \lambda_R, \Theta$: parameters column vector
- $f_C(\cdot)$: PDF of $C(t)$
- $g_R(t_i, \lambda_R)$: function of t_i and λ_R
- $g_\mu(t, \lambda_\mu)$: function of t_i and λ_μ
- $g_\sigma(t, \lambda_\sigma)$: function of t_i and λ_σ
- $T_{\text{RUL}}(t)$: RUL of the system at time instant t
- $L(\cdot)$: log-likelihood function
- t_{ch} : time instant of the change-point
- n_{ch} : number of the observation data at time instant t_{ch}
- ϕ : initial degradation
- θ, σ : drift and diffusion parameters
- $B(t)$: standard Brownian motion
- $E(\cdot)$: expectation operator
- $\varepsilon(t_i)$: individual difference random variable.

2.2. Problem Formulation of the New Approach for RUL Estimation. In this paper, we model the degradation process of the system as a stochastic process as $\{X(t), t \geq 0\}$, where $X(t)$ is the degradation quantity a time t . Therefore, the lifetime T of the system can be defined as follows:

$$T = \inf \{t : X(t) > \xi; t > 0\}, \quad (1)$$

where ξ is the failure threshold.

From (1), it is important to establish the model of stochastic degradation process. In general, a stochastic degradation process can be represented as

$$X(t) = R(t) + C(t), \quad t \geq 0, \quad (2)$$

where $R(t)$ is the trend term, $C(t)$ is the stochastic fluctuating term, and both of them change over time.

It is assumed that $C(t)$ is the complex stochastic process with the expectation μ_c and standard deviation σ_c . Note that σ_c determines the fluctuation of the stochastic degradation process. Thus, jointly modeling the standard deviation and trend items is necessary for RUL estimation. Generally, there are two methods to model the standard deviation: the first method is that the standard deviation is regarded as an independent failure factor, but the difficulty lies in how to set the failure threshold; the second method is to formulate a new failure function $\psi(\cdot)$ which establishes the linkage between the standard deviation σ_c and the trend $R(t)$. Accordingly, the lifetime of the system can be defined as follows:

$$T = \inf \{t : \psi(R(t), \sigma_c(t), \xi, \mathfrak{D}) > 0; t > 0\}, \quad (3)$$

where $\psi(\cdot)$ is the failure function, $\sigma_c(t)$ is the standard deviation, which is the function of the time instant t , and \mathfrak{D} is the parameters column vector.

Based on the estimated lifetime T , the RUL at time t_i is obtained as

$$T_{\text{RUL}}(t_i) = T - t_i, \quad (4)$$

where t_i is the time at the i CM points. In this way, the fluctuation in the degradation process could be incorporated into the RUL estimation.

From (3), we can observe that the fluctuation of the degradation data is taken into account in estimating the lifetime. Then the next section is to model the trend term $R(t)$ and the stochastic fluctuating term $C(t)$.

3. Degradation Modeling and RUL Estimation

In this section we describe how to model the degradation process and estimate the parameter based on the observed degradation data in detail and then how to obtain the RUL of the system via the proposed approach.

3.1. Degradation Modeling. Based on the problem formulation of our approach, the main algorithm formulation for degradation modeling and RUL estimation is outlined as follows.

First, we define the stochastic disturbance term $C(t)$ as a function of μ_c and σ_c :

$$C(t_i) = f_c(\mu_c, \sigma_c), \quad (5)$$

where both the expectation μ_c and the standard deviation σ_c are time-dependent and formulated as

$$\mu_c(t) = g_\mu(t, \lambda_\mu), \quad (6)$$

$$\sigma_c(t) = g_\sigma(t, \lambda_\sigma).$$

As a result, the PDF of $C(t)$ can be represented as

$$f_C(c; \mu_c, \sigma_c) = f_C(c; g_\mu(t, \lambda_\mu), g_\sigma(t, \lambda_\sigma)). \quad (7)$$

Suppose the trend $R(t)$ is also a function of t as follows:

$$R(t) = g_R(t, \lambda_R). \quad (8)$$

Then the degradation process defined in (2) can be further described as follows:

$$X(t) = g_R(t, \lambda_R) + f_c(g_\mu(t, \lambda_\mu), g_\sigma(t, \lambda_\sigma)). \quad (9)$$

In practice, the degradation process is often discretely monitored at time $0 = t_0 < t_1 < \dots < t_k$ and let $x_k = X(t_k)$ denote the degradation observation at time t_k . Then, the set of the degradation observations up to t_k is represented by $X_{1:k} = \{x_0, x_1, \dots, x_k\}$. In this paper, we can utilize the history of the degradation observations $X_{1:k}$ to evaluate the parameters $\lambda_R, \lambda_\mu, \lambda_\sigma$ in (4). The details of algorithm for parameter estimation are summarized in Appendix A.

3.2. Decomposing Trend Items and Fluctuation Items. As discussed in Section 3.1, the degradation process is decomposed into the trend item and fluctuation item at first. Nowadays the common methods of trend extraction, such as the average slope method, finite difference method, LPF (Low-Pass Filter) method, and least square fit method, need the form of the trend to be defined in advance, which leads to difficulty in applying those methods to the degradation signals with the unknown trend. Because the EMD (Empirical Mode Decomposition) method is an adaptive trend extraction method [14–16], which has been widely used for trend extraction, then, in our paper, the EMD method is adopted for trend extraction.

3.2.1. Estimation Parameters $\lambda_\mu, \lambda_\sigma$ of Fluctuation Items. Suppose $\mathbf{R}_{0:i} = \{r_0, r_1, \dots, r_i\}$ are the trend items obtained by EMD method; let $Y_i = X_i - R_i$, so, as discussed in Section 3.1, $\mathbf{Y}_{0:i}$ denotes the observed data of the stochastic fluctuating process $C(t)$.

Since the stochastic disturbance $C(t)$ is defined as a normal random process, so it could be concluded that the mean of stochastic fluctuating process is $\lambda_\mu = 0$ based on the good property of the normal random process. And it can be obtained as follows:

$$C(t) \sim N(0, \sigma_c^2), \quad (10)$$

where σ_c is defined as a function of t .

In engineering practice, many systems have two stages of degradation. In the first stage, the trend of the degradation is not obvious, and the fluctuation is stable. In the second stage, the trend of the degradation has an obvious increase, and the fluctuation becomes higher over time. So, it is reasonable to adopt a two-stage model to describe the degrading systems with large fluctuations. The two-stage model can be expressed by [17]

$$\sigma_c(t_i) = \begin{cases} \lambda_\sigma & t_i \leq t_{\text{ch}} \\ g_\sigma(t_i, \lambda_\sigma) & t_i > t_{\text{ch}} \end{cases}, \quad (11)$$

where t_{ch} is the time of the change-point. It is noted that the change-point assumed can be easily found and here we regard it as known information [17]. When $t_i \leq t_{\text{ch}}$, $\sigma_c = \lambda_\sigma$, λ_σ is the fixed value; when $t_i > t_{\text{ch}}$, $\sigma_c(t_i) = g_\sigma(t_i, \lambda_\sigma)$, which is the function of time t_i .

When $t_i \leq t_{\text{ch}}$, $\sigma_c = \lambda_\sigma$, λ_σ is a constant. λ_σ could be evaluated by the maximum likelihood estimation based on the property of normal distribution [18] as follows:

$$\lambda_\sigma = \sqrt{\frac{\sum_{i=1}^{n_{\text{ch}}} (Y(t_i) - \bar{Y}_{\text{ch}})^2}{n_{\text{ch}}}}. \quad (12)$$

In (12), n_{ch} denotes the number of the observed data at time t_{ch} and \bar{Y}_{ch} is the arithmetic average of the observed data before t_{ch} .

When $t_i > t_{\text{ch}}$, σ_c is the function of t_i . In order to simplify the modeling, it is assumed that $\sigma_c(t_i)$ is a linear function of time t_i , expressed as

$$g_\sigma(t_i, \lambda_\sigma) = \lambda'_\sigma t_i + \lambda''_\sigma. \quad (13)$$

Based on the maximum likelihood estimation method, we can easily obtain the log-likelihood function L . Taking the partial derivatives of the log-likelihood function to all parameters, we have

$$\begin{aligned} \frac{\partial L}{\partial \lambda'} &= \sum_{i=0}^k \left\{ -\frac{t_i}{\lambda'_\sigma t_i + \lambda''_\sigma} + \frac{Y^2(t_i) t_i}{(\lambda'_\sigma t_i + \lambda''_\sigma)^3} \right\} = 0 \\ \frac{\partial L}{\partial \lambda''_\sigma} &= \sum_{i=0}^k \left\{ -\frac{1}{\lambda'_\sigma t_i + \lambda''_\sigma} + \frac{Y^2(t_i)}{(\lambda'_\sigma t_i + \lambda''_\sigma)^3} \right\} = 0. \end{aligned} \quad (14)$$

It is observed from (14) that the analytic solution of those parameters via maximum likelihood estimation could not be obtained. To be solvable, the numerical method is adopted to estimate λ'_σ , λ''_σ , which is summarized in Appendix C.

3.2.2. Modeling the Trend Items. Because the systems in the same batch may have different degradation paths, we adopt the random variable $\varepsilon(t_i)$ to describe such individual difference. As such, the real trend item can be represented as

$$\mathbf{R}_{0:i} = \bar{\mathbf{R}}_{0:i} + \boldsymbol{\varepsilon}_{0:i}, \quad (15)$$

where $\bar{\mathbf{R}}_{0:i}$ is the trend item from initial time 0 to time instant t_i and $\boldsymbol{\varepsilon}_{0:i}$ is the random variable reflecting individual difference.

From the above formulation, it could be concluded that $R(t_i)$ is also random due to individual difference. So we could model the trend items by statistics-based data driven methods. Considering that the trend items may not be a monotonic process, we utilize Wiener process to describe this random trend process [18].

In order to simplify modeling, only the linear degradation model or the model that could be converted into linear form will be discussed in this paper. In general, a linear Wiener-process-based degradation model can be represented as follows [19]:

$$R(t_i) = \phi + \theta t_i + \sigma B(t_i), \quad (16)$$

where ϕ is the initial degradation, θ and σ are the drift and diffusion parameters, respectively, and $B(t_i)$ denotes the standard Brownian Movement (BM), which represents the stochastic dynamics. We assume that θ is the stochastic coefficient while σ and ϕ are deterministic. And we further assume that when $t_0 = 0$, $x_0 = 0$; thus $\phi = 0$.

Define $Z_i = R_i - R_{i-1} = \theta(t_i - t_{i-1}) + \sigma B_i - \sigma B_{i-1}$. Then the joint sampling distribution $f(Z_1, Z_2, \dots, Z_k | \theta)$ can be calculated as

$$\begin{aligned} f(Z_1, Z_2, \dots, Z_k | \theta) &= \frac{1}{\prod_{i=1}^k \sqrt{2\pi\sigma^2(t_i - t_{i-1})}} \\ &\cdot \exp \left[-\sum_{j=1}^k \frac{(Z_j - Z_{j-1} - \theta(t_j - t_{j-1}))^2}{2\sigma^2(t_j - t_{j-1})} \right] \\ &= \frac{1}{\prod_{i=1}^k \sqrt{2\pi\sigma^2(t_i - t_{i-1})}} \\ &\cdot \exp \left[-\sum_{j=1}^k \frac{(Z_j - \theta(t_j - t_{j-1}))^2}{2\sigma^2(t_j - t_{j-1})} \right]. \end{aligned} \quad (17)$$

In Bayesian framework, it is assumed that the prior distribution of θ follows $N(\mu_0, \sigma_0)$. Thus, we can obtain the following [20]:

$$\begin{aligned} f(\theta | Z_1, \dots, Z_k) &\propto f(Z_1, Z_2, \dots, Z_k | \theta) p(\theta) \\ &\propto \exp \left[-\sum_{j=1}^k \frac{(Z_j - \theta(t_j - t_{j-1}))^2}{2\sigma^2(t_j - t_{j-1})} \right] \\ &\cdot \exp \left(-\frac{(\theta - \mu_0)^2}{2\sigma_0^2} \right) \propto \exp \left[-\frac{(\theta - \mu_{\theta,k})^2}{2\sigma_{\theta,k}^2} \right]. \end{aligned} \quad (18)$$

Due to the property of the normal distribution, we can obtain the posterior estimate of θ as follows:

$$P(\theta | Z_1, \dots, Z_k) = \frac{1}{\sqrt{2\pi\sigma_{\theta,k}^2}} \exp \left[-\frac{(\theta - \mu_{\theta,k})^2}{2\sigma_{\theta,k}^2} \right] \quad (19)$$

with

$$\begin{aligned} \mu_{\theta,k} &= \frac{(\mu_0\sigma^2 + x_k\sigma_0^2)}{(t_k\sigma_0^2 + \sigma^2)} \\ \sigma_{\theta,k}^2 &= \frac{\sigma^2\sigma_0^2}{(t_k\sigma_0^2 + \sigma^2)}. \end{aligned} \quad (20)$$

It is obvious that when a new observation is available, the posterior estimate of θ can be easily updated. $\Theta = [\sigma^2, \mu_0, \sigma_0^2]$ is used to denote the unknown parameters. Actually, we can also estimate those unknown parameters in Θ via EM algorithm, which provides a possible framework for estimating the parameters involving hidden variables [19, 21, 22]. For example, let $\Theta_k = [\sigma_k^2, \mu_{0,k}, \sigma_{0,k}^2]$ denote the estimated Θ based on the observed data $\mathbf{Z}_{0:k}$. Then, Θ_k can be obtained as follows:

$$\begin{aligned} \sigma_k^{2(i+1)} &= \frac{1}{k} \sum_{j=1}^k \frac{(Z_j - Z_{j-1})^2 - 2\mu_{\theta,k}(t_j - t_{j-1})(Z_j - Z_{j-1}) + (t_j - t_{j-1})^2(\mu_{\theta,k}^2 + \sigma_{\theta,k}^2)}{(t_j - t_{j-1})} \\ \hat{\mu}_{0,k}^{(i+1)} &= \mu_{\theta,k} \\ \hat{\sigma}_{0,k}^{2(i+1)} &= \sigma_{\theta,k}^2. \end{aligned} \quad (21)$$

The details of the derivation are summarized in Appendix D.

3.3. *Joint Model for RUL Estimation.* If X is a normal distribution, then

$$P\{X < \mu + 3\sigma, X \sim N(\mu, \sigma)\} = 0.9987. \quad (22)$$

It is well-known that $[\mu - 3\sigma, \mu + 3\sigma]$ is frequently used to be the confidence interval of normal distributed random variable. Therefore, we assume that if $R(t) + 3\sigma_c$ does not reach the failure threshold ξ , it is reasonable that the degradation data $X(t)$ does not reach the failure threshold ξ . For those highly critical systems, the maintenance after failure is too expensive or the consequence of failure is disastrous. Thus, for those systems, it is essential that the conservative method for PHM be adopted to avoid unexpected failure. Therefore, the failure function is defined as

$$\psi(R(t), \sigma_t, \theta) = R(t) + 3\sigma_c. \quad (23)$$

Then, as we discussed before, the failure function can be further represented as follows:

$$\begin{aligned} \psi(R(t), R_t, \theta) &= R(t) + 3\sigma_c \\ &= \phi + \theta t_i + \sigma B(t_i) + 3(\lambda'_\sigma t_i + \lambda''). \end{aligned} \quad (24)$$

If t_{end} is used to denote the failure time, the following result can be obtained directly:

$$\phi + \theta t_{\text{end}} + \sigma B(t_{\text{end}}) + 3(\lambda'_\sigma t_{\text{end}} + \lambda'') = \xi. \quad (25)$$

If t_{now} is used to denote the current time, we have

$$\begin{aligned} \phi + \theta t_{\text{now}} + \sigma B(t_{\text{now}}) + 3(\lambda'_\sigma t_{\text{now}} + \lambda'') \\ = R(t_{\text{now}}) + 3\sigma_c(t_{\text{now}}). \end{aligned} \quad (26)$$

where $\sigma_c(t_{\text{now}}) = \lambda'_\sigma t_{\text{now}} + \lambda''$.

Solving the equations in (25) and (26), we can get

$$\begin{aligned} \theta(t_{\text{end}} - t_{\text{now}}) + \sigma(B(t_{\text{end}}) - B(t_{\text{now}})) \\ + 3\lambda'_\sigma(t_{\text{end}} - t_{\text{now}}) \\ = \xi - R(t_{\text{now}}) - 3(\lambda'_\sigma t_{\text{now}} + \lambda''). \end{aligned} \quad (27)$$

Based on the definition of RUL in (1), the RUL estimated at time t_j could be represented as

$$T_{\text{RUL}}(t_j) = t_{\text{end}}(t_j) - t_{\text{now}}(t_j). \quad (28)$$

Further, utilizing the property of Wiener process, the PDF of the RUL estimation at time t_j can be obtained:

$$\begin{aligned} f(T_k | \theta, \mathbf{X}_{1:k}) &= \frac{\xi - R(t_k) - 3(\lambda'_\sigma t_k + \lambda'')}{\sqrt{2\pi T_k^3 \sigma^2}} \\ &\cdot \exp\left(-\frac{(\xi - R(t_k) - 3(\lambda'_\sigma t_k + \lambda'') - \theta T_k - 3\lambda'_\sigma T_k)^2}{2\sigma^2 T_k}\right). \end{aligned} \quad (29)$$

Recall that θ follows $N(\mu_{\theta,k}, \sigma_{\theta,k})$; Theorem 1 in [20] can be used to estimate the PDF of the RUL as

$$\begin{aligned} f(T_k | \theta, \mathbf{X}_{1:k}) &= \frac{\xi - b(t_k) - 3(\lambda'_\sigma t_k + \lambda'')}{\sqrt{2\pi T_k^3 (\sigma^2 + \sigma_{\theta,k}^2 t_k)}} \\ &\cdot \exp\left(-\frac{(\xi - b(t_k) - 3(\lambda'_\sigma t_k + \lambda'') - \mu_{\theta} T_k - 3\lambda'_\sigma T_k)^2}{2T_k (\sigma^2 + \sigma_{\theta,k}^2 T_k)}\right). \end{aligned} \quad (30)$$

Clearly, there are five steps of RUL estimation in our approach, which are summarized below.

3.4. *A Procedure of Proposed Approach for RUL Estimation.* As discussed in the previous subsection, the procedure of the approach proposed in this paper for RUL estimation is summarized as follows.

Step 1. Through EMD method, the degradation data $\mathbf{X}_{0:i} = \{x_0, x_1, \dots, x_i\}$ are divided into the trend items $\mathbf{R}_{0:i} = \{r_0, r_1, \dots, r_i\}$ and the fluctuation items $\mathbf{Y}_{0:i} = \{y_0, y_1, \dots, y_i\}$ when the monitored observations $\mathbf{X}_{0:i} = \{x_0, x_1, \dots, x_i\}$ are available.

Step 2. The trend items $\mathbf{R}_{0:i} = \{r_0, r_1, \dots, r_i\}$ and the fluctuation items $\mathbf{Y}_{0:i} = \{y_0, y_1, \dots, y_i\}$ are modeled by Wiener process and a normal stochastic process separately; the details of algorithm and parameter estimation are summarized in Section 3.2.1 and Appendices B, C, and D.

Step 3. According to the failure function defined in Section 3.2.2 and the model proposed in Step 2, the PDF of the estimated RUL can be obtained.

Step 4. When the monitored observation X_{i+1} is available, let $t = t + 1$ and go to Step 1. Otherwise, go to Step 5.

Step 5. Using the PDF of the estimated RUL, the system's performance can be evaluated.

4. Case Studies

In this section, two practical cases for gyros in the inertial navigation system (INS) are provided to illustrate the application of our model and compare the performance of our model with traditional models in [12, 23].

4.1. *Case Description.* As discussed before, gyro plays a key role in intelligent vehicle. With the working hours increase, gyro may cause a kind of degradation that makes gyro drift. Usually, this gyro can be compensated using a specific compensating model. However, when gyro drift degrades to a predefined threshold, the gyro's performance can not satisfy the vehicle INS system requirement. The gyro's drift can not be monitored directly, and a performance indicator is used instead.

In the following, two practical cases are provided to illustrate the adaptability and rationality of our approach for RUL estimation.

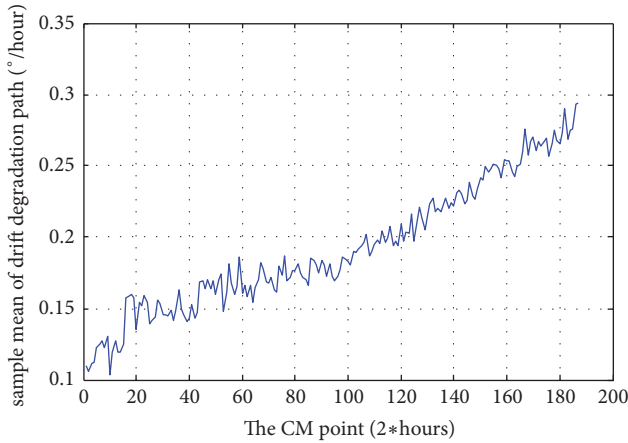


FIGURE 1: The sample mean of the gyro drift.

4.2. Two Practical Case Studies

4.2.1. Case 1: The Fluctuations of Degradation Data Are Stable. In this section, we utilize the degradation data from INS to illustrate, where its operating time is 374 hours and the interval is 2 hours. The collected data are shown in Figure 1.

In the practice of the INS health monitoring, it is usually required that the sample mean of the drift measurement along the sense axis should not exceed 0.30 (°/hour), which is predetermined at the design stage and is strictly enforced in practice since an INS is a critical device used in the navigated space system. From Figure 1, it could be observed that the degradation data is much similar to the linear case. As for this practical case, the distribution of the RUL could be obtained at each CM point by the proposed method. At the same time, the approach in [12] is adopted for comparison. Obviously, from Figures 2 and 3 our approach can reduce the uncertainty of the RUL estimation. At the last 6 points, it is observed that the estimated RUL of our approach is more accurate than the model in [12] from Figure 3. Compared with the actual RUL relying on the definition of FHT, the estimated RUL of our approach is more conservative, which shows the availability of our model.

Through the above comparisons, it is shown that our approach can deal with the degradation as well as the traditional approach and could decrease the influence of the fluctuations in the observed degradation signals.

4.2.2. Case 2: The Fluctuations of Degradation Data Are Diverged

(1) Description and Collection of the Degradation Data. With the development of technology, the stability of the gyro becomes better and better. In this case, the sample mean of the drift does not have obvious increase within a short time. Figure 4 shows another monitored INS in certain space system with test time of 420 hours; data of 210 points of drift coefficients were collected with regular CM intervals of 2 hours in the field condition. It is obvious that those data do not have obvious increase trend, which leads to the

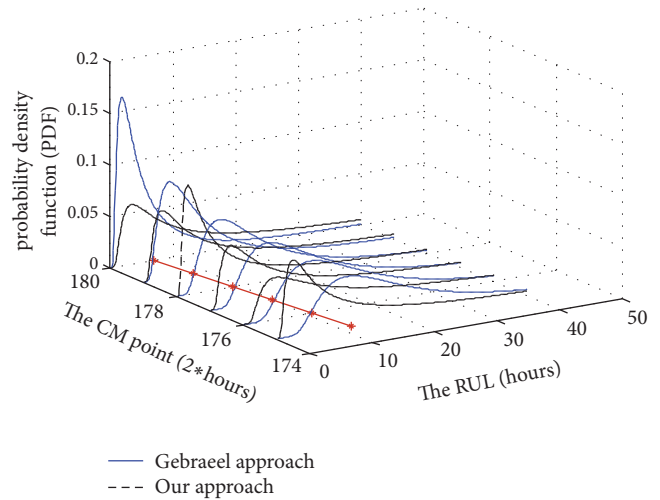


FIGURE 2: Illustration of the RUL distributions at last 6 CM points (* means actual RUL).

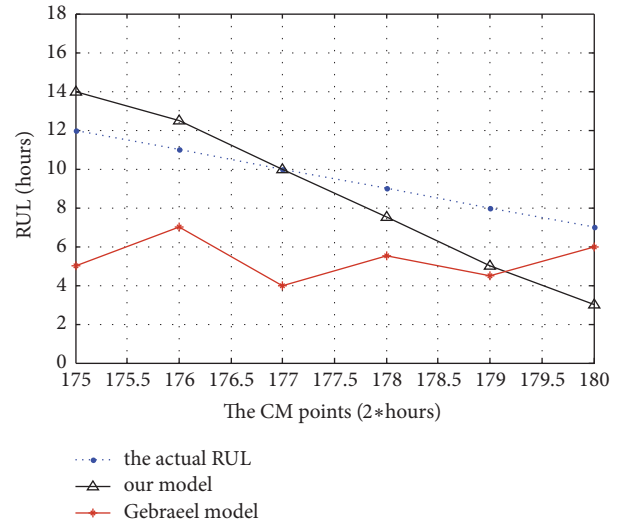


FIGURE 3: The estimated mean RUL and the actual RUL at last 6 CM points.

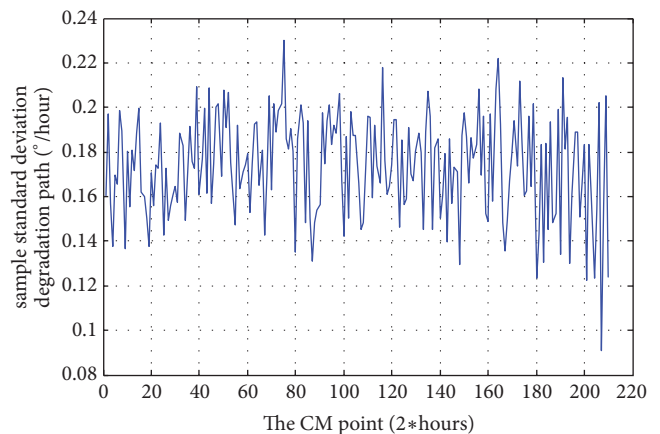


FIGURE 4: The sample mean of the gyro drift.

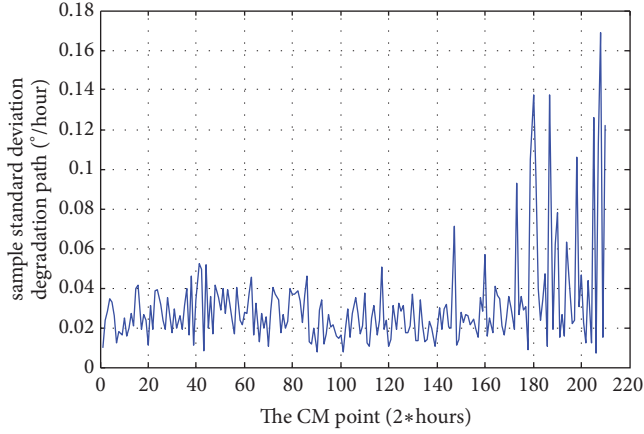


FIGURE 5: The sample standard deviation of the gyro drift.

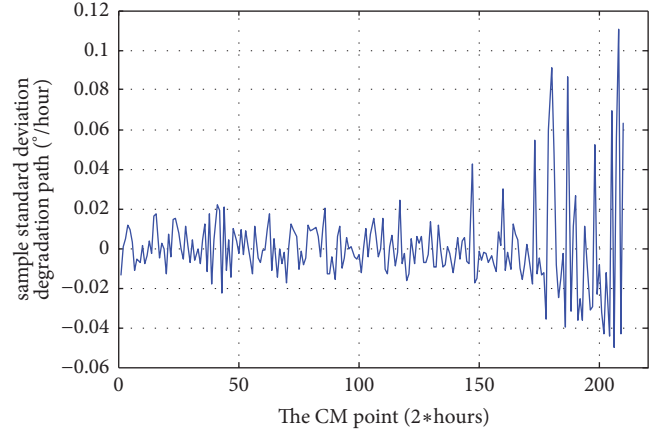


FIGURE 7: The fluctuation items.

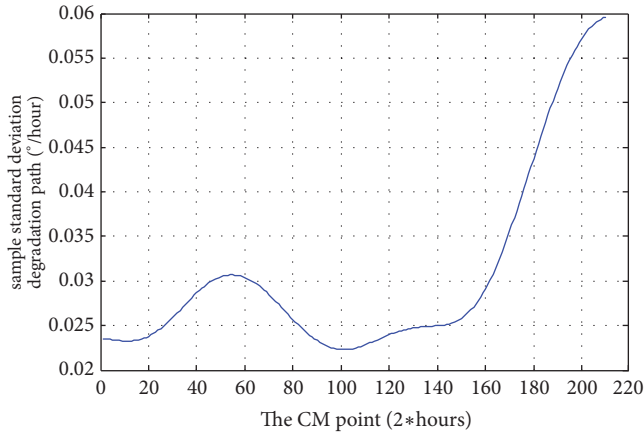


FIGURE 6: The trend items.

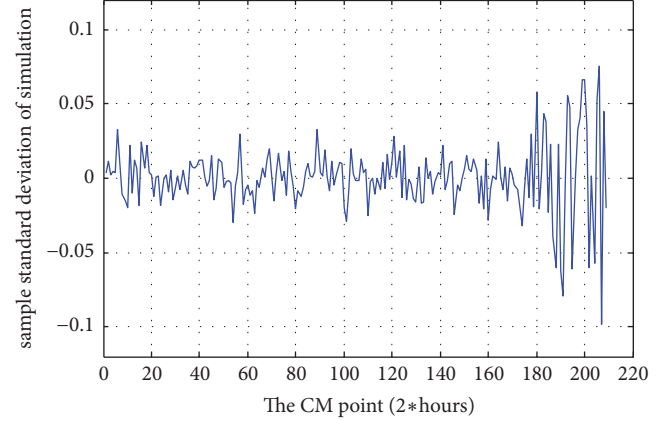


FIGURE 8: Simulation based on the parameter evaluations.

difficulty in analyzing the degradation data of the gyro based on the sample mean of drift. On the other hand, the sample standard deviation of drift has some variation trend over time, as shown in Figure 5. Therefore our model could be used for RUL estimation via the data of the drift sample standard deviation which usually required that the sample standard deviation of the drift measurement along the sense axis should not exceed 0.15 (°/hour).

(2) *Decomposition of Degradation Data.* As discussed in Section 3, the trend items and fluctuation items are obtained by EMD method. Figures 6 and 7 show the trend items and the fluctuation items which illustrate the changes of these terms over time.

(3) *Parameter Estimation.* It is obvious that both the trend items and the fluctuation items can be regarded as two-stage model. The first stage means that the gyro works normally and the second stage means that the gyros begin degrading. Here we only take the second stage into consideration for estimating the RUL. Based on the definition of two-stage model, the change-point is at the 150th CM point. As we have discussed in Section 3, λ'_σ , λ''_σ are almost the same before the 150th CM point via (18). It could be calculated that the

random items follow $N(0, 0.0103)$ in first stage, where $t_{\text{RUL}} = T_{\text{Rated}} - t_{\text{now}}$. Then the model discussed in Section 3 is used to evaluate and update the parameters, which are used to estimate the RUL.

(4) *Verification of Parameter Estimation.* In order to illustrate the accuracy of the estimated λ'_σ and λ''_σ , a numerical simulation is adopted. Figure 8 shows that the simulation is produced based on the evaluations of λ'_σ and λ''_σ , which are used to illustrate the accuracy of estimation for parameters λ'_σ and λ''_σ . Comparing Figure 8 with Figure 7, it is noted that the increases of the two fluctuation items are not the same when the degradation path begins stepping into the next stage, which is caused by the lack of the observed data. From Appendix C, it is noted that Std_i could be used to describe the change of standard deviation. So comparing Std_i of the simulation with the real fluctuation items, it is obvious that both of their paths are close, as shown in Figure 9. Thus, it could be concluded that evaluation of parameters is accurate.

(5) *Comparative Results.* Figure 10 shows the PDF of the estimated RUL at the last 8 CM points. From Figure 10, it is obvious that our approach can deal with the degradation with many fluctuations and get an explicit result, which is

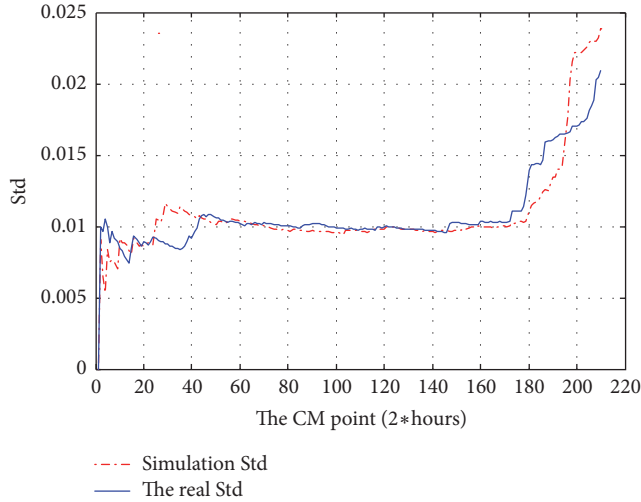


FIGURE 9: Comparison of the real Std and the simulation Std.

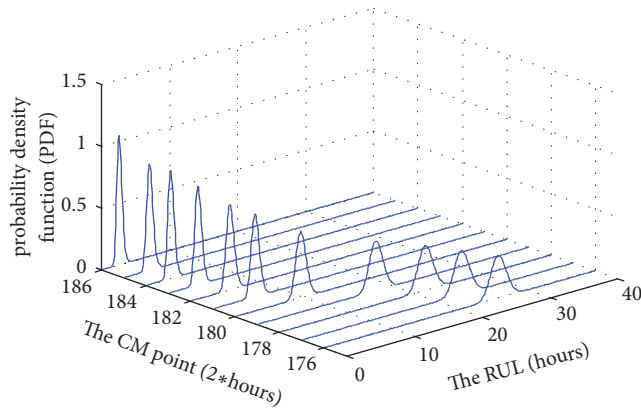


FIGURE 10: Illustration of the RUL distributions at last 10 CM points.

convenient for maintenance decision. From Figure 7, it is noted that the degradation data reach the failure threshold at the 205th CM point, but the result of our model shows that the gyro's failure occurs at about 187th CM point, which reflects that our approach is more conservative than the traditional approach, since the fluctuation is regarded as another performance variable for evaluating the performance of the gyro. Even through our approach is more conservative, it can be safer when the result of the RUL estimations is used for PHM of safety-critical systems such as gyros, whose maintenance cost after failure is too expensive and the consequence of failure are disastrous. And our approach can obtain the regular PDF of RUL which could be convenient for maintenance decision. It is shown in Figure 11 that the traditional approaches [8, 9] could not obtain regular PDF of RUL.

Comparing the results of case 1 and case 2, it is obvious that our approach can not only deal with the degradation with many fluctuations, but also get more reasonable result. Overall, these case studies imply that our approach is an effective model for RUL estimation, especially when the degradation data experience strong fluctuation.

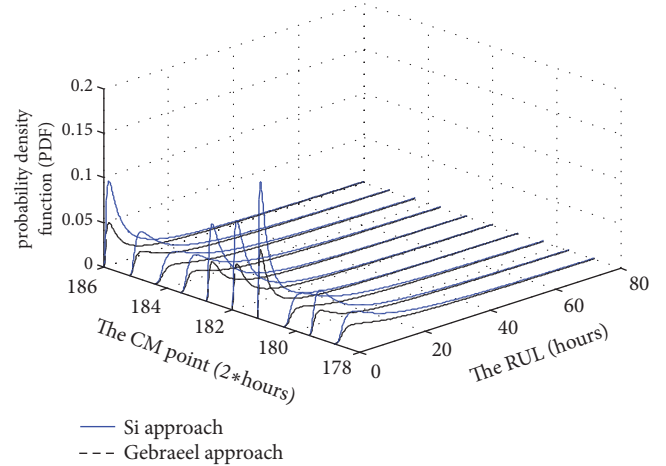


FIGURE 11: Illustration of the RUL distributions at last 8 CM points.

5. Conclusion

In this paper, we study how to estimate the RUL of dynamic degrading systems with high fluctuating degradation data. Specifically, we present a stochastic process-based degradation model with a time-varying standard deviation function to describe the degradation process of the system. Considering the fact that the fluctuation reflects the stability of the system, we define the fluctuation as an indicator of the system's health condition in addition to directly using the observed degradation data and further using the standard deviation to represent the degree of fluctuation. Then, based on the influence of the standard deviation, we define a failure threshold based method to estimate the marginal RUL distributions. And then the joint RUL distribution is formulated based on the correlation between two performance variables. Finally, through a practical case, the feasibility and applicability of the presented model are validated.

In this paper, we are concerned with a situation where the system is degrading with high fluctuation. Then the collected degradation data are difficult to model for evaluating the RUL of system by traditional approaches. In order to solve the above problem, we redefine the failure function that is depended on two aspects including the degradation trend and the fluctuations. So we decompose the degradation data into trend items and fluctuation items firstly, and then model the two items separately. Finally we evaluate the PDFs of RUL based on the failure function that has been defined above. Through the two practical cases, it is obvious that our model can deal with this problem well and get the reasonable result used for PHM.

Appendix

A. Formulation of Parameter Estimation

In order to estimate the parameters in (7), the maximum likelihood estimation method is adopted. Here two cases are considered.

Case 1 (the functional form of $g_R(t, \lambda_R)$ is already known). Because the functional form of $g_R(t, \lambda_R)$ is known, the probability density function of X_i can be defined as $f_{X(t)}(x; \lambda_\mu, \lambda_\sigma, \lambda_R, t)$. Therefore, the likelihood function for $\mathbf{X}_{1:i}$ can be written as

$$\begin{aligned} L(\lambda_\mu, \lambda_\sigma, \lambda_R) &= f(x_0, x_1, \dots, x_k | \lambda_\mu, \lambda_\sigma, \lambda_R) \\ &= \prod_{i=1}^k f_{X_i}(x_i; \lambda_\mu, \lambda_\sigma, \lambda_R, t). \end{aligned} \quad (\text{A.1})$$

In order to estimate those parameters in (A.1), we take the partial derivatives of the log-likelihood function of all parameters:

$$\begin{aligned} \frac{\partial L}{\partial \lambda_\mu} &= \sum_{i=0}^k \frac{1}{f_{X_i}(x_i; \lambda_\mu, \lambda_\sigma, \lambda_R, t_i)} \\ &\quad \cdot \frac{\partial f_{X_i}(x_i; \lambda_\mu, \lambda_\sigma, \lambda_R, t_i)}{\partial \lambda_\mu} = 0 \\ \frac{\partial L}{\partial \lambda_\sigma} &= \sum_{i=0}^k \frac{1}{f_{X_i}(x_i; \lambda_\mu, \lambda_\sigma, \lambda_R, t_i)} \\ &\quad \cdot \frac{\partial f_{X_i}(x_i; \lambda_\mu, \lambda_\sigma, \lambda_R, t_i)}{\partial \lambda_\sigma} = 0 \\ \frac{\partial L}{\partial \lambda_R} &= \sum_{i=0}^k \frac{1}{f_{X_i}(x_i; \lambda_\mu, \lambda_\sigma, \lambda_R, t_i)} \\ &\quad \cdot \frac{\partial f_{X_i}(x_i; \lambda_\mu, \lambda_\sigma, \lambda_R, t_i)}{\partial \lambda_R} = 0. \end{aligned} \quad (\text{A.2})$$

Solving the above system of equations in (A.2) numerically, we can obtain the estimations of λ_σ , λ_R , λ_μ .

Case 2 (the functional form of $g_R(t_i, \lambda_R)$ is unknown). In the practical case, the degradation data used to be nonlinear and different system may be in the different degradation path so that it is difficult to model the data by the same simple model, which makes the functional form of $g_R(t_i, \lambda_R)$ unknown. For this reason, we extract the trend items $\mathbf{R}_{0:i} = \{r_0, r_1, \dots, r_i\}$ from degradation data, which reflect the variation tendency of degradation. Let $Y_i = X_i - R_i$, so it could be assumed that Y_i denotes the value of stochastic disturbance $c(t)$ at time t_i ; then the likelihood function $L(\lambda_\mu, \lambda_\sigma)$ can be represented as

$$\begin{aligned} L(\lambda_\mu, \lambda_\sigma) &= f(y_0, y_1, \dots, y_k | \lambda_\mu, \lambda_\sigma) \\ &= \prod_{i=1}^k f_{Y_i}(y_i; \lambda_\mu, \lambda_\sigma, t). \end{aligned} \quad (\text{A.3})$$

Taking its partial derivatives of all parameters, we have

$$\begin{aligned} \frac{\partial L}{\partial \lambda_\mu} &= \sum_{i=0}^k \frac{\partial f_{C_i}(c_i; \mu_c, \sigma_c)}{\partial \lambda_\mu} \\ &= \sum_{i=0}^k \frac{f'_{C_{\mu_c}}(c; g_\mu(t_i, \lambda_\mu), g_\sigma(t_i, \lambda_\sigma))}{f_C(c; g_\mu(t_i, \lambda_\mu), g_\sigma(t_i, \lambda_\sigma))} \\ &\quad \cdot \frac{\partial g_\mu(t_i, \lambda_\mu)}{\partial \lambda_\mu} = 0 \\ \frac{\partial L}{\partial \lambda_\sigma} &= \sum_{i=0}^k \frac{\partial f_{C_i}(c_i; \mu_c, \sigma_c)}{\partial \lambda_\sigma} \\ &= \sum_{i=0}^k \frac{f'_{C_{\sigma_c}}(c; g_\mu(t_i, \lambda_\mu), g_\sigma(t_i, \lambda_\sigma))}{f_C(c; g_\mu(t_i, \lambda_\mu), g_\sigma(t_i, \lambda_\sigma))} \\ &\quad \cdot \frac{\partial g_\sigma(t_i, \lambda_\sigma)}{\partial \lambda_\sigma} = 0. \end{aligned} \quad (\text{A.4})$$

λ_σ , λ_R , λ_μ can be obtained by solving the above system of equations in (A.4). Then the functional form of $g_R(t_i, \lambda_R)$ can be obtained by modeling the history of degradation observations $X_{1:k} = \{x_1, x_2, \dots, x_k\}$.

B. Change-Point Detection

We can learn that the change-point of random items mainly relies on the change of its standard deviation. It is assumed that $\mathbf{X}_{0:n} = \{x_0, x_1, \dots, x_n\}$ denote the random items, $\bar{x} = \sum_{i=0}^n (x_i/n)$, $\text{Std}_n = \sqrt{\sum_{i=0}^n ((x_i - \bar{x})^2 / (n-1))}$. It is obvious that Std_n can reflect the change of standard deviation. Therefore we propose a simple method of change-point detection. The procedure for change-point detection can be summarized as follows.

Step 1. Calculate Std_i , via the observed data $\mathbf{X}_{0:i}$.

Step 2. Define $\bar{\text{S}}_i = \sum_{j=i-m}^i (\text{Std}_j/i)$, where m denotes the length of the moving window.

Step 3. Compare $\bar{\text{S}}_{i-1}$ and Std_i ; if $\bar{\text{S}}_{i-2} < \text{Std}_{i-2}$, Std_{i-1} , and Std_i , then the $(i-2)$ th CM point is change-point; else $i = i + 1$, and repeat the Steps 2 and 3.

C. Parameter Estimation in (17)

It is obvious that the analytic solution of parameters λ'_σ , λ''_σ could not be calculated via the maximum likelihood estimation method. Fortunately, there are only two parameters that need to be evaluated, so the numerical method can be adopted. Generally the common numerical method is needed to set the initial value. We mainly discuss how to set the initial values. It is noted that Std_i , discussed in Appendix B can reflect the trend of standard deviation σ_c and is less than the real standard deviation σ_c . There is a simulation case to illustrate the proposed point. We simulate a stochastic process with two

stages: one is a normal distribution with standard deviation $\sigma_c = 1$; another is a normal stochastic process with standard deviation $\sigma_c = 0.1t - 14$, where the time of change-point is at 150. Calculate Std_i of the stochastic process and compare Std_i and the real standard deviation σ_c shown in Figure 9. From Figure 9, it is obvious that the trend of Std_i is approximate with the real standard deviation. So Std_i can be used to set the initial value of the parameters λ'_σ and λ''_σ . And if the requirement of real-time is high, Std_i can be used as obtain the approximate solution of λ'_σ and λ''_σ .

D. Parameter Estimation of Θ

Due to $p(\mathbf{Z}_{1:k}, \theta | \Theta_k) = p(\mathbf{Z}_{1:k} | \theta, \Theta_k) + p(\theta | \Theta_k)$, we can obtain

$$\begin{aligned} E_\theta [\ln p(\mathbf{Z}_{1:k}, \theta | \Theta_k)] &= -\frac{k+1}{2} \ln 2\pi - \frac{1}{2} \sum_{j=1}^k \ln(t_j - t_{j-1}) - \frac{k}{2} \ln \sigma_k^2 \\ &\quad - \sum_{j=1}^k \frac{(z_j - z_{j-1})^2 - 2\mu_{\theta,k}(t_j - t_{j-1})(z_j - z_{j-1}) + (t_j - t_{j-1})^2 (\mu_{\theta,k}^2 + \sigma_{\theta,k}^2)}{2\sigma_k^2 (t_j - t_{j-1})} - \frac{1}{2} \ln \sigma_{0,k}^2 \\ &\quad - \frac{\mu_{\theta,k}^2 + \sigma_{\theta,k}^2 - 2\mu_{\theta,k}\mu_{0,k} + \mu_{0,k}^2}{2\sigma_{0,k}^2}. \end{aligned} \quad (\text{D.1})$$

Given $\partial E_\theta [\ln p(\mathbf{Z}_{1:k}, \theta | \Theta_k)] / \partial \Theta_k = 0$, then the unknown parameter $\Theta_k = [\sigma_k^2, \mu_{0,k}, \sigma_{0,k}^2]$ can be calculated as

$$\begin{aligned} \sigma_k^{2(i+1)} &= \frac{1}{k} \sum_{j=1}^k \frac{(z_j - z_{j-1})^2 - 2\mu_{\theta,k}(t_j - t_{j-1})(z_j - z_{j-1}) + (t_j - t_{j-1})^2 (\mu_{\theta,k}^2 + \sigma_{\theta,k}^2)}{(t_j - t_{j-1})} \\ \hat{\mu}_{0,k}^{(i+1)} &= \mu_{\theta,k} \\ \hat{\sigma}_{0,k}^{2(i+1)} &= \sigma_{\theta,k}^2. \end{aligned} \quad (\text{D.2})$$

Conflicts of Interest

The authors declare that they have no conflicts of interest.

Acknowledgments

This work was partially supported by the NSFC under Grants 61573365, 61374126, 61473094, 61673311, 61603398, and 61773386 and the Yong Elite Scientists Sponsorship Program (TESS) of China Association for Science and Technology (CAST) under Grant 2016QNRC001.

References

- [1] H. Darong, K. Lanyan, C. Xiaoyan, Z. Ling, and M. Bo, "Fault diagnosis for the motor drive system of urban transit based on

$$\begin{aligned} \ln p(\mathbf{Z}_{1:k}, \theta | \Theta_k) &= \ln p(\mathbf{Z}_{1:k} | \theta, \Theta_k) + \ln p(\theta | \Theta_k) \\ &= -\frac{k+1}{2} \ln 2\pi - \frac{1}{2} \sum_{j=1}^k \ln(t_j - t_{j-1}) - \frac{k}{2} \ln \sigma_k^2 \\ &\quad - \sum_{j=1}^k \frac{(z_j - z_{j-1} - \theta(t_j - t_{j-1}))^2}{2\sigma_k^2 (t_j - t_{j-1})} - \frac{1}{2} \ln \sigma_{0,k}^2 \\ &\quad - \frac{(\theta - \mu_{0,k})^2}{2\sigma_{0,k}^2}. \end{aligned} \quad (\text{D.1})$$

Take the expectation operator on both sides of (D.1), and we can obtain

- improved Hidden Markov Model," *Microelectronics Reliability*, vol. 82, pp. 179–189, 2018.
- [2] Z. J. Zhou, G. Y. Hu, and B. C. Zhang, "A model for hidden behavior prediction of complex systems based on belief base and power set," *IEEE Transactions on Systems Man Cybernetics Systems*, vol. 99, pp. 1–7, 2017.
- [3] D. Huang, C. Chen, G. Sun, and L. Zhao, "Recognition and Diagnosis Method of Objective Entropy Weight for Power Transformer Fault," *Dianli Xitong Zidonghua/Automation of Electric Power Systems*, vol. 41, no. 12, pp. 206–211, 2017.
- [4] M. G. Pecht, *Prognostics and Health Management of Electronics*, John Wiley, New Jersey, USA, 2008.
- [5] D.-R. Huang, C.-S. Chen, G.-X. Sun, L. Zhao, and B. Mi, "Linear Discriminant Analysis and Back Propagation Neural Network Cooperative Diagnosis Method for Multiple Faults of Complex Equipment Bearings," *Acta Armamentarii*, vol. 38, no. 8, pp. 1649–1657, 2017.

- [6] M. Mesbahul Alam and K. Suzuki, "Lifetime estimation using only failure information from warranty database," *IEEE Transactions on Reliability*, vol. 58, no. 4, pp. 573–582, 2009.
- [7] X.-S. Si, W. Wang, C.-H. Hu, and D.-H. Zhou, "Remaining useful life estimation—a review on the statistical data driven approaches," *European Journal of Operational Research*, vol. 213, no. 1, pp. 1–14, 2011.
- [8] X.-S. Si, W. Wang, C.-H. Hu, M.-Y. Chen, and D.-H. Zhou, "A Wiener-process-based degradation model with a recursive filter algorithm for remaining useful life estimation," *Mechanical Systems and Signal Processing*, vol. 35, no. 1-2, pp. 219–237, 2013.
- [9] N. Z. Gebraeel, M. A. Lawley, R. Li, and J. K. Ryan, "Residual-life distributions from component degradation signals: a Bayesian approach," *IIE Transactions*, vol. 37, no. 6, pp. 543–557, 2005.
- [10] S.-T. Tseng, J. Tang, and I.-H. Ku, "Determination of burn-in parameters and residual life for highly reliable products," *Naval Research Logistics (NRL)*, vol. 50, no. 1, pp. 1–14, 2003.
- [11] C. Hu, Z. Zhou, J. Zhang, and X. Si, "A survey on life prediction of equipment," *Chinese Journal of Aeronautics*, vol. 28, pp. 25–33, 2015.
- [12] C.-Y. Peng and S.-T. Tseng, "Mis-specification analysis of linear degradation models," *IEEE Transactions on Reliability*, vol. 58, no. 3, pp. 444–455, 2009.
- [13] H. Darong, T. Jianping, and Z. Ling, "A fault diagnosis method of power systems based on gray system theory," *Mathematical Problems in Engineering*, vol. 2015, Article ID 971257, 2015.
- [14] N. E. Huang, Z. Shen, S. R. Long et al., "The empirical mode decomposition and the Hilbert spectrum for nonlinear and non-stationary time series analysis," *Proceedings A*, vol. 454, pp. 903–995, 1998.
- [15] R. Yan and R. X. Gao, "A tour of the tour of the Hilbert-Huang transform: An empirical tool for signal analysis," *IEEE Instrumentation & Measurement Magazine*, vol. 10, no. 5, pp. 40–45, 2007.
- [16] G. Rilling, P. Flandrin, and P. Goncalves, *On empirical mode decomposition and its algorithms*, France, 2003.
- [17] W. Wang, "A two-stage prognosis model in condition based maintenance," *European Journal of Operational Research*, vol. 182, no. 3, pp. 1177–1187, 2007.
- [18] E. T. Lee and J. W. Wang, *Statistical methods for survival data analysis*, Wiley Series in Probability and Statistics, John Wiley & Sons, Inc., Fourth edition, 2013.
- [19] X.-L. Meng and D. B. Rubin, "Maximum likelihood estimation via the ECM algorithm: a general framework," *Biometrika*, vol. 80, no. 2, pp. 267–278, 1993.
- [20] X.-S. Si, W. Wang, M.-Y. Chen, C.-H. Hu, and D.-H. Zhou, "A degradation path-dependent approach for remaining useful life estimation with an exact and closed-form solution," *European Journal of Operational Research*, vol. 226, no. 1, pp. 53–66, 2013.
- [21] C. F. J. Wu, "On the convergence properties of the EM algorithm," *The Annals of Statistics*, vol. 11, no. 1, pp. 95–103, 1983.
- [22] T. B. Schön, A. Wills, and B. Ninness, "System identification of nonlinear state-space models," *Automatica*, vol. 47, no. 1, pp. 39–49, 2011.
- [23] W. Wang, M. Carr, W. Xu, and K. Kobbacy, "A model for residual life prediction based on Brownian motion with an adaptive drift," *Microelectronics Reliability*, vol. 51, no. 2, pp. 285–293, 2011.